UNIVERSIDADE FEDERAL DE MINAS GERAIS
Instituto de Ciências Exatas
Programa de Pós-graduação em Física

Renan Souza Cunha

# Nonlinear optics in amyloid plaques and two-dimensional materials

Belo Horizonte

2021

Renan Souza Cunha

# Nonlinear optics in amyloid plaques and two-dimensional materials

Tese de doutorado apresentada ao Programa de Pós-graduação em Física da Universidade Federal de Minas Gerais como requisito parcial para a obtenção do título de Doutor em Física.

Orientador: Prof. Dr. Leandro Malard Moreira

Belo Horizonte

2021

Dados Internacionais de Catalogação na Publicação (CIP)

C972n Cunha, Renan Souza.
Nonlinear optics in amyloid plaques and two-dimensional materials / Renan Souza Cunha. – 2021.
149f., enc. : il.

Orientador: Leandro Malard Moreira.
Tese (doutorado) – Universidade Federal de Minas Gerais, Departamento de Física.
Bibliografia: f. 122-145.

1. Óptica não-linear. 2. Espalhamento Raman. 3. Fluorescência. 4. Doença de Alzheimer. 5. Nitreto de boro. I. Título. II. Moreira, Leandro Malard. III. Universidade Federal de Minas Gerais, Departamento de Física.

CDU – 535 (043)

Ficha catalográfica elaborada por Romário Martins Ribeiro – CRB6 3595
Biblioteca Professor Manoel Lopes de Siqueira – Departamento de Física - UFMG

UNIVERSIDADE FEDERAL DE MINAS GERAIS
**INSTITUTO DE CIÊNCIAS EXATAS**
**PROGRAMA DE PÓS-GRADUAÇÃO EM FÍSICA**

## FOLHA DE APROVAÇÃO

A presente tese, intitulada **"Nonlinear optics in amyloid plaques and two-dimensional materials"** de autoria de **RENAN SOUZA CUNHA** submetida à Comissão Examinadora, abaixo-assinada, foi aprovada para obtenção do grau de **DOUTOR EM CIÊNCIAS**, em vinte e cinco de novembro de 2021.

Belo Horizonte, 25 de novembro de 2021.

| | |
|---|---|
| Prof. Leandro Malard Moreira | Profa. Ariete Righi |
| Orientador do estudante | Departamento de Física/UFMG |
| Departamento de Física/UFMG | |
| Profa. Ana Maria de Paula | Prof. Cid Bartolomeu de Araújo |
| Departamento de Física/UFMG | Departamento de Física/UFPE |

Prof. Luciano Bachmann
Faculdade de Filosofia, Ciências e Letras/USP-RP

Documento assinado eletronicamente por **Ana Maria de Paula**, **Professora do Magistério Superior**, em 25/11/2021, às 14:05, conforme horário oficial de Brasília, com fundamento no art. 5º do Decreto nº 10.543, de 13 de novembro de 2020.

Documento assinado eletronicamente por **Luciano Bachmann**, **Usuário Externo**, em 25/11/2021, às 14:12, conforme horário oficial de Brasília, com fundamento no art. 5º do Decreto nº 10.543, de 13 de novembro de 2020.

Documento assinado eletronicamente por **Ariete Righi**, **Professora do Magistério Superior**, em 25/11/2021, às 15:39, conforme horário oficial de Brasília, com fundamento no art. 5º do Decreto nº 10.543, de 13 de novembro de 2020.

Documento assinado eletronicamente por **Leandro Malard Moreira**, **Professor do Magistério Superior**, em 26/11/2021, às 20:28, conforme horário oficial de Brasília, com fundamento no art. 5º do Decreto nº 10.543, de 13 de novembro de 2020.

Documento assinado eletronicamente por **Cid Bartolomeu de Araújo**, **Usuário Externo**, em 27/11/2021, às 11:55, conforme horário oficial de Brasília, com fundamento no art. 5º do Decreto nº 10.543, de 13 de novembro de 2020.

A autenticidade deste documento pode ser conferida no site https://sei.ufmg.br/sei/controlador_externo.php?acao=documento_conferir&id_orgao_acesso_externo=0, informando o código verificador **1104576** e o código CRC **4D14E580**.

**Referência:** Processo nº 23072.260972/2021-46 SEI nº 1104576

# Agradecimentos

Chegar ao término de uma tese de doutorado é resultado de privilégios de vários tipos e esforços de várias partes. Por esse motivo, não serei capaz de citar todos que foram importantes nesse processo. Mas desejo que todos que contribuíram para tornar este documento possível saibam que essa é uma realização com projeções em cada um. Minha gratidão a todos.

Em especial, agradeço ao meu querido Deus, Jesus Cristo, pela maior de todas as providências. Da motivação ao cuidado de cada dia. Pelo amor de tornar tudo possível, nos seus mínimos detalhes. À Ele todas as coisas. *Ut ex invisibilibus visibilia fierent. Soli Deo Gloria*.

À minha amada esposa, Paula D'Ávila, que correu essa maratona comigo desde a graduação, sendo ela mesma uma das corredoras. Esta tese não é só resultado de apoio e companheirismo, mas também de inspiração pela talentosa e determinada competência que ela demonstra na física e na vida.

Aos meus amados pais pelo carinho, suporte, presença constante, amor e por conduzirem a trajetória, sempre me dirigindo aos mais altos valores. Esta tese não é mais minha do que deles.

Ao meu querido irmão pela melhor amizade e pelos inúmeros conselhos. Por todas as lutas que venceu comigo.

À minha grande família que me apoiou de várias formas. Avôs, avós, tios, tias, sogro e sogra, primos e primas que estiveram bem perto. Também à minha família da igreja IPBV por todo suporte de perto e em orações. Me perdoem por todos os churrascos que faltei por causa do doutorado!

Ao meu caro orientador professor Leandro Malard Moreira (Xubaka) por me aceitar como aluno e ter uma invejável paciência. Uma orientação que vai me marcar sempre e vai servir de modelo para mim mesmo. Da competência técnica à amizade. Sou grato pelo tanto que aprendi. E não só minha gratidão, mas meu enorme respeito e admiração. Espero que eu ainda possa retribuir o tanto que me foi oportunizado!

Aos professores Ado, Xubaka e Luiz Gustavo (Gusta) pela amizade, pelos conselhos e pelo excelente ambiente de convivência. Por tornar o Laboratório de Nanoespectroscopia (LabNS) um espaço extremamente favorável à colaboração científica multidisciplinar, ao crescimento profissional e ao entusiasmo e satisfação na ciência.

Aos meus companheiros de mesa óptica, Lucas Lafetá e Emerson Fonseca, cuja competência só ousa ser equiparada à ranzinzice. Agradeço a parceria, ensinamentos, colaborações e risadas.

À toda equipe do Alzheimer pelas colaborações e discussões. Foi um tempo excelente!

Agradeço à Márcia pelo profissionalismo e eficiência. Ao professor Rafael e ao Alexandre por tantas dúvidas respondidas. Ao João pela expertise nos dados. Ao professor Marco Aurélio pela infraestrutura e a colaboração que agora se estende no pós-doutorado na Faculdade de Medicina.

I thank Professor Igor Aharonovich, Professor Alexander Solntsev, and Dr. Sejeong Kim from the School of Mathematical and Physical Sciences at the University of Technology Sydney for collaborating with one of the samples studied in the thesis and for all the valuable discussions. Ao Sérgio do CT Nano e ao Alisson do Laboratório de Nanomateriais pelas colaborações.

Aos vários colegas do LabNS pela convivência diária ao longo do doutorado, soluções, risadas e cafés. Cassiano (Cacá), Hudson (Hudim), Filomeno (Filozim), Vítor (Vitão), Tiago (Tiagão), Liliane, Frederico (Fred), Bárbara, Plínio, Fabiano, Catarina, Katherine, Gustavo, Mateus, Áurea, pequeno Lucas, Rafael Nadas, Andreij, Douglas, Arthur, Danilo, Fabiano, Ana Clara.

Aos professores do Departamento de Física pelas instruções e conversas através das quais pude crescer muito. Agradeço até àqueles que me assustaram com provas que foram mais difíceis do que eu esperava! Aos professores que também contribuíram com idéias pelos corredores, empréstimo de equipamentos e elementos ópticos que serviram ao término dos projetos. Aqui destaco a professora Ariete, o professor Ubirajara (Bira) e a professora Ana Maria (Aninha). Aos professores Carlos Heitor, Plascak, Emmanuel, Monken, Mario Sérgio, Ubirajara (Bira), Elmo, Edmar e Wagner Nunes por terem sido modelos no ensino de física. Minha primeira experiência com uma turma de Fundamentos de Eletromagnetismo no estágio docente foi um tipo de combinação linear dos exemplos e posturas de cada um. Experiência excelente com uma turma incrível!

Também agradeço imensamente aos funcionários do departamento: secretarias, biblioteca, serviços gerais. Em particular, agradeço à Shirley, Gislene, Juliana, Ana Luiza e Marília pelos vários anos de convivência, excelente dedicação e diligência.

Aos colegas do departamento por tantos anos de convivência. Em especial, agradeço ao Sexteto (por ordem de tamanho: Hobbit, Leozim, Mateus, Paulo e Wescley), à Ana Paula, Arthur Matoso (Tutu), Davi, Flavio, Sheilla e minha turminha da época de graduação.

Agradeço à banca examinadora da tese de doutorado pela experiência de defesa e por todas as valiosas correções e contribuições.

Agradeço ao CNPq, à CAPES, à FAPEMIG, à Finep pelo financiamento de bolsas, projetos e congressos que tornam a ciência brasileira possível e tornou possível meu contínuo aprendizado.

***"...poi che due veri non possono mai contrariarsi."***

Galileo Galilei, Lettera a Madama Cristina di Lorena, Granduchessa di Toscana, 1615.

# Resumo

O estudo de interações luz-matéria é uma ampla área de pesquisa, descrevendo processos ópticos desde a reflexão em superfícies especulares em óptica geométrica até a dinâmica de átomos e fótons em eletrodinâmica quântica de cavidades. Dentro desse quadro está a óptica não linear, que engloba fenômenos que surgem devido à incidência de campos intensos na matéria. Uma vez que este ano marca sessenta anos desde o nascimento da óptica não linear moderna, a pesquisa nesta área evoluiu para diferentes tópicos, de estudos fundamentais a aplicações em ciência dos materiais e até em biomedicina. Esta tese está no escopo do último grupo: óptica não linear experimental para imageamento de tecidos biológicos e materiais bidimensionais (2D). Primeiro apresentamos um estudo baseado em imageamento multimodal para caracterização histopatológica de placas de beta-amilóide (Aβ) em um modelo animal de doença de Alzheimer (AD). Sem a utilização de marcadores exógenos, exploramos a fluorescência por excitação por dois fótons (TPEF), geração de segundo harmônico (SHG), espalhamento Raman espontâneo (SpRS), espalhamento Raman anti-Stokes coerente (CARS) e espalhamento Raman estimulado (SRS) para descrever e comparar imagens de placas de Aβ, principal traço da AD, em tecidos cerebrais de camundongos transgênicos. As imagens obtidas permitem localizar diferentes estruturas da placa de forma confiável e discutir a origem ainda pouco clara da SHG na placa. Também estudamos a viabilidade do imageamento SRS da placa com base em dois biomarcadores ópticos intrínsecos inexplorados com técnicas de espalhamento Raman coerente (CRS). Em um segundo trabalho, estudamos os efeitos de mudanças estruturais em um material 2D sobre a SHG. Em particular, estudamos modificações ópticas induzidas por defeitos em nitreto de boro hexagonal (h-BN). Realizando imageamento e espectroscopia de luminescência por excitação por um fóton (1PL), encontramos flocos de h-BN defeituosos cuja SHG exibiu desvios do comportamento esperado para o h-BN puro. Nossos resultados mostram que os defeitos modificam o perfil de intensidade, dependência de polarização e eficiência da SHG no h-BN. Além disso, caracterizamos a susceptibilidade de segunda ordem do h-BN com defeitos com um valor de uma ordem de grandeza maior que para o h-BN puro.

**Palavras-chave**: Óptica não-linear. Espalhamento Raman estimulado. Espalhamento Raman anti-Stokes coerente. Fluorescência por excitação por dois fótons. Geração de segundo harmônico. Doença de Alzheimer. Nitreto de boro hexagonal.

# Abstract

The study of light-matter interactions is a broad research area, describing optical processes from reflection on specular surfaces in geometric optics to the dynamics of atoms and photons in cavity quantum electrodynamics. Within that framework is nonlinear optics, which encompasses phenomena that arise due to the incidence of intense fields in matter. As this year marks sixty years since the birth of modern nonlinear optics, research in this area has evolved into different topics, ranging from fundamental studies to applications in material science and even in biomedicine. This thesis lies within the scope of the last group: experimental nonlinear optics for imaging biological tissues and two-dimensional (2D) materials. We first present a study based on multimodal imaging for histopathological characterization of amyloid-beta (Aβ) plaques in an animal model of Alzheimer's disease (AD). We explore label-free two-photon excitation fluorescence (TPEF), second harmonic generation (SHG), spontaneous Raman scattering (SpRS), coherent anti-Stokes Raman scattering (CARS), and stimulated Raman scattering (SRS) to describe and compare images of Aβ plaques, the main hallmark of AD, in brain tissues of transgenic mice. The obtained images allow for locating different plaque structures reliably and discussing the still unclear origin of SHG in the plaque. We also study the feasibility of SRS imaging of the plaque based on two intrinsic optical biomarkers unexplored with coherent Raman scattering (CRS) techniques. In a second work, we study the effects of structural changes in a 2D material on SHG. In particular, we study defects-induced optical modifications in hexagonal boron nitride (h-BN). Performing one-photon excitation luminescence (1PL) imaging and spectroscopy, we found defective h-BN flakes whose SHG exhibited deviations from the expected behavior for pristine h-BN. Our results show that defects modify the intensity profile, polarization dependence, and efficiency of SHG in h-BN. Additionally, we characterized the second-order susceptibility of h-BN with defects with a value of one order of magnitude larger than for pristine h-BN.

**Keywords**: Nonlinear optics. Stimulated Raman scattering. Coherent anti-Stokes Raman scattering. Two-photon excitation fluorescence. Second harmonic generation. Alzheimer's disease. Hexagonal boron nitride.

# List of abbreviations and acronyms

**α-helix** Alpha-helix

**AD** Alzheimer's disease

**Aβ** Amyloid-beta

**AFM** Atomic force microscopy

**β-sheet** Beta-sheet

**AOM** Classical anharmonic oscillator model

**CARS** Coherent anti-Stokes Raman scattering

**CRS** Coherent Raman scattering

**CSRS** Coherent Stokes Raman scattering

**CRM** Confocal Raman microscopy

**CW** Continuous-wave

**XPM** Cross-phase modulation

**DFWM** Degenerate four-wave mixing

**DTWM** Degenerate three-wave mixing

**DFG** Difference frequency generation

**FWM** Four-wave mixing

**h-BN** Hexagonal boron nitride

**LOM** Lorentz oscillator model

**$MoS_2$** Molybdenum disulfide

**NIR** Near-infrared

**NUV** Near-ultraviolet

**NA** Numerical aperture

**1PL** One-photon excitation luminescence

**OPO** Optical parametric oscillator

**PFA** Paraformaldehyde

**Phe** Phenylalanine

**PBS** Phosphate-buffered saline

**RIN** Relative intensity noise

**SHG** Second harmonic generation

**SBR** Signal-to-background ratio

**SNR** Signal-to-noise ratio

**SpRS** Spontaneous Raman scattering

**SRG** Stimulated Raman gain

**SRL** Stimulated Raman loss

**SRS** Stimulated Raman scattering

**SFG** Sum frequency generation

**SERS** Surface enhanced Raman scattering

**ThioS** Thioflavin S

**TWM** Three-wave mixing

**TMD** Transition metal dichalcogenide

**TPEA** Two-photon excitation autofluorescence

**TPEF** Two-photon excitation fluorescence

**2PL** Two-photon excitation luminescence

**UV** Ultraviolet

# Contents

# Chapter 1

# Introduction

The way in which electromagnetic radiation interacts with matter can depend on a number of aspects. For example, the answer to "why is this object blue?" may be completely different whether the object is a solid or a gas. Even more curious, the color of certain objects can dramatically depend on their dimensions. Other objects may be able to reflect radiation of one wavelength but transmit others. There is also a type of light-matter interaction in which certain phenomena are only observed when the light intensity is sufficiently high. This last condition interests us most in this thesis and gives rise to a myriad of optical effects which lie within the scope of *nonlinear optics*.

## 1.1 A brief history of nonlinear optics

The origin of nonlinear optics dates back to the late 19th century. Some precursors of nonlinear optical effects, such as acoustic nonlinearities, were already known in this period. John Strutt, better known as Lord Rayleigh, discussed some implications of these nonlinearities in his *Theory of Sound* [1, 2]. At about the same time, John Kerr studied electric nonlinearities. In 1875, he showed that the refractive index of different materials was slightly altered when applying a strong DC electric field so that the variation depended on the square of the field amplitude [3]. A few years later, in 1893, Friedrich Pockels showed that the refractive index variation in centrosymmetric materials depended linearly on the field amplitude [4]. An important phenomenological model of the interaction of electric fields with matter was proposed by Hendrik Lorentz in 1876 [5]. Preceding the discovery of the atomic nucleus bound to electrons, Lorentz considered matter as composed of electric dipoles connected by springs, exhibiting harmonic oscillations. His electromechanical description was successful in accounting for linear optical effects. As suggested by Nicolaas Bloembergen, if Lorentz had considered a slight anharmonicity in his model, these precursor events could have allowed the prediction of nonlinear optical effects on purely classical grounds [6]. However, the first steps toward the modern formulation of nonlinear optics begin with Maria Göppert-Mayer's doctoral thesis in 1931, with the quantum mechanical proposition of the simultaneous absorption of two photons by an atom [7].

What all the effects above have in common is the need for intense fields to be observed. For this reason, the discovery of laser action in 1960 was a critical point in nonlinear optics, paving the way for the manipulation of strong light fields [4]. In the following year, the first experimental observation of second harmonic generation (SHG) marked the birth of modern nonlinear optics. Franken *et al.* observed ultraviolet light emission at 347.15 nm ($\lambda/2$) from a quartz crystal excited with a ruby laser at 694.30 nm ($\lambda$) [8]. The advent of the laser was so fruitful for nonlinear optics that several of the best-known effects today were quickly discovered. The first observation of two-photon excitation fluorescence (TPEF), verifying the work of Göppert-Mayer, was also reported in 1961 [9]. Shortly after, stimulated Raman scattering (SRS) was discovered accidentally by Woodbury and Ng, and Eckhardt *et al.* in 1962 during experiments on Q-switching [10, 11]. In 1965, while studying different wave mixing effects, Maker and Terhune discovered a vibrationally resonant four-wave mixing (FWM), later called coherent anti-Stokes Raman scattering (CARS) [12]. Figure 1.1 illustrates the rapid development of nonlinear optics, showing a historical comparison between nonlinear optical laws and their linear counterpart.

| | Linear | Nonlinear |
|---|---|---|
| Law of reflection | 1st century (Hero of Alexandria) | 1962 (Bloembergen and Pershan) |
| Law of refraction | 1621 (Snell) | 1962 (Bloembergen and Pershan) |
| Intensity of reflected and refracted light | 1823 (Fresnel) | 1962 (Bloembergen and Pershan) |
| Conical refraction | | |
| Theory | 1833 (Hamilton) | 1969 (Bloembergen and Shih) |
| Experiment | 1833 (Lloyd) | 1977 (Schell and Bloembergen) |

Figure 1.1: Historical dates of linear and nonlinear optical laws. Adapted from reference [13].

With such rapid growth, it would not be surprising that nonlinear optics would find a place beyond fundamental physics. Currently, nonlinear optics covers multidisciplinary topics in basic and applied sciences, ranging from solid-state physics to biomedicine [14–17]. While many pioneering works in such topics have benefited from spectroscopic techniques, the potential of nonlinear optics for imaging was quickly recognized due to its intrinsic properties. One of the catalyst of this approach was the development of microscopy techniques with intrinsic three-dimensional (3D) sectioning based on SHG [18, 19], but especially the demonstration of a biocompatible microscope based on TPEF by Denk *et al.* in 1990 [20]. A few years later, similar techniques based on the other effects mentioned above were also developed [21]—some even recently, such as SRS microscopy [22, 23]. Once again, advances in nonlinear optics accompanied the development of new laser technologies [24], particularly the generation of ultra-short pulses.

Today, the association between laser science and the intrinsic properties of nonlinear effects

made room for investigating a wide variety of ultrafast phenomena, from the picosecond to the attosecond scale. The technological applications of this association reach diagnostic tools and even surgical centers. We will revisit several concepts introduced in this section throughout the text, highlighting the advantageous intrinsic properties of nonlinear effects for optical imaging.

## 1.2 Background and contributions

The fundamental aspects of nonlinear optical effects relevant for this thesis are their label-free and multiphoton nature, allowing the study of biological and 2D materials through, non-destructive, rapid, and optically sectioned imaging. That resulted in the publication of two main papers [25, 26].

In the first, we characterized Aβ plaques by label-free nonlinear imaging. We focused on three objectives: (1) to obtain higher quality images to enable a reliable characterization of Aβ plaques; (2) To identify and compare different structures of the same plaque by multimodal imaging; (3) To test the viability of vibrational biomarkers unexplored with SRS microscopy in different regions of the biological spectrum, emphasizing the imaging of the core.

In recent years, optical imaging has been part of AD research through the characterization of optical biomarkers provided by Aβ plaques in brain tissues [27]. The presence of Aβ plaques is the main histopathological change that allows discriminating an Alzheimer's brain tissue from normal tissue, being of great value for research in the early diagnosis of AD. Implementing rapid, label-free techniques is especially useful, as it enables the investigation of AD in-vivo without disturbing the studied environment. Previous studies reported label-free nonlinear imaging of Aβ plaques [28–33]. However, the images were presented with low contrast. The only published paper using SRS microscopy to study Aβ plaques presented images with higher contrast [33], however the investigation restricted the imaging of the core to the amide I vibrational mode. Our contribution addresses the above aspects of histopathological characterization of AD. We implemented a multimodal imaging, characterizing Aβ plaques through SpRS, SHG, TPEF, CARS, and SRS with high contrast, clearly showing different structures and discussing the possible origin of each signal. We also investigated the feasibility of SRS imaging beyond amide I. In particular, we imaged the plaque core through the vibrational mode of phenylalanine in the fingerprint region, unexplored with SRS microscopy, and the vibrational mode of amide B in the high-wavenumber region, unexplored with CRS microscopy.

The paper involved a multidisciplinary collaboration, and the three following authors shared the main authorship. The author of this thesis was primarily responsible for implementing the SRS microscopy technique, processing the images, analyzing the results, writing the manuscript, and obtaining some images. Lucas Lafeta was primarily responsible for obtaining the images, contributing to most of the images present in the paper. Emerson Fonseca was primarily responsible for preparing the samples and obtaining the hyperspectral images.

In the second paper, we studied defects-induced modifications on the SHG properties in

h-BN. We focused on two objectives: (1) to study the properties of SHG in h-BN flakes that exhibit 1PL of defects, some of which were generated by annealing protocols and were previously reported as single-photon emitters defects in samples obtained by liquid exfoliation; (2) To characterize the second-order electric susceptibility of the material.

Although the influence of defects on SHG is known for some materials [34–37], the study of SHG in 2D materials is a recent topic, and several works report the characterization of SHG in samples with low defects density [38–43]. In the case of h-BN, the SHG intensity profile as a function of the number of layers, its dependence on incident polarization, and second-order susceptibility were determined for mechanically exfoliated pristine samples [39]. Our contribution addresses the influence of different defects on SHG in h-BN. Instead of mechanically exfoliated samples, we studied h-BN samples obtained by liquid exfoliation. Such samples have recently been used in the characterization of single-photon emitter defects generated by simple annealing protocols [44–47]. At the time of our publication [26], no experimental report had demonstrated the influence of defects on the second-order nonlinear optical properties in such h-BN samples. Our results showed defects-induced modifications in the intensity profile, polarization dependence, and efficiency of SHG. We also characterized the second-order susceptibility of h-BN with defects with a value of one order of magnitude larger than for pristine h-BN [39].

The paper involved a collaboration with the School of Mathematical and Physical Sciences at the University of Technology Sydney. The sample with defects was prepared by the Aharonovich group, while the pristine sample was prepared by Alisson Cadore. The author of this thesis is the main author of the paper and was primarily responsible for obtaining and processing the images, analyzing the results, and writing the manuscript.

The study developed in the doctoral program also led to the publication of another five works, listed in section 5.2.

## 1.3 Structure and organization

The thesis is organized to allow a brief theoretical and experimental introduction to nonlinear optics. All chapters present a review of the subject to be discussed.

In chapter 2, we review the main concepts of nonlinear optics from classical models of light-matter interaction. We discuss the linear and nonlinear regimes and, mainly, present the optical effects explored in the thesis. We discuss the fundamentals of each of the effects, as well as their experimental implementation.

In chapter 3, we present the nonlinear optical effects discussed in chapter 2 in the context of biological imaging. We introduce general features of biological imaging and nonlinear optical microscopy, and we mainly review the role of CRS imaging in biomedicine. We present our work on multimodal imaging of brain tissues of an animal model of AD and a perspective on the study of the retina of the same animal model.

In chapter 4, we explore SHG imaging of 2D materials and the SHG dependence on structural properties of materials. We present our work on SHG in h-BN with defects, reporting

defects-induced modifications to the known SHG properties in pristine h-BN. Appendix A presents additional spectra of some of the defects found in our h-BN sample, while appendix B presents a calculation of the expected dependence of SHG in pristine h-BN on the incident laser polarization in our experimental setup. Appendix C shows a perspective of studying different materials through imaging based on third-order nonlinearities.

Finally, chapter 5 presents the conclusions of the thesis and the related list of publications.

# Chapter 2

# Light-matter interactions

## 2.1 Introductory remarks

In order to understand how nonlinear optics can be applied to the problems of interest in this thesis, it is first necessary to discriminate between the linear and nonlinear regimes. For that, we start with classical models of the interaction of light with matter to obtain an intuition about the microscopic origin of optical phenomena mediated by material media. In section 2.2, the LOM allows us to establish the limits at which optical phenomena fall within the scope of linear optics. Two important linear effects are SpRS and 1PL discussed in section 2.3. From the limits defined in linear optics, the AOM offers a generalization of the Lorentz treatment and allows us to discuss the origin of nonlinear optical phenomena in section 2.4. In this approach, we find the three central effects explored in this thesis: wave mixing in section 2.5, 2PL (also known as TPEF) in section 2.6, and CRS in section 2.7.

## 2.2 Linear optics

Whenever an electromagnetic field interacts with a medium, the electric field $E(t)$ distorts the charge distribution, inducing new dipoles or orienting pre-existing ones [5,15,48,49]. Positive bound charges are displaced in the direction of the field, while negative bound charges are displaced in the opposite direction, and the collection of dipoles give rise to a macroscopic polarization $P(t)$. Maxwell's equations in nonmagnetic matter with no free charges and currents allow us to relate the incident field $E(t)$ and the induced macroscopic polarization $P(t)$ through the wave equation [15]. Restricting ourselves only to a scalar description[1],

$$\nabla^2 E(t) - \frac{1}{c^2}\frac{\partial^2 E(t)}{\partial t^2} = \frac{1}{\epsilon_0 c^2}\frac{\partial^2 P(t)}{\partial t^2}, \tag{2.1}$$

where $\epsilon_0$ is the permittivity of free space and $c$ is the speed of light in vacuum.

[1] If $P(t)$ is a general polarization state (as will be discussed later), obtaining expression (2.1) involves further approximations. A discussion of the validity of such approximations can be found at [15].

In order to appreciate the role of polarization in equation (2.1), it is instructive to examine a simple model in the classical picture, as we do in section 2.2.1.

### 2.2.1 The Lorentz harmonic oscillator model

Figure 2.1A is an illustration of the Lorentz oscillator model (LOM), in which electrons are coupled to the stationary atomic nucleus through springs [5, 15, 48]. Driven by the external monocromatic field $E(t)$ oscillating at a frequency $\omega$ along the dipole axis, the electron moves in the opposite direction of the field and has its motion restored by the binding force associated with the Coulomb atomic potential [50], as in figure 2.1B. The displacement $x(t)$ from the equilibrium position defines the time-varying separation of the electric dipole. If this

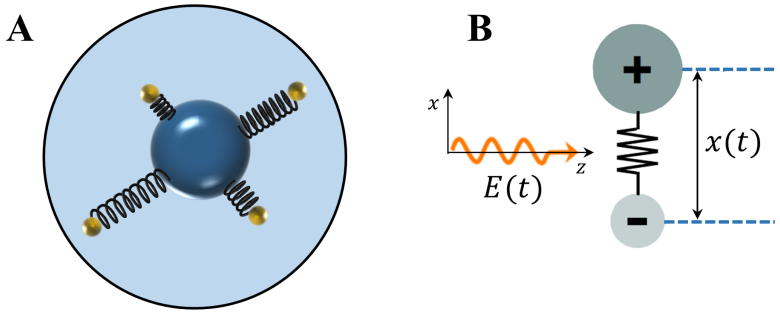


Figure 2.1: The Lorentz harmonic oscillator model. (A) The electrons (small, yellow spheres) are bound to the heavy, stationary nucleus (large, blue sphere) through springs (black), which represent the restoring forces. (B) The displacement of an atomic dipole from equilibrium position is treated classically as a damped harmonic oscillator forced by the electric field of light. Adapted from references [5, 51].

displacement is small enough, the motion of the oscillating dipole can be treated as a damped harmonic oscillator driven by the electric field:

$$\frac{d^2x(t)}{dt^2} + \gamma\frac{dx(t)}{dt} + \omega_0^2 x(t) = -eE(t)/m. \tag{2.2}$$

Here, the damping factor $\gamma$ is associated with loss of energy by the dipole [5, 51], $\omega_0$ is the natural frequency of the oscillator, while $-e$ and $m$ are, respectively, the charge and mass of the electron[2]. The small-displacement approximation can be understood through figure 2.2, which represents a more realistic interaction potential between an electron and an atomic nucleus. The third term in expression (2.2) indicates the parabolic potential regime (dashed, red parabola) represented in figure 2.2, in which the electron motion is subjected to a linear restoring force. This regime is a valid approximation when the incident field amplitude is small [15]. Physically, it is equivalent to using low-intensity light, so that the electron is only slightly distorted from its equilibrium position.

[2]More generally, it is necessary to introduce the mass of the dipole through the reduced mass given by $\mu = \frac{Mm}{M+m}$, where $M$ ($m$) is the mass of the nucleus (electron). However, the condition that the nucleus has a much greater mass ($M \gg m$) simplifies the expression. In this case, $\mu \approx m$.

Due to the applied field $E(t)$, the displacement of the electron from its equilibrium position produces a time-varying dipole moment $p(t) = -ex(t)$. For a medium with $N$ dipoles per

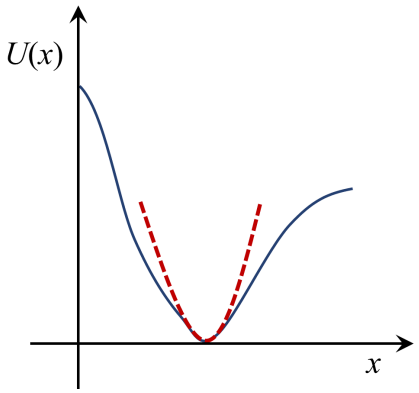


Figure 2.2: Illustration of the small-displacement approximation. The dipole binding potential (blue) can be approximated by a parabolic potential (red) when a low-intensity electric field produce only small displacements from the dipole equilibrium position.

unit volume, the macroscopic polarization is simply $P(t) = -Nex(t)$. Solutions to equation (2.2) lead to a linear relation between $P(t)$ and $E(t)$, from which the electric susceptibility of the medium can be defined [5, 15, 48]. Thus, the linear relation between the macroscopic polarization and the electric field can be written as the textbook expression

$$P^{(1)}(t) = \epsilon_0 \chi^{(1)} E(t), \tag{2.3}$$

where $\chi^{(1)}$ is presented as the electric susceptibility of the medium, a complex quantity related to the refractive index by $n_0^2 = 1+\chi^{(1)}$ [48]. Expression (2.3) defines a *linear medium* and light-matter interactions where the incident field produces a polarization described by expression (2.3) lie within the scope of *linear optics*. This is why we changed the notation $P(t)$ for any polarization state to the notation $P^{(1)}(t)$ for the linear (or first-order) case. Similarly, in this text, we shall refer to $\chi^{(1)}$ as the *linear* (or first-order) electric susceptibility.

### 2.2.2 The wave equation and linear optical parameters

Considering the relation between $n_0$ and $\chi^{(1)}$ and inserting expression (2.3) into (2.1), the wave equation (2.1) becomes

$$\nabla^2 E(t) - \frac{n_0^2}{c^2} \frac{\partial^2 E(t)}{\partial t^2} = 0. \tag{2.4}$$

And it is also interesting to analyze the wave equation (2.4) together with three macroscopic optical parameters derived from the classical model and related to the linear susceptibility [50]:

$$n_0 \propto Re\{\chi^{(1)}\}, \tag{2.5}$$

$$\alpha_0 \propto Im\{\chi^{(1)}\}, \tag{2.6}$$

$$I \propto \left|\chi^{(1)}\right|^2, \tag{2.7}$$

where $\alpha_0$ is the linear absorption coefficient and $I$ is the intensity of the radiated wave.

In expression (2.4), interaction of the field with a linear medium leads to a homogeneous wave equation, without source terms, and modifies the expression through the refractive index in equation (2.4). The absence of source terms is associated with the non-generation of new frequencies (in an effect known as wave mixing, discussed in section 2.5). This is a consequence of the superposition principle, which holds true in linear optics [15]. The refractive index, in turn, describes the propagation of the wave through the medium and is related to the real part of the electric susceptibility, as in expression (2.5). In the linear case, $n_0$ typically depends on the frequency of the incident field, while is independent of its intensity [15]. This case typically accounts for the optical effects in ray optics. As the wave propagates, the model also accounts for scattering in the medium, which can depend on frequency as well, such as in Rayleigh scattering [5]. If the frequency of the incident field is close to the natural frequency $\omega_0$ of the dipoles, the medium can absorb light, which is quantified by the absorption coefficient $\alpha_0$ [5]. In the linear case, where $\alpha_0$ is related to the imaginary part of $\chi^{(1)}$, scattering and absorption are also independent of the intensity of the incident electric field [15]. Although both effects are treated as loss mechanisms in the medium, they can participate in radiative processes: the first, through elastic and inelastic linear scattering, and the second, through linear photoluminescence (1PL). In all cases, the intensity of light leaving the medium is related to the square modulus of the linear susceptibility, as in expression (2.7), and scales linearly with the intensity of the incident electric field [50]. Since the model presented so far can not fully describe photoluminescence and inelastic scattering, we review these effects in the following section.

## 2.3 Linear scattering and linear photoluminescence

In photoluminescence, a medium illuminated with light of frequency $\omega$ usually emits redshifted (or Stokes shifted) light spontaneously [5]. This conversion process is not easily explained using the classical picture of macroscopic polarization, and therefore we need the semi-classical and quantum pictures [5]. In light scattering, light-matter interaction changes the direction and sometimes the frequency of incident light. The process is regarded as elastic if the scattered frequency remains unchanged and regarded as inelastic otherwise [5]. Unlike photoluminescence, there is an intuitive classical approach to a form of inelastic scattering known as SpRS. Several aspects of SpRS will also be useful in the main nonlinear optical effect of this thesis, the CRS discussed in section 2.7. For this reason, here we review some key concepts.

### 2.3.1 Spontaneous Raman scattering

In addition to atomic dipoles, which consist of electrons bound to atomic nuclei within the LOM, a medium can also have other types of dipoles. Figure 2.3 represents a polarizable[3]

[3]That is, even if the molecule is not initially polar, it can acquire a polarization.

diatomic molecule in which a spring connects the two atoms. So far, we considered that the atomic nuclei are at rest. In this case, the macroscopic polarization is of purely electronic

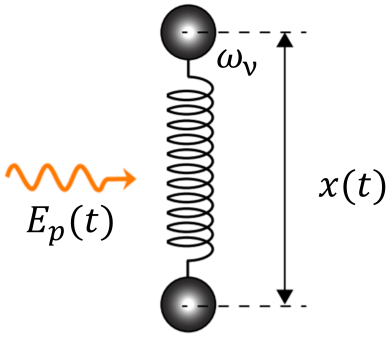


Figure 2.3: Spontaneous scattering in the presence of vibrational modes. The field $E_p(t)$ induces an oscillating dipole and, for small displacements, the time-varying nuclear separation $x(t)$ can be approximated by a damped harmonic oscillator. Adapted from [51].

origin [51]. Here, however, we consider that these molecules can vibrate around an equilibrium position. In this way, the nuclear motion will affect the electronic motion and polarization, since the electrons are bound to the nuclei, as discussed in section 2.2. This coupling is the origin of the spontaneous Raman scattering (SpRS) [5].

The classical treatment of the molecular vibration represented in figure 2.3 is similar to the LOM presented in section 2.2. It assumes that the molecule has a single vibrational mode of frequency $\omega_v$ and that the interaction with an electric field $E_p(t)$ (commonly known as pump field) of frequency $\omega_p$ oscillating along the molecule axis induces an oscillating dipole moment $p(t)$ [51]. The treatment also assumes that the motion of the molecule can be described by a damped harmonic oscillator forced by the electric field, which can be written as $E_p(t) = E_0\cos(\omega_p t)$. In addition, we also restrict the derivation to the scalar field approximation. The solution $x(t)$ for the nuclear motion is [51]

$$x(t) = x_v cos(\omega_v t), \tag{2.8}$$

where $x_v$ is the amplitude of the vibration. Assuming the interaction is far from resonance, the induced dipole moment can be written in the form [51]

$$p(t) = \epsilon_0 \beta(t) E_p(t) = \epsilon_0 \beta(t) E_0 cos(\omega_p t), \tag{2.9}$$

where $\beta^{(0)}(t)$ is the molecular polarizability[4]. Without knowing the exact functional form of polarizability [52], $\beta^{(0)}(t)$ can be expanded as a Taylor series with respect to nuclear coordinates within the small-displacement approximation for the nuclear motion [51]:

$$\beta(t) = \beta_0 + \left(\frac{\partial \beta}{\partial x}\right)_0 x(t) + \cdots, \tag{2.10}$$

[4]The standard notation for the molecular polarizability is $\alpha(t)$. However, we chose the unconventional representation $\beta(t)$ to avoid confusion with the standard notation for the absorption coefficient $\alpha$ in section 2.2.2.

where $\beta_0$ is the molecular polarizability in the absence of nuclear motion. Inserting (2.8) into (2.10) and the result into (2.9), and further noting that the macroscopic polarization of a medium containing a number density $N$ of molecules is $P(t) = Np(t)$, we have[5]

$$P(t) = N\epsilon_0\beta_0 E_0 \cos(\omega t) \tag{2.11a}$$

$$+ \frac{N\epsilon_0}{2} x_\nu \left(\frac{\partial\beta}{\partial x}\right)_0 E_0 \cos(\omega_p - \omega_\nu) \tag{2.11b}$$

$$+ \frac{N\epsilon_0}{2} x_\nu \left(\frac{\partial\beta}{\partial x}\right)_0 E_0 \cos(\omega_p + \omega_\nu). \tag{2.11c}$$

Expression (2.11) shows that the interaction of the field $E_p(t)$ with the medium produces three fields, two of them mediated by the coupling term with the nuclear coordinates $(\partial\beta/\partial x)_0$ and which vanish in the absence of nuclear motion. The term (2.11a) does not include nuclear

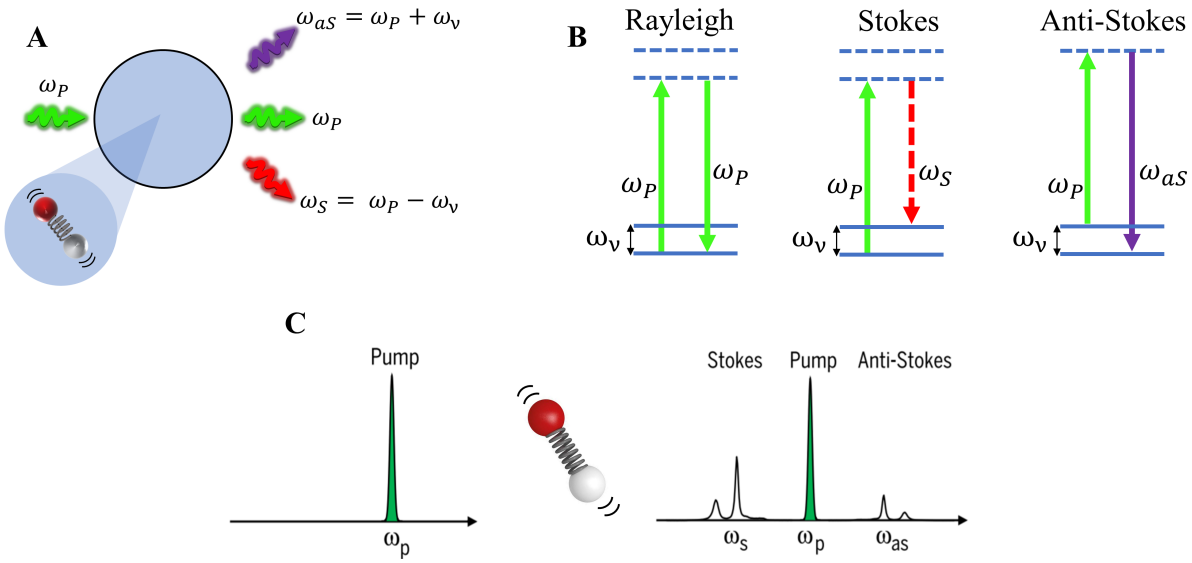


Figure 2.4: Spontaneous scattering in the presence of vibrational modes. (A) Three fields are generated in response to the incident field. One is insensitive to nuclear vibrational motion, and two are associated with this motion. (B) The first field accounts for Rayleigh scattering, in which no net energy is exchanged between the incident light and the medium. The other two account for SpRS: in Stokes scattering, light transfers energy to the medium, and its frequency is redshifted. In anti-Stokes scattering, the medium transfers energy to light, and the scattered light has its frequency blueshifted. (C) The Rayleigh scattering intensity is greater than the Stokes scattering intensity, and the latter is greater than the anti-Stokes scattering intensity. Adapted from reference [53].

motion, and this type of interaction produces fields at the same frequency as the incident field, as discussed in section 2.2. This term accounts for the Rayleigh (elastic) scattering. The terms (2.11b) and (2.11c) collectively account for SpRS [5, 51]. Light scattering due to interaction with a vibrational mode of frequency $\omega_\nu$ produces a Stokes field at frequency $\omega_S = \omega_p - \omega_\nu$ and an anti-Stokes field at frequency $\omega_{aS} = \omega_p + \omega_\nu$, as illustrated in figure 2.4A. The physical

[5] After using the trignometric relation $cos(a)cos(b) = [cos(a+b) + cos(a-b)]/2$.

mechanism associated with SpRS can be understood in the semi-classical picture. In the Rayleigh scattering of figure 2.4B, light is unaffected by vibrational levels, producing light at the same incident frequency. In the Stokes Raman scattering, the scattered light acquires a redshifted component at the cost of losing energy to the medium, leaving it in an excited vibrational state. In anti-Stokes Raman scattering, the blueshifted component appears due to energy transfer from the medium to the incident light. Figure 2.4C shows the intensity of each of scattering process, which is a measure of the probability of each effect. As can be seen, an interaction in which no net energy exchange occurs (Rayleigh scattering) is more likely than an interaction in which light transfers energy to the medium (Stokes scattering) and even more likely than an interaction in which the medium transfers energy to light (anti-Stokes scattering).

A critical feature of SpRS is the construction of the macroscopic signal. As the field propagates through the medium, the $N$ molecules cause the light to scatter. Considering the phase $\phi_j$ of the field produced by each scatterer, the field can be written in the exponential form $E_j = E_0 e^{(-i\omega t + i\phi_j)}$ + c.c., where c.c. is the complex conjugate. The overall intensity produced by the ensemble of molecules will be given by [54]

$$\langle I \rangle = \left\langle \left| \sum_j E_j \right|^2 \right\rangle = \sum_j \left|E_0\right|^2 + 2\left|E_0\right|^2 \sum_{j<k} \left\langle cos\left(\phi_j - \phi_k\right)\right\rangle . \tag{2.12}$$

In thermal equilibrium, the vibrations of these molecules are random and, therefore, the scatterers are considered uncorrelated [14,51]. Thus, the scattering produced by the $N$ molecules does not keep a definite phase relation, and the macroscopic signal arises incoherently [14], which makes the last term in the right hand side of expression (2.12) vanish. Therefore,

$$\langle I \rangle = \sum_j \left|E_0\right|^2 = N I_j, \tag{2.13}$$

where $I_j$ is the intensity produced by each scatterer. In other words, the various scattering events add up without any interference, neither constructive nor destructive. For the Stokes scattering, intensity is given by [14]

$$I(\omega_S) = N z \sigma_R(\omega_S) I_p, \tag{2.14}$$

where $I(\omega_S)$ is the output light intensity at Stokes frequency[6], $z$ is the length through which the incident light propagates, and $\sigma_R(\omega_S)$ is the Stokes Raman scattering cross-section, which expresses the efficiency of Stokes process. Equation (2.14) shows that the SpRS intensity scales linearly with the incident light intensity $I_p$ and with the density $N$ of molecules. The incoherence of the SpRS thus defined and the linearity defined from expression (2.14) will be of great relevance for this thesis, especially for the CRS effects discussed in section 2.7.

[6]The same holds for the anti-Stokes scattering.

### 2.3.2 One-photon excitation luminescence

As seen in section 2.3.1, the incident light can be inelastically scattered, creating new frequencies due to interaction with vibrational degrees of freedom. Inelastic scattering, however, is not the only frequency-shifting effect that can occur in a linear medium. As the incident light propagates through the medium, it can be absorbed and, after a certain time, re-emitted in a process known as photoluminescence [5]. As in SpRS, vibrational levels also play a frequency-shifting role in photoluminescence. Therefore, these two processes can be concomitant and competing. In this section we discuss the spontaneous photoluminescence process induced by the absorption of a single photon. As anticipated in section 2.2.2, one-photon absorption

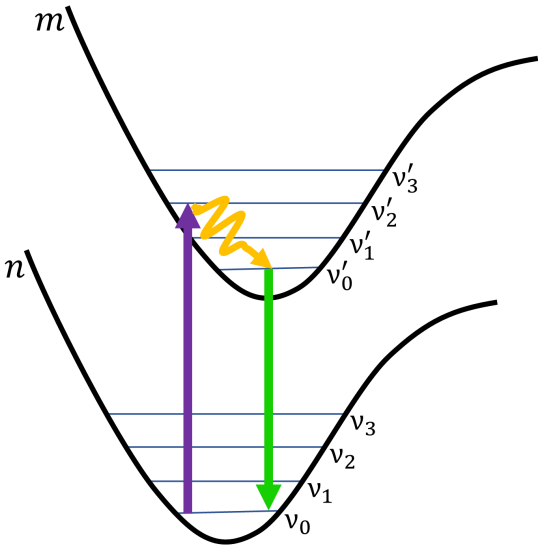


Figure 2.5: Energy diagram of one-photon excitation luminescence. Single photons are absorbed, leaving the system in an excited electronic and vibrational state when the energy of each photon matches the energy of the transition. The system relaxes, losing part of the absorbed energy in non-radiative processes. The remaining energy is then spontaneously emitted in the form of light.

is related to the imaginary part of $\chi^{(1)}$ through the absorption coefficient $\alpha_0$, which quantifies the absorption of light by the medium [5]. While $\alpha_0$ is independent of the incident light intensity, it strongly depends on light frequency. Such dependence accounts for the selectivity of absorption: some media may absorb one color but not others [5]. This process, however, is best described in the quantum picture.

Figure 2.5 shows an energy diagram for the effects of absorption and subsequent emission of light. Black curves represent different real electronic states $n$ and $m$. As indicated by the violet, upward arrow, the absorption process is characterized by the destruction of a photon, which leaves the medium in an excited electronic (and vibrational) state [55, 56]. For a two-level electronic transition, the process satisfies the energy conservation relation

$$\hbar\omega_i = \mathrm{E}_m - \mathrm{E}_n, \tag{2.15}$$

where $\hbar\omega_i$ is the energy of the incident photon that is annihilated in process of taking the

system from energy state $E_n$ to energy state $E_m$. Therefore, only a photon with frequency $\omega_i$ can induce the transition $n \rightarrow m$. Considering an incident field of intensity $I_p$, for one-photon absorption, the number of absorbed photons per unit time is [15, 56]

$$R \propto \sigma^{(1)} I_p, \tag{2.16}$$

where $\sigma^{(1)}$ is the one-photon absorption cross-section. Therefore, one-photon absorption is linearly dependent on the excitation intensity.

In general, the energy acquired in absorption can be lost through non-radiative processes involving vibrational transitions, such as thermal processes [5]. In Figure 2.5, the blue horizontal lines represent vibrational levels associated with each electronic level. The yellow, downward arrow represents a relaxation process in which the absorbed energy is lost, but no photon is emitted. After the system reaches the vibrational state $\nu'_0$, a spontaneous emission of light occurs. The energy relation between the emitted and absorbed light is given by [55]

$$\hbar\omega_p = \hbar\omega_{1PL} + \Delta E_\nu, \tag{2.17}$$

where $\hbar$ is the reduced Plank's constant (that is, $h/2\pi$), $\omega_p$ is the pump excitation frequency, $\omega_{1PL}$ is the emitted frequency, and $\Delta E_\nu$ is the energy loss to vibrational modes [55]. The emission process of $\omega_{PL}$ photons is known as one-photon excitation luminescence (1PL) or, also, one-photon excitation fluorescence. The energy conservation relation (2.17) shows that 1PL is generally redshifted from incident light when vibrational modes can be accessed, since $\Delta E_\nu > 0 \Rightarrow \omega_{1PL} < \omega_p$.

The resulting intensity of 1PL is related to the number of absorbed photons [57], which, as in expression 2.16, is linearly dependent on the excitation intensity $I_p$. Therefore, 1PL intensity $I_{1PL}$ is also linearly dependent on $I_p$ and closely follows Beer-Lambert's empirical law [58]:

$$I_{1PL}(z) = I_p e^{-\alpha_0 z}, \tag{2.18}$$

where $z$ is the interaction length. One-photon excitation luminescence will be specially explored in chapter 4.

### 2.3.3 Experimental implementation

The two main works of this thesis presented in chapters 3 and 4 use the WiTec alpha300 equipment to obtain SpRS and 1PL data. It consists of a confocal hyperspectral imaging system. Nonetheless, to demonstrate the implementation of the effects discussed in section 2.3, we describe the experimental setup in figure 2.6. The two experimental techniques we explore are imaging and spectroscopy. In both cases, the instrumentation resort to an optical microscope to probe microscopic volumes through tightly focused beams.

Figure 2.6A shows a CW laser interacting with the sample S through the scanning mirrors SM and objective O. After the interaction, the beam splitter BS splits the reflected signal. The dichroic mirror DM directs part of the signal to the photomultiplier tube PMT, where

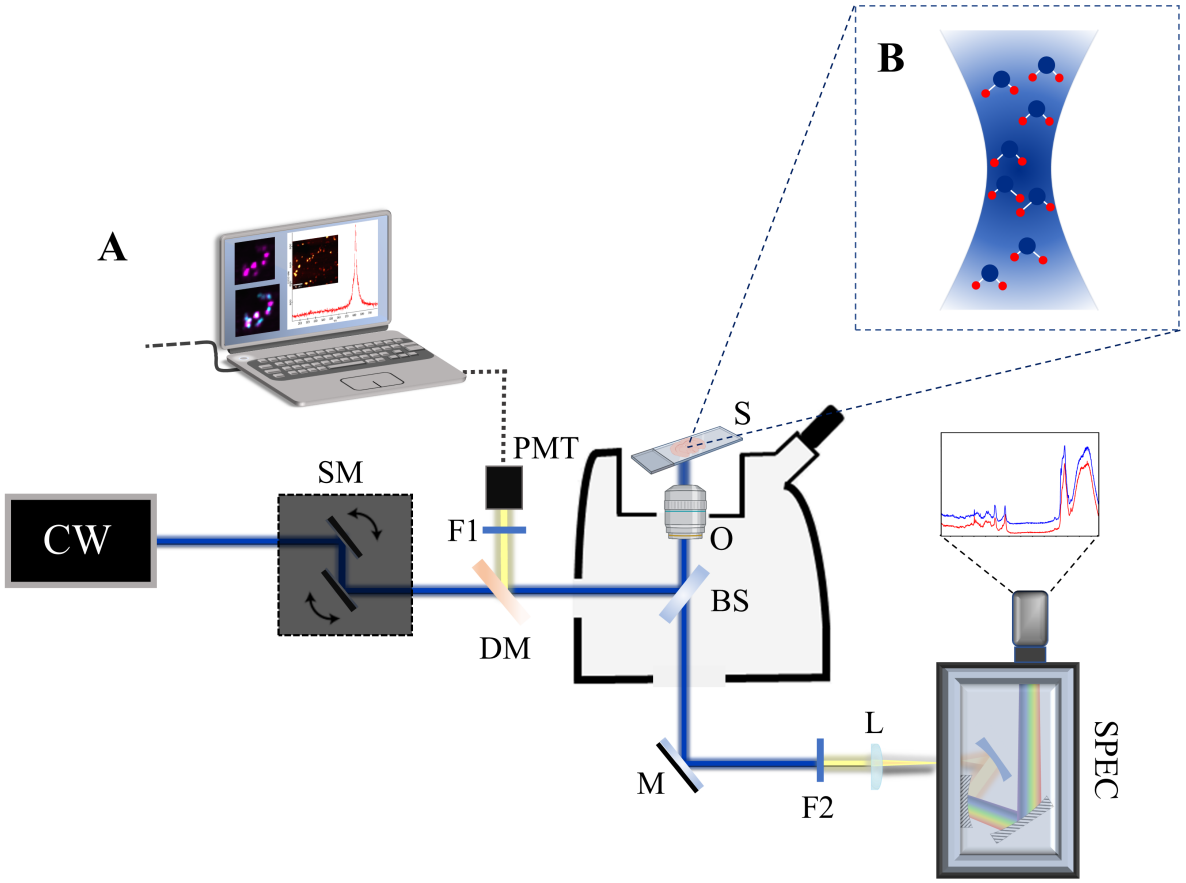


Figure 2.6: Optical setup for the experimental implementation of spontaneous Raman scattering and one-photon excitation luminescence. Adapted from reference [59].

the sample image can be taken. Filter F1 added in the detection can eliminate the laser wavelength (Rayleigh scattering) and select a spectral window. However, in general, it is not easy to separate 1PL from SpRS. The signal transmitted by the beam splitter is directed by the mirror M to lens L and focused on the spectrometer, which obtains the spectrum of light emitted by the sample. Filter F2 attenuates the Rayleigh scattering component.

Figure 2.6 illustrates an experimentally relevant property related to expressions (2.14) and (2.18). The linear dependence of the 1PL and SpRS signal on the incident laser intensity makes the effects have low focal discrimination. Since the occurrence of the effect does not require very intense signals, the incident laser can drive in-focus and out-of-focus molecules, which contribute to the detected signal. In order to achieve better optical sectioning, it is necessary to add pinholes in the detection. This condition is discussed in more detail in section 3.2. Furthermore, the incoherence captured by expression 2.13 is also represented in figure 2.6B. All the molecules vibrate in an uncorrelated manner. Therefore there is no coherent addition of the signal through phase matching.

## 2.4 Nonlinear optics

In the LOM discussed in section 2.2, the small-displacement approximation led to expression (2.2). Figure 2.2 illustrated how this approximation considers only the quadratic form of the interaction potential between the electron and the atomic nucleus, which describes the effects of matter under low-intensity light. When the amplitude of the incident electric field becomes sufficiently large compared to the atomic field, the LOM is no longer valid [15]. Under high-intensity light, the dipole is far removed from its equilibrium position. Hence a more general description of the interaction potential is needed.

### 2.4.1 The classical anharmonic oscillator model

As in the linear case, the electric field $E(t)$ affects the motion of an electron bound to a stationary atomic nucleus, producing a time-varying dipole moment $p(t)$. However, now with a field whose amplitude can be large, it is assumed that the electron displacement $x(t)$ can be described by the classical anharmonic oscillator model (AOM):

$$\frac{d^2x(t)}{dt^2} + \gamma\frac{dx(t)}{dt} + \omega_0^2 x(t) + c_2x^2(t) + c_3x^3(t) + \cdots = -eE(t)/m, \tag{2.19}$$

where $c_2$ ($c_3$, ...) is a parameter related to the strength of the nonlinearity in the potential [15, 48]. Because no general solution for equation (2.19) is known [48], a necessary additional assumption in the AOM is to restrict the coefficients $c_n$ (with $n = 2, 3, \ldots$) to small values. Such a restriction allows for a perturbative solution, such as the Rayleigh–Schrödinger procedure, in which the nonlinear terms are weaker than the linear term [15, 48]. Within this limit, it is possible to propose a power series expansion for the displacement $x(t)$ [15]:

$$x(t) = \lambda x^{(1)} + \lambda^2 x^{(2)} + \lambda^3 x^{(3)} + \cdots, \tag{2.20}$$

where $x^{(m)}$ and $\lambda^m$, with $m = 1, 2, 3, \ldots$, characterize the order and strength of the perturbation, respectively. Expression (2.19) then becomes [15]

$$\frac{d^2x(t)}{dt^2} + \gamma\frac{dx(t)}{dt} + \omega_0^2 x(t) + c_2x^2(t) + c_3x^3(t) + \cdots = -\lambda eE(t)/m, \tag{2.21}$$

and the perturbative procedure requires that the terms proportional to $\lambda^n$ (with $n = 1, 2, 3, \cdots$) each satisfy the equation separately[7] [15, 50]. The first-order solution (i.e. for terms proportional to $\lambda$) is equivalent to the harmonic oscillator of expression (2.2), which only involves the linear term in (2.19) and has an exact solution that depends on the frequency (frequencies) of the incident field (fields) [15]. As the perturbative treatment proceeds, this solution $x^{(1)}$ appears in different orders of perturbation, either as a cross term or subject to higher-order

[7] Classic textbooks on nonlinear optics often present this perturbative solution for the classical model (2.19) with only second-order ($c_2x^2$) and third-order ($c_3x^3$) nonlinearities. Higher orders are obtained by different methods. A fifth-order solution for the AOM can be found in reference [60].

powers in the expansion (2.19), giving rise to frequency mixing terms [15,48].

The macroscopic polarization $P(t)$ still expresses the dipole moment density in the medium, given by $P(t) = -Nex(t)$. Rewritting $x(t)$ as $-P(t)/Ne$ in (2.21) and considering that $x(t)$ can be solved for different orders in the perturbative procedure (2.20), the macroscopic polarization can also be written as [50]

$$P(t) = P^{(1)}(t) + P^{(2)}(t) + P^{(3)}(t) + \cdots , \tag{2.22}$$

where the first-order term $P^{(1)}(t)$ is the linear polarization derived from the LOM in expression (2.3), and the higher-order terms $P^{(m)}(t)$, with $m > 1$, are the nonlinear polarization. Treating the higher-order terms in model (2.19) as perturbations, and proposing a solution in form (2.20), is equivalent to considering the amplitude of the field $E(t)$ in expression (2.3) small enough[8] for $P(t)$ to admit a Taylor series expansion [48]. In such a case, $P(t)$ can be written as [15,48]

$$P(t) = \underbrace{\epsilon_0 \chi^{(1)} E(t)}_{P^{(1)}(t)} + \underbrace{\epsilon_0 \chi^{(2)} E^2(t)}_{P^{(2)}(t)} + \underbrace{\epsilon_0 \chi^{(3)} E^3(t)}_{P^{(3)}(t)} + \cdots , \tag{2.23}$$

where the first-order $\chi^{(1)}$ is the already defined linear electric susceptibility associated with linear optical effects, and all the higher-order $\chi^{(m)}$, $m > 1$, are the nonlinear electric susceptibility defined for each order and associated with different nonlinear optical effects. Convergence of the Taylor expansion (2.23) imposes that a term of a given order is smaller than the previous term [15]. Therefore, $\chi^{(m+1)} < \chi^{(m)}$ implies that the linear $\chi^{(1)}$ contribution is dominant. The higher-order polarization in expression (2.23) defines a *nonlinear medium* and light-matter interactions where the incident field produces a polarization described by expression (2.23) lie within the scope of *nonlinear optics*.

Interactions described by higher-order terms exhibit several novel features, some of which lack a linear analog. However, we should bear in mind that the expression (2.23) is constructed under the hypothesis of a medium composed of dipoles. In the macroscopic description, we only took into account the dipole moment term when computing the polarization. Rigorously, a general charge distribution can have non-vanishing contributions of all orders of a multipolar expansion. This means that some contributions, such as the quadrupole term[9], are not included in expression (2.23) [62]. Physical conditions where these higher-order contributions are appreciable can violate predictions derived from the polarization (2.23) [63].

### 2.4.2 The wave equation and nonlinear optical parameters

Combining expressions (2.22) and (2.23), the macroscopic polarization can be written in a convenient way:

[8] Small enough to treat terms $c_n x^n$ as perturbations in expression (2.19), but large enough to violate the linear model (2.2).

[9] A quadrupole correction of polarization (2.23) derived from the AOM can be found in reference [61].

$$P(t) = P^{(\mathrm{L})}(t) + \underbrace{P^{(\mathrm{NL})}(t)}_{P^{(2)}(t)+P^{(3)}(t)+\cdots}, \tag{2.24}$$

where $P^{(\mathrm{L})}(t) = \epsilon_0 \chi^{(1)} E(t) \equiv P^{(1)}(t)$ is the linear contribution to the total polarization and $P^{(\mathrm{NL})}(t)$ is all higher-order nonlinear contributions. Inserting (2.24) into (2.1), we have

$$\nabla^2 E(t) - \frac{n_0}{c^2}\frac{\partial^2 E(t)}{\partial t^2} = \frac{1}{\epsilon_0 c^2}\frac{\partial^2 P^{(\mathrm{NL})}(t)}{\partial t^2}. \tag{2.25}$$

Analogously to section 2.2, we also analyze the macroscopic optical parameters, which can be written as [50]

$$n_{m-1} \propto Re\{\chi^{(m)}\}, \tag{2.26}$$

$$\alpha_{m-1} \propto Im\{\chi^{(m)}\}, \tag{2.27}$$

$$I \propto \left|\chi^{(m)}\right|^2, \tag{2.28}$$

where $n_{m-1}$ e $\alpha_{m-1}$ are, respectively, the refractive index and the absorption coefficient of order $m$, with $m = 1, 2, 3, \ldots$; and $I$ is the intensity of the radiated wave.

On the left-hand side of expression (2.25), this wave equation shows the already known effect of the linear component of polarization (2.24): the modification of the wave speed through the refractive index $n_0$. However, the nonlinear component participates as a source term on the right-hand side of the wave equation (2.25). In contrast to the linear case, such a source term expresses the invalidity of the superposition principle. If sufficiently intense fields with different frequencies (or even a field with one frequency, as considered so far) interact with matter, the induced nonlinear macroscopic polarization will usually radiate at new frequencies. This frequency generation results from wave mixing effects and not mediation by electronic or vibrational levels as studied in section 2.3.

The nonlinear counterpart of the refractive index now relates to the real part of higher-order terms of the electric susceptibility, as in expression (2.26). The main consequence is that whereas the linear (zeroth-order) refractive index is independent of the intensity of the incident field (fields), the nonlinear (higher-order) refractive indices depend on different orders of the incident intensity [64]:

$$n = n_0 + n_2 I_0 + n_4 I_0^2 + \cdots . \tag{2.29}$$

This dependence means that the light propagating through the medium can itself alter the refractive index it experiences, causing a myriad of intensity-dependent self-action and cross-interaction effects[10], collectively known as Kerr nonlinearities, such as self-focusing, self-phase modulation, and cross-phase modulation [15, 50]. We will find some of these effects in

[10] These terms are generally used to distinguish between effects that the field itself, mediated by the medium, causes on itself (self-action); and, in the case of more fields, effects that one field, also mediated by the medium, has on the others (cross-interaction). In both cases, they are effects that the incident fields induce on the medium and alter its propagation through it.

section 2.7.

Similar to the nonlinear refractive index, the nonlinear counterpart of the absorption coefficient is also related to higher orders of the susceptibility, as in expression (2.27). In the linear case, the zeroth-order (linear) coefficient accounts for an intensity-independent loss by absorption. However, for higher-order coefficients, the absorption of light becomes dependent on different powers of the incident light intensity [64, 65]:

$$\alpha = \alpha_0 + \alpha_2 I_0 + \alpha_4 I_0^2 + \cdots . \tag{2.30}$$

Such dependence is related to nearly simultaneous absorption events, a phenomenon that we shall revisit in section 2.6, as the classical model does not fully capture it.

Finally, expression (2.28) describes the intensity of radiative effects in nonlinear interactions. This dependence on higher-order susceptibilities is associated with the nonlinear scaling of the radiated wave intensity with the incident light intensity, which we will see in section 2.5. This property will prove considerably advantageous to applications of nonlinear optics in biological imaging discussed in chapter 3.

### 2.4.3 Symmetry constraints on light-matter interactions

In the course of defining nonlinear optics from the AOM, symmetry considerations were implicit. The higher-order terms in (2.19) takes into account the asymmetric shape of the potential in figure 2.2. For a symmetric potential, some coefficients in expression (2.19) must vanish [15]. An illustrative case is second-order nonlinearities in centrosymmetric media. Figure 2.7 illustrates a material with an inversion center [5]. Applying the inversion symmetry

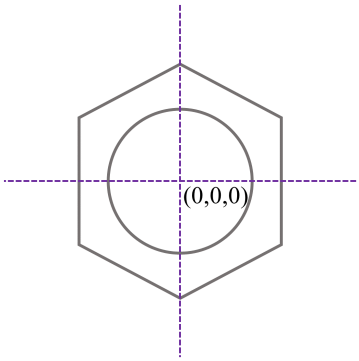


Figure 2.7: Center of inversion symmetry illustration. Representation of a benzene molecule, which has an inversion center at the origin of the coordinate system (0,0,0). The operation $(x, y, z) \rightarrow (-x, -y, -z)$ leaves the image invariant, illustrating the inversion symmetry.

operation $(x,y,z) \rightarrow (-x, -y, -z)$ at the inversion center (0,0,0) of figure 2.7 leaves the image invariant. This property characterizes a centrosymmetric material [5, 15]. Regarding second-order nonlinearities, a field $E(t)$ produces a polarization

$$P^{(2)}(t) = \epsilon_0 \chi^{(2)} (E(t))^2 . \tag{2.31}$$

If we reverse the direction of the field, effectively applying a field $-E(t)$, the polarization $P^{(2)}(t)$ becomes [5]

$$P^{(2)}(t) = \epsilon_0 \chi^{(2)} (-E(t))^2. \tag{2.32}$$

Instead of reversing the field, we can apply the field $E(t)$ and reverse the medium by applying the inversion operation $(x,y,z) \rightarrow (-x, -y, -z)$. With inverted coordinates, both the field $E(t)$ and the polarization $P^{(2)}(t)$ change sign in this reference frame [5]:

$$-P^{(2)}(t) = \epsilon_0 \chi^{(2)} (-E(t))^2. \tag{2.33}$$

For centrosymmetric media, the physical properties must be invariant under inversion symmetry operations [5]. This means that (2.33) must be equal to (2.32), which only holds when $\chi^{(2)} = 0$ [5, 15]. Therefore, the optical effects associated with the second-order susceptibility cannot occur as a result of inversion symmetry. In centrosymmetric media, the even-order terms in expression (2.19) vanish[11].

#### 2.4.3.1 Tensor nature of the electric susceptibility

Despite being an intuitive approach, some properties of light-matter interactions cannot be accounted for by the scalar-field approximation. For instance, the nonlinear response of the medium may depend on the direction of the incident fields: it is possible to apply two fields in different directions and generate optical effects in yet another direction [5]. In order to incorporate these features, the $i$-th Cartesian component of the polarization $\vec{P}$ can be written as [5]

$$P_i = \underbrace{\epsilon_0 \sum_j \chi^{(1)}_{ij} E_j}_{P_i^{(1)}} + \underbrace{\epsilon_0 \sum_{j,k} \chi^{(2)}_{ijk} E_j E_k}_{P_i^{(2)}} + \underbrace{\epsilon_0 \sum_{j,k,l} \chi^{(3)}_{ijkl} E_j E_k E_l}_{P_i^{(3)}} + \cdots, \tag{2.34}$$

where $\chi^{(1)}_{ij}, \chi^{(2)}_{ijk}, \chi^{(3)}_{ijkl}, \ldots$, are the components[12] of rank-$(m+1)$ tensors $\boldsymbol{\chi}^{(m)}$, with $m = 1, 2, 3, \ldots$, and each subscript $(i, j, k, l, \ldots)$ corresponds to the Cartesian coordinates $x$, $y$, and $z$. In the first term of equation (2.34), each of the three components of polarization $P_i$ is related to all three field components. Therefore, we need a $3^2$-elements susceptibility, which a rank-2 tensor $\boldsymbol{\chi}^{(1)}$ can describe. For the second term, each $P_i$ is related to all three components of the two fields[13]. We need a $3^3$-elements susceptibility and, therefore, a rank-3 tensor $\boldsymbol{\chi}^{(2)}$. Similarly, for the $m$-th term, we need a $3^{m+1}$-elements, rank-$(m+1)$ susceptibility tensor $\boldsymbol{\chi}^{(m)}$ [67].

We should note that expression (2.34) relates the components of polarization and incident field components through the properties of the medium encoded in the electric susceptibility

[11] Considering only electric dipole contributions in a nonmagnetic medium.

[12] A rank-0 tensor is a scalar, which here describes a one-dimensional interaction in the scalar-field approximation. A rank-1 tensor is a vector with independent components describing interactions along $x$, $y$, and $z$ directions. Higher-order tensors are represented by matrices whose elements express the interdependence of the spatial components along $x$, $y$, and $z$ [66].

[13] The fields in high-order interactions need not have different frequencies.

[51]. In crystalline media, these properties carry structural information that can be categorized according to their spatial symmetry[14] [5, 15]. Because of symmetry, several elements can vanish or share the same value, simplifying the susceptibility tensor [5, 15]. Consequently, by defining the form of the tensor, the symmetry properties of the medium can determine how optical effects occur. Such constraints will be an underlying concept in nonlinear optics applications in 2D materials discussed in chapter 4.

### 2.4.4 Nonlinear microscopic optical response

In the course of this chapter, we have used the terms macroscopic and microscopic without further examination of this scale transition. So far, the approach has been to use the classical picture of microscopic dipoles to define a macroscopic polarization and then relate that quantity to the external electric field. However, when moving from the microscopic to the macroscopic description in expressions (2.3) and (2.23), there is an implicit assumption that only the external field acts on each dipole. This is approximately true for rarefied matter such as gases, where each dipole in the medium is sufficiently distant from the others [5, 15]. In that case, neglecting the electric fields they generate is acceptable. In general, however, it is necessary to make a correction, where the effect of all dipoles in the medium is considered [5, 15]. This is because each dipole by itself generates an electric field, which acts on all other dipoles in the medium. Therefore, the field that a dipole feels is a superposition of the external field and the fields of all other dipoles in the medium. This effective field is known as the local field, and it changes the macroscopic response expected if only the external field were present [68]. The procedure of taking into account the superposition of all these fields is known as local-field correction and was also proposed by Lorentz for the linear regime [69]. Therefore, a classical description of nonlinear optics in molecular systems is more appropriate in terms of these microscopic definitions.

Similar to expression (2.34) for macroscopic systems, the microscopic nonlinear optical response of individual molecular units can be written in terms of hyperpolarizabilities and local field components instead of electric susceptibilities and external field components [15]. Hyperpolarizabities are higher-order terms of the molecular polarizability tensor describing nonlinear optical effects at the molecular level [70]. Although chapter 3 deals extensively with the molecular domain, the determination of hyperpolarizabilities of individual molecules is beyond the scope of the thesis. For the sake of brevity, we will ignore local-field corrections and the molecular description of nonlinear optics.

### 2.4.5 What is nonlinear optics?

Although the polarization expansion provides an operational definition of nonlinear optics, just looking at expression (2.23) and defining a linear and a nonlinear material can be misleading. That is because, in a sense, there are no linear media [13]. Within the discussed models, optical phenomena in matter can be described by a general electric susceptibility, which carries the

[14] Triclinic, cubic, hexagonal, for example.

properties of the medium. Nevertheless, some properties may not be accessible under certain conditions. That is the case when an electric field of small amplitude propagates through any medium. Under such a condition, expression (2.3) is sufficient to describe the observed phenomena, although insufficient to describe the medium itself. The susceptibility associated with this interaction is only a sub-description of the medium. In this sense, nonlinear optics is the domain in which optical phenomena violate the linear approximation. It encompasses light-matter interactions resulting in modifications in light itself that can only be described by higher-order terms[15] in expression (2.23). Consequently, the output light can display novel features with physically different attributes from the input light [71].

#### 2.4.5.1 How *nonlinear* is nonlinear optics?

Deriving the polarization expression (2.23) involved restricting the strength of nonlinearities to small values in (2.19). Physically, this comparison is made with the electric field that binds the valence electrons to the atom. The intensity of a light source compatible with such a field is around $10^{16}$ W/cm$^2$ [15]. If the incident light intensity is much lower, we are in the domain of linear optics[16]. As the light intensity increases, nonlinear effects become present[17]. The convergence of expression (2.23) requires that the higher the order, the smaller the strength of the nonlinearity and, therefore, the greater the light intensity needed to access it. Hence, the efficiency of nonlinear effects should decrease rapidly with the order of nonlinearity [15]. Nevertheless, under increasingly intense light, nonlinearities become more significant, giving rise to extreme nonlinear phenomena that violate the perturbative limit [73]. An illustrative case is high-harmonic generation[18] [73, 74]. For intensities around $10^{13}$ – $10^{16}$ W/cm$^2$ [15, 72], the higher-order effects show a strong deviation from the predicted perturbative behavior. Figure 2.8 shows three regions of the efficiency spectrum of odd-order harmonic generation [72]. The first region is the only one consistent with the perturbative limit, where efficiency decreases abruptly with the order of nonlinearity. In the "plateau" region, the efficiency drops more slowly[19]. Finally, in the third region, efficiency drops rapidly to the *cutoff*, beyond which no harmonics are observed [75].

As the incident light intensity increases further, new extremely nonlinear phenomena occur, even of a relativistic nature [15, 50]. Be that as it may, mentioning these phenomena and the above illustration is only in this text for completeness, as they demonstrate the vastness of nonlinear optics and how nonlinear it still can be. Hereafter, the term *nonlinear optics* will be used as a synonym for the perturbative limit. The discussion in this thesis comprises second

[15] It is possible to write the higher-order susceptibilities as a product of first-order susceptibilities for each polarization order in expansion (2.23) [15]. However, it is not the simple presence of first-order terms that characterizes a linear interaction but the sufficiency of a single first-order term to fully describe the interaction within the LOM.

[16] In many applications continuous-wave (CW) lasers are used with powers of less than 10 mW. If that power is focused on a 1 µm spot, this corresponds to an intensity around $10^6$ W/cm$^2$.

[17] The ultra-short laser pulses used in this thesis can deliver about 1500 W of maximum peak power. On a 1 µm spot, this corresponds to an intensity around $10^{11}$ W/cm$^2$. See section 2.5.3 for more details.

[18] In harmonic generation, the input frequency $\omega$ is converted into output frequency $n\omega$, where $n$ is the order of the nonlinearity. In section 2.5, we shall discuss the generation of second harmonic, where $\omega \rightarrow 2\omega$.

[19] Due to such behavior, Chang *et al.* observed harmonics of order up to 297 [74].

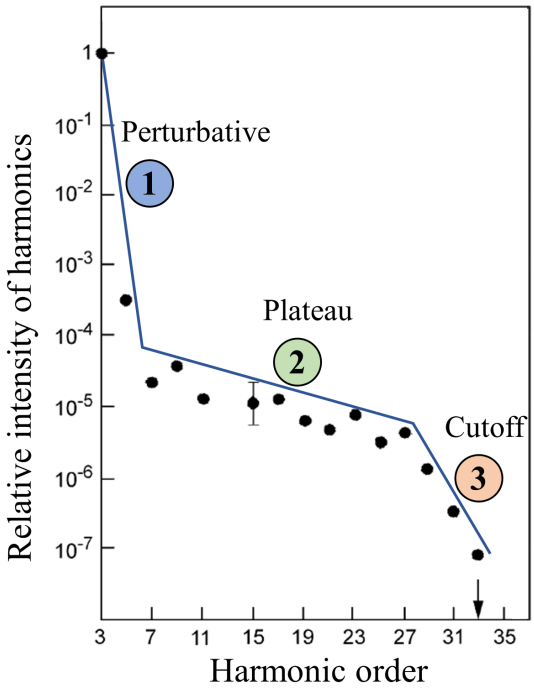


Figure 2.8: Dependence of nonlinear effects on the order of nonlinearity. Contrary to the behavior predicted by the perturbative approach, the efficiency of higher-order effects does not always drop quickly with the order of nonlinearity. The plot represents the generated harmonic intensity normalized by the third harmonic intensity (relative intensity) in gaseous argon [72]. Adapted from reference [15].

and third-order intensity-dependent wave mixing, refractive index, and absorption phenomena. These effects require only moderate light intensities, and the formalism presented in section 2.4 covers them appropriately.

## 2.5 Wave mixing

We mentioned three effects at the end of section 2.4: scattering, photoluminescence, and wave mixing. The linear case of the first two was reviewed in section 2.3, as they required extensions of the LOM. However, the wave mixing process is derived from the AOM, and, unlike scattering and photoluminescence, it does not have a linear counterpart. As stated in section 2.4, the absence of wave mixing is a consequence of the superposition principle, which is valid only in linear optics. As a result, the interaction of two or more fields with different (the same) frequencies (frequency), mediated by a linear medium, produces fields at the same incident frequencies. However, the wave mixing process is mediated by a nonlinear medium, allowing interactions between the input fields to produce output fields at new frequencies. For the sake of clarity, only nonlinear processes will be taken into account below, and co-occurring linear effects will be omitted.

### 2.5.1 Three-wave mixing

To start the discussion of the wave mixing process, we first consider an input light described by a dichromatic electric field in the form

$$E(t) = E_1 e^{-i\omega_1 t} + E_2 e^{-i\omega_2 t} + \text{c.c.}, \tag{2.35}$$

which represents two monochromatic waves oscillating at $\omega_1$ and $\omega_2$, and which we consider propagating in $\hat{k}$ direction. If the input field $E(t)$ interacts with a second-order nonlinear medium, the response of the medium will produce a polarization

$$P^{(2)}(t) = \epsilon_0 \chi^{(2)} E^2(t). \tag{2.36}$$

Introducing expression (2.35) into (2.36), we have

$$\begin{aligned}
P^{(2)}(t) &= P^{(2)}_0 + P^{(2)}_{\omega_1+\omega_2} + P^{(2)}_{\omega_1-\omega_2} + P^{(2)}_{2\omega_1} + P^{(2)}_{2\omega_2} + \text{n.f.c.} && \text{(2.37a)}\\
&= 2\epsilon_0 \chi^{(2)} \left(E_1 E_1^* + E_2 E_2^*\right) && \text{(2.37b)}\\
&+ 2\epsilon_0 \chi^{(2)} \left(E_1 E_2 e^{-i(\omega_1+\omega_2)t} + \text{c.c.}\right) && \text{(2.37c)}\\
&+ 2\epsilon_0 \chi^{(2)} \left(E_1 E_2^* e^{-i(\omega_1-\omega_2)t} + \text{c.c.}\right) && \text{(2.37d)}\\
&+ \epsilon_0 \chi^{(2)} \left(E_1^2 e^{-2i\omega_1 t} + \text{c.c.}\right) && \text{(2.37e)}\\
&+ \epsilon_0 \chi^{(2)} \left(E_2^2 e^{-2i\omega_2 t} + \text{c.c.}\right), && \text{(2.37f)}
\end{aligned}$$

in which n.f.c. are the negative frequency components of polarization due to the complex conjugate terms, and $E_1^*$ and $E_2^*$ are complex amplitudes.

As can be seen in expression (2.37), the field components with frequencies $\omega_1$ and $\omega_2$ lead to a polarization $P^{(2)}(t)$ with different contributions. Furthermore, it is convenient to analyze such contributions together with the nonlinear wave equation (2.25). The term (2.37b) as the source in expression (2.25) does not lead to the generation of electromagnetic radiation [15], as its second-order temporal derivative is null. This term represents the creation of a static electric field across the medium, known as optical rectification [15]. On the other hand, as the dichromatic field $E(t)$ propagates, the terms (2.37c) and (2.37d) account for two radiative mixing effects: sum frequency generation (SFG) at $\omega_1 + \omega_2$ and difference frequency generation (DFG) at $\omega_1 - \omega_2$, respectively. Similarly, the terms (2.37e) and (2.37f) account for second harmonic generation (SHG). These radiative effects characterize the three-wave mixing (TWM) process: two field components produce a third component at a new frequency [15].

#### 2.5.1.1 Second harmonic generation

In SHG, the incident field do not need to oscillate at different frequencies, since each frequency exhibits an upconversion in (2.37e) and (2.37f). As an example with frequency $\omega_1$ in (2.37e),

figure 2.9A illustrates the frequency doubling that characterizes the process. Since the two

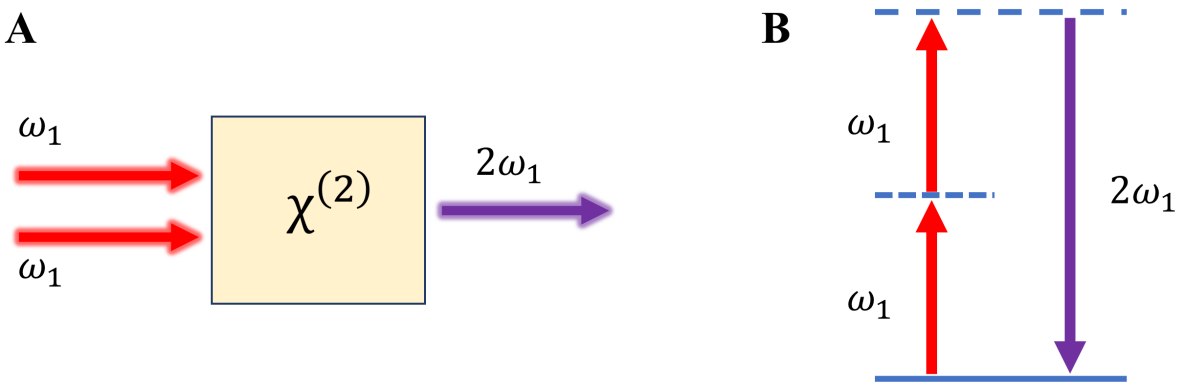


Figure 2.9: Second harmonic generation. (A) When propagating through a second-order nonlinear medium, two waves affect each other, mediated by the medium, to produce a third wave at twice the incident frequency. (B) The energy diagram shows how the medium acts in the process of converting the incident frequency into its double.

incident waves have the same frequency, SHG can be regarded as a degenerate three-wave mixing (DTWM) effect. Additionally, the resulting frequency doubling can also be understood as a degenerate case of SFG where the two incident frequencies ($\omega_1$ and $\omega_2$) are equal. The energy diagram in figure 2.9B provides a useful description of the process: two low-energy photons at $\omega_1$ are annihilated and a photon with exactly twice the incident frequency ($2\omega_1$) is simultaneously created [15]. The dashed lines represent virtual quantum levels, indicating that no real state absorption occurs. As anticipated in section 2.4.3, such interactions cannot occur in centrosymmetric media [5, 15], making SHG convenient for probing symmetry properties of materials.

Experimentally, SHG is a relatively easy effect to implement since it only requires a single laser beam, and the signal to be detected occurs far from the excitation frequency. Another experimentally advantageous feature of SHG is its nonlinear dependence on the incident light intensity [50]:

$$I(2\omega_1) \propto \left|\chi^{(2)}\right|^2 I_0^2 L^2 \mathrm{sinc}^2\left(\frac{\Delta k L}{2}\right), \tag{2.38}$$

where $I_0$ is the incident light intensity at $\omega_1$, $L$ is the optical path length in the medium, and $\mathrm{sinc}(x) = \sin(x)/x$ [50]. Because of the quadratic dependence on the incident light intensity, under tightly focused beam [14, 24], the relevant contribution of SHG comes from the focal volume [24]. Finally, in expression (2.38), $\Delta k$ is the scalar representation of the wavevector mismatch. It quantifies how different SHG fields generated along the interaction length $L$ contribute to the total SHG intensity. The condition $\Delta k = 0$ (known as perfect phase-matching) accounts for the case in which all fields add up in-phase (coherently) and interfere constructively [15], producing the maximum possible intensity in expression (2.38). The application of SHG in the imaging of biological and 2D materials will be discussed in chapters 3 and 4, respectively.

### 2.5.2 Four-wave mixing

Similar to the TWM process, four-wave mixing (FWM) is characterized by the generation of a fourth frequency due to the interaction between three frequency components. Now, however, the interaction is mediated by a third-order nonlinear medium. Accordingly, the possible mixing effects arise from the third-order polarization

$$P^{(3)}(t) = \epsilon_0 \chi^{(3)} E^3(t). \tag{2.39}$$

The description of FWM extends straightforwardly from the formalism presented in section 2.5.1. We consider an incident trichromatic field

$$E(t) = E_1 e^{-i\omega_1 t} + E_2 e^{-i\omega_2 t} + E_1 e^{-i\omega_3 t} + \text{c.c.}, \tag{2.40}$$

which now represents three monochromatic waves oscillating at $\omega_1$, $\omega_2$, and $\omega_3$, and which we also consider propagating in $\hat{k}$ direction. Inserting the field (2.40) into the polarization (2.39) will result in a lengthy expression, hence it is convenient simply to list the new frequency components generated in the FWM process [15]:

$$\begin{gathered}\omega_1, \omega_2, \omega_3, 3\omega_1, 3\omega_2, 3\omega_3, (\omega_1 + \omega_2 + \omega_3), (\omega_1 + \omega_2 - \omega_3), \\ (\omega_1 + \omega_3 - \omega_2), (\omega_2 + \omega_3 - \omega_1), (2\omega_1 \pm \omega_2), (2\omega_1 \pm \omega_3), \\ (2\omega_2 \pm \omega_1), (2\omega_2 \pm \omega_3), (2\omega_3 \pm \omega_1), (2\omega_3 \pm \omega_2),\end{gathered} \tag{2.41}$$

and also the negative frequency components (n.f.c.) from the c.c. terms. It follows from expressions (2.39), (2.40), and (2.41) that adding one more incident frequency component and increasing the order of interaction results in the emergence of multitudinous frequency components associated with a myriad of optical effects. Even though interactions described by expression (2.39) involve three incident waves, this does not physically imply that three light sources are necessary [50].

#### 2.5.2.1 Degenerate four-wave mixing

In the DTWM case of SHG, one frequency component participates in the interaction that generates the doubled frequency component. Similarly, here we explore a degenerate four-wave mixing (DFWM) case[20]. Since this case will be referred to in section 2.7, we consider the following dichromatic electric field:

$$E(t) = E_p e^{-i\omega_p t} + E_S e^{-i\omega_S t} + \text{c.c.}. \tag{2.42}$$

Analogously to the process that led to (2.41), the output frequency components can be calculated by inserting (2.42) into (2.39). The number of output frequencies will be smaller

[20]The term "degenerate four-wave mixing" is often used to refer to the case where all incident waves have the same frequency. Here, however, it will be used for the case where two (of the three) incident waves have the same frequency.

since there are fewer input components. Figure 2.10A illustrates the generation of a fourth

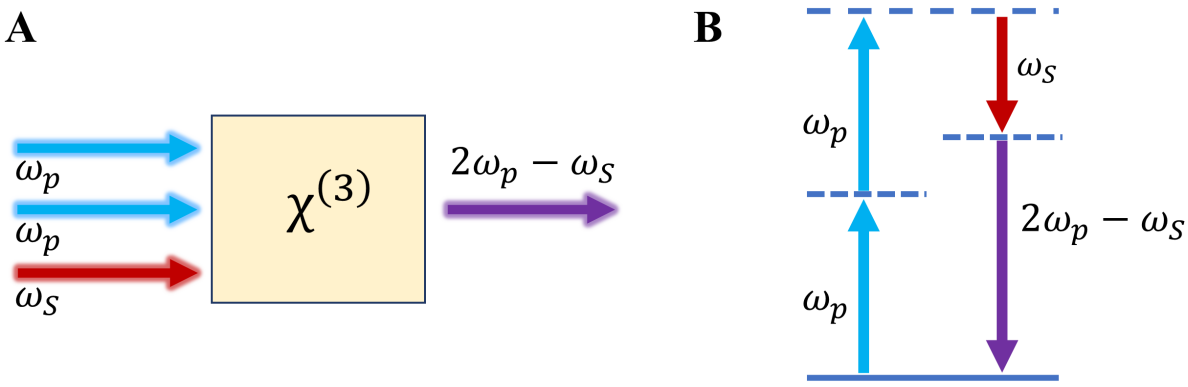


Figure 2.10: Degenerate four-wave mixing. (A) When propagating through a third-order nonlinear medium, three waves affect each other, mediated by the medium, to produce a fourth wave. (B) The energy diagram represents the mediation of the medium in the exchange of energy between the fields.

wave oscillating at $\omega_{\text{FWM}} = 2\omega_p - \omega_S$, characterizing one of several possible FWM outputs. Furthermore, the diagram in figure 2.10B shows the energy exchange between fields in this parametric[21] FWM process. Two photons of frequency $\omega_p$ are destroyed, bringing the system to a higher-energy virtual quantum state. Then[22], the input field at $\omega_S$ stimulates the decay to a lower energy virtual level through the emission of a photon with frequency $\omega_S$. Finally, a photon with frequency $2\omega_p - \omega_S$ is created [15]. Compared to SHG, DFWM is experimentally more difficult to implement since it involves more than one excitation beam, which must be temporally synchronized before interacting with the medium. Similar to SHG, the DFWM intensity also exhibits a nonlinear dependence on the excitation intensity [50]:

$$I(\omega_{\text{FWM}}) \propto \left|\chi^{(3)}\right|^2 I_p^2 I_S L^2 \text{sinc}^2\left(\frac{\Delta k L}{2}\right), \tag{2.43}$$

where $I_p$ and $I_S$ are the intensity of the incident waves (2.42), the physical implications are similar, and the notation is used analogously to equation (2.38). Four-wave mixing will be of great relevance in section 2.7. In particular, DFWM plays an important role in degenerate CARS.

### 2.5.3 Experimental implementation

Figure 2.11 shows an experimental setup that implements the wave mixing effects reviewed in section 2.5. As discussed throughout section 2.4, nonlinear optical effects are accessed through high-intensity beams. This requirement is incompatible with many cases of interest where the sample would be easily degraded by intensities far below what is needed to observe nonlinear

[21] In a parametric process, the initial and final quantum states of the system are identical. Consequently, the energy, linear momentum, angular momentum, and other quantities of the system remain unchanged after the interaction. In the context of the diagram of figure 2.10B, the virtual levels indicate that there is no net energy exchange between the fields and the medium.

[22] The arrows in an energy diagram are not necessarily ordered in time [14, 76].

effects. This conundrum is usually addressed with ultra-short pulse lasers, as illustrated in the inset 2.11A. During a pulse, the laser delivers a high amount of energy (enough to observe nonlinear effects) but in a short time interval (picoseconds, femtoseconds, and attoseconds). This interval corresponds to the duration of the pulse. Such operation is not continuous, and between two laser pulses, there is no emission of light. Therefore, it is convenient to define a characteristic period $T$ from the start of one pulse to next, as represented in figure 2.11A. The

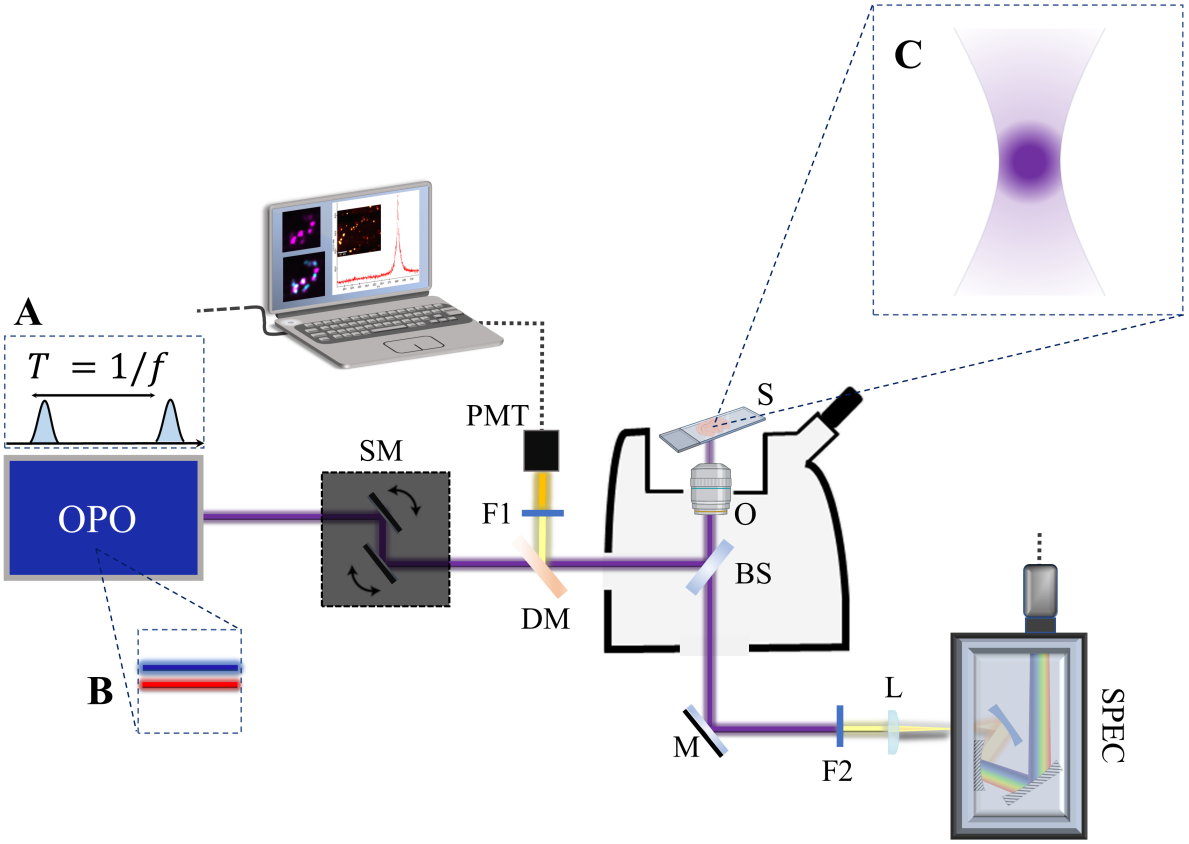


Figure 2.11: Optical setup for the experimental implementation of three and four-wave mixing effects. OPO: laser source. SM: scanning mirrors. DM: dicroic mirror. BS: beam splitter. O: objective. S: sample. F1: narrow bandpass filter centered at 408 nm for SHG imaging or 661 nm for FWM imaging. PMT: photomultiplier tube. M: mirror. F2: notch filter for attenuation of the Rayleigh scattering at ~ 816 nm. L: lens. SPEC: spectrometer. Adapted from reference [59].

inverse of this period is called the pulse repetition rate $f$. In many devices, the time between pulses (that is, the interval that the laser remains "off") is orders of magnitude greater than the duration of the pulse (the interval that the laser remains "on"). For a 5 ps pulse laser with repetition rate of 80 MHz ($T$ = 12500 ps), the laser is "on" during 5 ps and "off" during 12495 ps. In this way, the average power delivered by the laser to the sample is appreciably lower. For instance, the picoseconds laser source used in the works of this thesis is capable of delivering a peak power (power per pulse) of 75 W while maintaining an average power of 30 mW. The average power is the constant power that would be delivered by a CW laser, with the energy spread over the entire period $T$ and not restricted to pulse duration.

The *PicoEmerald* laser source used in the thesis is equipped with an optical parametric

oscillator (OPO), which provides two spatially overlapped and temporally synchronized pulse trains (as illustrated in figure 2.11B and represented as the overlapped purple beam in the setup). One of the beams is generated at a fixed wavelength (1064 nm, 7 ps, red beam in figure 2.11B) and the other at a tunable wavelength (720 nm – 990 nm, 5 – 6 ps, blue beam in figure 2.11B) with pulse repetition rate of 80 MHz. As the beams interact with the sample S, the scanning mirrors SM map the microscopic focal volume of the sample through the objective O, which is an apochromatic lens designed to correct chromatic aberration. This special objective lens focus different wavelengths to the same point, allowing the simultaneous interaction of all excitation beams. The response beams are partly reflected by the beamsplitter BS and then reflected by the dichroic mirror DM to the photomultiplier tube PMT, which allow the imaging of the sample. The importance of filter F1 in the detection is not only due to the elimination of Rayleigh scattering. For several sample types, many nonlinear effects occur simultaneously, with greater or lesser efficiency depending on the sample properties, strength of nonlinearities, and phase-matching conditions, as indicated in expressions (2.38) and (2.43). The choice of filter F1 determines the effects to be detected. With one of the excitation beams tuned at 816 nm, SHG is detected at 408 nm. Thus, a narrow bandpass filter centered at 408 nm is adequate to eliminate other effects. On the other hand, with 816 nm and 1064 nm excitation beams, DFWM discussed in section 2.5.2.1 occurs at $\sim$ 661 nm. A bandpass filter centered at 661 nm should be chosen. Finally, the response beams transmitted by the beamsplitter BS can be directed to lens L and focused on the spectrometer, where the spectrum of nonlinear effects can be obtained. Filter F3 attenuates Rayleigh scattering.

A last experimentally relevant feature is the excitation profile of nonlinear processes. Because of the nonlinear dependence on the excitation intensity, as described by expressions (2.38) and (2.43), wave mixing effects efficiently occur at the focus. Comparing figures 2.6B 2.11C, we can see the intrinsically confocal character of nonlinear techniques against the more uniform character of linear techniques [14, 24]. The consequence of such property for biological imaging is discussed in section 3.2.

## 2.6 Nonlinear photoluminescence

Within the classical model discussed in section 2.2, absorption is quantified by the absorption coefficient $\alpha$. As a result of low-intensity light incidence, $\alpha$ does not depend on the intensity of the excitation. In such a regime, electronic transitions are mediated by the absorption of a single photon. After a relaxation process, which usually involves interactions with vibrational modes [5], the medium can lose energy in the form of light emission, characterizing the 1PL process discussed in section 2.3.2.

As anticipated in section 2.4.2, single-photon absorption events is a feature of the linear approximation. When high-intensity fields excite the medium, the absorption coefficient is described by expression (2.30). The order of the coefficient indicates the number of photons that participate nearly simultaneously in an absorption event [64, 65, 77], characterizing the nonlinear interaction. Figure 2.12 illustrates a general case where $N$ photons participate in

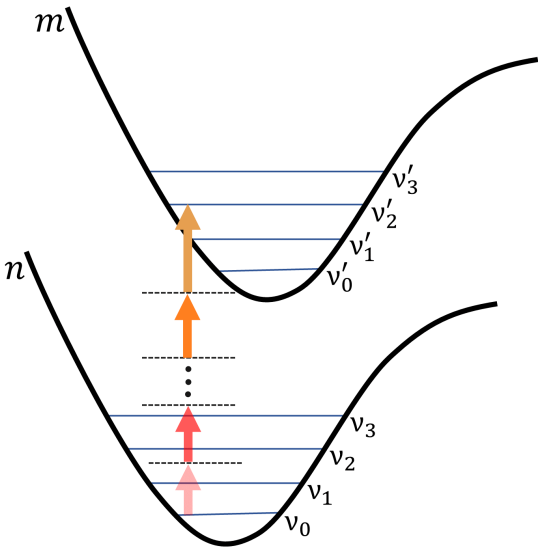


Figure 2.12: Energy diagram of general multi-color multi-photon absorption. Contrary to the linear case where only photons with the necessary energy can induce electronic transitions, in the nonlinear case several lower energy photons can bridge a transition.

a nonlinear absorption interaction. Contrary to the expression (2.15), where a photon with a specific frequency is associated with the electronic transition, in this general case, $N$ photons with arbitrary frequencies can mediate the transition [15]. The first photon induces a transition to a virtual quantum level. A second photon must interact with the system within the lifetime of this first virtual state, so that it can induce another upward virtual level transition. Analogous interactions must occur up to the $N$-th photon so that the $N$ photons can bridge the $n \rightarrow m$ real transition. Energy conservation requires that the sum of all frequencies be proportional to the energy of the real transition [7, 15, 78]. The greater the number of photons available to interact with the system in a given time interval, the greater the probability of multiphoton absorption. Therefore, this is a process that is highly dependent on the intensity of the incident light [15, 24].

### 2.6.1 Two-photon excitation luminescence

A special case of nonlinear absorption that we shall explore in chapter 3 is (degenerate) two-photon absorption. As indicated in expression (2.27), it is a third-order nonlinear process related to the second-order absorption coefficient $\alpha_2$ in (2.30), where $\alpha_2 \propto \mathrm{Im}\{\chi^{(3)}\}$ [15, 50]. For a better understanding of the effect and the sake of brevity, this section should be compared to section 2.3.2.

Figure 2.13 shows the energy diagram of the photoluminescence process induced by the absorption of two photons known as two-photon excitation luminescence (2PL) or two-photon excitation fluorescence (TPEF), as we shall refer to in chapter 3. Analogous to the 1PL process, the two red, upward arrows indicate the absorption process of two photons of frequency $\omega_{\frac{i}{2}}$, where $\omega_{\frac{i}{2}}$ is half the frequency $\omega_i$ in equation (2.15). As illustrated by the dashed line in figure 2.13, the process is mediated by a virtual level. For the two-level transition $n \rightarrow m$,

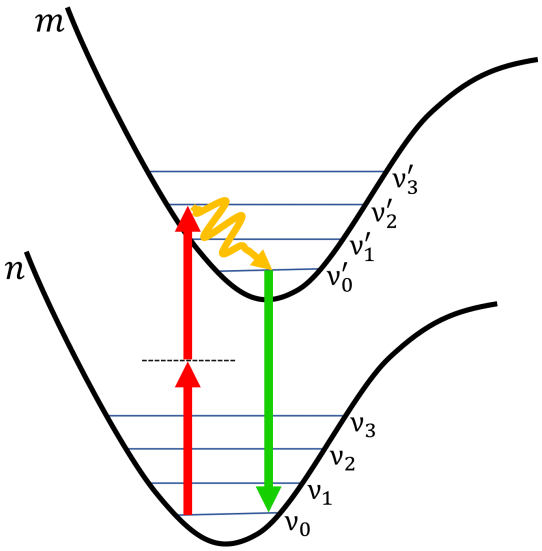


Figure 2.13: Energy diagram of single-color (degenerate) two-photon excitation luminescence. Two lower energy photons are nearly simultaneously absorbed and produce a transition possible only for photons with twice the energy in 1PL. Part of the absorbed energy is lost in non-radiative processes until the remaining energy is spontaneously emitted in the form of light.

energy conservation in (2.15) now reads as [78]

$$\hbar\left(\omega_{\frac{i}{2}} + \omega_{\frac{i}{2}}\right) = \mathrm{E}_m - \mathrm{E}_n. \tag{2.44}$$

Therefore, by increasing the intensity of the excitation, the transition energy still needs to be delivered. However, the condition that only a single photon must deliver this energy is relaxed.

Such as in 1PL, figure 2.13 shows that part of the energy acquired in the essentially simultaneous absorption of two photons is usually lost in effects mediated by vibrational modes. Compared to expression (2.17), the system satisfies the similar energy relation

$$\hbar\left(\omega_p + \omega_p\right) = \hbar\omega_{2\mathrm{PL}} + \Delta\mathrm{E}_\nu, \tag{2.45}$$

where $\omega_p$ and $\omega_{2\mathrm{PL}}$ are the excitation and emitted light frequencies, respectively. Now, however, $\omega_p$ can be smaller than $\omega_{2\mathrm{PL}}$ when $\Delta\mathrm{E}_\nu \neq 0$. The intensity of 2PL is related to the number $R$ of absorbed photons, which is quadratically dependent on the excitation intensity $I_p$ [15]:

$$R \propto \sigma^{(2)} I_p^2, \tag{2.46}$$

where $\sigma^{(2)}$ is the two-photon absorption cross-section. Therefore, 2PL intensity $I_{2\mathrm{PL}}$ is non-linearly dependent on the excitation intensity [24]:

$$I_{2\mathrm{PL}} \propto I_p^2. \tag{2.47}$$

As in the case of wave mixing discussed in section 2.5, this nonlinear dependence of 2PL on the intensity of the excitation will also be of experimental interest for the discussion in chapter

3.

### 2.6.2 Experimental implementation

Two-photon excitation luminescence (or TPEF) can be experimentally implemented through the optical setup of figure 2.11. In the simplest (degenerate) case described in (2.45), only a monochromatic laser beam is needed. The choice of the excitation wavelength is made based on the two-photon absorption spectrum of the material under study. The excitation wavelength (alone) must not be efficiently absorbed by the material so that there are no absorption that lead to 1PL. If the material efficiently absorbs in the blue spectral region, the excitation must be near the infrared region so that the combined energy of the photons is efficiently absorbed in the blue region [24]. For this reason, 2PL and SHG discussed in section 2.5.1.1 can be measured together and sometimes even be competing effects. Both are two-photon processes, quadratically dependent on the excitation intensity, in which the wavelength of the outgoing light is shorter than the wavelength of the incoming light. However, whereas SHG is a parametric effect usually involving transitions between virtual levels, 2PL (or TPEF) is a dissipative effect involving transitions between real levels. The former is a second-order nonlinear optical effect, while the latter is a third-order effect. Figure 2.14 illustrates the

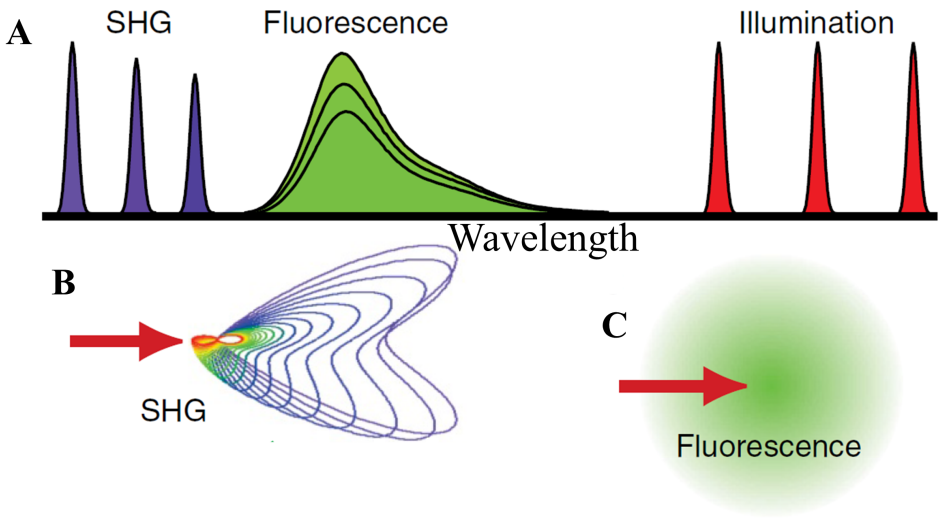


Figure 2.14: Differences between second harmonic generation and two-photon excitation luminescence. With the same excitation it is possible to observe SHG and 2PL. However, (A) whereas SHG occurs at exactly half the excitation wavelength (or twice the frequency), 2PL exhibits a broad spectrum. Furthermore, (B) SHG has a emission pattern that depends on structural properties of the medium, while (C) 2PL emission is isotropic. Adapted from reference [24].

two most notable practical differences. If the illumination occurs at three different excitation wavelengths, SHG will always be at half the incident wavelength, as shown in figure 2.14A. In 2PL, the emission is conditioned by the quantum selectivity of the absorption. If different illumination frequencies induce the same transitions, the emission will be the same. There will be no emission spectral shift following the incident light spectral tuning, as in the case of SHG.

Additionally, different non-radiative relaxation transitions can lead to radiative transition at different wavelengths. Hence, 2PL can exhibit various emission components in a wide spectral window, as in figure 2.14. Therefore, to measure SHG in the setup of figure 2.11, the filter F1 needs to be a narrow bandpass filter[23], as discussed in section 2.5.3. A spectrally broad filter would allow 2PL components to be measured as well. Figure 3.22 shows an experimental situation with SHG and 2PL present in the sample emission spectrum. For the same reasons, care should be taken in measuring 2PL. In such a case, the filter F1 needs to eliminate the SHG signal from the detection.

Finally, since SHG cannot occur in centrosymmetric media [5, 15], its emission exhibits a non-isotropic pattern. Figure 2.14B illustrates the directional nature of SHG, which depends on structural properties of the medium. On the other hand, 2PL exhibits an isotropic emission, as in figure 2.14C [24]. Therefore, polarization-resolved measurements is another way to discriminate between SHG and 2PL.

## 2.7 Nonlinear scattering

In the quantum picture, linear scattering is a type of interaction between a photon and the medium, leading to changes in the direction and sometimes in the frequency of the light. In this sense, the nonlinear character of scattering is usually attributed to its multiphoton nature: more than one photon participates in the same interaction with the medium. This process is in line with the classical description of nonlinear interactions discussed in section 2.4. To increase the chance of multiphoton interactions occurring, a sufficient number of photons must reach the medium within a short time interval. Therefore, it is expected that nonlinear scattering is mainly observed under high light intensities, which is the underline condition throughout this chapter for nonlinear effects in general.

In the classical picture, this multiphoton interaction leading to changes in the frequency of incident light also bears similarities to the wave mixing process. As discussed in section 2.5, dichromatic and trichromatic fields generate new frequency components when mediated by nonlinear media. This section explores how dichromatic fields, mediated by vibrational modes, produce nonlinear effects collectively known as coherent Raman scattering (CRS). Therefore, in this section we discuss the nonlinear counterpart of SpRS.

### 2.7.1 Coherent Raman scattering

As in section 2.3.1, we assume a molecule with a single vibrational mode of frequency $\omega_\nu$, but now interacting with a dichromatic field in the form

$$E(t) = E_p(t) + E_S(t) = E_p e^{-i\omega_p t} + E_S e^{-i\omega_S t} + \text{c.c.}, \tag{2.48}$$

[23] Alternatively, a shortpass filter can also be used to eliminate wavelengths longer than the SHG.

where (2.48) is the same field in (2.42). The subscripts "$p$" and "$S$" identify the fields components commonly called "pump" and "Stokes", respectively. Figure 2.15 illustrates the interaction of a molecule with the dichromatic field $E(t)$, resulting in the formation of a dipole whose electric dipole moment is given by

$$p(t) = \epsilon_0 \beta(t) \left( E_p e^{-i\omega_p t} + E_S e^{-i\omega_S t)} + \text{c.c.} \right). \tag{2.49}$$

Here, the dipole motion is also treated as a damped harmonic oscillator forced by the electric field, but now we write the equation of motion in the form

$$\frac{d^2x(t)}{dt^2} + 2\gamma \frac{dx(t)}{dt} + \omega_\nu^2 x(t) = F(t)/\mu, \tag{2.50}$$

where $\mu$ is the reduced mass of the system and $F(t)$ is not the Lorentz force as in (2.2). The

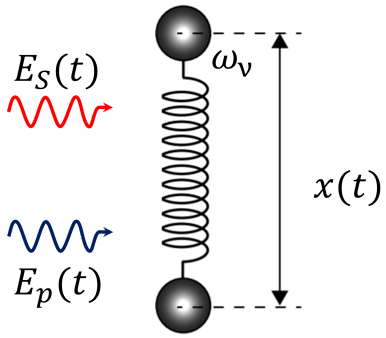


Figure 2.15: Interaction between a dichromatic field and a molecule with a single vibrational mode. It is assumed that each component of the field, separately, does not efficiently interact with the vibration mode. However, the beating of the incident components can drive the molecule into resonance. Adapted from reference [51].

total force $F_{\text{total}}$ on the dipole can be calculated from the energy $W = -p(t)E(t)$ needed for the field $E(t)$ in (2.48) to induce the dipole moment $p(t)$ in (2.49) [14, 51, 79]. In this case, $F_{\text{total}}$ is given by

$$F_{\text{total}}(t) = -\frac{\partial W}{\partial x} = \epsilon_0 \left( \frac{\partial \beta}{\partial x} \right)_0 \left( E_p E_S^* e^{-i(\omega_p - \omega_S)t} + \text{c.c.} + \cdots \right), \tag{2.51}$$

where the term $(\partial\beta/\partial x)_0$ indicates that the derivative with respect to the coordinate $x$ was evaluated only for small displacements. The parentheses in expression (2.51) show a cross-term of the field components, and the ellipses omit the other terms that depend on each component separately. Assuming that each component is far from resonance, the vibrational mode of the dipole is not efficiently driven by each component. Physically, this is equivalent to $\omega_p$ and $\omega_S$ being much higher than $\omega_\nu$, for instance. Therefore, it is possible to neglect such terms. However, the beating frequency $(\omega_p - \omega_S)$, where $\omega_p > \omega_S$, can be resonant with $\omega_\nu$. In that case, the joint action of the components of the field efficiently drives the dipole through the beating frequency $(\omega_p - \omega_S)$, and the force $F(t)$ in expression (2.50) is given

by [14,51,79]

$$F(t) = \epsilon_0 \left(\frac{\partial \beta}{\partial x}\right)_0 \left(E_p E_S^* e^{-i(\omega_p - \omega_S)t} + \text{c.c.}\right). \tag{2.52}$$

Inserting (2.52) into (2.50) allows for a solution $x(t)$ of the form [51]

$$x(t) = x_\nu e^{-i(\omega_p - \omega_S)t} + \text{c.c.}, \tag{2.53}$$

where

$$x_\nu = -\frac{\left(\epsilon_0/(\omega_p - \omega_S)\mu\right)\left(\partial\beta/\partial x\right)_0 E_p E_S^*}{\omega_\nu - (\omega_p - \omega_S) + i\gamma}. \tag{2.54}$$

Equation (2.54) expresses the dependence of the amplitude of motion with three important terms: the coupling between vibrational motion and electronic polarizability $(\partial\beta/\partial x)_0$, the mixing of the amplitude of the field components $E_p E_S^*$, and the beating frequency $(\omega_p - \omega_S)$. For intense fields chosen so that $\omega_p - \omega_S = \omega_\nu$, the amplitude of the vibrational motion becomes large, and the beating frequency of the dichromatic field induces a nonlinear behavior that depends on both the components of the field.

For a medium composed of $N$ dipoles, the induced macroscopic polarization is given by [14,51,79,80]

$$P(t) = Np(t) = N\epsilon_0 \beta(t) E(t), \tag{2.55}$$

which, taking into account the expansion (2.10), can be written as

$$P(t) = P^{(\text{L})}(t) + P^{(\text{NL})}(t) = N\epsilon_0 \left[\beta_0 + \left(\frac{\partial \beta}{\partial x}\right)_0 x(t)\right] E(t) \tag{2.56a}$$

$$= N\epsilon_0 \beta_0 \left(E_p e^{-i\omega_p t} + E_S e^{-i\omega_S t} + \text{c.c.}\right) \tag{2.56b}$$

$$+ N\epsilon_0 \left(\frac{\partial \beta}{\partial x}\right)_0 \left(x_\nu e^{-i(\omega_p - \omega_S)t} + \text{c.c.}\right)$$

$$\times \left(E_p e^{-i\omega_p t} + E_S e^{-i\omega_S t} + \text{c.c.}\right). \tag{2.56c}$$

Polarization (2.56) is the nonlinear counterpart of the polarization (2.11) in SpRS. The term $P^{(\text{L})}(t)$ is the linear part of the polarization, corresponding to the Rayleigh scattering of each component of the dichromatic field in (2.56b) and it is analogous to the term (2.11a). On the other hand, expression (2.56c) can be defined as the nonlinear contribution $P^{(\text{NL})}(t)$ in (2.56) and, expanding the parentheses, yields four new frequency components [14,51]:

$$P^{(\text{NL})}(t) = P(2\omega_S - \omega_p) e^{-i(2\omega_S - \omega_p)t} + P(2\omega_p - \omega_S) e^{-i(2\omega_p - \omega_S)t}$$
$$+ P(\omega_S) e^{-i\omega_S t} + P(\omega_p) e^{-i\omega_p t} + \text{n.f.c.}. \tag{2.57}$$

In the weak field limit, the coupling term $(\partial\beta/\partial x)_0$ acts by modifying the refractive index of the medium through vibrations, generating frequency shifts at $\pm\omega_\nu$, as in expression 2.11. With strong fields in 2.56, it additionally acts as a source of nonlinearity [79], allowing the medium to be responsive to the simultaneous interaction of the field components, generating mixing

terms related by frequency shifts[24] at $\pm\omega_v$, as in 2.57. These terms represent DFWM effects mediated by Raman-active vibrational modes. Also, since the occurrence of such effects is defined by the selection rule imposed by the coupling term, all effects depend on (and can be defined through) the Raman scattering cross-section $\sigma_R$ and carry the same vibrational information [14, 15, 51, 79]. Therefore, they are Raman-based third-order nonlinear effects.

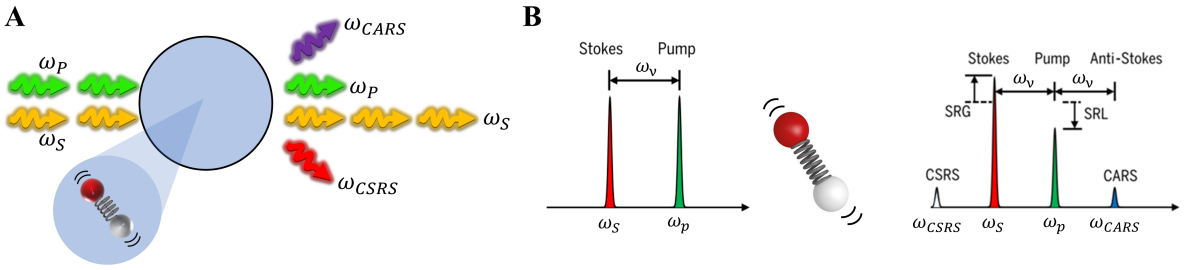


Figure 2.16: Coherent scattering in the presence of vibrational modes. (A) The incidence of a strong dichromatic field, mediated by vibrational modes, can produce four new effects in addition to the Rayleigh scattering that is always present and is insensitive to nuclear motion. Two effects (CSRS and CARS) occur at new frequencies, while two effects (SRG and SRL) occur at the same frequencies as the components of the dichromatic field. (B) The four effects are the result of the interaction of matter with the resonant beat of the dichromatic field. While CSRS appears at a redshifted frequency in relation to the lowest incident frequency, CARS is blueshifted in relation to the highest incident frequency. The SRG effect manifests as an increase in the field intensity at $\omega_p$, whereas SRL manifests as a decrease at $\omega_S$. Adapted from reference [53].

Figure 2.16A illustrates the general picture: an intense dichromatic field with spatially overlapped and temporally synchronized components propagates through a medium with Raman-active vibrational modes. One of these excitation components (of frequency $\omega_S$) corresponds to the Raman Stokes scattering frequency (that is, $\omega_S = \omega_p - \omega_v$) of the excited vibrational mode. In this way, the excitation beating frequency is resonant with the vibrational mode ($\omega_p - \omega_S = \omega_v$). Under these conditions, four third-order nonlinear effects arise simultaneously. Unlike incoherent, spontaneous Stokes and anti-Stokes scattering, we now have coherent Stokes Raman scattering (CSRS) at frequency $\omega_{\text{CSRS}} \equiv 2\omega_S - \omega_p$, coherent anti-Stokes Raman scattering (CARS) at $\omega_{\text{CARS}} \equiv 2\omega_p - \omega_S$, stimulated Raman gain (SRG) at $\omega_S$, and stimulated Raman loss (SRL) at $\omega_p$. These last two are together known as SRS. The four effects are collectively known as CRS and, although they carry the same vibrational information, they have different characteristics, especially regarding their detection: as shown in figure 2.16B, CSRS manifests as a redshifted signal, while CARS manifests as a blushifted signal. Stimulated Raman gain and SRL manifest as an intensity increase and decrease at the excitation frequencies, respectively. Nevertheless, they also share important properties, which we briefly discuss below.

[24] See section 2.7.1.2.

#### 2.7.1.1 The nonlinear nature of CRS

The first similarity between CRS effects is that they are third-order nonlinear effects, described as FWM processes in the classical picture. Hence, besides being described by a nonlinear polarization, the intensity of the effects scales nonlinearly with the excitation intensity. As an example, for CARS [14, 51, 81]

$$I_{\text{CARS}} \propto \left|\chi^{(3)}\right|^2 I_p^2 I_S, \tag{2.58}$$

which can be compared to expression (2.43) for DFWM in section 2.5.2.1. Some authors define the term "nonlinear" in CRS based on this nonlinear dependence on the intensity of excitation[25] [14, 84].

#### 2.7.1.2 The stimulated nature of CRS

For historical reasons, the term "stimulated Raman scattering" refers specifically to SRG and SRL processes. However, all CRS effects are stimulated scattering processes[26] [14, 85]. The joint action of the pump ($\omega_p$) and Stokes ($\omega_S$) components in the excitation stimulates the dipoles into resonance [14]. The presence of vibrational modes at $\omega_\nu$ modulates the refractive index so that an incident field experiences frequency shifts at $\pm\omega_\nu$ [15]. The incident beating frequency ($\omega_p - \omega_S$) also induces changes in the optical properties of the medium, modulating the refractive index at $\omega_p - \omega_S$ [14, 80]. Since, in CRS, $\omega_p - \omega_S = \omega_\nu$, this process stimulates the creation of sidebands at $\pm\omega_\nu$ [15], which results in the CRS effects [14]. As illustrated in figure 2.16B, each effect is shifted by $\pm\omega_\nu$ with respect to the incident components $\omega_p$ and $\omega_S$. For example, once the beating frequency stimulates the medium into resonance ($\omega_p - \omega_S = \omega_\nu$), the interaction of the frequency component $\omega_p$ with the medium will efficiently produce CARS at $\omega_p + \omega_\nu = \omega_p + (\omega_p - \omega_S) = 2\omega_p - \omega_S$. The same frequency component will experience SRG at $\omega_p - \omega_\nu = \omega_p - (\omega_p - \omega_S) = \omega_S$. The generated Stokes component produced in SRG can be many orders of magnitude more likely than the Stokes component produced in SpRS [14, 15]. While tipically 1 part in $10^{-6}$ of the incident light will produce the Stokes component in SpRS, more than 10% of incident light can be converted into Stokes light in SRG [15, 51, 79]. This amplification of the vibrational response of the medium is one of the reasons CRS-based imaging techniques are fast, as discussed in chapter 3.

#### 2.7.1.3 The coherent nature of CRS

The term "coherent Raman scattering" is most commonly used to describe all the nonlinear Raman processes discussed so far, as we have also done. That is not without reason, as all these processes are coherent in the sense that the CRS excitation coherently drive the dipole oscillations, generating a coherent macroscopic signal through phase matching. Since the

[25] This is because some authors argue that, in the full quantum treatment, SpRS is related to $\chi^{(3)}$. This discussion can be found in references [14, 51, 79, 82, 83].

[26] For a brief discussion of the conditions under which SpRS can be recast as a stimulated effect, see reference [51].

excitation beating frequency is resonant with the vibrational modes ($\omega_p - \omega_S = \omega_v$), the phase of the oscillators is determined by the relative phase of the incident field components and not by random fluctuations as in SpRS[27] [14]. For comparison with SpRS, we consider expression (2.12) again, which gives the overall intensity produced by the ensemble of $N$ dipoles. Assuming the field produced by each scatterer has the for $E_j = E_0 e^{(-i\omega t + i\phi_j)} + \text{c.c.}$, we have

$$\langle I \rangle = \left\langle \left| \sum_j E_j \right|^2 \right\rangle = \sum_j \left|E_0\right|^2 + 2\left|E_0\right|^2 \sum_{j<k} \left\langle \cos\left(\phi_j - \phi_k\right) \right\rangle . \tag{2.59}$$

As in SpRS, the first term on the right side of (2.59) is the intensity produced by each of the $N$ scatterer. However, unlike SpRS, the second term does not vanish. On the contrary, since the phase of the oscillations is defined by the excitation, $\phi_j = \phi_k$ and accounts for interference between the scatterers. The number of scatterers participating in the interference process is the combination $C_{N,2}$ of the $N$ scatterers taken two at a time [88]. Therefore,

$$\langle I \rangle = N I_j + 2 I_j \frac{N^2 - N}{2} = N^2 I_j . \tag{2.60}$$

This result can be derived from the restrictions on the summation in the second term on the right side of expression (2.59). For each index $j$ and $k$, the sum is performed for $N$ scatterers, accounting for the mutual interaction between the $N$. However, the summation is restricted to $j < k$ to eliminate ambiguities and repetitions. If there was no such restriction, the number of elements $s_{ij}$ in the sum is represented by a matrix $M$ with $N^2$ elements:

$$M = \begin{bmatrix} \boldsymbol{s_{11}} & s_{12} & s_{13} & \cdots & s_{1N} \\ \boldsymbol{s_{21}} & \boldsymbol{s_{22}} & s_{23} & \cdots & s_{2N} \\ \boldsymbol{s_{31}} & \boldsymbol{s_{32}} & \boldsymbol{s_{33}} & \cdots & s_{3N} \\ \vdots & \vdots & \vdots & \ddots & \vdots \\ \boldsymbol{s_{N1}} & \boldsymbol{s_{N2}} & \boldsymbol{s_{N3}} & \cdots & \boldsymbol{s_{NN}} \end{bmatrix} \tag{2.61}$$

However, the diagonal of matrix $M$ contains $N$ elements (in blue) that do not involve mutual interactions. These $N$ elements have already been accounted for in the first term on the right side of the expression (2.59) and, thus, can be understood as the scattering caused by each dipole. Hence, only $N^2 - N$ terms are associated with mutual interactions. Also, as the elements highlighted in red are equivalent to the elements above the diagonal, we divide the remaining $N^2 - N$ elements by 2. Thus, the number of scatterers participating in the second term in the expression (2.59) is $(N^2 - N)/2$, represented by the black matrix elements in (2.61). Therefore, the quadratic dependence of the intensity of CRS effects on the number density $N$ of scatterers is a consequence of the coherent excitation of the vibrational modes. This quadratic scaling is also known for other coherent nonlinear effects such as SFG [15]. Nevertheless, we shall see that the intensity of coherent effects can also scale linearly with $N$

[27] For a discussion of local phase relation in SpRS and a recent experimental measurement of coherence at macroscopic scale in SpRS, see references [86, 87].

depending on how it is detected.

All of these aspects are general properties of the CRS effects. Therefore, the following sections review particular properties of CARS and SRS, the CRS effects explored experimentally in this thesis. Not considering CSRS does not imply loss of generality once all CRS effects carry the same vibrational information.

### 2.7.2 Coherent anti-Stokes Raman scattering

Figure 2.17 shows the energy diagram of coherent anti-Stokes Raman scattering (CARS). As can be seen, the CARS process occurs parametrically: the final and initial state of the medium after interaction are the same. In the resonance condition ($\omega_p - \omega_S = \omega_\nu$), the frequency components $\omega_p$ and $\omega_S$ induce a real vibrational transition of energy $\hbar\omega_\nu$. Simultaneously, the component $\omega_p$ promotes the system to a virtual electronic level, finally decaying to the ground state and emitting the $\omega_{\text{CARS}}$ component.

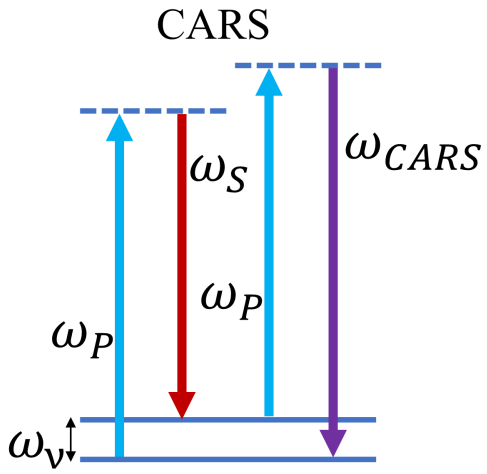


Figure 2.17: Coherent anti-Stokes Raman scattering energy diagram. Mediated by a real vibrational transition, three incident waves mix to produce the $\omega_{\text{CARS}}$ component efficiently.

In the classical picture, the only resonant source for the frequency component $\omega_{\text{CARS}}$ comes from the polarization $P(2\omega_p - \omega_S)$ in (2.57), given by [14, 51]

$$P(2\omega_p - \omega_S) \propto \chi^{(3)} E_p^2 E_S^*. \tag{2.62}$$

Thus, the generated field $E^{(3)}_{\text{CARS}}(t) = E_{\text{CARS}} e^{-i(2\omega_p - \omega_S)t} + \text{c.c.}$ associated with the component $\omega_{\text{CARS}} \equiv 2\omega_p - \omega_S$ is proportional to $P(2\omega_p - \omega_S)$. Therefore, the intensity at such frequency is [14, 51]

$$I(\omega_{\text{CARS}}) \propto \left|E_{\text{CARS}}\right|^2 \propto \left|\chi^{(3)}\right|^2 I_p^2 I_S, \tag{2.63}$$

as anticipated in section 2.7.1.1. A significant consequence for CARS is that the intensity at $\omega_{\text{CARS}}$ is not due solely to the resonant contribution in (2.56). In other words, CARS is not the only nonlinear third-order effect whose intensity can be detected at $\omega_{\text{CARS}}$.

As discussed in section 2.5.2.1, when the dichromatic field (2.48) interacts with a third-

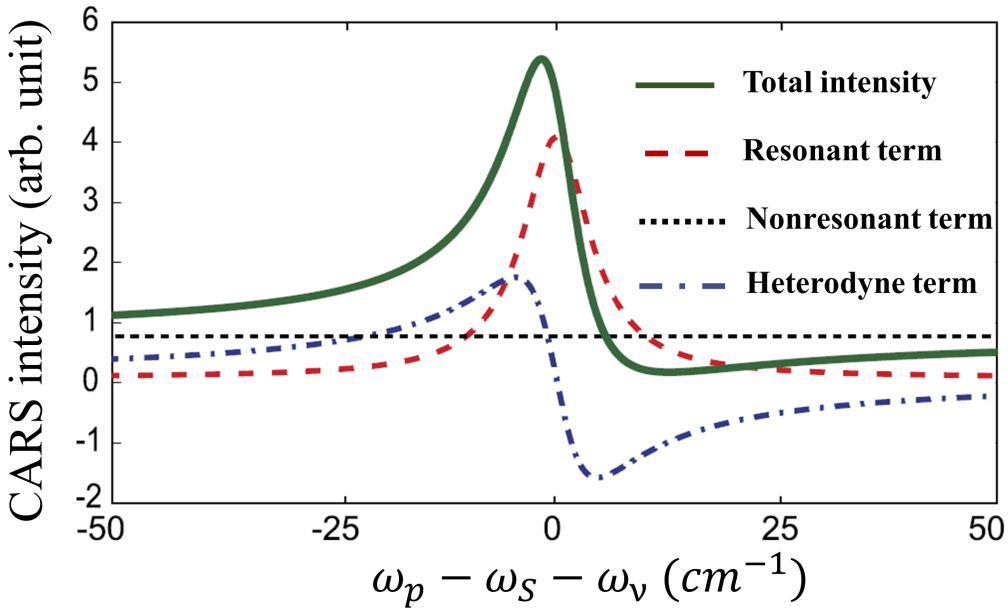


Figure 2.18: Homodyne-detected Coherent anti-Stokes Raman scattering spectrum. The spectral distortion of CARS is a consequence of different contributions at the same frequency. The total intensity is the result of an interference between the vibrationally resonant term (intrinsic CARS term) and the nonresonant DFWM. Therefore, the CARS spectrum does not match the SpRS spectrum. Adapted from reference [51].

order nonlinear medium, it induces a third-order polarization that gives rise to multiple FWM components, which do not depend on the resonance condition and, accordingly, do not carry vibrational information. One such component is DFWM that occurs exactly at $2\omega_p - \omega_S \equiv \omega_{\text{CARS}}$. Thus, the third-order susceptibility can be written as [14, 51, 80]

$$\chi^{(3)} = \chi_R^{(3)} + \chi_{NR}^{(3)}, \tag{2.64}$$

where $\chi_R^{(3)} = \text{Re}\{\chi_R^{(3)}\} + i\text{Im}\{\chi_R^{(3)}\}$ is the vibrationally resonant part of $\chi^{(3)}$ that gives rise to the CARS intrinsic signal and $\chi_{NR}^{(3)}$ is the purely real nonresonant part that gives rise to FWM effects at the same frequency $\omega_{\text{CARS}}$, known as the nonresonant background. Inserting (2.64) into (2.63), the intensity at $\omega_{\text{CARS}}$ can be written as [14, 51, 81]

$$I(\omega_{\text{CARS}}) \propto \left|E_{\text{CARS}}\right|^2 \propto \left(\left|\chi_R^{(3)}\right|^2 + \left|\chi_{NR}^{(3)}\right|^2 + 2\text{Re}\left\{\chi_R^{(3)}\chi_{NR}^{(3)}\right\}\right) I_p^2 I_S. \tag{2.65}$$

As expression (2.65) shows, if the intensity of CARS is detected at $\omega_{\text{CARS}}$, all terms will be probed. Such a measurement is known as homodyne detection[28]. Figure 2.18 is a simulation of the homodyne-detected CARS spectrum: the resonant term yields the characteristic Raman peak of the vibration; the nonresonant DFWM term is treated as a constant since it is assumed

[28] In the context of CRS, the detection is homodyne if the component $\omega_{\text{CARS}}$ is absent in the excitation, and the CARS intensity is measured at the generated $\omega_{\text{CARS}}$ as the square modulus of the CARS field [14]. The experiments presented in this thesis are with homodyne-detected CARS. SpRS is another example of homodyne-detected effect, as it involves only an incident monochromatic field and the detection measures the intensity at new output frequencies.

to be far from any resonance; and the third term in (2.65), also known as the heterodyne term [14,51], represents the interference between the resonant and nonresonant contributions. Therefore, homodyne-detected CARS intensity measured at $\omega_{\text{CARS}}$ is spectrally distorted and does not precisely correspond to the SpRS spectrum [14, 51, 81]. Nonetheless, in many practical applications, the nonresonant background may only represent a small contribution to the total CARS signal and may not pose a severe problem.

It is also possible that one of the components ($\omega_p$, for example) or both of the components of the dichromatic field (2.48) induce two-photon absorptions (at $2\omega_p$ or $\omega_p + \omega_S$), generating 2PL emission at $\omega_{\text{CARS}}$ [14,52]. As discussed in section 2.6.1, two-photon absorption is a third-order nonlinear effect, where the absorption coefficient $\alpha_2$ is proportional to $\text{Im}\{\chi^{(3)}\}$ [15,50]. Consequently, expression (2.64) should be appropriately modified to include the term $\chi^{(3)}_{2PA}$ due to two-photon absorption [52]. However, the effect is conditioned to the availability of real transitions and is only significant when the incident field matches such transitions efficiently. Therefore, in various situations of interest, $\omega_p$ and $\omega_S$ incident components can be chosen to avoid such two-photon transitions [52]. For this reason, we neglected this correction in expressions (2.64) and (2.65).

Finally, we note that $P(2\omega_p - \omega_S)$ is a component of the nonlinear polarization (2.57), which is proportional to the number density $N$ of scatterers in the general polarization (2.56). Since the CARS field is proportional to $P(2\omega_p - \omega_S)$, and intensity at $\omega_{\text{CARS}}$ is proportional to $\left|P(2\omega_p - \omega_S)\right|^2$, the homodyne-detected CARS intensity $I(\omega_{\text{CARS}})$ in 2.65 scales quadratically with $N$, as expressed in (2.60).

### 2.7.3 Stimulated Raman scattering

As illustrated in figure 2.16B, stimulated Raman scattering (SRS) manifests as an intensity variation in the incident frequency components $\omega_p$ and $\omega_S$: an increase in intensity in the Stokes beam and a decrease in intensity in the pump beam, which are the stimulated Raman gain (SRG) and stimulated Raman loss (SRL) components of SRS, respectively. In the quantum picture, SRS is a dissipative process in which $\omega_p$ photons from the pump beam are annihilated, and $\omega_S$ photons from the Stokes beam are created, while the energy difference $\hbar(\omega_p - \omega_S)$ is stored in the medium in the form of vibrational excitation. Originally, SRS was described in the context of stimulated emission theory. Hellwarth interpreted the effect as a two-photon Raman scattering [89]. Figure 2.19A illustrates his phenomenological description: in a Fabry-Perot cavity, there are $n_p$ photons in the incident mode at $\omega_p$, which interacts with a Raman-active medium. This medium exhibits an intense vibrational mode at $\omega_\nu$. At first, the incident mode undergoes SpRS, whose transition rate $W_{\text{Sp}}$ is proportional to the number of photons $n_p$, $W_{\text{Sp}} \propto n_p$, populating the Stokes scattering mode at $\omega_S$ [79]. The cavity mirrors then redirect both field modes back to the medium, and both fields participate in the interaction, eventually in a coherent way. The transition rate $W_{\text{St}} \propto n_p(n_S + 1)$ now also depends on the number of photons $n_S$ in the Stokes mode [79, 80, 89]. While for $n_S = 0$, $W_{\text{St}}$ reduces to $W_{\text{Sp}}$, for $n_S \gg 1$, the ratio of stimulated scattering to spontaneous scattering

is [48, 51, 79]

$$\frac{W_{\mathrm{St}}}{W_{\mathrm{Sp}}} \propto n_S + 1. \tag{2.66}$$

The overall process, shown in the energy diagram of figure 2.19B, consist of anihilating a photon from a radiation mode at $\omega_p$ (that is, $n_p - 1$) and creating a photon in a radiation mode at $\omega_S$ (that is, $n_S + 1$), as in SpRS [79, 89]. However, the diagram of figure 2.19B does not explicitly show the number of photons in each incident field mode, where lies a notable difference between the effects. Whereas $n_S = 0$ in SpRS, $n_S \gg 1$ renders the SRS process enhanced, as indicated in expression (2.66). In other words, because the number of photons $n_S$ in the stimulating Stokes beam is initially high, the increase of the emission rate in $\omega_S$ is significant [79].

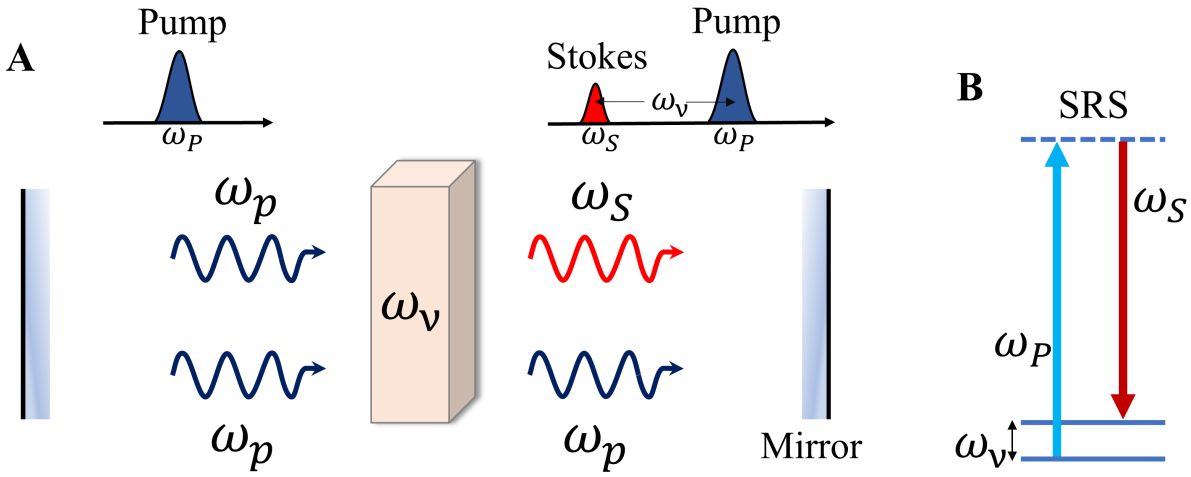


Figure 2.19: Stimulated Raman scattering in a laser cavity. (A) The frequency $\omega_p$ of the incident beam is redshifited to the frequency $\omega_S = \omega_p - \omega_v$ in Raman-active medium through SpRS. Upon interacting again with the medium, eventually in a coherent way, the presence of $\omega_S = \omega_p - \omega_v$ mode in the excitation stimulates the Stokes shift of $\omega_p$. (B) The energy diagram shows that this process of energy transfer from the fundamental beam at $\omega_S$ to the created Stokes mode is a dissipative process where the energy difference $\hbar(\omega_p - \omega_S)$ creates a vibrational excitation in the medium. Figure based on reference [79].

In the classical picture, as the strong off-resonance dichromatic field in (2.48) propagates through the medium, the resonant beating ($\omega_p - \omega_S = \omega_v$) induces a third-order nonlinear polarization, which produces weak fields at $\omega_p$ and $\omega_S$ [14, 51]:

$$E^{(3)}_{\mathrm{SRG}}(t) = E^{(3)}_S e^{-i\omega_S t} + \text{c.c.}, \tag{2.67a}$$

$$E^{(3)}_{\mathrm{SRL}}(t) = E^{(3)}_p e^{-i\omega_p t} + \text{c.c.}. \tag{2.67b}$$

The diagram in figures 2.20A and 2.20B illustrates the DFWM generation process of the intrinsic SRS fields (2.67a) and (2.67b), respectively. For the SRG (SRL), three waves oscillating at $\omega_p$, $\omega_S$, and $\omega_p$ ($\omega_p$, $\omega_S$, and $\omega_S$) generate the fourth wave at $\omega_S$ ($\omega_p$), differing from other DFWM processes due to the mediation by real vibrational levels. As mentioned in section 2.7.1.2, SRG can be described (at resonance) as the generation of a sideband at

$\omega_p - \omega_v = \omega_S$ . Analogously, for SRL, the process can be described (at resonance) as a sideband at $\omega_S + \omega_v = \omega_p$. However, the shifts at $\pm\omega_v$ does not allow the fields (2.67a) and (2.67b) to be interpreted as Stokes and anti-Stokes components of SRS, as they would be in SpRS. Some authors regard this terminology as confusing since there is no analog for anti-Stokes in SRS [90,91]. For instance, Harbola *et al.* showed that the temperature-dependent Stokes and anti-Stokes scattering intensity asymmetry[29], a hallmark of SpRS, is absent in SRS [92]. Both SRG and SRL have the same intensity [92]. For that reason, SRG and SRL are often referred to as the red side and blue side of SRS [91,92], respectively.

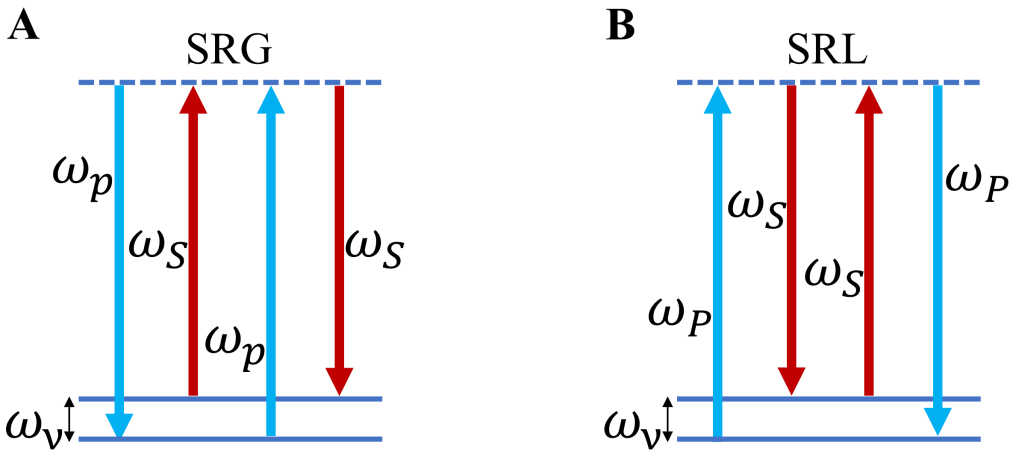


Figure 2.20: Stimulated Raman scattering as a degenerate four-wave mixing process. (A) Energy diagram for SRG, where three waves oscillating at $\omega_p$, $\omega_S$, and $\omega_p$ generate the fourth wave at $\omega_S$, while (B) for SRL, the waves at $\omega_p$, $\omega_S$, and $\omega_S$ produce the fourth wave at $\omega_p$. Both effects are mediated by the vibrational transtion of frequency $\omega_v$. Figure based on reference [51].

As in CARS, the origin of SRS fields in (2.67a) and (2.67b) is, respectively, the nonlinear polarization components in (2.57) [14,51]:

$$P(\omega_S) \propto \chi^{*(3)} E_p^2 E_S, \tag{2.68a}$$
$$P(\omega_p) \propto \chi^{(3)} E_p E_S^2. \tag{2.68b}$$

Unlike CARS, the fields (2.67a) and (2.67b) are generated at the same frequencies as the components of the incident field (2.48). Thus, when the induced and incident fields propagate in the same direction [79], the total intensity at $\omega_S$ and $\omega_p$, at the far-field, is given by [14,51]

$$I(\omega_S) \propto \left|E_S^{(3)} + E_S\right|^2 \propto \left|E_S^{(3)}\right|^2 + \left|E_S\right|^2 + 2\mathrm{Re}\left\{E_S^{(3)} E_S^*\right\}, \tag{2.69a}$$
$$I(\omega_p) \propto \left|E_p^{(3)} + E_p\right|^2 \propto \left|E_p^{(3)}\right|^2 + \left|E_p\right|^2 + 2\mathrm{Re}\left\{E_p^{(3)} E_p^*\right\}, \tag{2.69b}$$

where $E_S^{(3)}$ $\left(E_p^{(3)}\right)$ and $E_S$ $(E_p)$ are the nonlinear induced field amplitude and the incident

[29] Anti-Stokes scattering intensity approaches zero as temperature tends to zero, whereas Stokes scattering intensity is finite. As temperature tends to infinity, Stokes and anti-Stokes scattering tends to be equally intense [51].

field amplitude at $\omega_S$ ($\omega_p$), respectively. Therefore, expressions (2.69a) and (2.69b) show that the induced and incident components interfere at $\omega_S$ and $\omega_p$. The square modulus of the amplitudes $E_S^{(3)}$ and $E_p^{(3)}$ denotes the intensity at the generated $\omega_S$ and $\omega_S$, which are comparable in magnitude to the intensity of the CARS term in (2.63). Additionally, since they are also proportional to $P(\omega_S)$ and $P(\omega_p)$, they also exhibit a similar dependence on the intensity of the dichromatic field components in (2.63) and a quadratic dependence on the number density $N$ of scatterers [14]. Therefore, since $\left|E_S^{(3)}\right|^2 \propto \left|P(\omega_S)\right|^2$ and $\left|E(3)_p\right|^2 \propto \left|P(\omega_p)\right|^2$, expressions (2.69a) and (2.69b) can be written as [14, 84]

$$I(\omega_S) \propto \left|\chi^{(3)}\right|^2 I_p^2 I_S + I_S + 2\mathrm{Re}\left\{E_S^{(3)} E_S^*\right\}, \tag{2.70a}$$

$$I(\omega_p) \propto \left|\chi^{(3)}\right|^2 I_p I_S^2 + I_p + 2\mathrm{Re}\left\{E_p^{(3)} E_p^*\right\}, \tag{2.70b}$$

where $I_S \propto \left|E_S\right|^2$ and $I_p \propto \left|E_p\right|^2$ are the intensities of the incident field components. It is noteworthy to compare the first term in the right hand side of (2.70a) to (2.63). Although CSRS is not part of the discussion in this thesis, the first term in the right hand side of expression (2.70b) exhibits a functional form analogous to the CSRS intensity [84].

When compared to the intensity of the incident components $\left|E_S\right|^2$ and $\left|E_p\right|^2$, the intensities $\left|E_S^{(3)}\right|^2$ and $\left|E_p^{(3)}\right|^2$ are vanishingly small [14, 51]. Therefore, these intensities are not usually measured. Yet, the interference terms in (2.69a) and (2.69b) can still be significant [51, 79]. Hence, intensities (2.69a) and (2.69b) reduce to [14, 51]

$$I(\omega_S) \propto I_S + 2\mathrm{Re}\left\{E_S^{(3)} E_S^*\right\}, \tag{2.71a}$$

$$I(\omega_p) \propto I_p + 2\mathrm{Re}\left\{E_p^{(3)} E_p^*\right\}. \tag{2.71b}$$

In order to determine the role of the interference terms, it is necessary to consider the relationship between the induced fields (2.67) and the polarization components $P(\omega_S)$ and $P(\omega_p)$. Within the plane wave approximation [14, 51, 93]

$$E_S^{(3)} \propto iP(\omega_S), \tag{2.72a}$$

$$E_p^{(3)} \propto iP(\omega_p). \tag{2.72b}$$

Together with expressions (2.68a) and (2.68b) for each polarization component, expressions (2.72a) and (2.72b) show that the induced fields have a phase shift of $\pi/2$ relative to the incident field components. Using (2.72a) and (2.72b), respectively, into (2.71a) and (2.71b), we have

$$I(\omega_S) \propto I_S + 2\mathrm{Re}\left\{iP(\omega_S) E_S^*\right\}, \tag{2.73a}$$

$$I(\omega_p) \propto I_p + 2\mathrm{Re}\left\{iP(\omega_p) E_p^*\right\}. \tag{2.73b}$$

Then, substituting $P(\omega_S)$ and $P(\omega_p)$ in expressions (2.73a) and (2.73b) by expressions (2.68a)

and (2.68b), the total intensity at $\omega_S$ and $\omega_p$ can be written as

$$I(\omega_S) \propto I_S + 2I_S I_p \mathrm{Re}\left\{i\chi^{*(3)}\right\}, \tag{2.74a}$$

$$I(\omega_p) \propto I_p + 2I_S I_p \mathrm{Re}\left\{i\chi^{(3)}\right\}. \tag{2.74b}$$

As in the case of CARS in (2.64), $\chi^{(3)}$ can be written as $\chi^{(3)} = \mathrm{Re}\{\chi_R^{(3)}\} + i\mathrm{Im}\{\chi_R^{(3)}\} + \chi_{NR}^{(3)}$. Hence [14, 15, 51, 79],

$$I(\omega_S) \propto I_S + 2I_S I_p \mathrm{Im}\left\{\chi_R^{(3)}\right\} \equiv I_{\mathrm{SRG}}, \tag{2.75a}$$

$$I(\omega_p) \propto I_p - 2I_S I_p \mathrm{Im}\left\{\chi_R^{(3)}\right\} \equiv I_{\mathrm{SRL}}. \tag{2.75b}$$

Expressions (2.75a) and (2.75b) are the experimentally measured quantities describing the SRS signal in figure 2.16B. For that reason, they are usually referred to as the SRS effect. As expressions (2.75a) and (2.75b) show, in the classical picture, the incident field component $E_S(t)$ ($E_p(t)$) in (2.48), in the resonance condition, induces an in-phase (out-of-phase) field $E_{\mathrm{SRG}}^{(3)}(t)$ ($E_{\mathrm{SRL}}^{(3)}(t)$). Therefore, SRS is a vibrationally resonant DFWM process leading to constructive interference at $\omega_S$ and a resonant DFWM leading to destructive interference at $\omega_p$. The former, SRG, results in an increase in the total intensity at $\omega_S$, whereas the latter, SRL, results in a decrease in the total intensity at $\omega_p$.

Measuring the interference term, also called the heterodyne term, is known as heterodyne-detection[30]. This type of measurement has several advantages. First, the interference term is proportional to the imaginary part of $\chi_R^{(3)}$, which describes the dissipative response of the medium [79]. Such dependence means that if there is no energy transfer from the incident field components to the medium, which is necessary for the SRS effect to occur, the interference term cannot be measured, because $\mathrm{Im}\{\chi_R^{(3)}\} = 0$ [14, 51, 79]. Second, as $\mathrm{Im}\{\chi_R^{(3)}\} \propto \sigma_R$, where $\sigma_R$ is the Raman scattering cross-section, the heterodyne-detected SRS exhibits the same spectral lineshapes as probed in SpRS [79]. These two features are also related to the absence of the nonresonant background term (see expression (2.65) for CARS) in expressions (2.75a) and (2.75b). All these attributes give the heterodyne-detected SRS great vibrational selectivity: when off-resonance, the interference term vanishes, and, in resonance, it is unaffected by nonresonant DFWM effects described by $\chi_{NR}^{(3)}$. Its spectrum coincides with that of SpRS, while being orders of magnitude more efficient. Figure 2.21 shows the experimental CARS, SRS (SRL), and SpRS spectra of retinol [81].

It is worth mentioning that the absence of the nonresonant background term $\chi_{NR}^{(3)}$ in (2.75a) and (2.75b) does not mean that SRS is free of any form of Raman-independent background. Processes that can lead to intensity variation at $\omega_S$ and $\omega_p$, such as photothermal and intensity-dependent propagation effects, may spuriously contribute to intensity variation in (2.75a) and (2.75b). Several works discuss coexisting effects acting as background sources in SRS and

[30] The detection is heterodyne if the detected component $\omega_S$ ($\omega_p$) is already present in the excitation and the measured intensity is extracted from the interference term. The experiments performed in thi sthesis are with heterodyne-detected SRS [14].

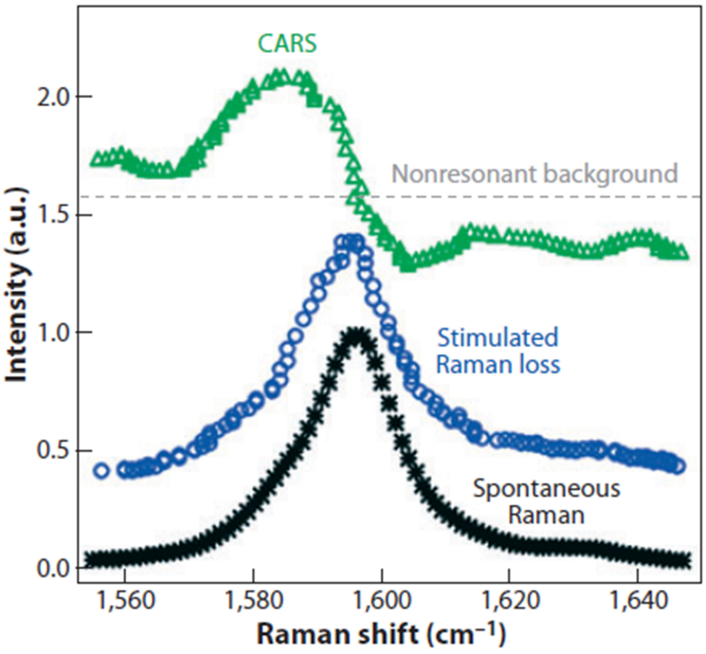


Figure 2.21: Absense of spectral distortion in the stimulated Raman scattering spectrum. Coherent anti-Stokes Raman scattering, SRS (SRL) and SpRS spectrum for retinol around the Raman peak at 1595 $cm^{-1}$. Unlike CARS, which exhibits spectral distortion due to the nonresonant background, the recorded SRS spectrum exhibits a Raman peak with the same resonant shape as the SpRS spectrum. Adapted from reference [81].

strategies to circumvent them to extract only vibrationally relevant information [93–100]. Some of these effects are not included in the approach used so far to define the SRS process. One such effect is 2PL due to single-color and two-color two-photon absorption, as discussed in section 2.7.2 for CARS.

An important competing effect is spatial cross-phase modulation (XPM). As anticipated in section 2.4, it is a third-order nonlinear effect mediated by the second-order refractive index $n_2 \propto \mathrm{Re}\{\chi^{(3)}\}$ in expression (2.29). If we consider the spatial dependence of amplitudes $E_S = E_S(x,y,z)$ and $E_p = E_p(x,y,z)$, the relationship between the amplitudes as the field components (2.48) propagate through the medium is given by [101–103]

$$\frac{\partial E_S}{\partial z} - \frac{-i}{2k_S}\left[\frac{\partial^2 E_S}{\partial x^2} + \frac{\partial^2 E_S}{\partial y^2}\right] = \frac{ik_S n_2}{n_{0S}}\left(|E_S|^2 + 2|E_p|^2\right)E_S, \tag{2.76a}$$

$$\frac{\partial E_p}{\partial z} - \frac{-i}{2k_p}\left[\frac{\partial^2 E_p}{\partial x^2} + \frac{\partial^2 E_p}{\partial y^2}\right] = \frac{ik_p n_2}{n_{0p}}\left(|E_p|^2 + 2|E_S|^2\right)E_p, \tag{2.76b}$$

where $n_{0S}$ ($n_{0p}$) is the linear refractive index at $\omega_S$ ($\omega_p$) and $k_S$ ($k_p$) is the Stokes (pump) incident wavevector. The second term in the parentheses on the right side of equations[31] (2.76a) and (2.76b) show that the amplitude $E_S$ ($E_p$) of the field component $E_S(t)$ ($E_p(t)$) depends on the amplitude of the field $E_p(t)$ ($E_S(t)$), so they become correlated. Because

[31] The first term in the parentheses is associated with the refractive index variation induced by the presence of the field itself. This effect is called self-phase modulation.

of such correlation, as the Stokes (pump) component propagates, the experienced refractive index $n_S$ ($n_p$) is modified by the presence of the pump (Stokes) component. Each component experiences a variation in the refractive index given by [51, 94]

$$\Delta n_S \propto \mathrm{Re}\left\{\chi^{(3)}\right\} I_p, \tag{2.77a}$$

$$\Delta n_p \propto \mathrm{Re}\left\{\chi^{(3)}\right\} I_S. \tag{2.77b}$$

If the refractive index is negative, the pump component can experience a defocusing induced by the intensity profile of the Stokes component [50, 94], for example. In practical situations where the beam is detected after being transmitted by an aperture, this intensity-dependent divergence modulation can be translated into intensity variation by aperture clipping if the aperture is not able to collect the entire spatial distribution of the beam [14, 94, 104]. In many cases, XPM can be the main form of background in SRS detection.

Finally, we note that the interference term depends linearly on the pump intensity, as in SpRS. Unlike SpRS, however, it also depends on the Stokes intensity. Therefore, while the generation of SRS involves the interaction of three fields, as in CARS, the interference term carries only a dependency on two field components [84]. This dependence is oftentimes referred as an overall quadratic dependence of heterodyne-detected SRS as opposed to the overall cubic dependence of homodyne-detected CARS, which depends on three incident field components [14, 84]. Furthermore, because the interference term is directly proportional to $P(\omega_S)$ ($P(\omega_p)$) in expression (2.73a) and (2.73b), it is linearly dependent on $N$, which is especially favorable when the number of scatterers within the focal volume is small [14, 79, 84].

### 2.7.4 Experimental implementation

For the implementation of CRS effects, it is important to emphasize that the conditions for all four forms of scattering discussed in section 2.7.1 are essentially the same. The energy difference of the beams must be resonant with the energy of a Raman transition, and the pump and Stokes beams must simultaneously interact with the sample. However, for the purpose of this thesis, the effects can be divided into two types: those whose frequency response of the medium occurs at a different frequency from the excitation (type I) and those which occur at the same frequency (type II) [85]. Thus, the instrumentation is similar for all processes, except at the detection[32]. Therefore, the implementation follows two steps: preparation, which is approximately the same for all CRS effects, and detection, which depends on whether the effect lies within one of the two types. Homodyne-detected CARS is a type I effect and can be implemented with the same setup discussed in figure 2.11 for the wave mixing effects. Consequently, the setup differences in figure 2.22A are essentially due to heterodyne-detected SRS, which is a type II CRS effect.

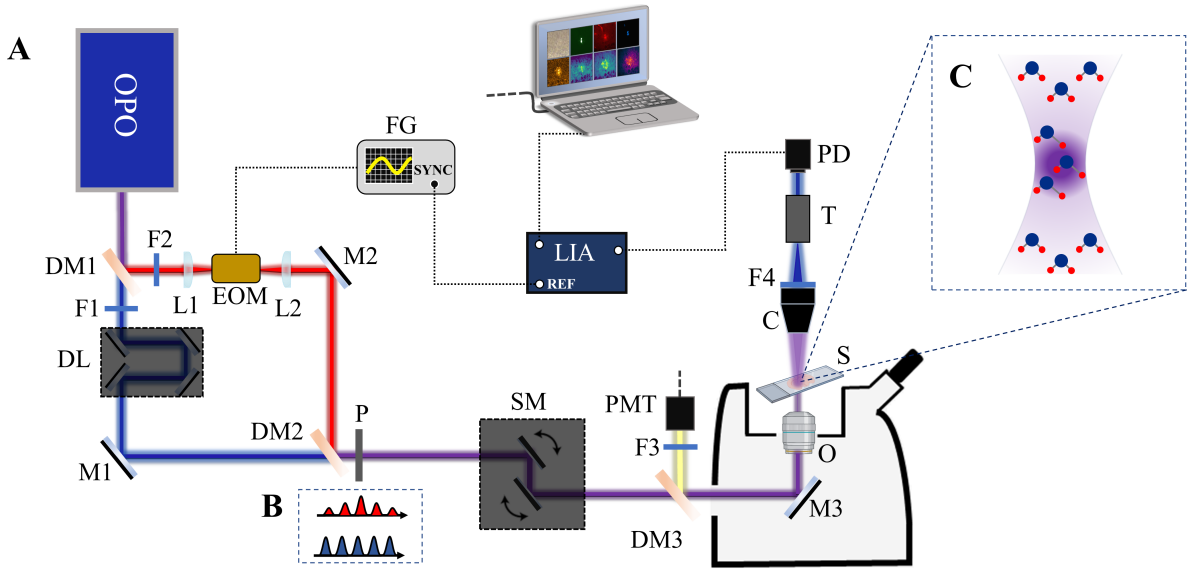


Figure 2.22: Optical setup for the experimental implementation of coherent anti-Stokes Raman scattering and stimulated Raman scattering. OPO: laser source. DM1 (DM2, DM3): dicroic mirror. M1 (M2): mirror. L1 (L2): lens. F1 (F2): filter that ensures that there is no pump (Stokes) beam component in the Stokes (pump) beam arm. DL: delay line. EOM: electro-optic modulator. P: polarizer. SM: scanning mirrors. F3: narrow bandpass filter centered at 661 nm for CARS imaging. PMT: photomultiplier tube. O: objective. S: sample. C: condenser. F4: bandpass filter that efficiently blocks the Stokes beam. T: telescope. PD: photodiode. LIA: lock-in amplifier. FG: function generator. Adapted from reference [59].

### 2.7.4.1 Preparation

Since the excitation must stimulate the vibration into resonance, we use the tunable laser source described in section 2.5.3. The resonance condition can be realized with a fixed wavelength Stokes beam (1064 nm, red beam in figure 2.22A) and a tunable wavelength pump beam (blue beam in figure 2.22A). Tuning the pump beam wavelength controls the energy difference (and, hence, the beating frequency) of the beams, allowing the resonant excitation to probe different vibrations. For comparison with section 2.5.3, we consider the pump beam tuned at 816 nm so that the excitation is the same as in the DFWM implementation. The beating of pump and Stokes beams is proportional to the wavenumber[33] 2856 $cm^{-1}$. In a biological tissue, the beating would be in resonance with the lipid-based vibration of $CH_2$ stretching mode (see chapter 3). Satisfying such a condition allows the intensity of CRS effects to grow coherently. However, in many applications, specially in high-speed microscopy, this coherent addition alone is often not enough to produce a sufficiently strong signal [84]. For that reason, ultra-short pulse lasers are commonly employed as excitation. The relationship between the experimental parameters introduced in section 2.5.3 and the intensity of CRS effects is given

[32] References on different detection schemes for CRS effects can be found in reference [85]

[33] $\left(\frac{1}{816\times10^{-9}\text{ m}} - \frac{1}{1064\times10^{-9}\text{ m}}\right) \times 10^{-2} \approx 2856\text{ cm}^{-1}$, where $cm^{-1}$ is a unit commonly used in spectroscopy to refer to molecular vibrations.

by [84]

$$I_{\mathrm{CRS}} \propto \frac{P^n}{(f\tau)^{n-1}}, \tag{2.78}$$

where $P$ is the average excitation power, $f$ is the pulse repetition rate, and $\tau$ is the pulse duration (see section 2.5.3). For homodyne-detected CARS, $n = 3$, while $n = 2$ for heterodyne-detected SRS [84]. Expression (2.78) show that for a fixed average power, the intensity of CRS effects increase as the pulse duration decreases. For the CRS applications presented in this thesis, we use the picosecond pulsed source described in section 2.5.3.

In figure 2.22A, at the output of the OPO, the pump and Stokes beams are generated spatially and temporally overlapped, in addition to being horizontally polarized. The dichroic mirror DM1 separates the two beams in a March-Zehnder-type geometry. This split is necessary so that only the Stokes beam interacts with the resonant electro-optic modulator EOM required for SRS heterodyne detection. The filter F1 (F2) ensures that there is no pump (Stokes) beam component in the Stokes (pump) beam arm. The mirrors M1 and M2 control the spatial overlap of the beams on the dichroic mirror DM2, where the beams are recombined collinearly. The delay line DL on the pump beam arm allows for temporal synchronization of the beams, while the polarizer P ensures that both beams are horizontally polarized. The scanning mirrors SM and the mirror M3 direct the beams to all points in the sample S, allowing the mapping of the focal volume. The final element of preparation is the high numerical aperture (NA) objective O, which needs to be an apochromatic lens to focus beams of different wavelengths on the same spot. In this way, both the resonance condition and the simultaneous interaction can be carried out experimentally.

#### 2.7.4.2 Detection

As the CARS response is generated at a new wavelength (~ 661 nm in the case considered here), the CARS beam is homodyne-detected by the photomultiplier tube PMT. The dichroic mirror DM3 reflects the backscattered response to the PMT, where a bandpass filter F3 (centered at 661 nm in the case illustrated here) isolates the CARS beam from the excitation beams.

On the other hand, the SRS signal cannot be optically isolated from the excitation beams because the effect occurs at the same wavelengths. However, such isolation can be done with electronic filtering based on modulation transfer. Figure 2.22A only considers the detection of SRL as implemented in the works of this thesis. For SRL detection, four electronic elements are used: the resonant EOM, the function generator FG, the lock-in amplifier LIA, and the large-area photodiode PD. All these elements are electronically synchronized. The FG applies a sinusoidal voltage at a high frequency[34] (in our case, 10 MHz) to the EOM crystal, causing a rapid change in the polarization state of the Stokes beam[35]. These two elements act on the

[34]Frequency and resonance in this context relate to the voltage signal provided by the function generator and the components of the circuits associated with the modulator. The modulation is only effective when the frequency of the generated voltage signal is resonant with the circuit frequency. Although this is a high-frequency operation in the circuit, this frequency is orders of magnitude lower than the oscillation of the laser beams.

[35]This change occurs as a result of variation in the refractive index of a non-centrosymmetric material induced by a strong electric field. Such a process is a second-order nonlinear effect known as the linear electro-optic effect

Stokes beam as a variable wave plate and the polarizer P at a fixed orientation (horizontal, in our case) transforms polarization modulation into amplitude modulation. Therefore, after the action of the polarizer P, the Stokes beam (and only the Stokes beam) acquires a particular intensity profile, as illustrated in figure 2.22B. After both beams (unmodulated pump and modulated Stokes beams) interact with the sample, the forward scattered response is collected by the high NA condenser C, which must be aligned appropriately, for example, using the Köhler illumination method [23]. The filter F4 efficiently blocks the Stokes beam, and the (initially unmodulated) pump beam is detected by the PD connected to the LIA, which, in turn, is connected to the synchronization port of the FG. The telescope T image the scanning mirrors onto the PD to eliminate beam-movement due to laser scanning [23]. Since SRS depends on both beams, the (modulated) Stokes beam intensity profile is transferred to the pump beam when SRS occurs in the sample. Therefore, part of the response generated at 816 nm also becomes modulated after the interaction. However, most of the response of the sample at 816 nm is due to Rayleigh scattering, which is not dependent on both beams and thus remains unmodulated. When the PD detects the response beams at 816 nm, the LIA mixes the detected signal provided by the response beams with the modulation reference signal provided by the sync output port of the FG. Therefore, the LIA can separate the modulated part from the unmodulated part of the detected signal[36]. The combined action of these electronic elements is to amplify the modulation-synchronized response signal and eliminate any other signal, effectively discriminating SRS from Rayleigh scattering.

The first feature highlighted in the experimental implementation of CARS and SRS is the excitation profile in figure 2.22C. As in the case of wave mixing discussed in section 2.5.3, the occurrence of CRS effects is only relevant at the focus, where the intensity is highest. Furthermore, the effect of coherent excitation is also illustrated in the behavior of the molecules. The molecules do not respond to the excitation efficiently outside the focal region and are represented as static. In the focal region, the vibrations result from the resonance induced by the beating fields, and, therefore, the molecules vibrate in phase. Figure 2.22C can be compared to 2.6B of the SpRS experimental implementation where molecules vibrate randomly outside and inside the focal region.

Another evident aspect is the complexity difference in detecting CARS and SRS. However, the simplicity of homodyne-detected CARS comes at the cost of a considerable vulnerability to the nonresonant background. For the parameters used here, CARS is generated at $\sim 661$ nm. That is the same wavelength as DFWM is generated in section 2.5.3. Therefore, when nonresonant DFWM becomes as intense as CARS, the problem of detecting CARS becomes equivalent to that of SRS: discriminating coexisting effects at the same wavelength.

On the other hand, in addition to the SRS interference term (2.75) being free of the nonresonant background that affects CARS, the modulation transfer scheme in heterodyne-detected SRS eliminates other competing effects, such as self-phase modulation, which only depends on one of the beams. However, two-color two-photon absorption results in modulation

or Pockels effect. Chapter 11 in reference [15] discusses the Pockels effect and general principles of electro-optic modulators.

[36] Chapter 3 in reference [14] discusses signal processing by LIAs in more detail.

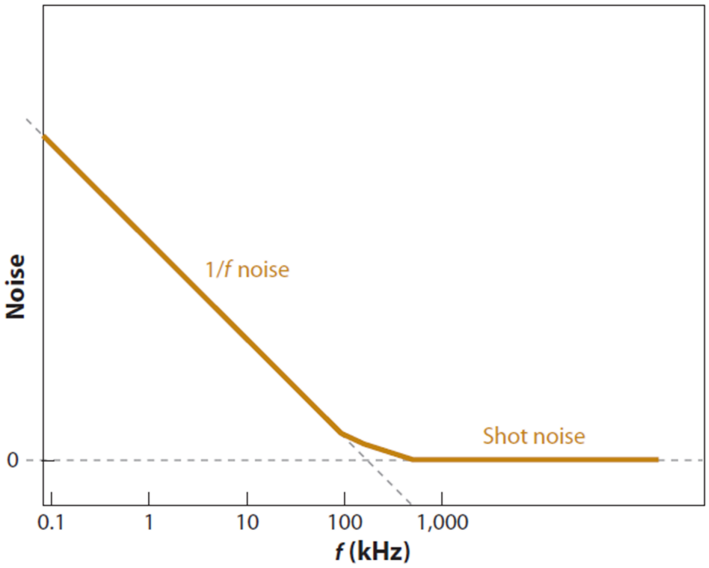


Figure 2.23: Relative intensity noise. Spectrum of the RIN of typical laser sources as a function of fluctuation frequency $f$, demonstrating the importance of modulating the Stokes beam at a high frequency. Figure reproduced from reference [81].

transfer similar to SRS and, therefore, intensity variation in the pump beam. Hence, excitation should be chosen to avoid resonance with electronic transitions [14]. Likewise, XPM-induced Kerr-lensing effects, as discussed at the end of section 2.7.3, can also result in modulation transfer. Upon propagating through the sample, the pump beam may experience a variation in the refractive index that carries the intensity profile of the Stokes beam, according to (2.77b). Such a process can result in modulation of pump beam divergence. If the condenser is misaligned or its NA is not high enough to collect the emission of the sample, the divergence modulation becomes amplitude modulation due to clipping on the condenser aperture. Proper alignment and a condenser lens with higher NA than the objective lens can minimize such drawbacks. Moreover, clipping on the edges of the detector can also occur, leading to similar spurious amplitude modulation. That is also one of the reasons to use a large area PD and a telescope to reduce beam movement on the PD screen.

Finally, the detection of CARS and SRS is not only influenced by competing physical effects, which can be evaluated by a sensitivity factor known as the signal-to-background ratio (SBR). Detection sensitivity is also accounted for in terms of the signal-to-noise ratio (SNR), which includes noise associated with instrumentation operation. The noise level will determine the pixel dwell time needed for the CRS effect to be well-resolved upon detection. The pixel dwell time is the time that the focused laser beam rests on a single pixel of the detector. Therefore, the longer the pixel dwell time, the more photons can be collected per pixel. The more photons that contribute to the signal and not the noise, the shorter the acquisition time to obtain a well-resolved signal. This process has a fundamental limit imposed by the quantum nature of the interaction of light with the detector. The random fluctuations generated in this interaction set a lower limit on the amount of light contributing to the noise known as shot

noise[37]. Nevertheless, before reaching this limit, there are several sources of noise that can decrease detection sensitivity [106].

Figure 2.23 illustrates the relative intensity noise (RIN) in the low-frequency range, a type of noise associated with laser power instability (and intensity variation) that can significantly affect CRS experiments [107]. This influence can be more easily understood in the SRS: the effect occurs at the same excitation wavelength as a laser intensity variation, while the laser itself is already subject to variations by several other processes [14, 107, 108]. One of these processes is RIN, which decreases detection sensitivity as a result of fluctuations associated with mechanical vibrations and different forms of microenvironmental change [14, 106]. As the figure shows, RIN is most significant for slower fluctuations, below 100 kHz, where it follows a $1/f$ functional dependence. This property of laser noise highlights the importance of modulating the amplitude of the Stokes beam at a high modulation frequency. In our case, the modulation frequency is in the order of 10 MHz, where the noise influence on detection is low. A review of the influence of noise in CARS and SRS can be found in references [106–108].

## 2.8 Concluding remarks

This chapter reviewed the basic concepts of linear and nonlinear optics needed to discuss the application of different optical effects in imaging biological tissues in chapter 3 and 2D materials in chapter 4. We explored the classical picture, which offers an intuitive approach to light-matter interaction. In particular, the chapter emphasized the CRS effects, which are the main subject of the thesis.

[37] This limit can be lowered using quantum correlations, as shown in a recent work with squeezed light quantum SRS [105].

# Chapter 3

# Nonlinear optics for biological imaging

## 3.1 Introductory remarks

Multiple disciplinary approaches is an increasingly emphasized topic in science. Still, the interplay between physics, biology, and medicine is far from a recent event. Well-known examples of this interest can be seen in works of many physicists and polymaths [109–112]. Presently, when discussing this relation, it is not uncommon for the field of radiology to be brought up. Technological advances in the twentieth-century enabled this interplay to produce medical exams based on ultrasound, radiography, computed tomography, positron emission tomography, nuclear magnetic resonance, to name a few. Undoubtedly, what is now known as medical imaging is a representative example of the prolific success of this involvement. However, this relation is not limited to radiology. There is a long tradition of physicists and physics-based techniques making significant contributions to biology and medicine [113]. In particular, the history of optics and microscopy carries a significant part of the history of the association of these three disciplines. An early example is the works of Robert Hooke. Hooke is primarily remembered by one of the shortest statements in physics – *ut tensio, sic vis* – (as the extension, so is the force), expressing his law of linearity between the spring's displacement and the force applied to it. Nevertheless, Hooke's expertise in experimental optics allowed him to introduce relevant modifications in a microscope of his time [114]. In his book *Micrographia* [115], he produced one of the first materials with illustrations of samples seen under a microscope, presenting appreciable art of animals, plants, and other objects. Therefore, through the development and application of the microscope, Hooke originated in optics, the first steps toward microbiology, micro-imaging, and areas dedicated to examining fine details.

Reaping the benefits of this historical process, we investigate biological structures as an application of the advances in optics, having the microscope as an essential instrument. In this chapter, we find the light-matter interactions discussed in chapter 2, with a special interest in vibrational imaging for biomedicine. The main work of the chapter is the multimodal imaging of brain tissues of transgenic mice for AD. In section 3.2, we overview the contribution of nonlinear optical effects in biological imaging. In section 3.3, we narrow down and have a

short survey on (nonlinear) vibrational imaging in biomedicine. Finally, in section 3.4, we present our main results, with some perspectives in section 3.5.

## 3.2 Nonlinear magic

In several cases, advances in biological imaging resulted from modifications in the microscope illumination mode, one of the critical aspects of optical microscopy. Hooke himself, mentioned in the previous section, introduced a different illumination scheme into his microscope to improve the quality of his images [114]. One of the oldest and most used families of techniques in biological imaging is widefield illumination, with bright field microscopy being the most popular of them. In this mode, the entire sample is evenly exposed to light, often from a white light source. Image formation depends on contrast[1], which is based on the absorption of light by the material [116–120]. The use of this technique for biological imaging, however, carries two main difficulties: weakly and equally absorbing samples and blurry appearance of out-of-focus objects [118].

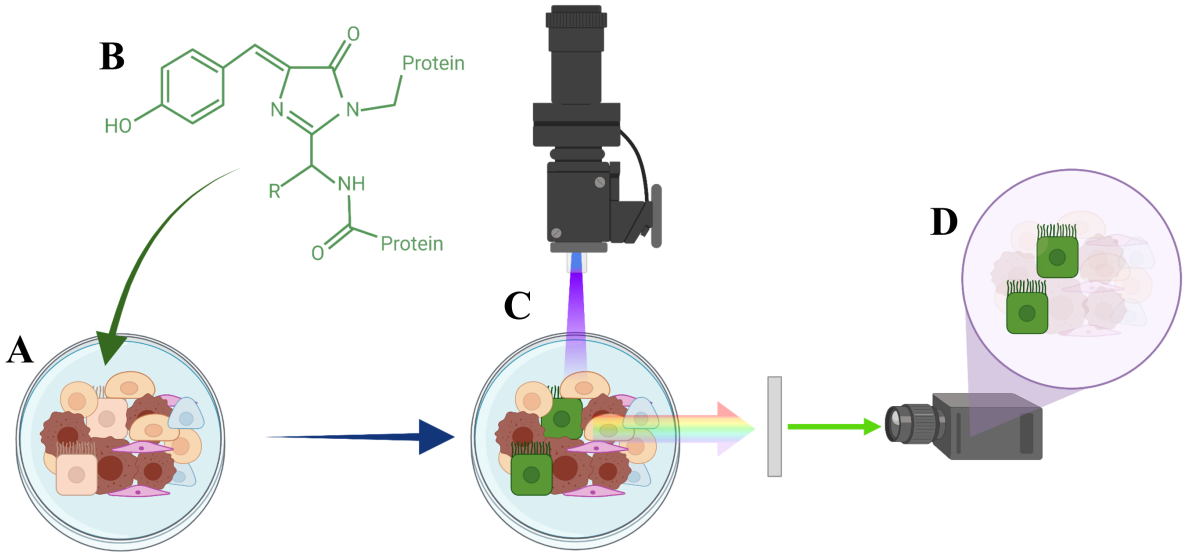


Figure 3.1: Fluorescent labeling. (A) A biological system, such as a particular cell type, can be more easily distinguished from the environment by (B) incorporating a fluorescent compound that specifically binds to it. (C) Under illumination with an optimal wavelength for absorption of the compound, the label emits distinctively at longer wavelengths, (D) having its signal separated from the background through a suitable filter. Adapted from references [121, 122].

The first difficulty lies in the interaction of light with the sample. Many biological components have low effective absorbance and different biomolecules absorb light in similar spectral regions, notably in the region between blue and near-ultraviolet (NUV) [55, 117]. Such condition contributes to the reduction of image contrast. Also, due to the typical sizes of biological objects, the most likely form of scattering in tissues is Rayleigh scattering, whose intensity is

[1]The term "contrast" is used here and throughout the chapter in the simple sense of the ability to distinguish the signal from the background or noise [116].

proportional to $1/\lambda^4$ [55]. This means that the illumination in the blue-NUV region suffers much scattering, reducing the imaging depth and also the contrast. One way to mitigate these problems is to insist on the same contrast generation mechanism - absorption - and increase the efficiency of the emitted signal. That can be done with fluorescent (or photoluminescent) labeling: xenobiotic stain-based approaches in which highly fluorescent compounds, having a well-known emission profile[2], are coupled to the target object to distinguish it from the background. Figure 3.1 illustrates such a procedure: a set of different cells (figure 3.1A) receive a fluorescent compound specific to one of them (figure 3.1B). Under illumination with optimal wavelengths for the absorption of this label, all cells produce a radiative response (figure 3.1C). Nevertheless, the label exhibits a distinctive fluorescence at a known spectral window, which allows its filtering and discrimination of the labeled cells from other cells (figure 3.1D). While this is a simple solution, it is not without inconvenience. Special preparation and labeling strategies may be required, depending on sample type [123, 124]; Some fluorescent labels may perturb transport properties of the target [23], particularly for small molecules [81]; Some can interfere with the information of interest and hamper the interpretation of relevant data [25, 125, 126]; And many stains are unsuitable for *in vivo* biomedical applications [23, 81].

A simple view of the second difficulty, based on the description given by Webb [116], is illustrated in figure 3.2, where a white light source evenly illuminates a thick sample and a lens collects the response of a cell, allowing its imaging with a detector. Figure 3.2A shows the case where the image of Cell A, deep in the tissue, is formed at the focal point $x$. Figure 3.2B, on the other hand, shows the case in which the image of Cell B, more superficial, is formed at the focal point $x'$, posterior to $x$. Due to the even illumination of the tissue, the two cases coexist, as shown in figure 3.2C. However, as indicated in figure 3.2C, the image of Cell B is of suboptimal quality, as the ideal image formation occurs at a posterior plane. For a general situation, if we are interested in imaging only Cell A, not only the in-focus Cell A (as in figure 3.2A) contributes to image formation, but also different cells in the sample, outside the focus of the lens. In other words, the image formed at the detector is a superposition of a well-resolved object at the focal plane and unresolved objects out of focus, adding a blurry haze to the image [116, 120]. The lack of an out-of-focus light rejection mechanism is responsible for the considerable reduction in contrast in the image of the object of interest, even if it is labeled. Furthermore, the even illumination can be even more unpleasant for low-absorbing target objects, where higher intensity light is needed. In this case, out-of-focus objects may be too much exposed and suffer photobleaching and phototoxicity, together also referred as photodamage[3].

One of the ingenious methods used to circumvent the out-of-focus rejection problem was

[2] Such as intensity and spectral energy range.

[3] Photobleaching is a process whereby an initially fluorescent object is rendered non-fluorescent upon exposure to high-intensity light. The phenomenon appears to be associated with photochemical modifications, transitions between singlet and triplet spin states, and bonds with the environment. On the other hand, phototoxicity is a process that results in changes in the molecular structure of biological components, causing reactive species that are hostile to the environment. It is associated with several factors, such as light wavelength, intensity, and exposure time, and in extreme cases, it can lead to cell death. For a discussion of the processes, see references [55, 117]

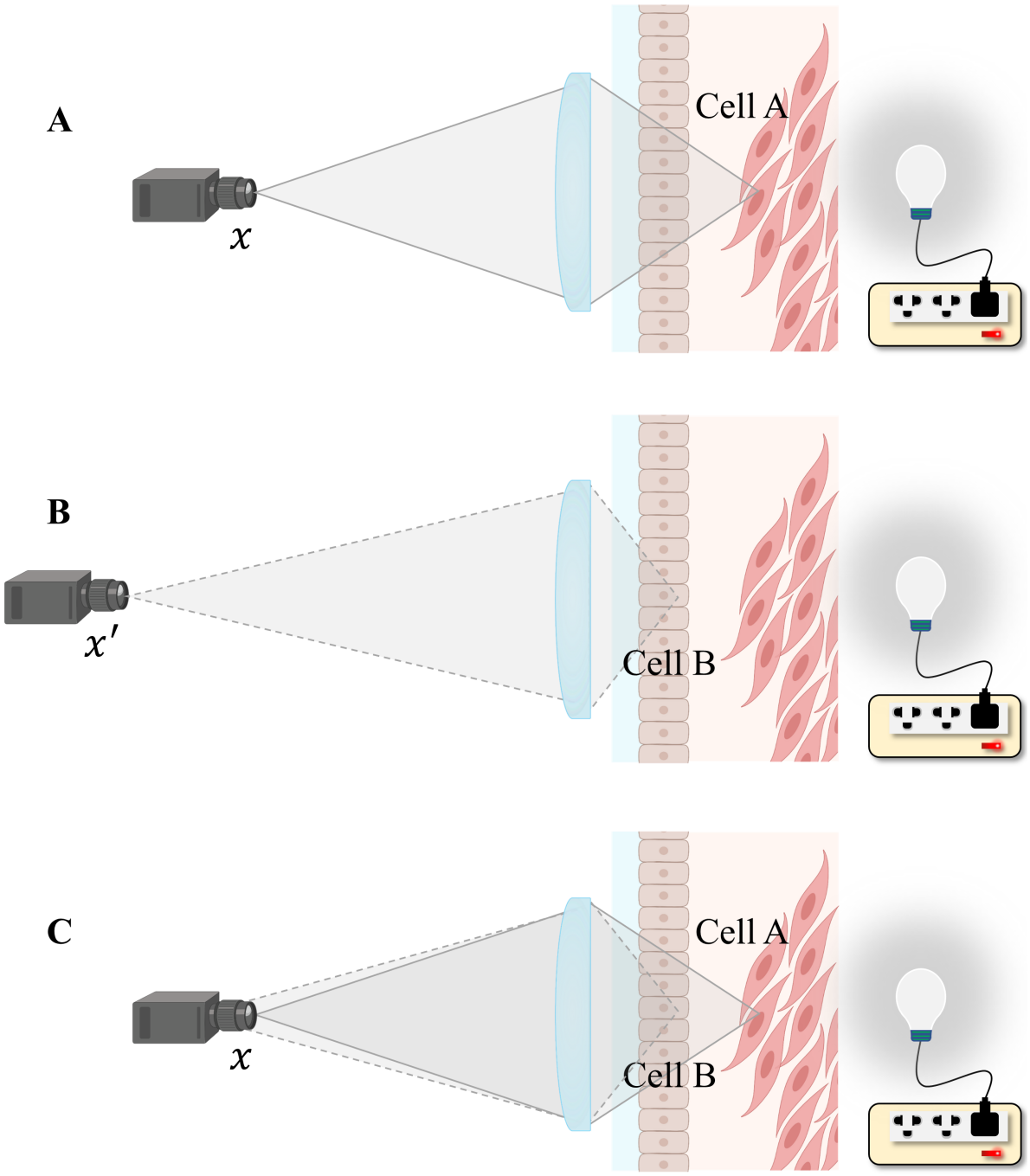


Figure 3.2: A simple view of widefield microscopy. (A) At the focal point $x$, a lens forms the image of Cell A, which is deep in the tissue. (B) For the more superficial Cell B, this same lens forms the image at posterior focal point $x'$. With even illumination, (C) the two situations coexist. The detector at $x$ registers a superposition of the well-resolved image of the in-focus Cell A and a blurry image of the out-of-focus Cell B. Adapted from references [122, 127].

invented in the late 1950s in the context of brain research [128]. Figure 3.3 is a simplification of the rejection mechanism of what is known as confocal microscopy [116]. Comparing figures 3.2C and 3.3, we can see the transition between widefield and confocal modes. In figure 3.3A, the insertion of a pinhole $p$ at the focal point $x$ allows the collection of light emitted by Cell A, simultaneously with the rejection of Cell B emission, whose image would

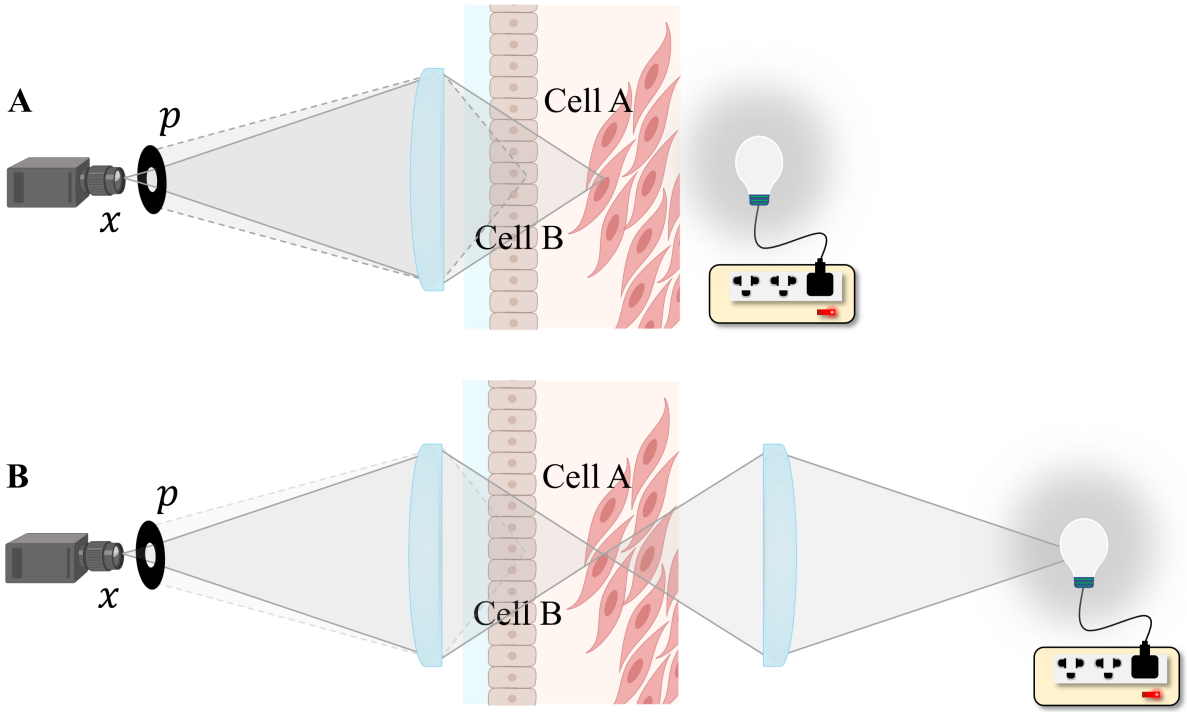


Figure 3.3: Simple view of confocal microscopy. (A) With the pinhole at the focal point $x$, the detector registers the signal emitted by Cell A while blocking the emission of Cell B. (B) The lens inserted between the light source and the tissue, confocal with the pinhole, allows only the cell to be more efficiently illuminated, adding selectivity to the excitation as well. Adapted from references [122, 127].

be formed at a posterior plane [116]. In Figure 3.3B, the light source is confocal with Cell A and the pinhole (hence the name of the technique), which adds selectivity to the illumination. Therefore, receiving less light, Cell B also produce less emission, as indicated in figure 3.3B. Moreover, the discrimination of focal planes (or depth), known as optical sectioning, is responsible for the three-dimensionality gain of the technique, especially propitious for thick samples. Figure 3.4 show two different biological systems studied with widefield (figures 3.4A and 3.4C) and confocal (figures 3.4B and 3.4D) microscopies, demonstrating the improvement in imaging. While confocal microscopy has several advantages, it also inserts some drawbacks. We can immediately recognize a practical one: the insertion of small pinholes as a spatial filter usually requires a more careful alignment. Setup vibrations and experimental errors causing misalignment can result in intensity variations, making it difficult to interpret and quantitatively analyze the data. A similar difficulty can arise from the interaction of light with the sample. Highly scattering media, such as brain tissue, can be a problem for confocal microscopy [117, 129]. Light generated by in-focus objects can be scattered on its way out of the tissue, producing more divergent emissions. Consequently, these emissions end up being rejected by the pinhole, even though they were originally generated in the focus [117, 129]. Finally[4], as the incident cone of light can still excite out-of-focus objects in confocal microscopy, photodamage remains an issue to be addressed.

[4] A more detailed discussion of the characteristics, advantages, and limits of confocal microscopy in biological imaging, as well as comparisons with other illumination modes, can be found in references [55, 116, 117].

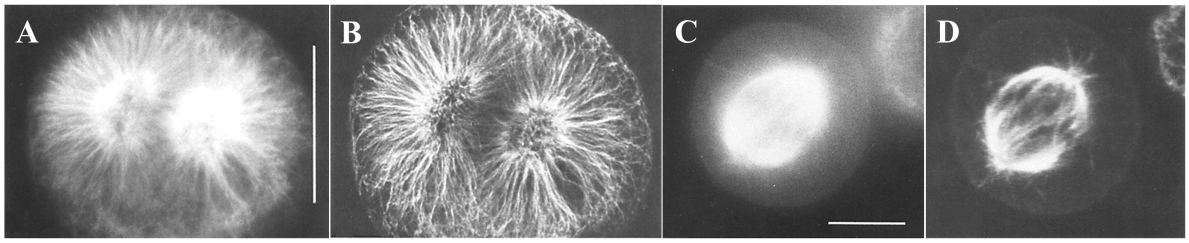


Figure 3.4: Widefield *versus* confocal imaging. (A) Widefield and (B) confocal images of fertilized egg of a sea urchin (scale bar is 50 µm. Similarly, (C) widefield and (D) confocal images of HeLa Cell (scale bar is 5 µm) also demonstrate the differences between the two techniques. Adapted from reference [130].

The advantages and limitations highlighted here allow us to present what Zipfel *et al.* called the "nonlinear magic" [24]. This rather eye-catching title has no intention of turning nonlinear optics in biological imaging into a cure-all [84, 117]. On the contrary, it just wants to stress that when the benefits presented here are well-matched to the problems of a specific study, nonlinear optics can provide a convenient approach. As underlined by the authors, nonlinear microscopy has become an important tool in studying thick tissues and live animals. In particular, it has received a great deal of attention in brain research [25, 29, 31–33, 126, 129, 131–137] but also in several other biomedical areas [53, 76, 138–145]. The "magic" is because certain designed features of some microscopy modalities are intrinsic physical properties of nonlinear interactions [15, 48]. The three attributes that most interest us here are: intrinsic optical sectioning, lower energy excitation, and intrinsic label-free character.

As discussed in section 2.4, nonlinear effects occur in high-intensity interactions. Signals coming from this interaction are essentially limited to the focal point, where the intensity is much higher. In other words, nonlinear signals originate from the interaction of light with in-focus objects. This intrinsic confocality brings with it the previously mentioned advantages of confocal microscopy - three-dimensionality and absence of out-of-focus emissions -, but without the insertion of a small pinhole. Without it, we also get rid of the drawbacks associated with this spatial filter. Furthermore, with large-area detectors, we can alleviate the problem of divergent emissions due to scattering in the tissue.

The use of lower energy excitation is rooted in the multiphoton nature of the nonlinear optical effects. Even though much of the absorption in biological materials takes place in the blue-NUV window, in the nonlinear case, such interaction is the result of nearly simultaneous absorption of photons[5] in the near-infrared (NIR) window. Near-infrared excitation also allows for a greater imaging depth, as this wavelength undergoes less Rayleigh scattering in the tissue. Additionally, photodamage is virtually restricted to only the focal point, as NIR propagation at a lower intensity[6] does not excite most of the molecules [14, 24, 55, 117].

Multiphoton interaction also makes the resulting intensity of nonlinear effects dependent on higher orders of incoming light intensity. For example, in TPEF, focusing twice as much light gives four times as much fluorescence. In homodyne CARS, twice as much incoming intensity

[5] More than one.

[6] Insufficient enough for simiultaneous multiphoton absorption.

gives six times as much signal [14]. This allows weakly absorbing biomolecules to be probed more easily, sometimes even by autofluorescence[7] of specific structures [117]. Furthermore, we do not need to insist on just one contrast generation mechanism, such as absorption. The very physical nature of light-matter interactions allows for a multitude of contrast generation mechanisms, carrying with them new information. Biological structures can carry a level of organization captured by interactions sensitive to symmetry-based information, such as SHG, SFG, and DFG. On the other hand, some molecules can be Raman-active, and nonlinear interactions with vibrational states can carry biochemical information, as is the case with CARS and SRS. Therefore, whether through electronic, structural, or vibrational mediators intrinsic to biological systems, some nonlinear interactions provide what is necessary for label-free imaging, thereby avoiding tissue-processing artifacts or special preparations. That is precisely the kind of interaction we are particularly interested in here.

The following section will briefly review some nonlinear microscopy applications in biomedicine, with a specific interest in label-free contrast mechanisms. In particular, we will explore the role of CARS and SRS microscopies.

## 3.3 Coherent Raman imaging in biomedicine

As stated at the end of the previous section, instead of restricting ourselves to the contrast mechanism based on electronic absorption and using specially fluorescent molecules, here we will rely on vibrational scattering, providing a label-free contrast mechanism. In particular, we will explore Raman scattering as a tool for biomedical studies. Although several label-free imaging and spectroscopic techniques exist, SpRS has been conceptualized as a prominent tool in biomedicine [146], including applications in surgery and intraoperative data acquisition [147–150]. Among several factors, this is due to the amount of information that SpRS makes available. For example, after theoretical analysis it is possible to infer information about the length, strength, angle of bonds, chemical structure, and geometric conformation of molecules from the vibrational spectrum of proteins [151]. The position, intensity, width, and displacement of a spectrum band provide significant bases for interpreting the molecular system. An important example is amide I, whose C=O backbone vibration encodes information about protein secondary structure in the form of band shift [151,152]. The secondary structure of a protein concerns its 3D arrangement (or conformation) [52,153]. Due to protein folding, the linear polypeptide chain assumes different configurational states that depend on the interaction between different parts of the chain itself. These chemical bonds within the folded chain impose constraints on protein geometry, generating different 3D structures. Two common polypeptide conformations are alpha-helix (α-helix) and beta-sheet (β-sheet) [52,153], whose different interactions exhibit different vibration frequencies, making it possible to discriminate them in the SpRS spectrum. This distinction will be of particular relevance in section 3.4.

On a similar note, we can maximize this information delivery by combining SpRS-based spectroscopy with confocal microscopy. In that case, we could build an image of the distribu-

[7] That is, the photoluminescence of native biomolecules unassisted by labels.

tion of chemicals. A Raman image would be a biochemical map of the object of interest. Such an idea is realized in confocal Raman microscopy (CRM)[8] [154, 155], and it is performed in biological imaging with great success. Notwithstanding its value, the primary disadvantage of such SpRS-based technique is the acquisition time. In not-so-unusual setups, it can take about 7 minutes to image a single 10 µm cell [155]. In this context, CRS described in section 2.7.1, together with microscopy, brings the numerous advantages of CRM while circumventing the disadvantage of long acquisition times.

### 3.3.1 Intrinsically label-free, yet fast

Adding to its popularity in biological imaging, two advantages of fluorescence imaging are apparent: its specificity (through labels) and its speed [117]. Although it is not the purpose of this thesis to revisit all possible comparisons between fluorescence and vibrational imaging, we will at least consider those two aspects. For this reason, it would be counterproductive to continue this discussion without first dealing with a "typical" Raman spectrum. Figure 3.5 shows an example of a SpRS spectrum recorded from a cervical cancer cell line [156]. When we use the term "typical" here, it should not be understood that different biological systems have the same spectrum, just that biological spectra share common characteristics: features of different systems are often displayed in the same regions.

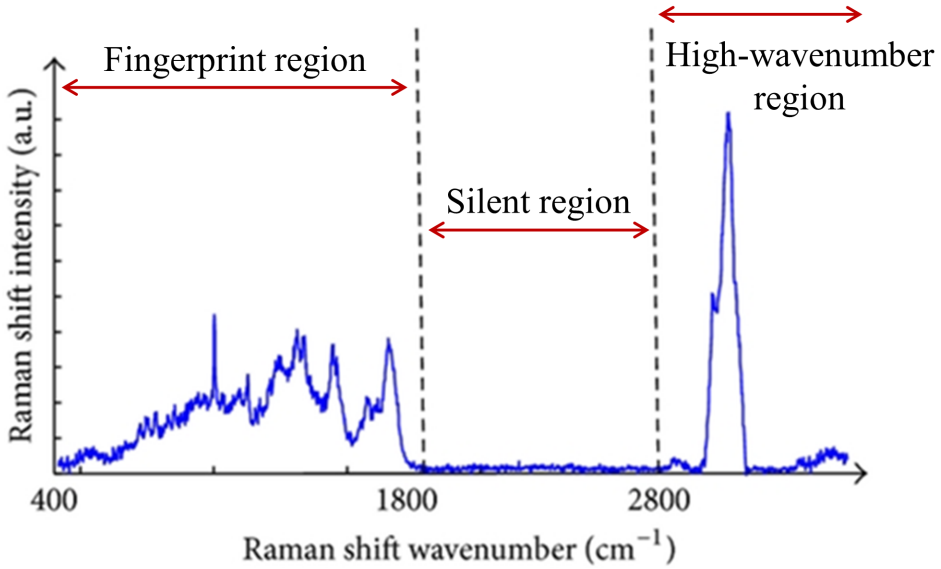


Figure 3.5: Typical spontaneous Raman scattering spectrum of biological material. Spontaneous Raman scattering spectrum of cervical cancer cell line highlighting the three main regions of biological investigation. Adapted from reference [156].

Typically, biologically relevant regions in a SpRS spectrum can be divided into three different spectral windows[9], as shown in figure 3.5. The first, called the "fingerprint region" ($\sim$ 400 – 1800 cm$^{-1}$), is where more specific vibrational components of organic molecules

[8] In a broad sense, the term "confocal Raman microscopy" can designate any form of Raman-based confocal microscopy. Here, however, we restrict the meaning to the application of SpRS in confocal microscopy.

[9] The spectral limit of each region varies a little in the literature.

are found, but it is also a "crowded" region [14, 157]. The peaks are mostly associated with C-C, C=C, and C=O vibrational modes [158]. Figure 3.6A shows the assignment of some biomolecules. On the other hand, the "silent region" ($\sim$ 1800 – 2700 cm$^{-1}$) is an "empty" window, absent of Raman peaks of endogenous biomolecules [157, 159]. Finally, the high-wavenumber, high-frequency, or "C-H stretching region" ($\sim$ 2800 – 3500 cm$^{-1}$) is neither as "crowded" nor as specific peaks as the fringerprint region [14, 157]. The peaks are mostly associated with CH vibrational modes in lipids and proteins, as shown in figure 3.6B, which are abundantly present in biological systems [14, 76, 81, 107, 157]. The main advantage is that the peaks appear with higher intensities compared to the peaks in the fingerprint region.

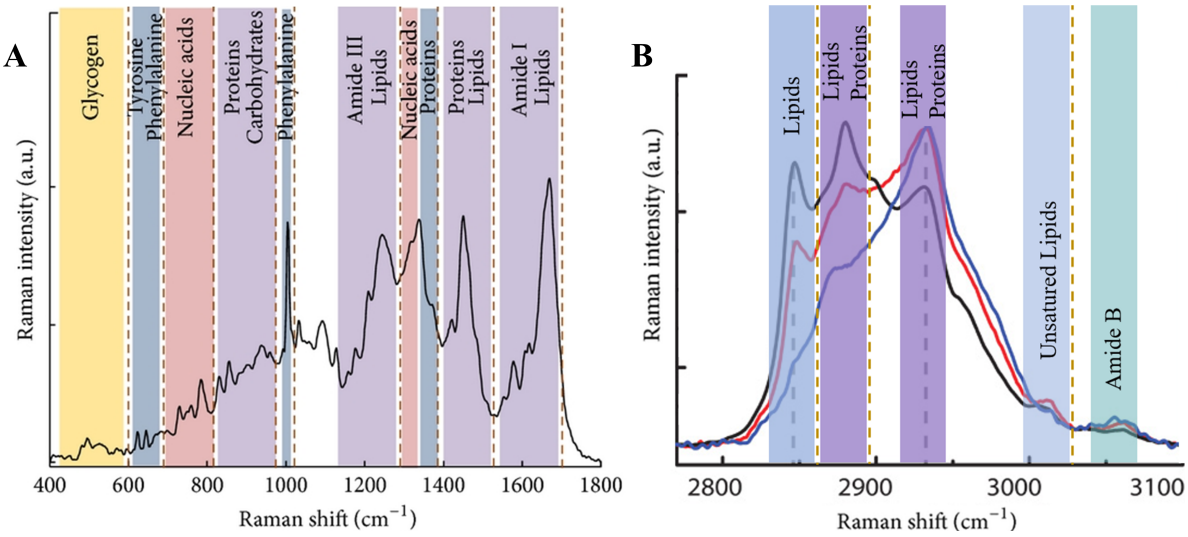


Figure 3.6: Vibrational signatures of biomolecules. (A) Cervical cancer cell line spectrum in the fingerprint region, which has several vibrational signatures, offering greater analytical power, but with weak signals. (B) In the high-wavenumber region, signals are stronger, but there are few signatures. The three spectra correspond to different regions of mouse brain tissue. Adapted from references [156, 160].

Although different approaches in Raman imaging can use extrinsic mechanisms to obtain higher sensitivity, the contrast of a Raman image need not *necessarily* be given by the fluorescence of an exogenous label. It can be based on the vibrational modes of native biomolecules themselves, which lies at the heart of a label-free approach. As illustrated for a diatomic molecule in sections 2.3.1 and 2.7.1, molecular vibrations are associated with chemical bonds between atoms [151, 152]. Those vibrational degrees of freedom, in turn, are quantized, following specific rules. Since all molecules have different chemical bonds and structures, vibrations are a chemically specific source of information in a biological system [157]. Moreover, as a means of validation, we can compare label-free contrast based on vibrational modes to what it can be done with fluorescent labels. Figure 3.7 shows images of a human malignant glioma cell line studied by confocal immunofluorescence (row in figure 3.7A)[10] and CRM

[10]Immunofluorescence combines fluorescence microscopy with immunochemical labeling techniques that takes advantage of the high specificity of antibody-antigen binding. A fluorescent compound coupled to a type of antibody is transported by it to a specific antigen, such as a certain protein. Fluorescence of the compound now coupled to the antigen allows its imaging.

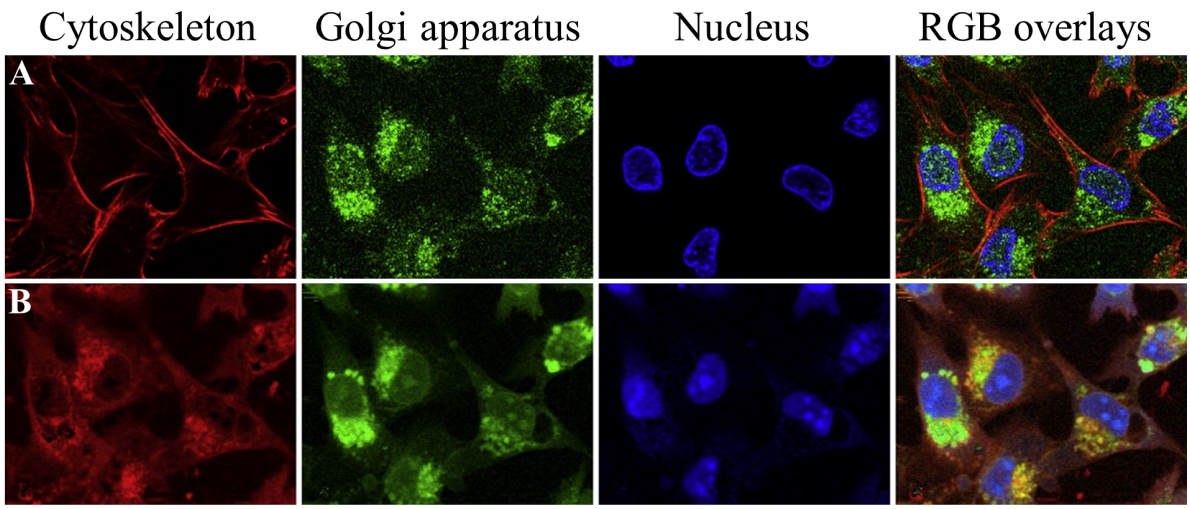


Figure 3.7: Label-free linear contrast mechanism. Different organelles of LN-18 glioma cells imaged by (A) linear fluorescence (1PL) of exogenous labels and (B) SpRS. Adapted from reference [154].

(row in figure 3.7B) [76, 154]. Comparing both linear techniques reveals we can observe intracellular structures with remarkable similarity.

The same happens when we compare images produced by the nonlinear counterpart of these two techniques. Figure 3.8 shows images of TPEF and CARS in two different studies [143, 161]. In figures 3.8A and 3.8B, TPEF of doxorubicin (figure 3.8B) is used for colocalization in a human rectal carcinoma H630 cell line imaged by CARS resonant with $CH_2$ vibration (figure 3.8A) [143]. In figures 3.8C and 3.8D, the TPEF image of doxorubicin (figure 3.8D) is used to verify the contrast of CARS at $CH_2$ vibration (figure 3.8C) in smooth muscle cells of carotid arteries of healthy Yorkshire pigs [161]. Whether in the linear or nonlinear case, the comparisons demonstrate the feasibility of label-free biological vibrational imaging.

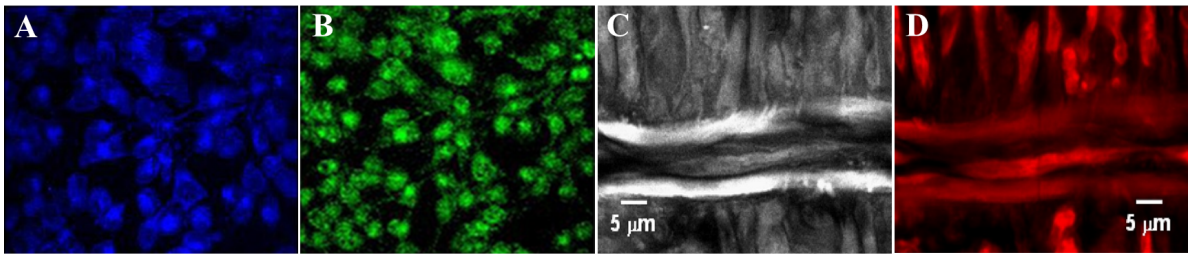


Figure 3.8: Label-free nonlinear contrast mechanism. Human rectal carcinoma H630 cell line imaged by (A) TPEF with doxorubicin labeling and (B) lipids-based ($CH_2$ stretching mode, ~ 2850 $cm^{-1}$) CARS. Smooth muscle cells of carotid arteries of Yorkshire pigs imaged by (C) TPEF with doxorubicin labeling and (D) lipids-based ($CH_2$ vibration) CARS. Adapted from references [143, 161].

It is in the speed, however, that coherent Raman imaging has no linear vibrational analog[11] [76, 84]. Among the parameters associated with acquisition times, we can quickly mention at

[11] An exception is surface enhanced Raman scattering (SERS), which uses nanostructures to obtain an increase in the Raman signal.

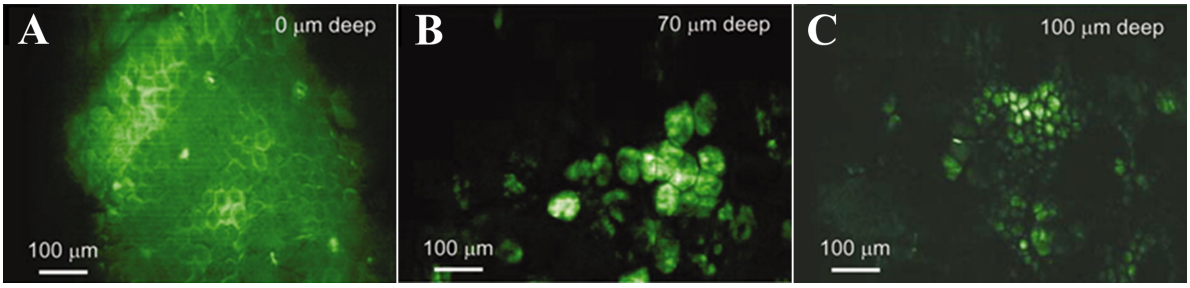


Figure 3.9: Video-rate coherent anti-Stokes Raman scattering shows different layers of mouse ear skin *in vivo*. Coherent anti-Stokes Raman scattering resonant at $CH_2$ stretching mode (~ 2845 $cm^{-1}$) enables fast label-free imaging of the (A) stratum corneum, (B) adipocytes of the dermis, and adipocytes of the subcutaneous layer. Adapted from reference [164].

least three elements associated with the properties of the CRS signal and how we measure it. The first, and most discussed in sections 2.7.1, 2.7.2, and 2.7.3 is the strong signal amplification through coherent excitation and stimulated emission in CARS and SRS [81, 157]. Although Raman transitions mediate these nonlinear processes, producing biochemically specific images analogous to figures 3.7B, the probability of CARS and SRS is orders of magnitude greater than the probability of SpRS. Such improvement translates into faster acquisition times [53,81,162]. Another element is the tradeoff between speed and spectral information in single-frequency CRS microscopy. In other words, an increase in imaging speed is accompanied by a loss of spectral information [14, 84]. With only one excitation wavelength, SpRS is inherently a broadband effect and, therefore, spectrally rich. On the other hand, with two excitation wavelengths, single-frequency CRS[12] can be limited to resonance with only a single vibration frequency, which allows for faster acquisition times. Such a tradeoff is particularly interesting when aiming at distinguishing elements. For example, in studying adipocytes, nervous tissues, fatty liver tissue, and breast tissue, it may be advantageous to give up spectral richness to aim at only lipids, which have a large scattering cross-section and are present in high concentrations in those systems [163]. Finally, imaging speed depends not only on the signal but also on the sensitivity of the experimental apparatus [107], which, in turn, can be accounted for by the SNR briefly discussed in section 2.7.4.2. As calculated by Zhang *et al.* for specific conditions, CRS can be $10^8$ times faster in achieving the same SNR value as the SpRS [107]. In terms of imaging speed, this means that a 500x500 pixels image can be acquired within 30 ms, which is compatible with a pixel dwell time of 100 ns [107]. Again, this performance can be compared to fluorescence microscopy, which delivers similar results [14, 84, 157].

The importance of speed in biological imaging is the possibility of capturing dynamic processes. Both CARS and SRS were implemented with video-rate acquisition speed (~ 160 ns and 100 ns of pixel dwell time, respectively) , similar to the calculations presented by Zhang *et al.* [107]. Figures 3.9 and 3.10 illustrate part of these works [164, 165].

Figure 3.9, shows CARS images of the ear of a hairless mouse submitted to *in vivo*

[12]In single-frequency CRS, only two excitation wavelengths are used, as discussed in section 2.7.4. As it is the only CRS technique implemented in this thesis, we refer to single-frequency CRS simply as CRS, unless specified otherwise.

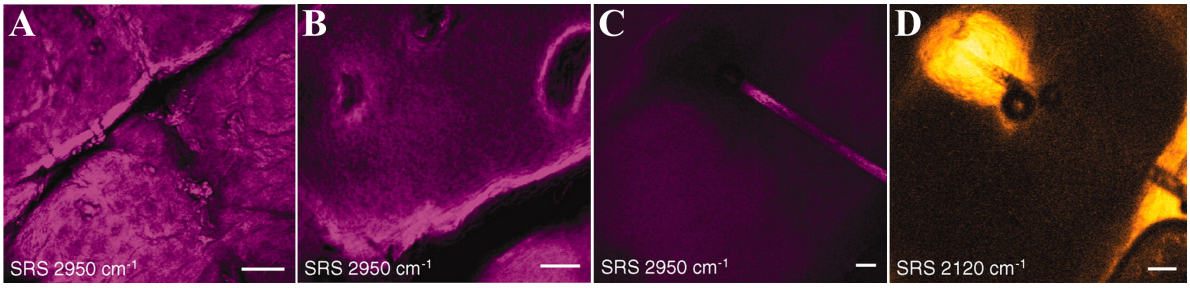


Figure 3.10: Video-rate stimulated Raman scattering enables drug tracking in human skin. Images of the (A) stratum corneum, (B) viable epidermis, and (C) a hair on the skin surface based on the $CH_3$ stretching mode. (D) the diffusion of deuterated dimethyl sulfoxide on the skin was traced with SRS set at C-D vibration, revealing the accumulation of the chemical in the hair shaft. Adapted from reference [165].

imaging [164]. The authors imaged different layers of mouse ear skin with CARS set at $CH_2$ stretching mode ($\sim$ 2845 $cm^{-1}$), recognizing *in vivo* different structures as the focus was shifted to different levels of depth. Figures 3.9A-3.9C show the stratum corneum (figure 3.9A), adipocytes of the dermis (figure 3.9B), and adipocytes of the subcutaneous layer (figure 3.9C). The authors provided a video in the supplementary material demonstrating the dynamic features of the technique. Moreover, with the application of mineral oil on the surface of the ear, it was possible to track its diffusion through the animal epidermis [164].

A similar experiment was carried out with *in vivo* SRS imaging of human skin in a drug tracking demonstration [165]. Figures 3.10 show images of the stratum corneum (figure 3.10A), the viable epidermis (figure 3.10B), and a hair on the skin surface (figure 3.10C), all based on the $CH_3$ stretching mode in the high-wavenumber region. Penetration-enhancing small molecules (deuterated dimethyl sulfoxide) were used on the skin to demonstrate the traceability of SRS. Its accumulation in the hair shaft, manifested as a increased signal, can be seen in figure 3.10D, with the image based on the specific vibration of the C-D bond, where D represents an isotope of hydrogen (deuterium). Additionally, in the supplementary material, the authors provided a movie of a region of 100 µm with 512x512 pixels and a frame acquisition time of 37 ms, capturing the flow of red cells in a capillary in the living mouse skin based on the $CH_3$ stretching mode of native proteins and lipids [165].

All these examples show that on top of the benefits of nonlinear excitation of biological materials, such as intrinsic three-dimensionality, we can take advantage of the highly scattering nature of many biological materials by exploring CRS microscopy. Although confocal fluorescence microscopy is widely used for its label-based specificity and high speed, we have seen that CRS microscopy is intrinsically label-free and yet comparably fast.

### 3.3.2 The high-wavenumber region

As discussed in section 2.7.1, the CRS signal is dependent on the concentration of scatterers and the Raman scattering cross-section. For this reason, we expect that the more abundant the Raman-active biomolecules, and the greater the probability of Raman scattering, the greater

the intensity of the observed signal. As illustrated in Figure 3.5, it is in the high-wavenumber region that we find prominent peaks, almost always associated with CH bonds. The most used in several studies are mainly attributed to the stretching modes of the CH2, $CH_3$ bonds. These are associated with lipids and proteins, which are abundantly present in biological materials. That is why this region plays a prominent role in applying CRS microscopy in biology and medicine, which is the reason the high-wavenumber region receives exclusive attention in this section.

#### 3.3.2.1 Cellular biology

Coherent Raman scattering microscopy provides a convenient means to study the dynamics of vital cellular processes without affecting cell function. A critical process is cell division, characterized by a series of molecular events (collectively known as the cell cycle) that lead to duplication and partitioning of cell components [166]. It is through this process that many structures in the organism are regenerated and, therefore, the study of cellular processes is crucial.

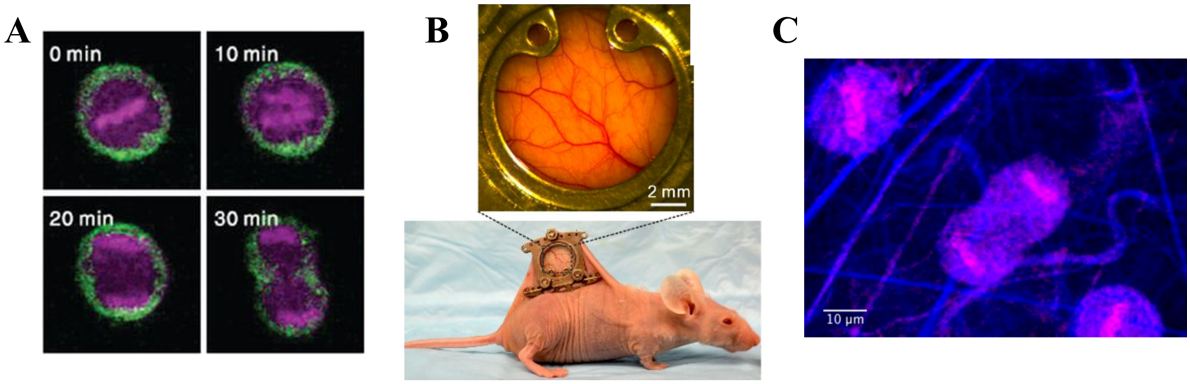


Figure 3.11: Cell imaging with SRS in the high-wavenumber region. (A) Time-lapse SRS of HeLa cell undergoing cell division with label-free contrast based on DNA (~ 2967 $cm^{-1}$, magenta) and lipids (~ 2850 $cm^{-1}$, green) vibrations. (B) Human cancer cells were injected into a animal model stabilized with a dorsal skinfold chamber. (C) The *in vivo* SRS imaging of cancer cells undergoing cell division in the mouse skin based on DNA (~ 2967 $cm^{-1}$, magenta) and proteins (~ 2926 $cm^{-1}$, blue) vibrations. Figure adapted from [167].

Lu *et al.* implemented time-lapse SRS imaging to monitor lipid, protein, and nuclei acid distributions and to observe general morphological changes in cells during the process of mitosis [167]. Figure 3.11A shows the chromosome dynamics of cultured HeLa cell undergoing cell division (movie presented in the supplemental material of reference [167]). DNA (~ 2967 $cm^{-1}$, magenta) and lipid (~ 2850 $cm^{-1}$, green) vibrations in the high-wavenumber region provide the label-free contrast in each image. DNA contrast allows monitoring of the movement of chromosomes, while lipid contrast allows observation of morphological changes in the cell [167]. The authors also used such time-lapse SRS in an animal model of cancer. Human cancer cells were injected into an immune-deficient mouse. Figure 3.11B shows the dorsal skinfold chamber, a tool used to stabilize the animal and reduce artifacts in *in vivo*

imaging, and figure 3.11C is a SRS frame of cell division captured in the mouse skin (movie presented in the supplemental material). The image is based on the vibrations of DNA (~ 2967 $cm^{-1}$, magenta) and proteins (~ 2926 $cm^{-1}$, blue) [167].

#### 3.3.2.2 Neuroendocrinology

Coherent Raman scattering microscopy was also used to study the relationship between neural mechanisms associated with energy demand and food availability. Barros *et al.* addressed the role of dopamine signaling in fat content in the nematode *Caenorhabditis elegans*, shedding light on the discussion of the interplay of dopamine in fat regulatory mechanisms [168].

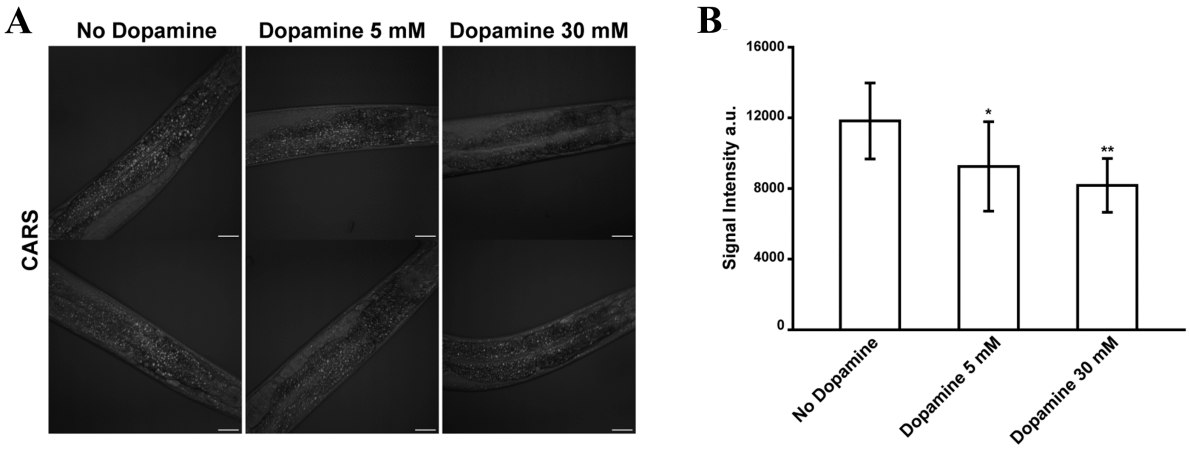


Figure 3.12: Coherent anti-Stokes Raman scattering imaging for quantitative analysis of fat storage and dopamine signaling. (A) Lipids-based (~ 2845 $cm^{-1}$) CARS images of *Caenorhabditis elegans* reveal the fat content (bright spots) under increasing quantities of dopamine. (B) The plot of CARS intensity against dopamine concentration suggests an anti-correlation between the two. Adapted from reference [168].

Figure 3.12A shows lipid-based CARS images of the worms. They were exposed to increasing concentrations of dopamine, and the CARS signal was recorded for each concentration. Figure 3.12B shows the CARS signal intensity in each dopamine concentration group. The intensity profile based on $CH_2$ stretching mode (~ 2845 $cm^{-1}$) allows the quantitative analysis of the fat storage of the animals. The experiment shows that animals exposed to exogenous dopamine exhibited a diminished amount of triglycerides as measured by the CARS signal [168].

#### 3.3.2.3 Neurocytology

Another noteworthy application of CRS microscopy is in imaging nervous system structures and quantitative neurobiological studies.

Figure 3.13 shows lipid-based CARS images of myelin sheath wrapping axons in ex vivo spinal tissue [169]. Figures 3.13A-3.13B show normal, and figures 3.13C-3.13D show swollen samples. The authors analyzed the CARS signal in response to chemically induced abnormalities [169]. With the analysis of different samples, the authors verified that the inducer

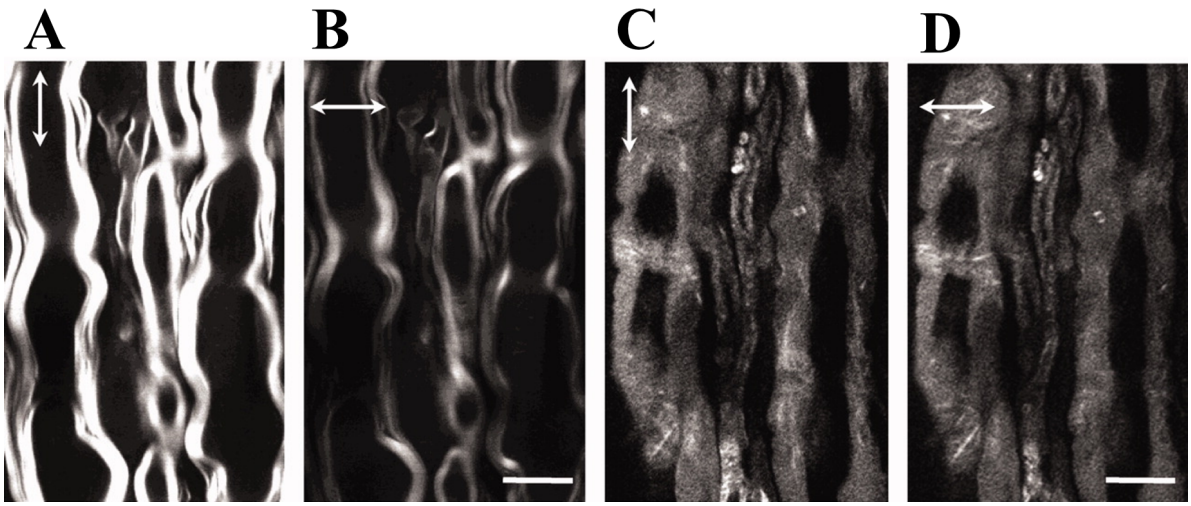


Figure 3.13: Coherent anti-Stokes Raman scattering signal shows degradation of the myelin sheath. Lipids-based CARS images of normal myelinated axons generated by (A) vertical and (B) horizontal polarization laser excitation. (C,D) Chemically induced abnormal samples lost the polarization dependence and exhibited a weaker CARS signal. Scale bars are 10 µm. Adapted from reference [169].

causes a consistent intensity reduction in the CARS signal, as can be seen comparing figures 3.13A and 3.13C, indicating a decrease in the lipid packing density [169]. Furthermore, due to the organization of the myelin sheath, the CARS signal is dependent on the laser incident polarization [169]. Figures 3.13A and 3.13B show images of normal samples excited with vertical (figure 3.13A) and horizontal (figure 3.13B) incident polarization. The same test was performed with the swollen samples (figures 3.13C and 3.13D), in which the loss of this polarization dependence was verified, also suggesting a structural degradation of the myelin sheath. Abnormalities in the myelin sheath are a hallmark of central nervous system disorders [170], making sensitivity to these changes necessary. The versatility of CRS microscopy, therefore, becomes of great value.

These examples in the high-wavenumber region demonstrate the success of CRS microscopy in biological imaging and also demonstrate how it can be widely used to meet the needs of various studies.

### 3.3.3 The fingerprint and silent regions

In section 3.3.2, we saw how it is feasible for single-frequency CRS microscopy to be widely applied in biomedicine and capture dynamic features due to the achievable high-speed imaging with vibrational modes in the high-wavenumber region. In the fingerprint and silent regions, however, some subtleties can limit the experimental approaches and applications of CRS microscopy.

#### 3.3.3.1 Cellular biology in the fingerprint region

In the fingerprint region, there are functional groups with unique vibrations, making the peaks much more specific [14, 157]. On the other hand, the number of biomolecules contributing to each peak is not as large as in the less specific high-wavenumber region, making the signal relatively low. This weaker signal poses a major obstacle for CARS. As discussed in section 2.7.2, the homodyne-detected CARS signal is proportional to $\left|\chi^{(3)}\right|^2$, where $\chi^{(3)} = \chi_R^{(3)} + \chi_{NR}^{(3)}$. Thus, the signal depends on resonant ($\chi_R^{(3)}$) and nonresonant ($\chi_{NR}^{(3)}$) terms. The only resonant contribution occurs when the beating frequency ($\omega_p - \omega_S$) of the incident beams coincides with the frequency of one vibrational mode of the biological material ($\omega_\nu$). Nonetheless, the nonresonant part is frequency independent and, therefore, other possible wave mixing effects can generate a response at $\omega_{\text{CARS}}$, irrespective of $\omega_\nu$. Coherent anti-Stokes Raman scattering signal is more easily distinguished from the nonresonant background when the resonant component is intense, substantially surpassing the background. However, this is not the case in the fingerprint region, with weak Raman signals [14, 157]. Simply increasing the excitation power is not a solution, as the background response will also increase, and we can also cause sample damage. In a parallel direction, we could think that a possible solution would be to use a femtosecond excitation and not picoseconds as we have done so far in this text. As captured by expression (2.78) in section 2.7.4.1, the the overall CRS signal grows when the temporal pulse width decreases (or, conversely, when the spectral pulse width increases), and we could have higher peak power with tolerable average power, avoiding photodamage [84]. Unfortunately, this recipe for achieving greater sensitivity does not hold for CARS [171]. Both the resonant signal and nonresonant background increase as the spectral pulse width increases (temporal pulse width decreases). However, while the resonant signal grows to saturation, the nonresonant background grows quadratically, further decreasing the SBR [171]. Additionally, since the typical linewidth in the fingerprint region is about 10-15 $\text{cm}^{-1}$, spectral broadening can also come at the cost of too low spectral resolution to probe individual peaks [14, 84, 171]. For example, a bandwidth-limited Gaussian[13] pulse of $\sim$ 100 fs has a spectral width of $\sim$ 150 $\text{cm}^{-1}$ around 800 nm [84]. Since the various peaks in the fingerprint region are closely spaced, for such low resolution, the main attribute of the fingerprint region is lost, namely its greater specificity.

Stimulated Raman scattering microscopy has usually been the favored technique, as the nonresonant background is not a significant obstacle most of the time. Still, single-frequency SRS has its limitations [79, 84]. Due to the congestion of vibrational components, it can be difficult to associate a response to individual peaks in some cases. It may be necessary to obtain images based on several peaks and still employ data processing to extract quantitative information [14]. For this reason, improving the analytical capacity of CRS microscopy is a challenging research topic since it involves a delicate balance between spectral broadening,

[13] A bandwidth-limited (or Fourier-limited) pulse is a laser pulse whose product of temporal and spectral widths equals a dimensionless numerical constant. This constant, called the time-bandwidth (or duration-bandwidth) product, depends slightly on the pulse shape. Assuming a Gaussian pulse shape means that the constant is approximately 0.441, so both temporal width ($\Delta\tau$) and spectral width ($\Delta\nu$) are defined reciprocally by the product $\Delta\tau\Delta\nu = 0.441$ [172].

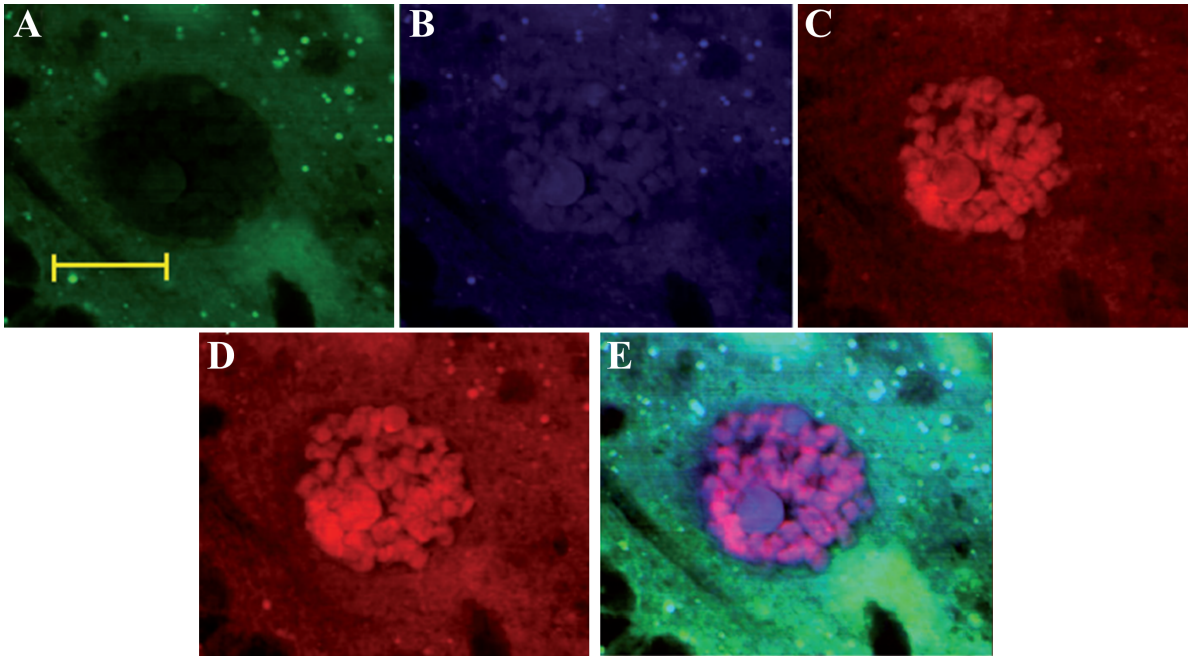


Figure 3.14: Cell imaging with stimulated Raman scattering in the fingerprint region. Salivary gland cell of *Drosophila melanogaster* larvae images based on (A) lipids vibration (2845 $cm^{-1}$), (B) proteins vibration (amide I, 1655 $cm^{-1}$), and nucleic acids vibrations at (C) 785 $cm^{-1}$ and (D) 1090 $cm^{-1}$. (D) Multicolor superposition of A-C. The scale bar is 20 µm. Adapted from reference [173].

spectral resolution, speed, and sensitivity. Currently, several reviews on this topic can be found [14, 79, 84]. Nevertheless, further discussion on this topic is beyond the scope of the thesis and single-frequency SRS is the only technique we explore in this section.

For a didactical comparison with section 3.3.2, we present an application of SRS microscopy in cell biology. Figure 3.14 shows SRS images of a single salivary gland cell of *Drosophila melanogaster* larvae [173]. As the main objective, Zhang *et al.* mapped the distribution of lipids, proteins, and nucleic acids, studying the specificity of the peaks in the fingerprint region. Figure 3.14A shows a lipid-based image. The dark region is colocalized with the cell nucleus, poor in lipids. The bright spots in the cytoplasm are mainly lipid droplets, structures associated with fat storage [173]. Figure 3.14B shows the same region but based on amide I vibration, allowing protein mapping. The signal distribution is nearly uniform, as both the nucleus and the cytoplasm contain large amounts of proteins [173]. As a property of the fingerprint region is closely spaced peaks, the authors discussed the presence of lipid droplets as an interference of the unsaturated lipids peak in the fingerprint region [173]. This overlap suggests probing for additional protein peaks, such as phenylalanine (Phe), for improved analytical capability.

Figures 3.14C (resonant at 785 $cm^{-1}$) and 3.14D (resonant at 1090 $cm^{-1}$) show DNA-based images. In the first case, there is still some interference showing lipid droplets. The authors attributed this interference to the vicinity of peaks assigned to C-C bonds, also related to lipids. In the second case, far from those peaks, the same interference does not happen. Figure 3.14E is the multicolor superposition of all images. Interestingly, the pinkish-colored

nucleus, resulting from the strong correlation between amide I-based and DNA-based images, suggests the active participation of proteins in the cell nucleus.

These images demonstrate the feasibility of applying SRS microscopy in the fingerprint region, although they also highlight its difficulties. While in section 3.3.1, video-rate frames were presented, here, the lower signal limits the acquisition speed. On the other hand, the greater availability of resonances also allows for greater analytical power.

#### 3.3.3.2 Vibrational tags in the silent region

The silent region, in contrast to the other two, is absent from Raman responses of endogenous biomolecules. This, however, is not an impediment for the nonresonant background of CARS to be dominant since it exists regardless of nearby resonances. It is in an attempt to avoid this background that most studies in this region have used SRS. Although SRS was conceived as a label-free technique, in this region, the approach consists of adding vibrational (and not fluorescent) tags that have unique modes, different from any endogenous biomolecule [53, 174]. Along with alkyne (that is, C≡C bond) incorporation, a well-known approach is isotope substitution: replacing atoms (e.g., hydrogen of a CH bond) with its more massive stable isotopes (e.g., deuterium, D) reduces the energy of the vibration, causing redshifted frequencies now at the silent region, free of any endogenous interference.

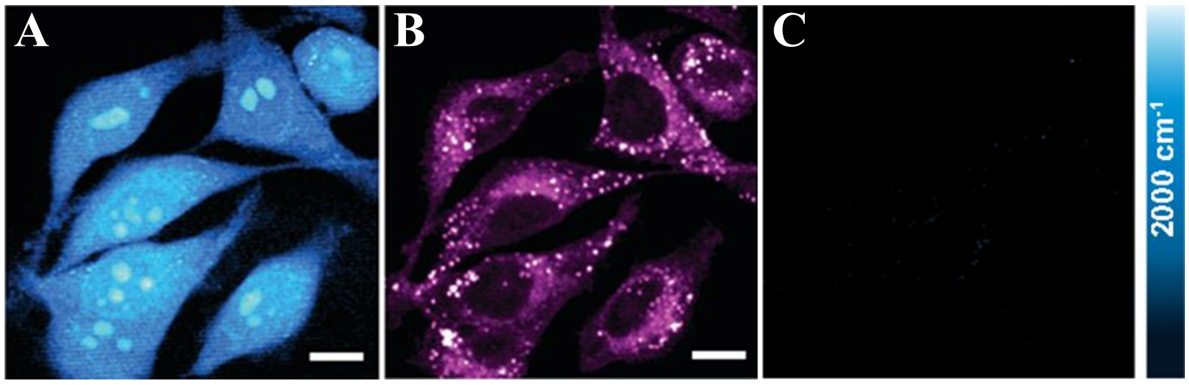


Figure 3.15: Stimulated Raman scattering imaging in the silent region. After incorporation of a deuterium-labeled set of amino acids, HeLa cells were imaged based on (A) C-D (2133 $cm^{-1}$) and (B) lipids (2840 $cm^{-1}$) vibrations. (C) off-resonance image (2000 $cm^{-1}$) shows the specificity of the technique. Scale Bars are 10 µm. Adapted from references [53, 174].

Figure 3.15 shows SRS images of HeLa cells based on three different vibrations. In figure 3.15A, the CD-based image (resonant at ~ 2133 $cm^{-1}$) shows newly synthesized proteins by metabolic incorporation of a deuterium-labeled set of amino acids [53, 174]. For comparison, figure 3.15 shows a lipid-based image (~ 2840 $cm^{-1}$), which only highlights more external structures of the cell. Finally, the off-resonance (~ 2000 $cm^{-1}$) image in figure 3.15 shows the complete absence of features, demonstrating the specificity of the technique.

Since this thesis aims to use label-free techniques, vibrational tags are part of this brief review for the sake of completeness. Exploring the subject further is beyond the scope of the text. Notwithstanding this selection criterion, there is literature covering the topic

[157, 158, 162].

### 3.3.4 Moving into the clinic

For the closing of this review, we will briefly highlight the extent of CRS microscopy in clinically relevant problems. Given the potential of CRS microscopy to locate structures, offer a biochemical mapping, and allow the extraction of quantitative information, a growing effort is expended toward the study of pathologies. The following are two examples where CRS microscopy is used as a tool in disease identification.

#### 3.3.4.1 Histopathological diagnosis of skin cancer

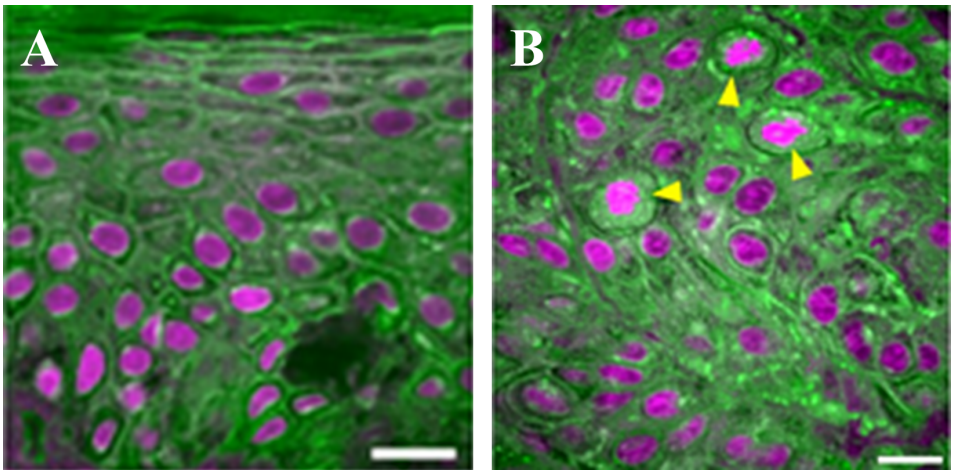


Figure 3.16: Stimulated Raman scattering imaging for histopathological diagnosis of skin cancer. (A) Normal and (B) neoplastic human skin tissue based on lipids (2850 $cm^{-1}$, green) and DNA (2967 $cm^{-1}$, magenta) vibrations. Morphological changes and mitotic figures (yellow arrowheads) allow for tissue discrimination. The scale bars are 20 µm. Adapted from reference [167].

A typical histopathological approach identifies hallmarks of a disease, from which it may be possible to monitor biomarkers, carrying information about the stage of the disease. Figure 3.16 shows SRS images of fresh human skin cancer tissue from three surgical cases of squamous cell carcinoma [167]. Lu *et al.* showed that it is possible to identify mitotic figures and morphological features that correlate with the level of cell proliferation and, therefore, are diagnostic indicators of cancer aggressiveness [167].

Figure 3.16A shows normal human skin tissue, while Figure 3.16B shows neoplastic tissue. In both cases, the resonances are in the high-wavenumber regions: the green channel is the lipid-based image ($\sim 2850\ cm^{-1}$), and the magenta channel is the DNA-based image ($\sim 2967\ cm^{-1}$). Neoplastic tissue can be distinguished from normal tissue by abnormalities captured by SRS imaging: mitotic figures appear in an increased number and are identified by a more intense signal and altered morphology (yellow arrowheads in figure 3.16B) [167].

#### 3.3.4.2 Histopathological diagnosis of brain tumor

Another valuable class of study is experimentation with animal models. Animals, sometimes genetically modified to express genes leading to human diseases, are used to study hallmarks that have diagnostic potential. A remarkable experiment was performed by Ji *et al.* with an animal model for glioblastoma multiforme tumor [160]. The aim was to verify the feasibility of *in vivo* identification of brain tumor margins using SRS microscopy.

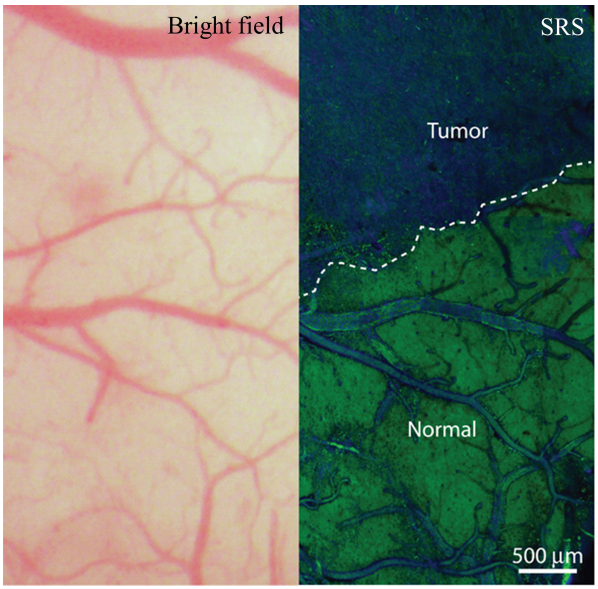


Figure 3.17: Histopathological diagnosis with an *in vivo* animal model for human brain tumor. The same mouse brain tissue seen with (left) bright field imaging and (right) SRS imaging based on lipids (2845 $cm^{-1}$, green) and proteins (2930 $cm^{-1}$, blue). Unlike bright field imaging, SRS exhibit the normal/tumor margin in the tissue. Adapted from reference [160].

Figure 3.17 shows an image of mouse brain tissue with the human tumor seen with bright field microscopy (left) and SRS microscopy (right). The composite SRS image is based on lipids ($\sim$ 2845 $cm^{-1}$, green channel) and proteins ($\sim$ 2930 $cm^{-1}$, blue channel). As can be seen, bright field microscopy cannot discriminate between normal and abnormal regions. In contrast, SRS microscopy easily determines a brain-tumor interface [160]. Subsequent studies in human brain tissues compared the performance of SRS histology with conventional methods, demonstrating that not only did SRS have satisfactory results, but it also led to a slightly higher rate of correct diagnosis made by different neuropathologists [175–177].

Histopathological characterization in animal models, particularly in brain studies, will be the central theme of the next section, dedicated to AD.

## 3.4 Multimodal imaging to study Alzheimer's disease

In section 3.2, we introduced general features of biological imaging and how nonlinear effects can intrinsically circumvent some problems, especially for thick tissues. Particularizing a little more, in section 3.3, we discussed some properties of CRS microscopy and reviewed how

each spectral region has been explored in the literature, concluding the review with clinically relevant applications, such as histopathology with animal models. In the process, and as a means of validation, we emphasized how CRS microscopy can be compared to fluorescence microscopy, producing similarly specific and fast images. Nevertheless, it is even more interesting when different types of microscopy produce complementary results, thus leading to multimodal imaging. In this section, we seek to take advantage of the main discussions so far: with an animal model, we will study a neuropathological hallmark capable of providing biomarkers of AD. We will combine different nonlinear optical effects in a multimodal platform to obtain intrinsically sectioned and label-free images in a histopathological study of the brain [25]. Rapid biochemical characterization is explored both in the fingerprint and in the high-wavenumber regions.

## 3.4.1 Alzhemer's disease neuropathology

Since the first report by Alois Alzheimer [178], Alzheimer's disease (AD) has been described as a progressive neurodegenerative disorder characterized by cognitive and behavioral impairments, ultimately leading to death [178, 179]. The disease is well-known for its clinical stage, where the symptoms are already present. It is at this point that many patients experience memory loss, aggressiveness, difficulty in walking, among others [178, 179]. For a long time, AD diagnosis relied on the analysis of changes present when such symptoms were already manifested [180]. Nevertheless, advances in basic research have shown that AD has a long subclinical stage, with brain changes preceding the onset of symptoms [179, 181, 182]. In this subclinical stage there is a series of molecular events that generate damage and structural changes in the brain. One of the efforts in the study of AD is the characterization of such disease-related structural changes with the potential to indicate the state of the progression before clinical manifestations [179, 182]. This suggests the possibility of an early distinction between a healthy and an Alzheimer's brain.

### 3.4.1.1 Amyloid-beta plaques

A hallmark of such distinction is the presence of amyloid-beta (Aβ) plaques [179, 181, 182]. Figure 3.18 is an illustration of a healthy brain (figure 3.18A) and an Alzheimer's brain (figure 3.18B), where the diffuse spherical structures are accumulations of Aβ peptides forming Aβ plaques (figure 3.18C). As figure 3.18C illustrates, these plaques consist of a core (dashed, black arrow) formed predominantly by misfolded Aβ peptides, rich in β-sheet conformation [153], surrounded by a predominantly lipidic halo (solid, red arrow), in the brain extracellular matrix[14] [179, 182, 184–188].

Although the precise link between Aβ and the cause of AD is still under debate, they are a pathological hallmark of the disease, which can allow a better understanding of the AD pathophysiology and provide new perspectives into its early diagnosis [179, 182, 184].

[14]The brain extracellular matrix is the non-cellular portion of nervous tissue. It is a space between typical brain cells, neurons and glia, forming a structural support environment [183].

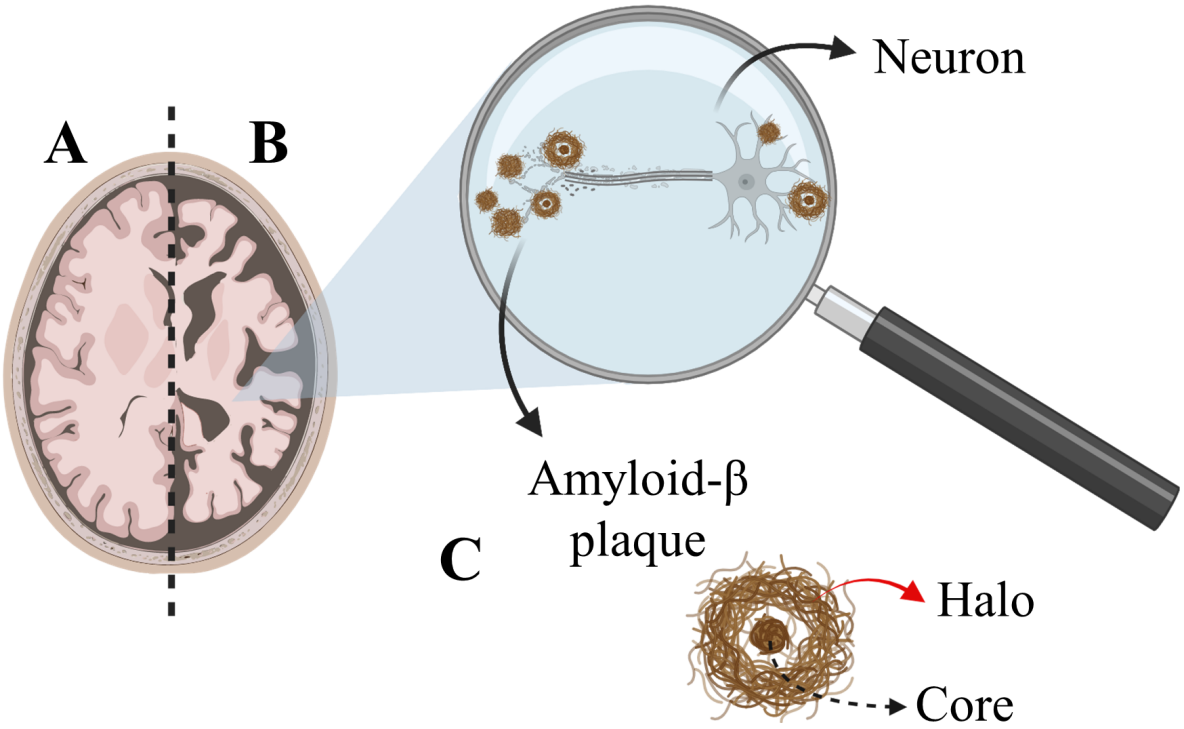


Figure 3.18: Normal *versus* Alzheimer's brain. Illustration of (A) a normal and (B) an Alzheimer's brain, highlighting pathological structural changes. A hallmark of the disease is the accumulation of (C) Aβ plaques outside brain cells (e.g., neurons). The plaques exhibit two main structures: a protein-rich core and a lipid-rich halo. Adapted from reference [189].

Intending to study AD, in this work, we restricted ourselves to characterize Aβ plaques by different label-free optical methods [25].

#### 3.4.1.2 An animal model

Since AD is a multi-factorial, complex disease, its study has benefited from a reductionist approach: the use of genetically engineered animals, reproducing some aspects of the disease spectrum [181, 190]. As AD appears to be unique to humans [181], the modification of these animals serves as a model to the extent that critical processes of this human disease can be experimentally examined. In our study, we used a APP:PS1 double transgenic male mice (Tg) purchased from the Jackson Laboratories. While wild-type mice do not develop Aβ plaques in the course of normal aging [180], these transgenic mice have the human amyloid precursor protein gene containing the Swedish mutation K594N/M595L and ΔE9 mutant human presenilin-1 gene, causing accelerated Aβ deposition in the brain after 5 months of age [191–193]. Here, we used mice of 6 and 12 months old. The mice were anesthetized and sacrificed, then had the brain removed and kept overnight in 4% paraformaldehyde (PFA), followed by cryosectioning of the frontal cortex and hippocampus (40 µm thick slices). These slices were washed three times with phosphate-buffered saline (PBS) and covered with a coverslip to spectroscopic analyses. After the multimodal imaging, tissue sections were stained using 1% thioflavin S (ThioS) solution (w/v) in 50% ethanol (v/v) (Sigma-Aldrich). The samples were immersed for 8 minutes in ThioS solution, immediately immersed three

times in 50% ethanol, washed with PBS, and seeded directly onto coverslips for TPEF imaging. Our investigation is in agreement with the Guide for the Care and Use of Laboratory Animals and was approved by the Ethics Committee for Animal Utilization in Research (CEUA) of the Federal University of Minas Gerais (protocol 225/2014), under the criteria of the National Animal Experimentation Control Council (CONCEA).

### 3.4.2 A multimodal platform for label-free imaging

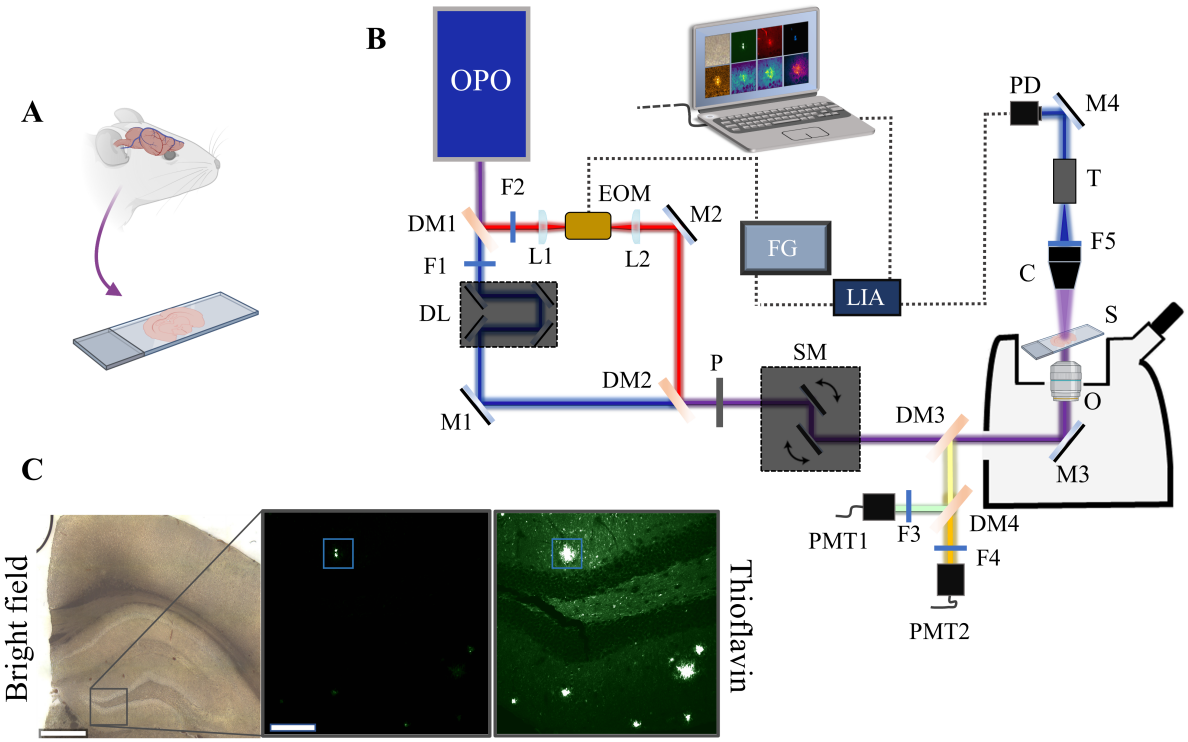


Figure 3.19: Experimental implementation and thioflavin S validation. (A) Sections of brain tissue obtained from an animal model of AD examined with the (B) experimental setup described in section 3.4.2. Frontal cortex and hippocampus located with (C) bright field microscopy (left, scale bar is 500 µm) and TPEF ThioS staining validation of Aβ plaques in the tissue (center), which can be recognized in the saturated TPEF ThioS staining image (right). Scale bar is 100 µm (center, right). Adapted from references [25, 59].

As represented in figure 3.19A, the prepared brain tissues served as samples for our multimodal platform in figure 3.19B. The platform consists of the experimental integration of the main nonlinear optical effects studied in chapter 2. For TPEF and SHG, we used a pump beam of 180 fs pulse-width and 80 MHz repetition rate, tuned at 810 nm. The beam is transmitted through the dichroic mirrors DM1 and DM2 (following the path of the purple beam) and is focused by a 60x apochromatic oil objective O (maximum NA of 1.4). The sample image is obtained through a scanning laser microscope (LaVision Biotec). The dichroic mirrors DM3 and DM4 direct the reflected signal generated by the material to the photomultipliers PMT1 and PMT2. Bandpass filters F3 and F4 can be inserted before the PMT1 and PMT2, respectively, allowing an unambiguous measurement of the effects.

For the implementation of single-frequency CARS and SRS, the optical parametric oscillator OPO (APE picoEMERALD) provides two beams: a 5-6 ps pump beam of tunable frequency $\omega_P$ and a 7 ps Stokes beam at a fixed frequency $\omega_S$, in blue and red, respectively, as in figure 3.19B. Frequency $\omega_P$ is tuned so that the beat frequency is resonant with the frequency of the vibrational mode.The dichroic mirror DM1 splits the beams in a Mach-Zehnder configuration where the filter F1 (F2) ensures no contamination of the Stokes (pump) beam in the arm of the pump beam (Stokes). The electro-optical modulator EOM connected to the function generator FG produces a high-frequency (10 MHz) polarization-modulation in the Stokes beam. The dichroic mirror DM2 recombines both beams in a collinear configuration. Temporal synchronization is achieved through a delay line DL. The polarizer P after the recombination of the beams transforms the EOM polarization-modulation into amplitude-modulation and ensures that both the unmodulated (pump) and modulated (Stokes) beams have the same polarization state. The scanning mirrors SM allow the beams to map the sample when focused by the 60x apochromatic oil objective O (maximum NA of 1.4) in the scanning laser microscope. The backscattered CARS signal is homodyne-detected: it is directed to the PMT1 photomultiplier by the dichroic mirrors DM3 and DM4. A bandpass filter (F3) eliminates signal contamination by TPEF. The forward SRS signal is collected by the collimator C and the filter F5 eliminates the Stokes component of the beam. The telescope T reduces the beam movement on the detector area of the photodiode PD, where the SRS signal is extracted with the help of the lock-in amplifier LIA coupled to the PD and connected to the EOM via the synchronization port of the FG.

For SpRS images and spectra, we used the WITec alpha300 SAR confocal system operating with a 532 nm CW laser excitation, focused by a 60x oil objective (maximum NA of 1.4), and scanned with steps of ~260 nm. We generated both images and spectra with the Project 5 WITec software.

In figure 3.19C, we have a bright field image (left) of a section of the mouse brain and the TPEF image of an enlarged section in the hippocampus, a brain component associated with memory [194]. Figures 3.19C (center) and 3.19C (right) are TPEF images showing the same region, but figure 3.19C (right) is saturated, favoring the identification of the tissue. The bright features in the TPEF images are Aβ plaques identified by the ThioS fluorescence. These ThioS stained images were obtained after the label-free measurements (see figure 3.20), thereby providing a gold standard validation of the label-free techniques. Thioflavin S is a fluorescent compound widely recognized as a specific label in neurodegenerative diseases studies, particularly for detecting Aβ plaques in AD models [136, 185, 195–198]. The blue square in figures 3.19C (center, right) identifies the plaque studied in our label-free multimodal analysis of figure 3.20.

With this setup, we generated figure 3.20, where we show images of the same Aβ plaque (in figure 3.19C) based on linear and nonlinear microscopies. In order to better address the techniques employed in the multimodal platform and the contrast mechanisms of each image, it is instructive to divide the analysis of the results in figure 3.20 into individual sections, as we do in the following discussion.

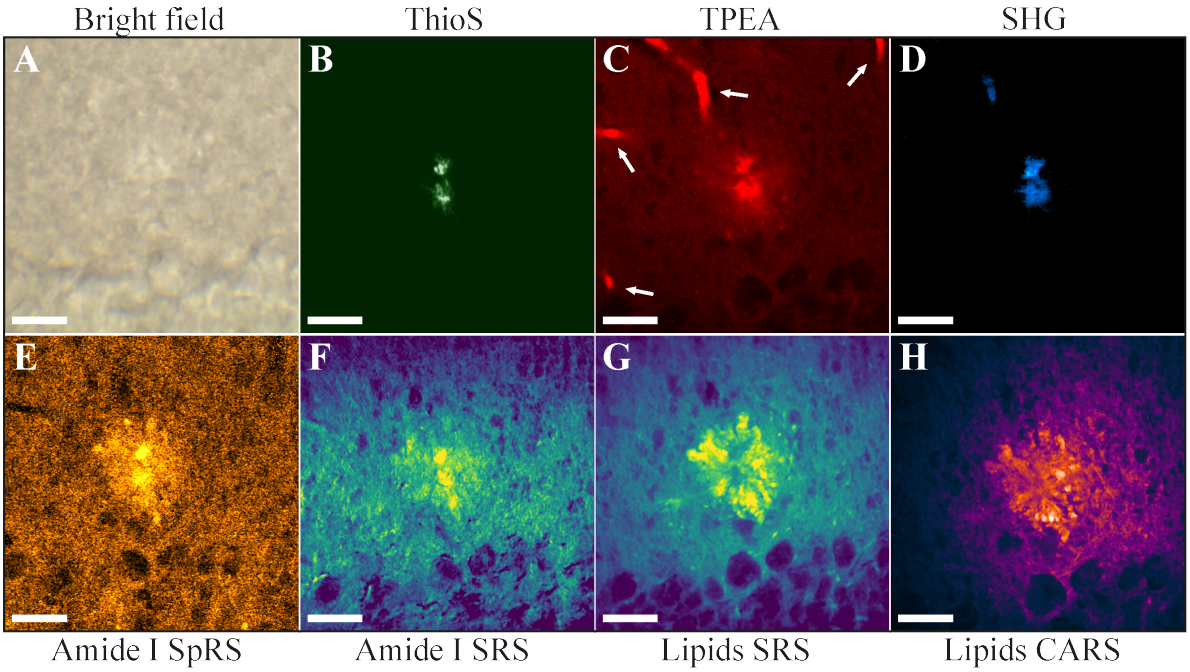


Figure 3.20: Multimodal imaging of an Aβ plaque from the hippocampus of a 12-month-old mouse brain tissue. (A) Bright field zoomed image from figure 3.19C. (B) TPEF image of the tissue after ThioS staining. (C) TPEA and (D) SHG images. (E) SpRS image at 1675 $cm^{-1}$. (F) SRS image at 1675 $cm^{-1}$ and (G) 2850 $cm^{-1}$. (H) CARS image at 2850 $cm^{-1}$. All images are of the same region. All scale bars indicate 20 µm. Reprinted from reference [25].

### 3.4.3 Intrisic fluorescent biomolecules

As can be seen in figure 3.20A, the contrast mechanism based on linear absorption in the bright field image does not reveal any plaque features. The image contrast is based on intrinsic fluorescent biomolecules, which are not efficiently probed with this type of illumination. On the other hand, figure 3.20C shows the two-photon excitation autofluorescence (TPEA) image of the same region. We obtained the image with the laser excitation wavelength at 810 nm and no filters at the detection in order to collect the entire emission window. There is a small contribution of the SHG emission (see below) to the TPEA image, and therefore SHG is subtracted from the TPEA image, generating figure 3.20C. As in the TPEF ThioS staining image of figure 3.20B, in the TPEA image only the plaque core has a distinct signal. The origin of TPEA of biological tissues can be attributed to endogenous fluorophores, native fluorescent biomolecules such as nicotinamide adenine dinucleotide (NADH), flavin adenine dinucleotide, flavoproteins, tyrosine, tryptophan, collagen, elastin, and lipopigments, to name a few [29, 30, 199–201]. These fluorophores emit light across the visible region with overlapping emissions [30, 200].

Figure 3.21A shows the linear fluorescence (1PL) spectrum of the main fluorophores present in biological tissues, with some biomolecules exhibiting broad and overlapping emissions [200]. Lipopigments such as lipofuscin, present in neurons, and associated with age-related neurodegeneration [30, 202], appear in essentially the entire visible range [30, 200, 202].

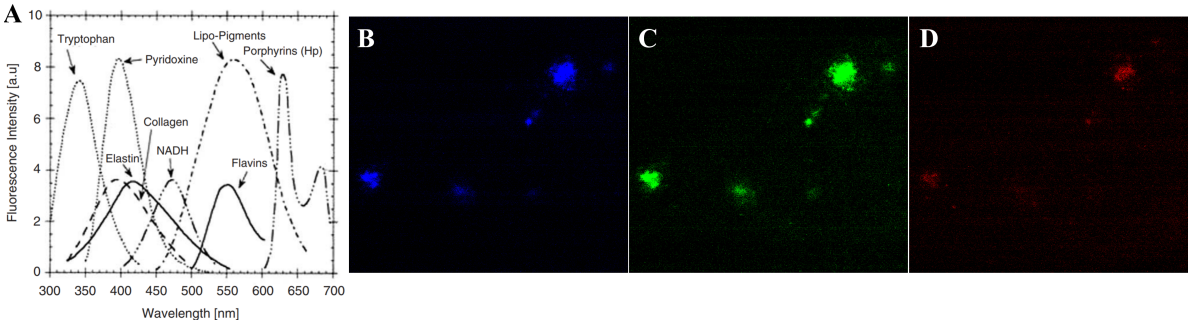


Figure 3.21: Fluorescence of biological components and Aβ plaques. (A) linear autofluorescence spectrum of different emitters in biological tissues, which exhibit broad signals in a wide spectral range. Two-photon excitation autofluorescence images of Aβ plaques (bright spots) obtained with a 10X objective (maximum NA of 0.45) and (B) 470/40 nm, (C) 525/50 nm, and (D) 620/60 nm bandpass filters. Adapted from reference [200].

We also observed a broad TPEA in Aβ plaques. Figures 3.21B-3.21D shows TPEA images of Aβ plaques (bright spots) in three different spectral regions: 450-490 nm (figure 3.21B, blue), 500-550 nm (figure 3.21C, green), and 590-650 nm (figure 3.21D, red). For this reason, although the Aβ plaque is present in the TPEA image of figure 3.20C, the precise contribution of autofluorescent biomolecules to the observed signal is still under discussion, and proper characterization of biomarkers is a non-trivial task. Therefore, the extraction of information from the TPEA image only by optical characterization can be impractical [201]. Additionally, since those autofluorescent biomolecules are not exclusive to Aβ plaques, other bright features are also present. In our TPEA images, blood vessels are observed, highlighted by the arrows in figure 3.20C.

### 3.4.4 Intrinsic symmetry-based properties

Another technique that can also be implemented using a single laser wavelength is SHG microscopy. As already discussed in this text, SHG can be present in materials lacking inversion symmetry [15, 48]. Therefore, the contrast mechanism in an SHG image relies on the anisotropy that particular biological structures exhibit, giving rise to appreciable second-order susceptibility values [203–206]. Kwan *et al.* were the first to confirm SHG in Aβ plaques [29]. As shown in figure 3.22, they detected a narrow emission at half the excitation wavelength (830 nm), together with a broad TPEF emission. In addition to being broad, TPEF is not strictly excitation-dependent, as electronic relaxation mechanisms typically involves non-radiative processes. For this reason, TPEF usually occurs at wavelengths longer than half the incident wavelength. However, SHG is a narrow, excitation-dependent emission, as the authors confirmed by tuning the excitation to different wavelengths.

Figure 3.20D shows an SHG image acquired with the laser excitation wavelength at 810 nm and a bandpass filter centered at 405 nm (10 nm width). In this case, the narrow bandpass filter is important to block the TPEA emission. As shown in figures 3.20C and 3.20D, these two techniques can be reliable in identifying the Aβ core without any extrinsic

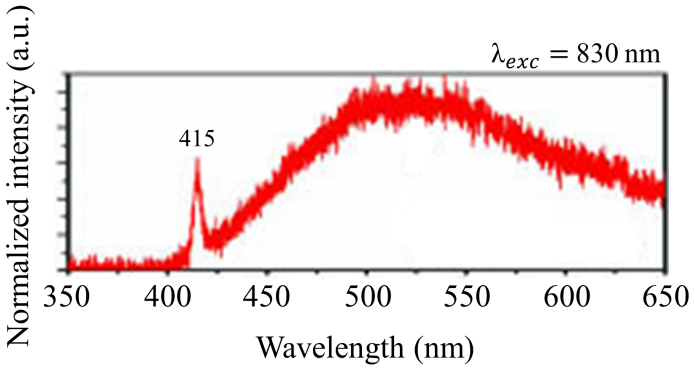


Figure 3.22: Second harmonic generation in Aβ plaques. Spectrum of Aβ plaques excited with a pulsed laser tuned at 830 nm. The narrow SHG peak is observed at half (415 nm) the excitation wavelength, while the broad TPEA signal is observed at longer wavelengths. Adapted from reference [29].

fluorescent label. Nevertheless, as is the case of TPEA, the molecular origin of the SHG and proper characterization of symmetry-based biomarkers provided by Aβ plaques is also still under discussion. Biological structures that typically produce SHG include collagen, microtubules, and other non-centrosymmetric proteins [203–206]. In the brain, collagen fibrils have been suggested to affect the detection of amyloid fibrils [207], and the origin of SHG was also attributed to collagen or microtubules in neurites of plaques [28, 30]. However, our image in figure 3.20D clearly shows that the primary source of SHG is the core, where it would not be expected to observe interaction with collagen and where there are no neurites. Previous studies with immunohistochemistry of neurites, astrocytes, and microglia, demonstrated that these cells are present in the surrounding halo, rather than in the core of the Aβ plaques [196–198, 208]. Additionally, comparing SHG, TPEA, and TPEF ThioS staining images in figures 3.20B-3.20D allows us to observe similarities in the core images, suggesting a common origin. Furthermore, ThioS is considered a characteristic ligand of the β-sheet conformation [196,209]. Sum-frequency generation[15] spectroscopy studies of β-sheet conformation of *in vitro* and *in situ* amyloid structures suggest that the origin of SHG is due to interfacial and symmetry properties of protein structures [210–212], which is supported by our core image. Therefore, we consider that the origin of the SHG is better associated with these symmetry aspects of protein structures in the core rather than due to the above-mentioned suggestions regarding collagen, microtubules, and neurites.

Again, while we can identify the plaque by highlighting the core, we still do not have information about the halo. A full biochemical characterization of the core and halo requires techniques that can retrieve chemical information.

### 3.4.5 Intrinsic vibrational modes

Figure 3.23 shows the SpRS spectrum of an Aβ plaque in transgenic mouse brain tissue. Here we can recognize the fingerprint and the high-wavenumber regions, but the silent region is

[15] Another symmetry-dependent second-order nonlinear effect.

ommited. In vibrational microscopy, the plaque core has been commonly accessed through the C=O stretching mode of amide I ($\sim 1675\ cm^{-1}$) in the fingerprint region [33,151,152,185–187]. That happens because the misfolding of $A\beta$ peptides, one of the leading events for plaque formation, manifests as a blueshifted ($\sim 15\ cm^{-1}$) amide I signal in the SpRS spectrum. This shift is consistent with a β-sheet secondary structure conformation, allowing its discrimination from the α-helix secondary structure (peak at $1660\ cm^{-1}$). Figure 3.20E shows a SpRS image set at such a vibrational mode ($1675\ cm^{-1}$), in which the core is clearly visible. Therefore, amide I shift is regarded as a potential optical biomarker of AD.

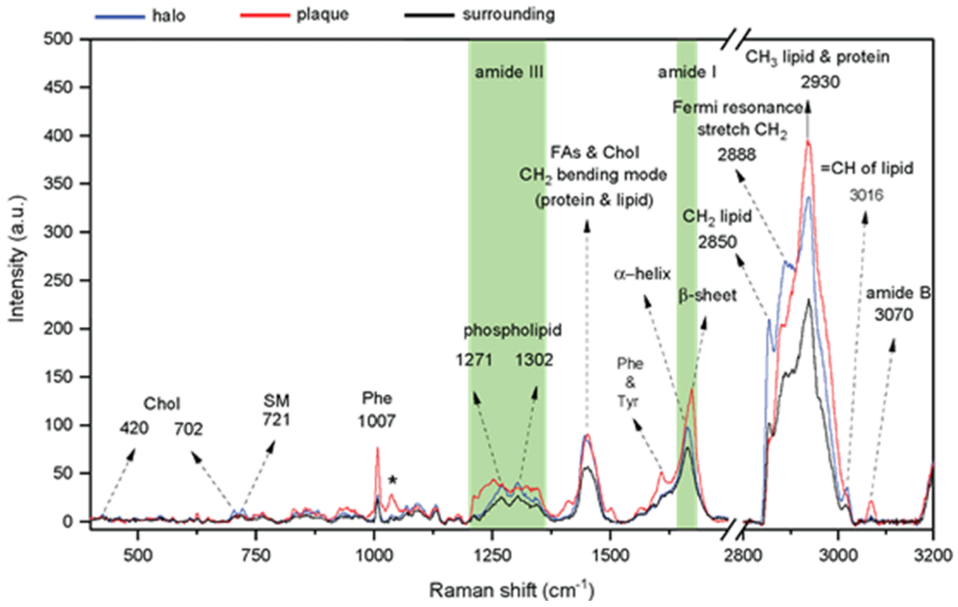


Figure 3.23: Spontaneous Raman scattering of Aβ plaques. Spontaneous Raman scattering spectra of the core (red), halo (blue), and sorrounding tissue (black), highlighting the main vibrational signatures in the fingerprint and high-wavenumber regions. Adapted from reference [213].

Since SpRS is an incoherent effect, its major disadvantage is that a hyperspectral image like the one shown in figure 3.20E took approximately 20 hours, making this a time-consuming technique for histopathological studies and unfeasible for *in vivo* studies. On the other hand, as discussed in this chapter, such a disadvantage is circumvented by CRS microscopy, which keep the rich chemical information provided by SpRS spectroscopy without the drawback of low throughput [33, 53]. Figures 3.20F and 3.20G show the SRS images taken at $1675\ cm^{-1}$ (amide I) and $2850\ cm^{-1}$ (lipids), respectively. As also discussed throughout this chapter, the peak at $\sim 2850\ cm^{-1}$ is ascribed to vibrational modes of lipids in the high-wavenumber region. Unlike the previous techniques, this allows Raman-based microscopies to identify the halo around the core as shown in figure 3.20G. The possibility of studying the halo is a significant advantage since several works call attention to its role in AD.

Figure 3.20H shows the CARS image tuned at $2850\ cm^{-1}$, also revealing the lipid-rich halo around the plaque core. For the CARS image, we used a bandpass filter (660/13 mn) to measure only the CARS contribution; however, there is a residual TPEA signal from the core. Hence, although at the same vibrational frequency of the SRS (figure 3.20G), the CARS image

also shows a signal from the core. Additionally, the implemented homodyne detection scheme does not prevent nonresonant background [33]. Furthermore, due to the poor sensitivity of our PMT in the near-infrared region, and the limitations of CARS in the fingerprint region discussed previously (see section 3.3.3), our experimental setup for CARS does not allow us to measure vibrational modes below 2500 $cm^{-1}$.

As we can conclude from figure 3.20, label-free, nonlinear optical microscopies are suitable for multimodal imaging to study AD. Techniques such as TPEA and SHG can be considerably useful to locate Aβ plaques with a simple configuration, requiring only a single excitation wavelength. They can provide information about the core and the precise determination of the molecular origin of these signals is essential for the research of optical biomarkers of the disease. However, TPEA and SHG are limited for retrieving chemical information. Vibrational microscopies circumvent this limitation, also allowing to locate other structures, such as the halo. The amount of information provided by these techniques may offer quantitative resources that shed light on AD pathophysiology[16]

#### 3.4.5.1 Stimulated and spontaneous Raman scattering

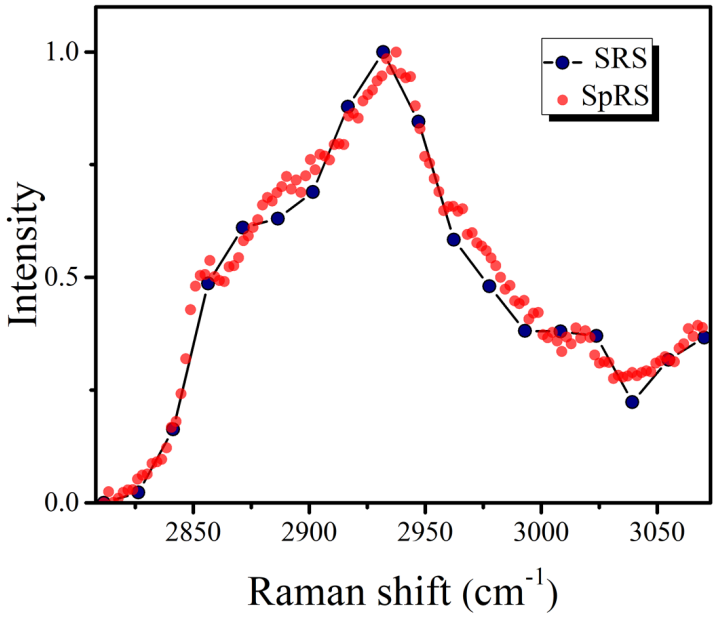


Figure 3.24: Stimulated *versus* spontaneous Raman spectra. Comparison of SRS (blue) and SpRS (red) spectra obtained from mouse brain tissue images. The images were acquired from different scattering geometries (transmission for SRS and reflection for SpRS), but demonstrate a high spectral correspondence. Reprinted from reference [25].

In figure 3.20E we can see the similarity between the SRS and SpRS images in the fingerprint region. Hence, we further explored this compatibility. Since the SRS signal is unaffected by a nonresonant background and proportional to the scatterers concentration, SRS and SpRS share virtually identical spectra [33, 53]. Figure 3.24 shows a comparison of an Aβ plaque SRS and SpRS spectra in the high-wavenumber region, from 2800 to 3075 $cm^{-1}$.

[16] i.e., the mechanisms of origin and operation of a disease.

We obtained these spectra in different scattering geometries: the plot shows the forward SRS signal and the backscattered SpRS signal.

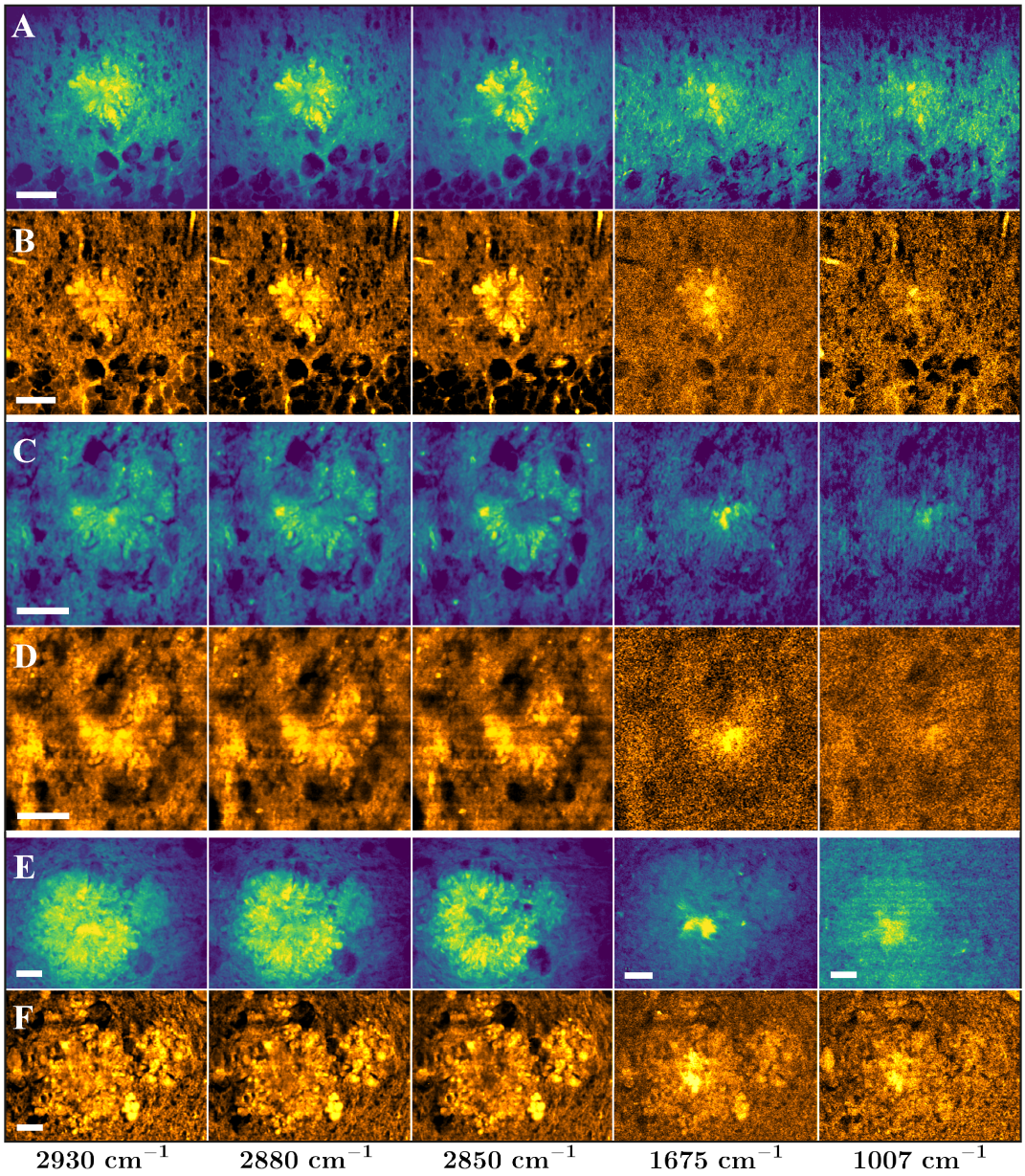


Figure 3.25: Comparison of single-frequency stimulated Raman microscopy and spontaneous Raman microscopy in different scattering geometries. Three different Aβ plaques imaged by (A, C, E) SRS and (B, D, F) hyperspectral SpRS, taken at different vibrational frequencies, as listed at the bottom of the images. All scale bars are 20 µm. Images without a scale bar share the bar of the leftmost image in the same line. Reprinted from reference [25].

Subsequently, we also tested the compatibility of the two effects on imaging of Aβ plaques. Figure 3.25 shows a comparison of SRS and SpRS images for different vibrational frequencies of the plaque in figure 3.20 (figures 3.25A and 3.25B) and of other two different plaques (figures 3.25C-3.25F). The plaques were located at the hippocampus (figures 3.25A-3.25D) and at the cortex (figures 3.25E and 3.25F). In all our images in figure 3.25, there is a good correspondence between SRS and SpRS microscopies. This demonstrates that we can

combine the chemical specificity and full spectral data of SpRS spectroscopy with the speed and resolution of SRS microscopy reliably and straightforwardly.

#### 3.4.5.2 Vibrational biomarkers

The first three columns of figure 3.25 shows images in the high-wavenumber region. They are based on vibrational modes already mentioned throughout section 3.3: the $CH_2$ stretching modes at $\sim$ 2850 $cm^{-1}$ (mainly associated with lipids) and $\sim$ 2880 $cm^{-1}$ (proteins/lipids), and $CH_3$ stretching mode at $\sim$ 2930 $cm^{-1}$ (proteins/lipids) [185]. As we can see, 2850 $cm^{-1}$ is a reliable lipid signature and only the halo is visible. By changing to higher frequencies, vibrational modes of lipids and proteins start to overlap and, therefore, the core is also present in the SRS and SpRS images taken at 2880 $cm^{-1}$ and 2930 $cm^{-1}$. The exact influence of the halo on the neurotoxicity of Aβ plaques is not known. Previous studies have explored the relation between neuroinflammation and AD [214,215], which is associated with the presence of astrocytes, microglia, and dystrophic neurites distributed in the halo surrounding the Aβ fibrillar deposits in the core [196, 197, 216, 217]. These findings highlight the need for tools capable of characterizing halo biomarkers (in addition to core biomarkers) and show how the specific information provided by SRS and SpRS microscopies can be useful. Moreover, part of these studies involves the colocalization of the imaged structures. Accordingly, it is necessary to obtain images with appropriate contrast and resolution to discriminate different structures in the halo. Prior to the publication of our multimodal imaging, discussed in this section, there was only one work with SRS exploring potential halo biomarkers. Yet, the images we present here offer an increase in quality. Our group advanced this SRS/SpRS characterization with the recent publication of an analytical study in which halo biomarkers can reveal information about AD progression [213], again suggesting the relevance of studying different halo biomarkers.

Stimulated Raman scattering and SpRS microscopies also go a further step in studying the core compared to TPEA and SHG. Due to the well-established chemical specificity of SRS and SpRS, it is possible to resolve different signals produced in the core. The fourth column (from left to right) of figure 3.25 shows amide I-based (1675 $cm^{-1}$) images, through which the core is identified. Having already been used in section 3.3, the amide I band is a typical protein band in SpRS spectra associated with the polypeptide backbone [151, 152]. To date, it has been the only vibrational signature used to identify the core with SRS microscopy [33]. In a similar motivation to the study of nucleic acids in the fingerprint region in section 3.3.3, we investigated the feasibility of using new core signatures in the fingerprint region and discuss its relation with Aβ plaques.

We imaged the plaque through the vibrational mode ($\sim$ 1007 $cm^{-1}$, last column of figure 3.25) of Phe, a hydrophobic, aromatic amino acid found in two positions of the Aβ peptide primary structure [152, 218]. Its position and contact with other amino acids seem to have a fundamental role in the β-sheet fibril conformation [218, 219]. Furthermore, a significant difference of Phe concentration was obtained between the core and surrounding tissue [185], making the image of the core clear, which suggests its use in the study of Aβ plaques. We

also show a comparison between the spatial distribution of amide I and Phe in the plaque of figure 3.25A, which is the same of figure 3.20. The gray area is mainly the lipid-based (~ 2850 $cm^{-1}$) image of the tissue and plaque. When we compare (figure 3.26C) the distribution of amide I (magenta, figure 3.26A) and Phe (cyan, figure 3.26B), we observe the specificity of Phe in the core. Although the Phe signal appears weaker than the amide I and its distribution less sparse, it is unclear how much interference from overlapping vibrations contributes to the amide I signal, as discussed in section 3.3.3. Despite that, we see that Phe can be used in the characterization of Aβ plaques. Therefore, we regard Phe as a potential core biomarker in the fingerprint region in addition to amide I.

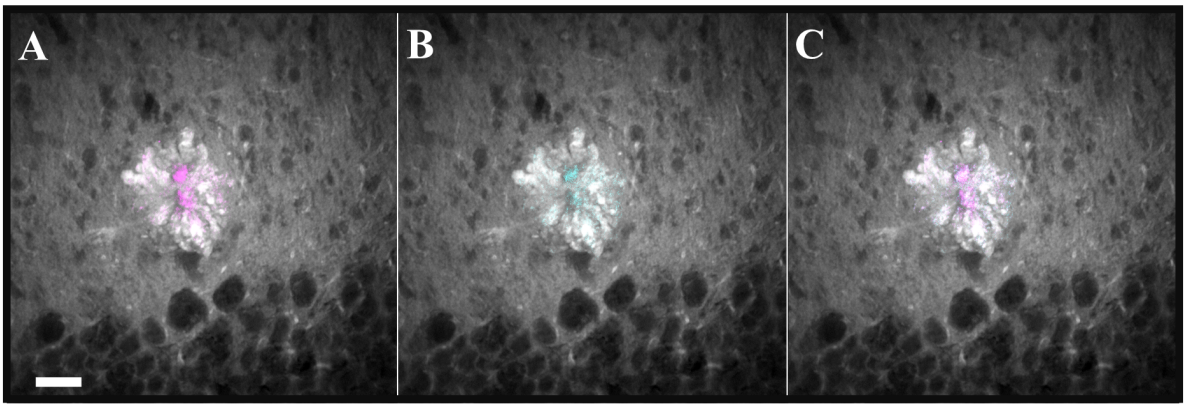


Figure 3.26: Spatial distribution of amide I and phenylalanine in the plaque. (A,B) merged image of the halo and core, demonstrating the spatial distribution of (A) amide I and (B) Phe. There is a spatial correlation in the distribution of both biomarkers in the core, although they present appreciable differences. (C) the merged image of amide I (A) and Phe (B) also demonstrate this distribution. In all figures, the halo image is based on lipids frequency (2850 $cm^{-1}$). Images without a scale bar share the bar of the leftmost image in the same line, which is 20 µm. Reprinted from reference [25].

As we shown in section 3.3, there are overlapping lipid and protein peaks in the high-wavenumber region. When studying Aβ plaques, this gives rise to halo and core signals in the same image. One way to obtain only core images with vibrations in the high-wavenumber region is by image arithmetic, such as pixel subtraction. Figure 3.27 compares the subtraction image with the amide I image (~ 1675 $cm^{-1}$) of different plaques. The subtraction image is obtained by digitally subtracting the lipid-based image (~ 2850 $cm^{-1}$, figure 3.27) from the lipid/protein-based image (~ 2930 $cm^{-1}$, figure 3.27) with an image processing software. As we can see, such pixel subtraction generates a core image similar to the amide I-based image with only high-wavenumber vibrations. To the best of our knowledge, such a specific image in this region could only be presented by this type of subtraction, and no high-wavenumber core signature has been reported.

To investigate further vibrational signatures of the core in the high-wavenumber region, we also applied the combination of SpRS spectroscopy and SRS microscopy. Figure 3.28A shows typical SpRS spectra of the core (blue) and the halo (red) of an Aβ plaque in the high-wavenumber region. We analyzed the spectrum of each structure side-by-side to look for signatures that best discriminate the nucleus from the halo. Besides the already commented

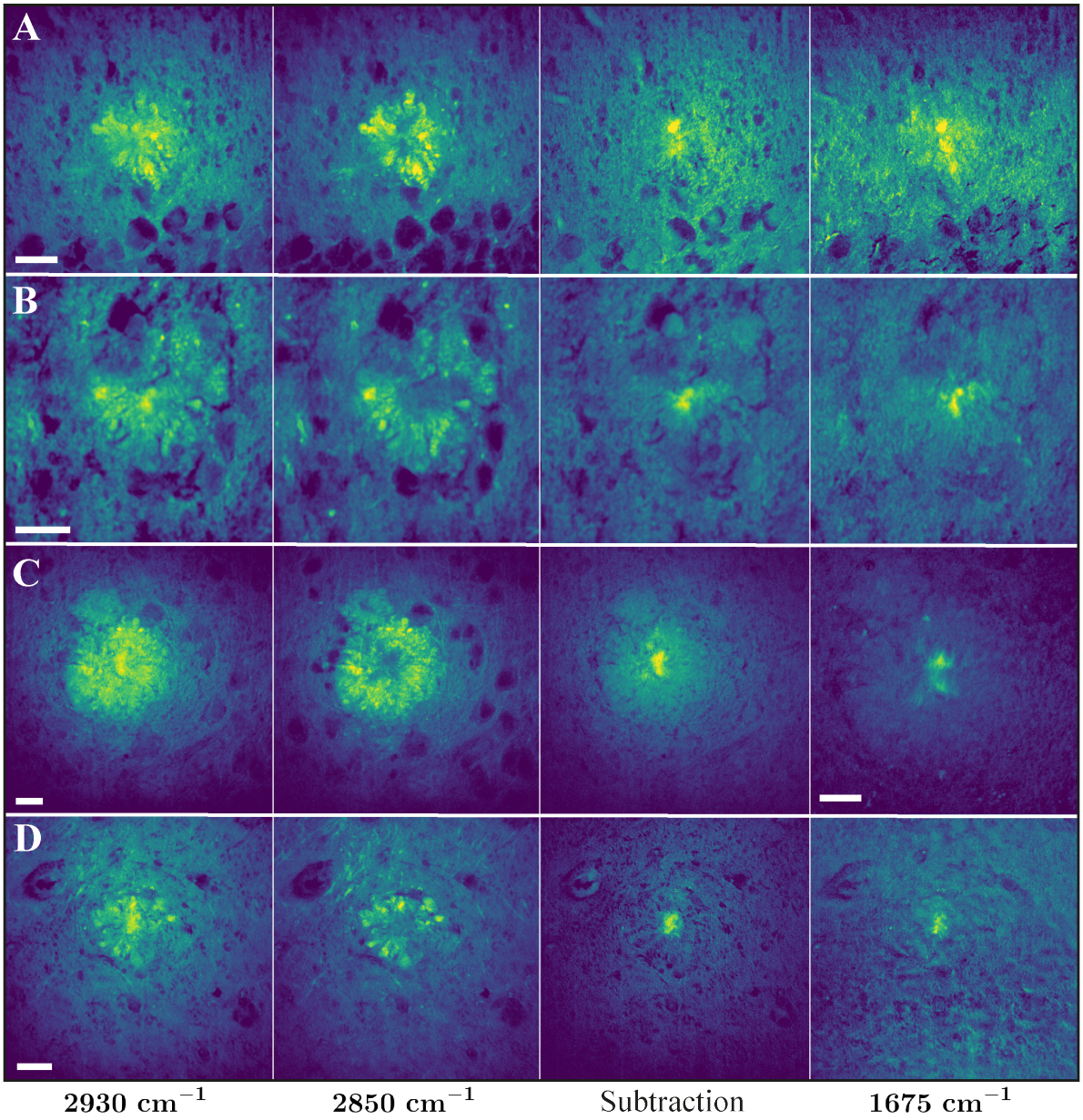


Figure 3.27: Subtraction of stimulated Raman scattering images in the high-wavenumber region and comparison with stimulated Raman scattering images based on the vibrational mode of amide I. (A-D) different Aβ plaques distributed in three vibrations: 2930 cm$^{-1}$ (proteins/lipids), revealing both the core and the halo; 2850 cm$^{-1}$ (lipids), with only the halo in evidence; and 1675 cm$^{-1}$ (amide I), with only the core in evidence. This last column should be compared to the subtraction column obtained by subtracting images at frequencies 2930 cm$^{-1}$ and 2850 cm$^{-1}$. The images based on amide I and those obtained by subtraction show a significant spatial correlation. Scale bars are 20 µm. Reprinted from reference [25].

Raman bands from 2800 to 3000 cm$^{-1}$, there is a pronounced band between 3050 and 3090 cm$^{-1}$ with a peak at ~ 3070 cm$^{-1}$ in the core spectrum. This signal has been assigned by infrared spectroscopy as the amide B vibrational mode present in proteins due to N-H stretching modes [220]. It is usually part of a Fermi resonance doublet (amide A and B), and it is resonant with an amide II combination mode in β-sheet conformation [151,220]. This is of

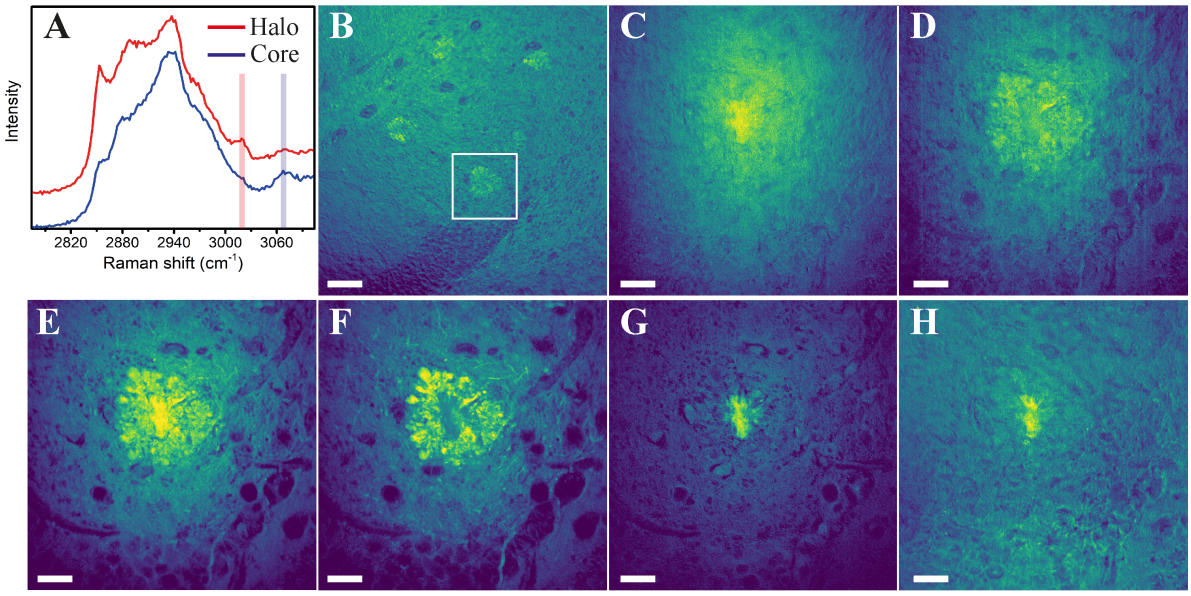


Figure 3.28: Amide B and unsaturated lipids as core and halo biomarkers, respectively, in the high-wavenumber region. (A) Typical SpRS spectrum of the halo (upper, red) and core (lower, blue) in the high-wavenumber region. The purple vertical bar identifies the frequency region of the SRS image in (C), while the orange bar identifies the frequency region of the image in (D). (B) Overview SRS image of the hippocampus with several Aβ plaques. The white rectangle identifies the plaque in (C-H). Scale bar is 60 µm. (C) SRS image taken at 3070 $cm^{-1}$, attributed to amide B vibration. (D) SRS image taken at 3019 $cm^{-1}$, attributed to unsaturated lipids and exhibiting a good correlation with lipids vibration in (F). (E) SRS image taken at 2930 $cm^{-1}$ (protein/lipids), (F) SRS image taken at 2850 $cm^{-1}$ (lipids), and (G) the subtraction of images in (E) and (F). (H) SRS image taken at 1675 $cm^{-1}$, attributed to amide I vibration. All scale bars in (C)-(H) are 20 µm. Reprinted from reference [25].

substantial significance since the amide II band is considered too weak or absent in the SpRS spectrum [151, 220], but it provides valuable structural information, and it is suggested for secondary structure prediction as a counterpart of amide I [220, 221]. Figure 3.28B shows an overview SRS image of a hippocampus with several Aβ plaques based on lipids $CH_2$ stretching mode (2850 $cm^{-1}$) and acquired with a 20x objective (maximum NA of 0.75). The white rectangle identifies the plaque shown in figures 3.28C-3.28H. Figure 3.28C shows the SRS image taken at 3070 $cm^{-1}$, which images the core clearly, thus demonstrating the feasibility of using the amide B frequency to locate the core of Aβ plaques. We also compared the amide B (3070 $cm^{-1}$, 3.28C) and amide I (1675 $cm^{-1}$m figure 3.28H) images with the subtraction (figure 3.28G) of lipids/proteins (2930 $cm^{-1}$, figure 3.28E) and lipids (2850 $cm^{-1}$, figure 3.28F) images. As we can see, neither the amide B image nor the amide I image is simply a subtraction image. Nevertheless, while figure 3.28H shows a more defined core image, such a correlation is still present in the amide B image, demonstrating the applicability of this vibrational mode for protein-based imaging of Aβ plaques.

Figure 3.29 shows the spatial distribuition of amide I and amide B in the plaque. As in figure 3.26, here the gray area is also mainly the lipid-based ($\sim$ 2850 $cm^{-1}$) image of the tissue and plaque, and Figure 3.29C is the merged image. Regardless of interference with other

vibrations, both the amide I (magenta, figure 3.29A) and amide B (blue, figure 3.29B) signals are stronger in the core. Therefore, we regard amide B as a potential core biomarker in the high-wavenumber region.

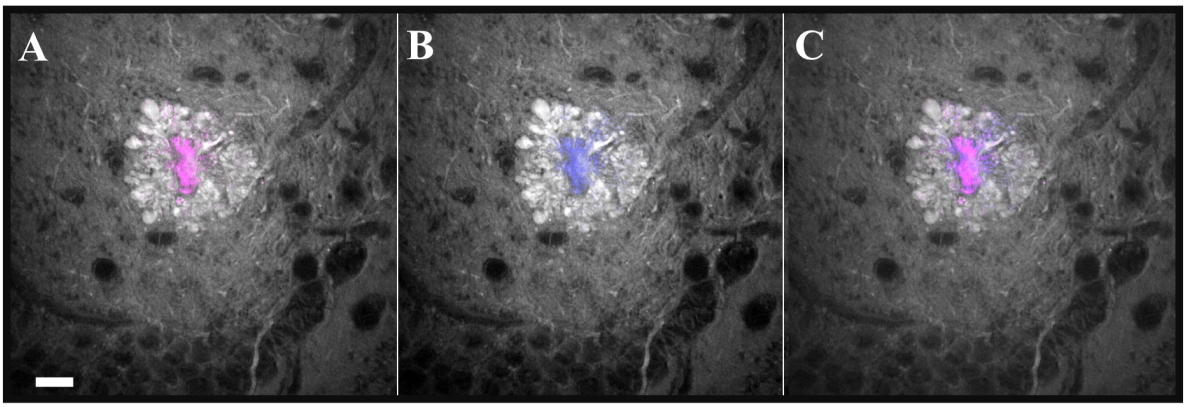


Figure 3.29: Spatial distribution of amide I and amide B in the plaque. (A,B) merged image of the halo and core, demonstrating the spatial distribution of (A) amide I and (B) amide B. There is a spatial correlation in the distribution of both biomarkers in the core. (C) Merged image of amide I (A) and amide B (B). In all figures, the halo image is based on lipids frequency, 2850 $cm^{-1}$. Images without a scale bar share the bar of the leftmost image in the same line, which is 20 µm. Reprinted from reference [25].

The importance of these results for microscopy can also be appreciated in two ways: the analysis of different signatures for the core, such as amide I, Phe, and amide B vibrational modes, can reveal complementary information about the plaque, which can be valuable for its basic understanding and its precise role in AD-related neurodegeneration. Also, while amide B is described as a weakly absorbing component in infrared spectroscopy [151,220], it allowed the acquisition of core images with high contrast, high intensity, and few accumulations with SRS. In our experiment, we obtained SRS images at the amide B frequency with approximately 7 times higher mean contrast than those obtained at the amide I frequency. Thus, while the image of amide I forms a more defined core, amide B allows for faster imaging. This result suggests amide B as a novel signature to be incorporated in the study of Aβ plaques for diagnostic applications, where the acquisition time is of great relevance. However, further studies are necessary to determine whether this is an intrinsic property of amide B vibration, associated with the contrast difference between the core and the halo, or an experimental feature of our setup.

Using the same combination of SpRS spectroscopy and SRS microscopy, we found a weaker signal but more pronounced in the halo than in the core, which had not yet been reported in the study of Aβ plaques. In figure 3.28A, the halo spectrum shows a band between 3010 $cm^{-1}$ and 3025 $cm^{-1}$ (peak at 3019 $cm^{-1}$) associated with =CH bindings and attributed to unsaturated lipids [222]. Figure 3.28D shows the SRS image at 3019 $cm^{-1}$, which correlates with the characteristic SRS image of the halo at 2850 $cm^{-1}$ in figure 3.28D. Therefore, it is also possible to use this Raman band to locate the halo by SRS imaging in addition to the other established halo biomarkers in the high-wavenumber region. Figure 3.30 shows two other

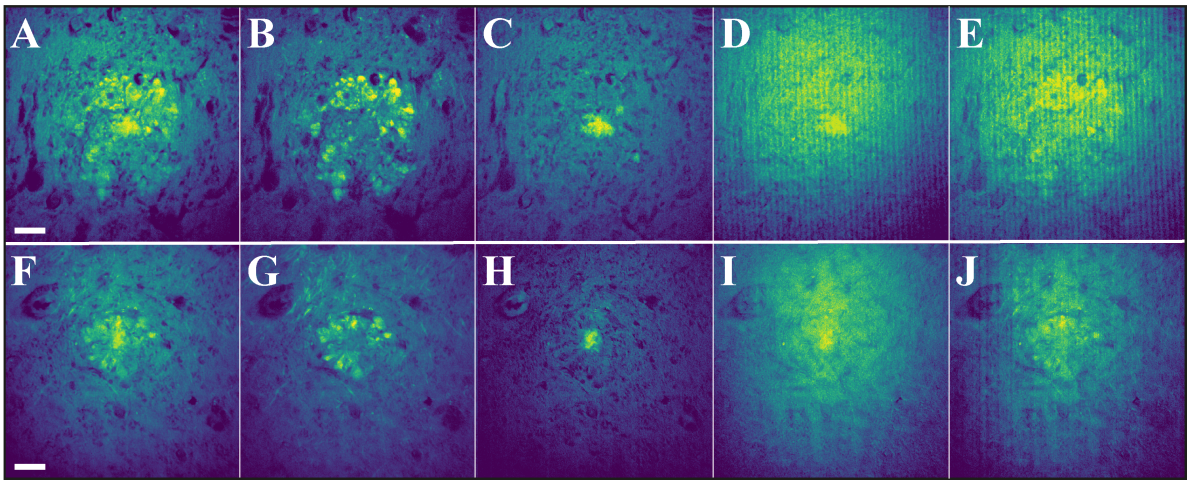


Figure 3.30: Stimulated Raman scattering image with core and halo biomarkers in the high-wavenumber region for two different Aβ plaques. (A,F) and (B,G) are images based on the known 2930 $cm^{-1}$ (proteins/lipids) and 2850 $cm^{-1}$ (lipids) frequencies, respectively. (C,H) is the subtraction of these images, showing the core. (D,I) are images based on the 3070 $cm^{-1}$ (amide B) frequency, which shows the core in the high-wavenumber region, correlating with the image obtained by subtraction (C,H). (E,J) are halo images based on the 3019 $cm^{-1}$ frequency attributed to unsaturated lipids. Images without a scale bar share the bar of the leftmost image in the same line, which is 20 µm. Reprinted from reference [25].

plaques through these three high-wavenumber imaging bases: subtraction (figures 3.30C and 3.30H), amide B (figures 3.30D and 3.30I), and unsaturated lipids (figures 3.30E and 3.30J).

In summary, we performed label-free multimodal imaging by nonlinear and vibrational microscopies to study and present high-resolution images of Aβ plaques in the hippocampus and cortex of brain tissues of bitransgenic mice AD model [25]. The results allow us to reach different conclusions about each technique. First, although exogenous labels are undesirable, TPEA imaging may be non-ideal due to the different overlapping signals. Finding more plaque-specific autofluorescent signals can be advantageous since TPEA imaging is a technique with less experimental complexity, facilitating applications. Second, SHG imaging of the core suggests a protein-related origin of the SHG signal, as we compared with TPEF ThioS staining and TPEA images, together with an analysis of results in the literature. Like TPEA, SHG imaging is also less complex, and studying the origin of the signal and its relationship with AD may bring future applications.

Unlike TPEA and SHG, using vibrational microscopy based on SpRS, CARS, and SRS allowed us to study the core and halo. Nevertheless, CARS and SRS showed different suitability in this study. As discussed in section 3.3.3.1, CARS can be severely hampered by a spurious background in the fingerprint region. However, this background may also be relevant in the high-wavenumber region. Although many works use CARS based on lipid vibrations due to the distinctive signal, the background represented considerable interference in our study of Aβ plaques. When comparing CARS and SpRS images, we observed a substantial distortion. Thus, the third aspect suggested by the results is that CARS microscopy does not always represent an interesting vibrational technique, especially if the information about the

spatial distribution of intensity is critical. Finally, the results also suggested the feasibility of studying Aβ plaques using SRS microscopy. Contrary to CARS, SpRS and SRS microscopies produced virtually identical images, even in different experimental setups. This allows for a straightforward combination of SpRS spectroscopy information with the advantages of SRS microscopy. From this combination, we showed vibrational biomarkers in the fingerprint and high-wavenumber regions not yet reported in SRS microscopy studies of Aβ plaques. The implementation of SRS microscopy was the main contribution of this thesis and proved to be promising in studying biological tissues.

## 3.5 Perspectives

One of the next steps of what we presented in section 3.4 is the study of Aβ plaques in the retina. Since the retina is an interface between the eyes and the brain, it is considered a candidate for *in vivo* studies of AD. This idea suggests the possibility of simplifying complex neuroimaging tests to routine eye examinations. Intraocular CRS imaging emerges as a tool for rapid imaging, seeking to identify properties of Aβ plaques captured by vibrational biomarkers.

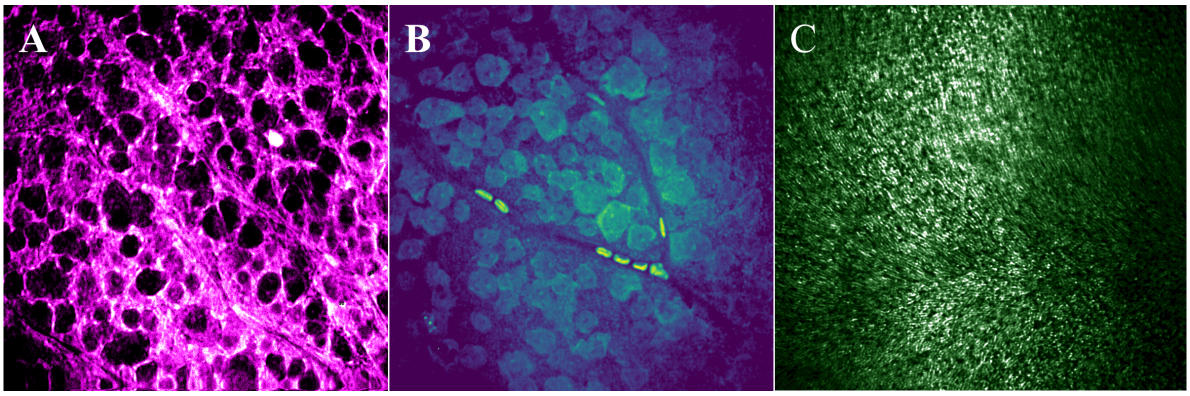


Figure 3.31: Stimulated Raman scattering imaging of different layers of mouse retinal tissue. (A) Ganglion cells, (B) blood vessels with bright erythrocytes, and (C) Photoreceptors. All images are based on lipid vibration (2850 $cm^{-1}$).

While we present this idea as a perspective here, figure 3.31 shows images of different layers of the retina obtained by SRS imaging of retinal tissues from *ex vivo* mice. Figure 3.31A shows ganglion cells, more superficial in the tissue. In a deeper layer, we find blood vessels with bright erythrocytes, as shown in figure 3.31B. Finally, in one of the deepest layers of the retina, we can see the photoreceptors in figure 3.31C. All images are lipid-based.

## 3.6 Concluding remarks

As final considerations, we look at the approach proposed in this chapter. We started with a simple overview of common techniques in biological imaging, especially those based on light absorption by exogenous labels to obtain contrast with specificity. We briefly discussed some

of the problems these techniques carry, and we saw that nonlinear optics could work around some of them due to the very nature of nonlinear interactions. In particular, when we change the contrast mechanism based on linear absorption for one based on nonlinear scattering, we can probe biological systems in a label-free and specific manner. Coherent Raman scattering microscopy appears as a fast and biochemically specific imaging alternative, allowing its application in several topics. We reviewed the use of this technique in biomedicine in recent years, highlighting its importance in clinically relevant problems. Then, we presented a study of AD from the multimodal imaging of Aβ plaques in brain tissues of an animal model of the disease, concluding with perspectives for new developments in this work. We, therefore, recognize how nonlinear optics can be a prolific tool in biological imaging.

# Chapter 4

# Nonlinear optics for imaging 2D materials

## 4.1 Introductory remarks

In chapter 2, we primarily resorted to the classical picture of light-matter interactions. For that reason, the term *medium* represented a macroscopic material composed of electric dipoles, without specific mention of the internal structure of this material. However, numerous material characteristics can influence optical properties, such as size, dimensionality, thickness, and defects [5, 15, 26, 34, 35]. For example, photoluminescence can be size-dependent [223], and the Raman spectrum of materials can exhibit different features for different thicknesses, even if their composition remains the same [224]. In particular, emphasis was given in this text to the dependence of SHG on the symmetry[1] of the medium. This nonlinear effect depends on shape, size, organization of atoms, among others, since symmetry has a strong relationship with the structural characteristics of the medium. In this chapter, we explore further the relationship between structural properties and SHG. In section 4.2 we introduce the concept of dimentionality of the medium and review its consequence on the SHG in few-layer $MoS_2$ in section 4.3. We also revisit these consequences in h-BN in sections 4.4 and 4.5. Since defects also occur in the form of structural changes, we briefly review the influence of defects on the optical properties of h-BN in section 4.6 and present the results we obtained for the influence of defects on the SHG in h-BN in section 4.7.

## 4.2 Two-dimensional materials

An important concept in the study of materials is dimensionality. If one or more dimensions of a material are reduced to the nanoscopic scale, the resulting material can exhibit drastically different optical properties from its 3D counterpart, commonly referred to as bulk [225–227]. In this way, materials can be characterized by the number of dimensions confined to the nanoscopic scale [225, 228]. If all three dimensions are nanoscopic, we have a zero-dimensional (0D) material, such as quantum dots [228]. If two dimensions are nanoscopic,

[1] That is not to say that SpRS and other effects used in chapter 3 cannot reveal any aspect of symmetry. We just do not explore this possibility in this thesis.

we have a one-dimensional (1D) material, such as nanowires [229]. Finally, if the material has only one nanoscopic dimension, we have a two-dimensional (2D) material, such as nanosheets [226]. The term nanosheet is used in analogy to a sheet of paper, where two dimensions are much larger than the third. Therefore, 2D materials can be broadly defined as structures whose total thicknesses vary from one atomic layer to tens of nanometres [226].

The birth of experimental research in 2D materials takes place in the extreme limit, where one of the three dimensions is not only nanoscopic, but atomically thin. Since graphene is one-atom-thick, and it was the first 2D material discovered [230], it is sometimes referred to as the archetypal example of 2D material [231]. Nevertheless, several other materials have been the subject of intense research, especially layered materials. This class of structures consists of bulk materials formed by stacking their 2D layers [232]. While the in-plane atomic bonds are strong in such materials, interlayer interactions are comparatively weak since the atoms are attached to sheets above and below by van der Waals forces [226], facilitating the process of producing nanosheets. Again, graphene is considered an archetypal example, as its bulk counterpart (graphite) consists of stacked graphene monolayers [232]. A notable property of layered materials, and of special interest for this chapter, is that the quantum confinement of one of the dimensions can lead to novel optical properties. Therefore, layered materials in their 2D form can exhibit strong nonlinear optical properties absent in their bulk counterparts [38, 39, 233, 234].

## 4.3 Layer-number dependence of SHG

An illustrative case of the modification of nonlinear optical properties of layered materials is in the family of transition metal dichalcogenide (TMDs). These materials have the formula $MX_2$, where M is a transition metal and X is a chalcogenide [38, 233, 234]. They are the main 2D materials studied in addition to graphene. Among them, molybdenum disulfide ($MoS_2$) was the first 2D TMD in which SHG was observed [38, 39, 235]. Bulk $MoS_2$ with 2H (AA') stacking order is known to belong to the centrosymmetric group $D_{6h}$ [38, 39]. Thus, as discussed in sections 2.4.3 and 2.5.1.1, bulk $MoS_2$ is expected not to exhibit SHG. However, Malard *et al.* and other groups showed that by reducing the material thickness to a few layers, $MoS_2$ could emit SHG [38, 39, 235].

In their study, single and few layers were obtained by mechanical exfoliation of natural bulk hexagonal $MoS_2$. Figure 4.1A shows the optical image of a flake with different thicknesses. The number of layers in the flake delimited by the dashed triangle was inferred from the atomic force microscopy (AFM) image in figure 4.1B. When compared to the SHG image of the same region in figure 4.1C, we see that only regions with an even number of layers do not exhibit significant SHG [38]. Regions with an odd number of layers have a strong emission. This pattern can be understood from figure 4.1D, which shows the side and top views of the AA' stacking of a $MoS_2$ bilayer. A single $MoS_2$ layer lacks inversion symmetry and belongs to the non-centrosymmetric group $D_{3h}$ [38, 39]. Thus, it is expected that the monolayer exhibit SHG. However, inversion symmetry is restored in the bilayer, which belongs to centrosymmetric

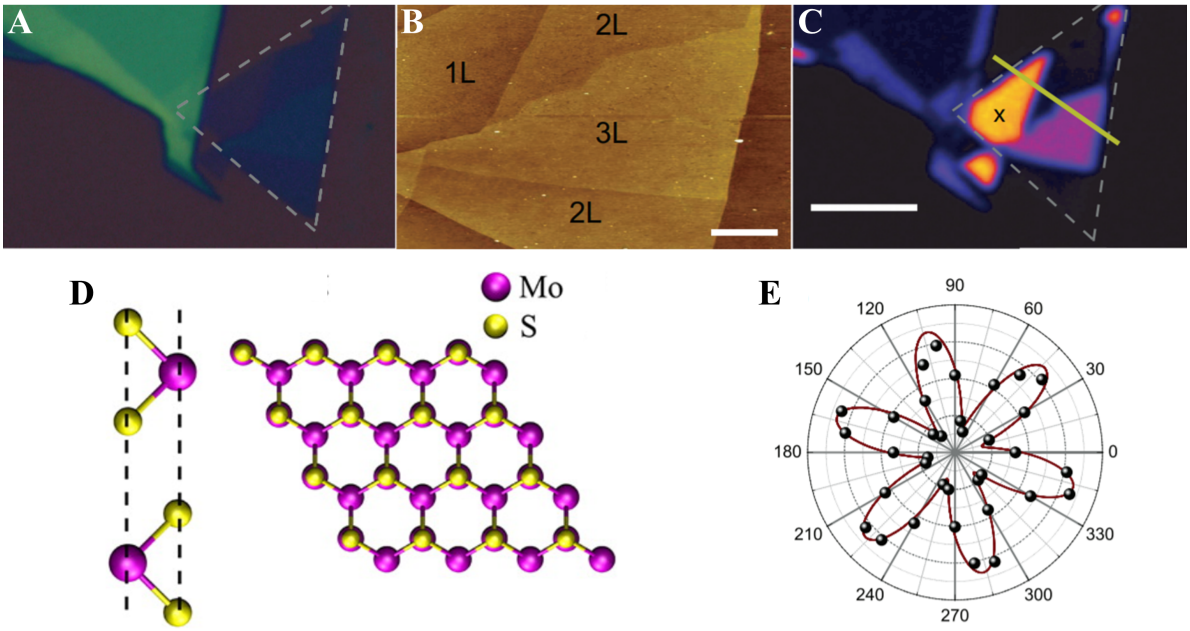


Figure 4.1: Layer-number dependence of second harmonic generation in molybdenum disulfide. (A) Optical image of $MoS_2$ thin films. (B) Atomic force microscopy image of the dashed triangle (A), allowing the inference of the thickness: 1L for monolayer, 2L for bilayer, and 3L for trilayer. The scale bar is 1 µm. (C) Second harmonic generation image of the same region in (A,B). Brighter colors mean stronger SHG intensity. The scale bar is 5 µm. (D) Illustration of the side and top views of the AA' stacking order of two layers of $MoS_2$ demonstrating the lack of inversion symmetry in the monolayer and recovering of inversion symmetry in the bylayer. (E) Polar plot of the SHG intensity as a function of the $MoS_2$ monolayer angle. Adapted from references [38, 236].

group $D_{3d}$ [38, 39]. Hence, SHG should be absent in the dipole approximation [5, 15, 61–63], as discussed in sections 2.4.3 and 2.5.1.1. In such a case, bulk $MoS_2$ can be described as an AA' stacking of 2D $MoS_2$ layers, in which the SHG emission depends on the amount of material composing the total thickness. Intriguingly, as can be observed in figure 4.1C, the monolayer has a stronger SHG intensity than the trilayer, although more material is present in the latter [38].

Furthermore, as discussed in section 2.6.2, SHG intensity profile depends on the symmetry of the material. This makes SHG sensitive to the polarization of incident light. Malard *et al.* performed polarization-resolved measurements by varying the polarization of the incident laser and rotating the sample placed on top of a precision rotation stage. Figure 4.1E shows the monolayer SHG intensity as a function of the sample rotation angle. The clear six-fold rotational pattern demonstrates the SHG dependence on the orientation of the sample, showing the capability of probing structural-based information with SHG. Such orientational dependency is also illustrated in figure 2.14.

## 4.4 Hexagonal boron nitride

Another material of importance in 2D materials research is boron nitride. Boron nitride is a compound formed by atoms of boron and nitrogen through covalent bonds [237]. This material is synthesized in four primary crystalline phases which include the cubic, hexagonal, rhombohedral, and wurtzite [238,239]. Hexagonal boron nitride (h-BN), where boron nitride is analogous to graphite and is sometimes referred to as "white graphite", can be distinguished from the others by its Raman spectrum [240], which exhibits a characteristic peak around 1366 $cm^{-1}$ due to the $E_{2g}$ vibrational mode of B-N bonds [241]. Figure 4.2A shows the characteristic SpRS spectrum of h-BN, the material studied in this chapter.

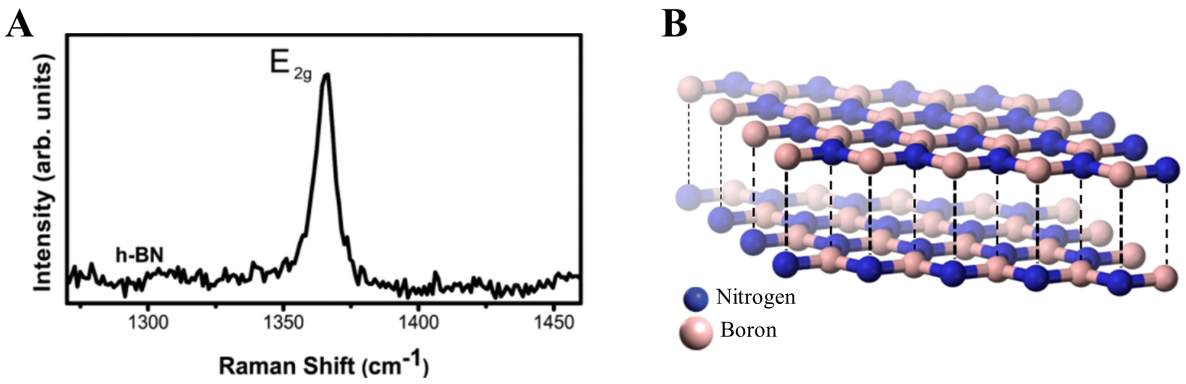


Figure 4.2: Hexagonal boron nitride. (A) Spontaneous Raman scattering spectrum of h-BN. (B) AA' stack of h-BN layers showing the lack of inversion symmetry in the monolayer and the recovering of inversion symmetry in the bilayer. Adapted from references [242,243].

While graphene is a zero band gap material and TMDs generally have a small band gap, h-BN has a band gap of ~ 6 eV [244], with typical absorption in the ultraviolet (UV) region [245]. Hence, studying h-BN with absorption-based optical contrast techniques and SpRS can be challenging. For example, its $E_{2g}$ Raman-active mode is far from electronic resonances [240,241], giving h-BN a weak SpRS signal compared to other 2D materials. The $E_{2g}$ mode is about 50 times stronger in graphene [241]. Additionally, the large energy gap, low concentration of defects, and atomically flat surface led h-BN to be known for its use as a substrate for graphene and other 2D materials [246,247], as well as a dielectric in electronic devices [244]. Nevertheless, h-BN is a layered material with several interesting properties such as high thermal conductivity, and chemical stability. [237,245,248,249].

As a layered material, h-BN layers also exhibit distinct properties from their bulk counterparts, as discussed in section 4.3 for $MoS_2$. As is the case of $MoS_2$, AA' bulk h-BN belongs to the $D_{6h}$ centrosymmetric group [39]. Figure 4.2B shows the structure of two layers of h-BN in AA' stacking order. In such a case, boron (nitrogen) atoms in one layer are positioned above the nitrogen (boron) atoms in the other h-BN layer [39,244]. Because of its honeycomb structure with different atoms, single layers of h-BN lack inversion symmetry, as shown in figure 4.2B, and belongs to the non-centrosymmetric group $D_{3h}$ [39]. This symmetry breaking gives rise to a finite second-order electric susceptibility ($\chi^{(2)} \neq 0$), which is associated with several nonlinear phenomena in the material [15,48,250], and which allows for SHG

in the material. As can also be seen in figure 4.2B, the inversion symmetry is recovered in h-BN bilayers, which belong to the centrosymmetric group $D_{3d}$ [39]. Therefore, while h-BN monolayers exhibit SHG, bilayers do not [39]. Since SHG is not necessarily associated with material composition, electronic transitions, or lattice vibrations, it is not subject to the previously mentioned restrictions of absorption-based optical techniques and SpRS, making SHG-based techniques valuable tools for studying h-BN.

## 4.5 Second harmonic generation in pristine h-BN

Concomitantly with the report of the observation of SHG dependence on the number of layers in few layers of $MoS_2$ [38], Li *et al.* studied SHG in high-quality mechanically exfoliated h-BN on a silica substrate and verified the thickness-dependent SHG response in h-BN [39]. In several aspects, the results for h-BN are similar to the results for $MoS_2$ revisited in section 4.3. Figure 4.3A shows a histogram with the SHG intensity as a function of the number of layers of h-BN. As in the case of $MoS_2$, SHG is evident in odd layers, although it becomes vanishingly weak in even layers. This effect also can be seen as a consequence of inversion symmetry [39]. As shown in figure 4.2B, in even-layer thickness, the inversion symmetry is recovered, and hence the absence of SHG is expected in the dipole approximation. Unlike $MoS_2$, however, for odd-layer thickness, h-BN exhibits SHG with approximately the same intensity of the monolayer, regardless of thickness [39].

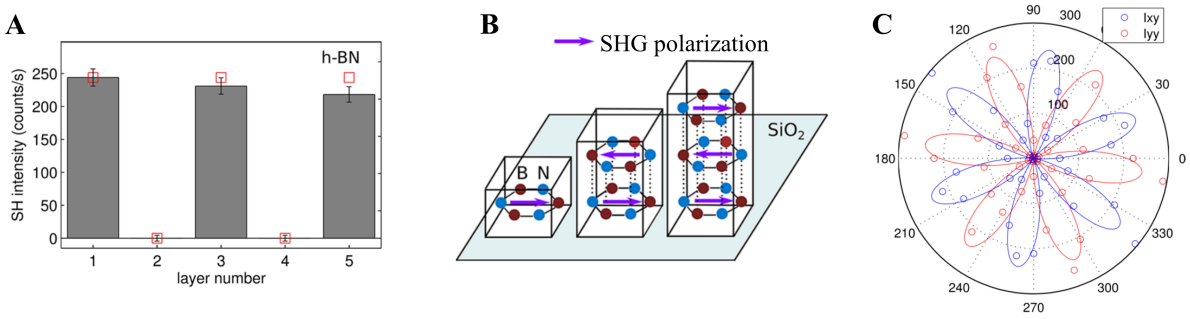


Figure 4.3: Second harmonic generation in pristine hexagonal boron nitride. (A) Histogram showing the SHG intensity dependence on the sample thickness. (B) Illustration of the model for the propagation of SHG through the layers to explain the behavior observed in the histogram (A). The AA' stacking order leads to sign alternation of the second-order electric susceptibility and of the SHG polarization in each layer. (C) Polar plot of SHG angular dependence detected at parallel and perpendicular directions in relation to the polarization of the laser. Each SHG component exhibits a six-fold rotational symmetry. Adapted from reference [39].

Li *et al.* proposed a model for the propagation of SHG through the layers to explain the behavior observed in the histogram of figure 4.3A. Figure 4.3B illustrates the model, which assumes that the layers of h-BN are stacked in AA' order, as illustrated in figure 4.2B. Therefore, the orientation of the layers follows an alternating pattern. This pattern leads to sign alternation of the second-order electric susceptibility in each layer [39], changing the direction of SHG polarization (purple arrow) [39]. Second harmonic generation in the bilayer results

from totally destructive interference, completely suppressing the signal from such even-layer thickness h-BN [39]. For a block with an odd number of layers $N$ (for $N > 1$), the SHG signal through the $N - 1$ layers experience destructive interference, and only the signal from the last layer can be measured [39]. This accounts for the thickness-independent emission and the monolayer profile in samples with an odd number of layers. The model provided by the authors correctly describes the behavior in the few layers regime. Nonetheless, Kim *et al.* recently extended this result for mechanically exfoliated multilayer h-BN, reporting the same behavior for h-BN samples with more than 100 layers [251].

Finally, Li *et al.* also performed polarization-resolved measurements by varying the polarization of the incident laser and rotating the sample [39]. Figure 4.3C shows the angular dependence of monolayer SHG intensity, also revealing a six-fold rotational symmetry. They also showed that the same rotational symmetry is present in three and five layers[2] of h-BN.

## 4.6 Defects-induced optical properties in h-BN

As discussed so far, SHG is sensitive to the various structural changes that occur in a material medium. These modifications are usually tested on high quality (pristine) samples, with a low defect density, in order to obtain controllable results. Since defects can also occur in the form of structural changes [231, 252], they can influence optical properties sensitive to such changes. Different types of defects can also be broadly classified according to their dimensionality as two-dimensional (stacking faults, folding, and rippling), one-dimensional (edges and grain boundaries) and zero-dimensional (vacancies, anti-site, and substitutional defects) [231, 253]. In many cases, several types of defects can be present in a material and modifications in the SHG can allow information acquisition in a fast and non-destructive way [252]. In the case of h-BN, zero-dimensional defects-induced modifications in 1PL have been known since the 1970s [254–256]. Although the characteristic 1PL emission of h-BN is in the UV region [237, 245, 257], the presence of such defects can manifest as midgap states, enabling 1PL emissions at much lower energies [254–256, 258–260].

Due to the importance of single-photon emitters for the development of quantum information technologies, much attention has been given to the ability of materials to host single-photon emitters at zero-dimensional defects in recent years [258–262]. Tran *et al.* showed that single-photon emitters defects could be created in h-BN monolayers and few-layers, which the authors assumed to be AA' stacked based on stability reasons [44, 244, 263], through simple annealing processes [44, 46, 47]. These single-photon emitters defects are detected as strong and sharp 1PL emissions in the visible region [44, 46, 47]. Figure 4.4A shows the confocal 1PL map of a defective sample recorded at room temperature with a 532 nm CW laser as the excitation source [44]. The authors attributed the majority of bright spots to single defects centers hosted by the h-BN, which was identified as few-layer thickness due to the peak at $\sim 1366\ \mathrm{cm}^{-1}$ obtained by SpRS spectroscopy [44]. The 1PL spectrum in Figure 4.4B shows a well-resolved peak at $\sim 623$ nm consistently present throughout the sample. Tran

[2] See supporting information of reference [39].

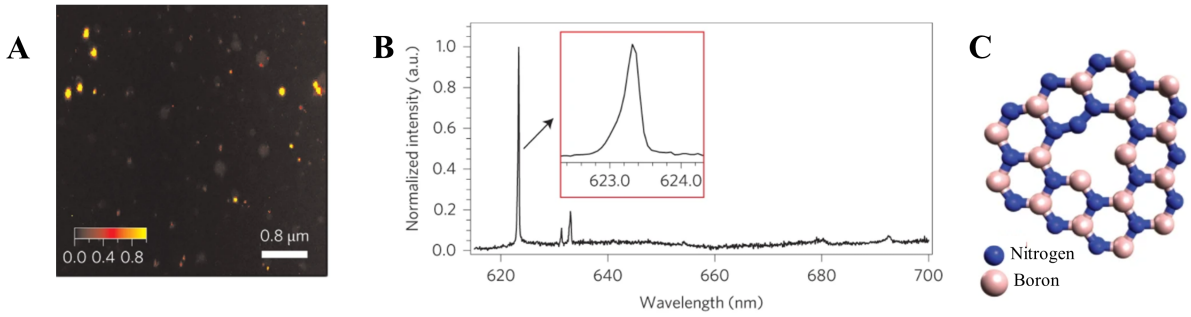


Figure 4.4: Point defects in hexagonal boron nitride. (A) One-photon excitation luminescence image of the defective sample showing h-BN bright spots in the visible spectral region. (B) One-photon excitation luminescence spectrum of subgap emissions associated with point defects. (C) Illustration of structural defects in a monolayer of h-BN. Adapted from referene [44].

*et al.* performed photon anti-bunching experiments, determining that such emissions have a single-photon profile (not shown in figure 4.4) [44]. The other two weaker peaks in figure 4.4B were attributed to different defects present in the sample [44]. Figure 4.4C illustrates an h-BN layer with vacancy-related defects, depicting the structural changes in the material.

## 4.7 Second harmonic generation imaging in h-BN with defects

In sections 4.2 and 4.3, we introduced concepts relevant to this chapter that were not yet discussed in this thesis. In particular, how the dimensionality of the medium influences the properties of SHG. We particularized the discussion for h-BN in sections 4.4 and 4.5. However, up to this point, we assumed (pristine) materials with low defect density. Determining the role of defects in materials can be an important task both for the fundamental understanding of their influence on material properties and for future applications [26, 262]. For this reason, in section 4.6, we revisited the influence of defects on the optical properties of h-BN. This section presents the results we obtained for the influence of defects on SHG in h-BN [26]. We report deviations from the results presented in section 4.5 for pristine h-BN and discuss possible mechanisms for such behaviors.

### 4.7.1 Sample information and setup for SHG imaging

The sample S used in this study was provided by the School of Mathematical and Physical Sciences at the University of Technology Sydney. It is a commercial liquid exfoliated h-BN sample (Graphene Supermarket) [44]. The solution was dropcasted in an amorphous quartz substrate and annealed at a temperature of 850 °C under 1 Torr of argon atmosphere. After this thermal treatment the sample was allowed to cool to room-temperature under continuous gas flow [44]. The number of h-BN layers present in the sample can vary from 1 to 5 according to references [44, 264]. Previous works have shown that this type of sample generate different

type of single defects in h-BN structure, leading to bright 1PL peaks with energy below the h-BN band gap [44–47]. These defects consist of nitrogen and boron vacancy-related defects, defects formed by the interaction of vacancies with impurities of C, O, H, Ba atoms. Such defects were studied by different experimental techniques and computational modeling in the literature [47, 257, 265–272]. Other structural defects, such as grain boundaries, edges and stacking faults, are also present in these type of samples. Additionally, a mechanically exfoliated from bulk h-BN sample was used for comparison with the defective sample, since the concentration of defects is much smaller.

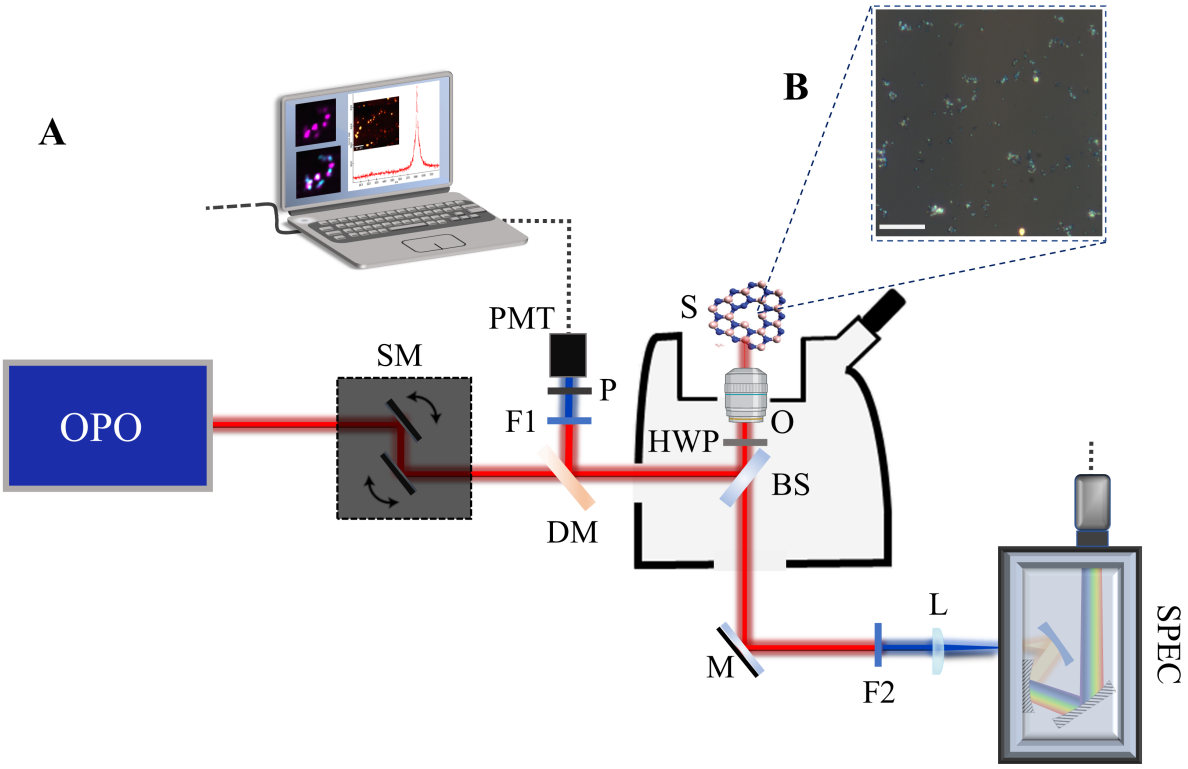


Figure 4.5: Optical setup for the experimental implementation of second harmonic generation imaging and spectroscopy. (A) OPO: laser source. SM: scanning mirrors. DM: dicroic mirror. BS: beam splitter. HWP: half-wave plate. O: objective. S: defective h-BN sample. F1: 405/10 nm bandpass filter for SHG imaging. P: polarizer. PMT: photomultiplier tube. M: mirror. F2: notch filter for attenuation of the Rayleigh scattering at ~ 810 nm. L: lens. SPEC: spectrometer. (B) Optical image of a 50×50 µm area of the sample. Scale bar is 10 µm. Adapted from references [44, 59].

The experimental setup used to study SHG in h-BN is shown in figure 4.5A. It is the same setup discussed in section 2.5.3 with few modifications. The excitation wavelength here is provided by a femtosecond tunable laser source of 180 fs pulse-width and 80 MHz repetition rate, tuned at 810 nm. The incident beam is focused by a 40x objective with NA of 0.95. The scanning mirrors system (Lavision Biotec) allows mapping the sample S. Part of the reflected SHG from the sample is reflected by the beamsplitter BS, and also by the dicroic mirror DM, to the detector PMT. The 405/10nm bandpass filter F1 attenuates other signals from the sample. The part transmitted by the BS is directed by the mirror M to the lens L, which focus the signal on the spectrometer SPEC. The notch filter F2 attenuates the Rayleigh scattering,

allowing the recording of SHG spectrum. The setup also allows to perform polarization-resolved measurements by the introduction of the half-wave plate HWP before the objective O and a polarizer P at the detection. Finally, figure 4.5B shows an optical image of a region of the sample.

One-photon excitation luminescence and SpRS hyperspectroscopic mapping was done on a Witec alpha300, operating with a 457 nm excitation laser that was focused onto the sample through a 50x objective with NA of 0.55. All measurements were done at room temperature.

### 4.7.2 Characterization of the defective sample

The first step of our study was the characterization of SHG and 1PL in the defective h-BN sample. Figure 4.6A shows an SHG image of the sample. In this image, the excitation wavelength is ~ 810 nm and a bandpass filter (405/10 nm) was used for detection. Figure 4.6B shows an image obtained when the laser is tuned to ~ 790 nm and the same bandpass filter is used for detection. As discussed in section 2.6.2, no SHG signal should be detected (as SHG now occurs at ~ 395 nm). The SHG spectrum in figure 4.6C confirms that the only relevant signal is SHG. The spectrum was obtained with a 5 ps laser tuned to ~ 810 nm and without filters at the region < 780 nm were used in front of the spectrometer.

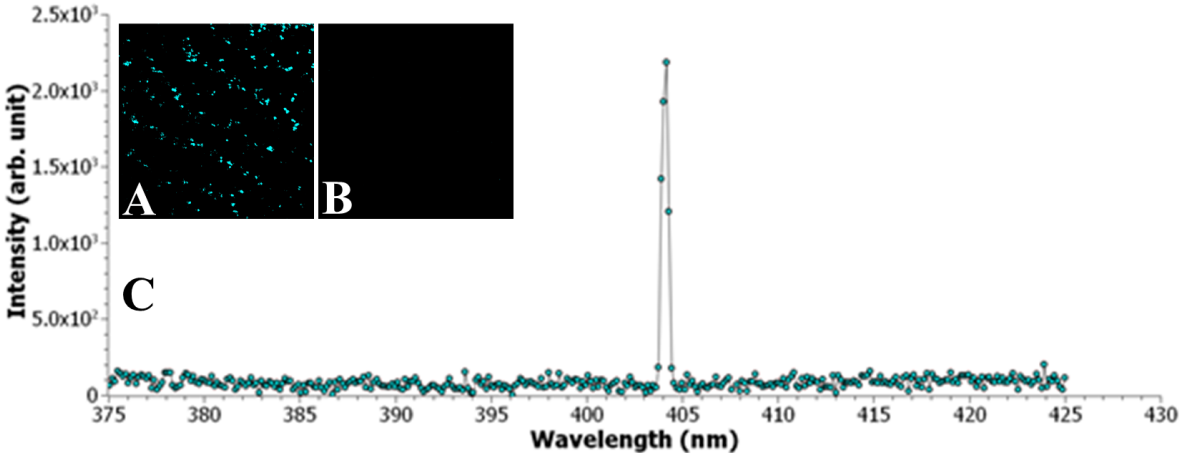


Figure 4.6: Confirmation of the second harmonic generation signal. Images obtained with a pump beam at (A) ~ 810 nm and (B) ~ 790 nm. A 405/10 nm bandpass filter was used in front of the detector for acquisition of imagens (A,B). (C) Spectrum of the signal of the sample obtained with a pump laser tuned to ~ 810 nm. No filter at the region < 780 nm was used in front of the spectrometer. Adapted from reference [26].

We selected regions of the sample that with isolated 1PL and SHG emissions as shown in figures 4.7A–4.7D. Figures 4.7A and 4.7C show the 1PL intensity images in the 500 – 700 nm window. The two isolated bright spots exhibiting 1PL correspond to different flakes. Figure 4.7E shows the 1PL emission spectrum of each spot. The lower plot in magenta corresponds to the spot of figure 4.7A, while the upper plot in red corresponds to the spot of figure 4.7C. As h-BN cannot exhibit 1PL with such low energy [237], these emissions can therefore be attributed to the presence of defects produced during the exfoliation and annealing processes.

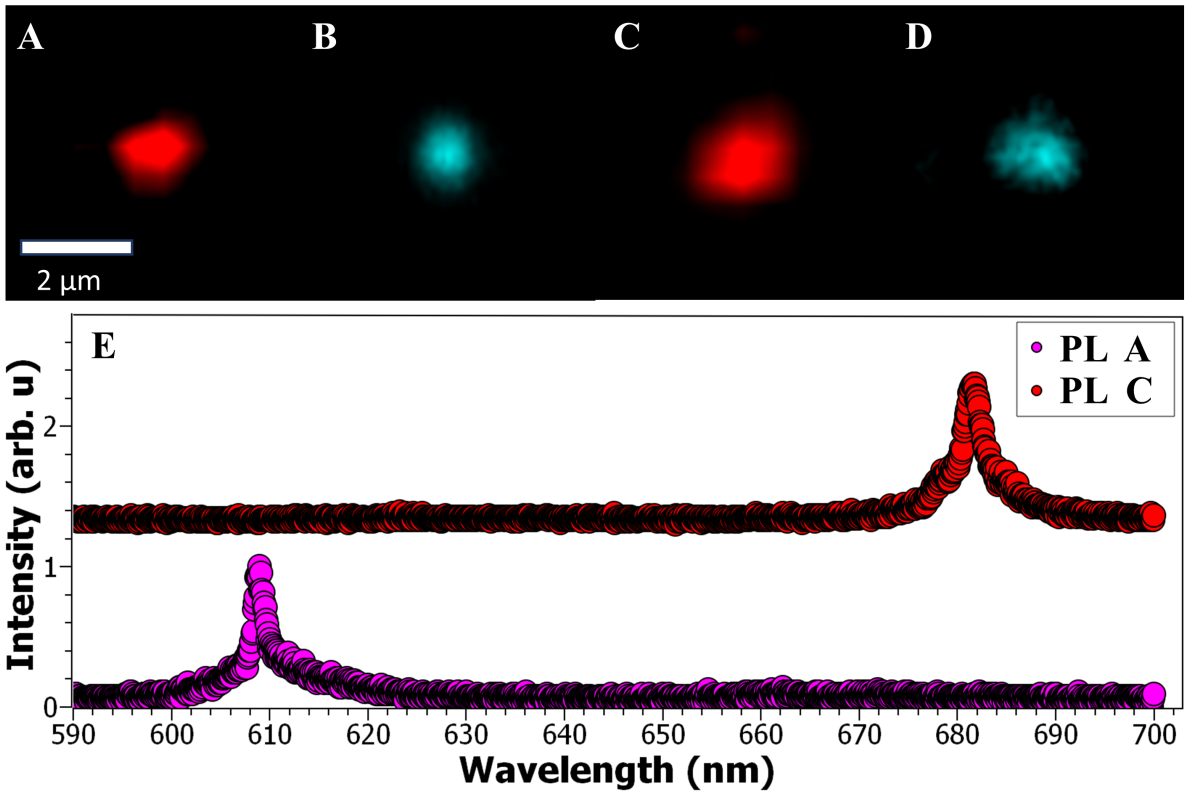


Figure 4.7: Characterization of the sample. (A, C) One-photon excitation luminescence intensity image in the 500–700 nm region. (B, D) Second harmonic generation intensity image of the same regions in (A, C), respectively. (E) One-photon excitation luminescence spectrum of the spots in (A) (top spectrum) and (C) (bottom spectrum). Adapted from reference [26].

Spectra in figure 4.7E and others in appendix A have been previously reported in literature. Although the identification of defects from 1PL spectra is still under discussion, *ab initio* calculations propose the association of some of these spectra with certain types of defects, such as charged and neutral nitrogen and boron vacancy-related defects [44, 270–272].

Figures 4.7B and 4.7D show SHG images of the same spots in figures 4.7A and 4.7C. Notwithstanding the differences in the physical origin of each effect, both 1PL and SHG can be used to map and locate h-BN, showing that the bright spots on one image correspond almost identically to the bright spots on the other[3].

As a non-centrosymmetric material, h-BN is expected to exhibit SHG, as discussed in sections 2.4.3, 2.5.1.1, and 4.5. However, the presence of defects modifies the linear optical properties of the material, as also discussed in section 4.6. Since structural defects can modify SHG [34, 35], in the next sections we turn to the question of whether the presence of defects also modifies the nonlinear optical properties of h-BN.

[3]The supplementary material of reference [26] show other images of 1PL and SHG, demonstrating such spatial correspondence.

### 4.7.3 Defects modify the intensity profile of SHG

In order to investigate further the role of defects on SHG, we compared h-BN spots with different intensities. Figure 4.8 shows images obtained by (A) SHG, (B) SpRS and (C) 1PL of the same two bright spots.

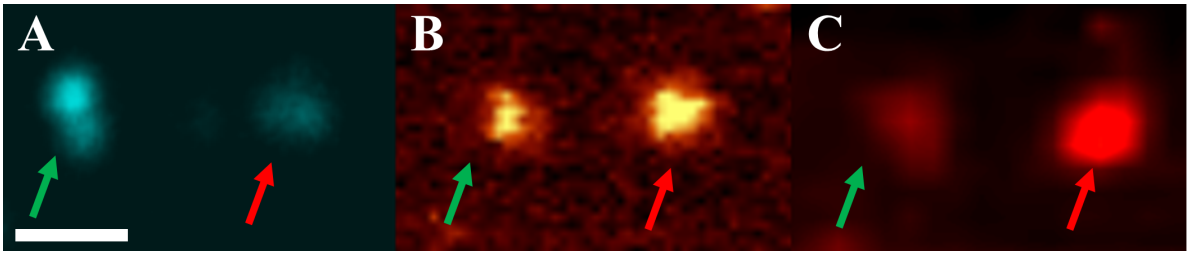


Figure 4.8: Comparison of second harmonic generation, spontaneous Raman scattering, and one-photon excitation luminescence images. (A) Second harmonic generation intensity image of two bright spots with distinct intensities (green and red arrows). (B) Spontaneous Raman scattering and (C) 1PL (in the 500–700 nm region) intensity images of the same two spots. Scale bar is 2 µm and is the same for all three images. Adapted from reference [26].

It is possible to see that the most (less) intense spot in the SHG image, identified by the green (red) arrow, does not show the same intensity trend in the SpRS and 1PL images. In the case of figure 4.8B, SpRS scales linearly with material concentration, as discussed in section 2.3.1. The comparison of figures 4.8A and 4.8B suggests that even if the concentration of h-BN generally contributes to the intensity of SHG, the presence of defects is modifying its emission intensity. In addition to the comparison of figures 4.8A and 4.8B, figure 4.8A alone already carries deviations from expected behaviors for h-BN. As discussed in section 4.5, an odd number of layers of h-BN produce SHG with the same intensity as the monolayer [39]. According to the model proposed by Li *et al.*, this effect is associated with the symmetry of the material and can be explained in terms of the AA' stacking order, which provides the necessary conditions for totally destructive interference in even layers [39]. However, figure 4.8A shows two bright spots exhibiting SHG in distinct intensities, evidencing that defects such as stacking faults can be influencing the SHG in h-BN. Another possible mechanism that can explain the distinct SHG, SpRS and 1PL intensities is resonant SHG. Since SpRS intensity is density-dependent and 1PL intensity is dependent on the radiative recombination rate of midgaps state from single defects in h-BN, the SHG intensity can be modulated by the resonance of one or two-photon absorption with these midgap states. Different h-BN spots can have different types of defects [269], which also have different energies (see figure 4.7E), and, accordingly, may have different resonances with the SHG. Throughout this sample we observed spots with 5 to 10 times more SHG than others. However in our experiments we did not find any correlation between the emitted 1PL energy and the SHG intensity from different h-BN flakes[4].

[4]See the SHG dependence on 1PL wavelength in the supplementary material of reference [26].

### 4.7.4 Defects modify the polarization dependence of SHG

Since defects affects the uniformity of the SHG intensity in h-BN, we performed polarization-resolved measurements to test modifications in the angular dependence of SHG intensity. Figure 4.9 shows the SHG intensity as a function of the incident laser polarization. In such measurements, the laser incident polarization angle $\phi$ is rotated by the HWP inserted in the setup of figure 4.5A, while the polarization analyzer P in front of the detector and the sample are kept fixed. In this case, the expected SHG intensity $I(2\omega)$ dependence with laser polarization is given by $I(2\omega) \propto sin^2(2\phi)$, revealing a four-fold rotational symmetry, as shown in appendix B. This is expected for samples belonging to point group $D_{3h}$, which is the case for an odd number of layers of h-BN and other semiconducting transition metal dichalcogenides [38,39]. Figures 4.9A–4.9D show the SHG intensity polarization dependence for four different h-BN

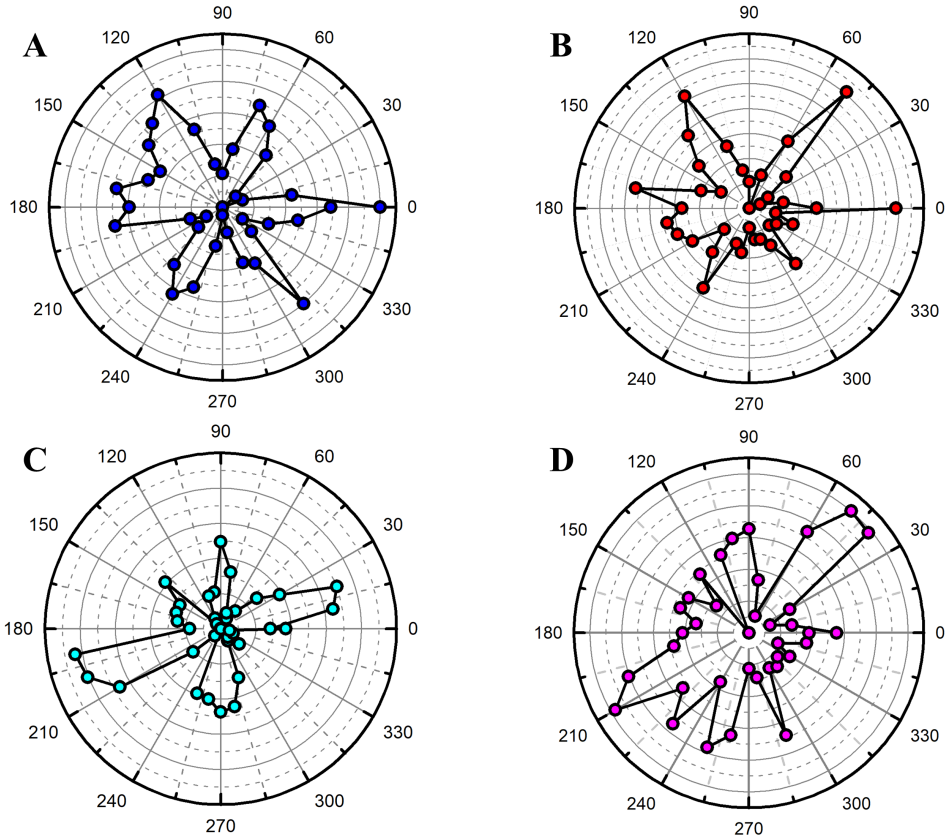


Figure 4.9: Polar plot of second harmonic intensity from four distinct defective hexagonal boron nitride spots. (A–D) Second harmonic intensity as a function of the incident laser polarization is used to show the influence of the defects on the overall second harmonic signal. While a four-fold rotational symmetry is expected for a pristine h-BN sample in our experimental conditions, h-BN with defects exhibit a complicated angular dependence. Adapted from reference [26].

flakes. It is possible to observe large deviations from the expected four-fold SHG intensity dependence in pristine h-BN, confirming that the presence of defects is influencing the SHG in h-BN.

Two main mechanisms can explain the polarization behavior in figure 4.9. The first

mechanism follows recent calculations based on group theory that showed that certain defects in h-BN, some of them present in this sample[5], belong to point groups that lack inversion symmetry [270–272]. Therefore, part of the signal can be attributed to single SHG dipoles generated by the different single defect states. Also, because of the anisotropic structure of each defect, the dipoles are expected to present different orientations [273]. Contrary to a four-fold emission expected in the absence of defects, we can observe an enhancement of the SHG for some angles due to the overlap with the contribution coming from the defect. In that case, the overall picture of the second harmonic intensity is given by the dependence of a single SHG dipole coming from the defect plus the angular dependence of the pristine h-BN, giving rise to the complicated SHG angular dependence in figure 4.9.

The other possible explanation is that the presence of defects changes the condition for totally destructive interference for SHG signal in an even number of layers, and therefore different layers contribute to the total SHG signal. In such a case, the perfect AA' stacking sequence present in bulk h-BN would be disturbed, leading to SHG intensity variations and angular dependence that are not expected for pristine h-BN.

### 4.7.5 Defects modify the efficiency of SHG

Because of the changes in SHG intensity caused by defects, we turn to the question of efficiency in this sample. To this end, we measured the SHG intensity produced by h-BN with defects $I(2\omega)_{\text{h-BN}}$ and compared with the intensity of a monolayer of $MoS_2$ $I(2\omega)_{MoS_2}$. The SHG intensity of both materials were measured with the same experimental conditions: both samples were on transparent quartz substrates and the parameters for excitation laser and detection was kept fixed. In order to evaluate the average intensity of SHG produced by h-BN with defects, we obtained an SHG image of a region of interest and averaged the SHG intensity of different emitting spots[6]. Once again, our analysis is restricted to simple regions, with only isolated spots, to reduce the number of uncontrollable factors. Finally, we can express the sheet second-order susceptibility of h-BN with defects as [26]:

$$\chi^{*(2)\ s}_{\text{h-BN}} = \frac{\sqrt{I(2\omega)_{\text{h-BN}}}}{\sqrt{I(2\omega)_{MoS_2}}}\chi^{(2)\ s}_{MoS_2}, \tag{4.1}$$

where $\chi^{(2)\ s}_{MoS_2} = 4.8 \times 10^{-14}$ esu is the second-order electric susceptibility of a sheet of $MoS_2$ [39]. With the measured intensities, we find that the sheet second-order electric susceptibility for the h-BN with defects is $\chi^{*(2)\ s}_{\text{h-BN}} = 3.44 \times 10^{-14}$ esu, which shows a value of about one order of magnitude greater than the measured values for the second-order electric susceptibility of pristine h-BN which is equal to $1.66 \times 10^{-15}$ esu [39]. Figure 4.10 illustrates this result showing that, even visually, the defective h-BN sample in figure 4.10A exhibits SHG with higher intensity compared to the high-quality mechanically exfoliated h-BN sample shown in figure 4.10B.

[5] See appendix A.

[6] See the supplementary material of reference [26].

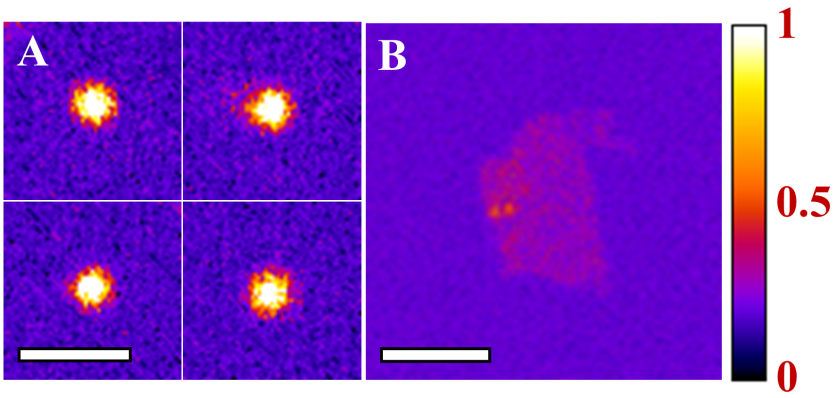


Figure 4.10: Efficiency of second harmonic generation in hexagonal boron nitride with defects. Second harmonic generation intensity image of (A) the defective sample and (B) the high-quality mechanically exfoliated sample. Both images were obtained under the same conditions and have the same intensity scale. Scale bars are (A) 2 µm and (B) 5 µm. Adapted from reference [26].

It is important to note here that we extracted the sheet $\chi^{(2)}$ of h-BN, assuming that few layers are present in the sample [44, 244, 263, 264]. As mentioned above, the AA' stacking may not be present in this case and, therefore, such high value of the sheet $\chi^{(2)}$ can be due to the sum of SHG coming from individual layers. In order to exclude such effects, further measurements with a controlled type of defects would be necessary.

## 4.8 Concluding remarks

In this chapter, we revisited the influence of dimensionality on SHG and mainly studied the influence of defects on SHG in h-BN. We found that the presence of defects modifies the optical properties of h-BN. In summary, we found a spatial correlation between SHG and 1PL images, although the two effects are not necessarily correlated. The intesity profile and angular dependence of SHG exhibited deviations from pristine h-BN samples, which reveals that defects are perturbing the crystal symmetries. Moreover, we characterized the second-order nonlinear susceptibility, which exceeds the typical value of pristine h-BN by one order of magnitude. Further studies are still necessary in order to understand the impact of different types of defects (single defects, grain boundaries, stacking faults, to name a few) on the SHG in h-BN. Therefore, controlling the defects responsible for this enhancement can be of great interest in order to enhance the nonlinear optical effects in 2D materials. Finally, we note that exploring structure-based information through SHG allowed us to investigate the extent of results previously established in the literature for high-quality h-BN and highlight the fast and non-destructive character of nonlinear optical imaging in 2D materials research.

# Chapter 5

# Conclusion

## 5.1 General remarks

Nonlinear optics is a phenomenologically rich area, and this thesis explored only a fraction of the numerous nonlinear optical effects that can be experimentally observed. The first part of this text introduced the subject and reviewed the effects relevant to the thesis. We started from linear optics, a regime characterized by low-intensity excitation. In this regime, we revisited the effects of 1PL and SpRS. The discussion of the LOM allowed us to immediately see that linear optics is a particular type of light-matter interaction. However, when the excitation becomes sufficiently intense, LOM no longer captures the effects observed experimentally, which are part of the scope of nonlinear optics. In this regime, we reviewed wave mixing effects, nonlinear photoluminescence, and CRS, which received particular attention.

The second part of the text was devoted to the application of nonlinear optics in biological imaging. As a multidisciplinary topic, we first defined how exploring these physical effects is particularly relevant to address problems in biological imaging. The center of the discussion was label-free imaging based on CRS microscopy, where we revisited different works that allowed us to see how CARS and SRS can be applied in biomedicine. Following recent applications of CRS in histopathological diagnosis, we presented a study based on multimodal imaging for histopathological characterization of Aβ plaques in an animal model of AD. This study improved the quality of images reported in the literature, allowing clear label-free identification of Aβ plaque structures through different nonlinear optical techniques. In addition, we explored the feasibility of using SRS for core imaging based on vibrational modes associated with Phe in the fingerprint region and amide B in the high-wavenumber region. The latter should be subject to further study to determine its diagnostic potential. We also observed that plaque images are formed from the vibration associated with unsaturated lipids in the high-wavenumber region. Our results suggest the conclusion that even in the high-wavenumber region, CARS is greatly affected by the nonresonant background. Tissue also exhibited a strong TPEA signal, further complicating the study of Aβ plaques through homodyne CARS. On the other hand, we showed that the correspondence of the SRS and SpRS signals is robust even to differences in scattering geometry. Furthermore, study through

Phe vibration showed that single-frequency SRS can reach lower frequencies than amide I, even at resonance with a substantially less intense peak. Such results allow us to conclude that even single-frequency SRS microscopy is feasible for studying AD.

The third and final part of the thesis emphasized the dependence of optical effects on the structural properties of materials. We revisited the concept of medium dimensionality and reviewed its consequences for SHG in two layered materials: $MoS_2$ and h-BN. The focus of this discussion was the modification of nonlinear properties as a function of the number of layers. The revisited studies report results for high-quality 2D materials with low defect density. However, different types of defects induce structural changes in materials and, therefore, modify optical properties. Thus, we presented a study of defect-induced modifications in the optical properties of h-BN. We observed a spatial correspondence between SHG images and 1PL images in the visible region, present in the sample due to defects. Such correspondence suggests an influence of defects on certain properties of SHG. We showed that defects modify the intensity profile, polarization dependence, and efficiency of SHG in h-BN. Finally, we determined the value of the second-order electric susceptibility of defective h-BN, which surpassed the value previously reported in the literature by one order of magnitude. Further studies are still necessary to understand the impact of different defects (single defects, grain boundaries, stacking faults) on SHG in h-BN. Controlling the defects responsible for the observed enhancements can be of great interest in 2D materials research. Our results led us to conclude that SHG is a suitable optical effect to study defect-induced optical properties and can be used to detect the presence of defects, diagnosing sample quality.

## 5.2 List of publications

### Second harmonic generation in hexagonal boron nitride

Renan Cunha, Alisson Cadore, Ramos, Sérgio L. L. M., Kenji Watanabe, Takashi Taniguchi, Sejeong Kim, Alexander S. Solntsev, Igor Aharonovich, and Leandro Malard. Second harmonic generation in defective hexagonal boron nitride. Journal of Physics: Condensed Matter, 32(19), 19LT01, 2020.

### Multimodal imaging for label-free characterization of amyloid plaques

Renan Cunha, Lucas Lafeta, Emerson A. Fonseca, Alexandre Barbosa, Marco A. Romano-Silva, Rafael Vieira, Ado Jorio, and Leandro Malard. Nonlinear and vibrational microscopy for label-free characterization of amyloid-β plaques in Alzheimer's disease model. Analyst, 146(9), 2945-2954, 2021.

### Statistical unmixing analysis of hyperspectral data of amyloid plaques

Emerson A. Fonseca, Lucas Lafetá, Renan Cunha, Hudson Miranda, João Campos, Helton G. Medeiros, Marco A. Romano-Silva, Raigna A. Silva, Alexandre S. Barbosa, Rafael P.

Vieira, Leandro M. Malard, and Ado Jorio. A fingerprint of amyloid plaques in a bitransgenic animal model of Alzheimer's disease obtained by statistical unmixing analysis of hyperspectral Raman data. Analyst, 144, 7049-7056, 2019.

## Aging process characterization in a model of Alzheimer's disease

Emerson A. Fonseca, Lucas Lafetá, João Campos, Renan Cunha, Alexandre S. Barbosa, Marco A. Romano-Silva, Rafael Vieira, Leandro M. Malard, and Ado Jorio. Micro-Raman spectroscopy of lipid halo and dense-core amyloid plaques: aging process characterization in the Alzheimer's disease APPswePS1ΔE9 mouse model. Analyst, 146(19), 6014-6025, 2021.

## Studying 2D materials with advanced Raman spectroscopy

Leandro Malard, Lucas Lafetá, Renan Cunha, Rafael Nadas, Andreij Gadelha, Gustavo Cançado, and Ado Jorio. Studying 2D materials with advanced Raman spectroscopy: CARS, SRS and TERS. Physical Chemistry Chemical Physics, 23(41), 23428-23444, 2021.

## A proposal for Alzheimer's disease early diagnosis

Ado Jorio, Alexandre S. Barbosa, Emerson A. Fonseca, Leandro M. Malard, Lucas Lafetá, Rafael P. Vieira and Renan Cunha. "Intraocular optical spectroscopy: a proposal for Alzheimer's disease early diagnosis", Advances in Ophthalmic Optics Technology (Series in Emerging Technologies in Optics and Photonics). Book chapter in final publication process.

## Scanning laser ophthalmoscope

Ado Jório de Vasconcelos, Leandro Malard Moreira, Rafael Pinto Vieira, Emerson Alberto da Fonseca, Plínio Salgado Borges, João Luiz Elias Campos, Renan Souza Cunha, Alexandre Simões Barbosa, Lucas Lafetá Prates da Fonseca, Márcia Dias Diniz Costa. Oftalmoscópio de varredura a laser - OLV (K-H-05-2020), 2021. Know-How registration certificate.

# Bibliography


[1] Lord Rayleigh. *The theory of sound, Vol. 1*. Dover Publications, New York, 1945.

[2] Robert T. Beyer. Lord Rayleigh and nonlinear acoustics. *The Journal of the Acoustical Society of America*, 98(6):3032–3034, 1995.

[3] John Kerr. Xl. A new relation between electricity and light: Dielectrified media birefringent. *The London, Edinburgh, and Dublin Philosophical Magazine and Journal of Science*, 50(332):337–348, 1875.

[4] G. H. C. New. Nonlinear optics: the first 50 years. *Contemporary Physics*, 52(4):281–292, 2011.

[5] Mark Fox. *Optical properties of solids*. Oxford University Press, 2010.

[6] Nicolaas Bloembergen. *Encounters in nonlinear optics: selected papers of Nicolaas Bloembergen (With Commentary)*. World Scientific, 1996.

[7] Maria Göppert-Mayer. Elementary processes with two quantum transitions. *Annalen der Physik*, 18(7-8):466–479, 2009.

[8] P. A. Franken, A. E. Hill, C. W. Peters, and G. Weinreich. Generation of optical harmonics. *Physical Review Letters*, 7(4):118, 1961.

[9] W. Kaiser and C. G. B. Garrett. Two-photon excitation in $CaF_2$:$Eu^{2+}$. *Physical Review Letters*, 7(6):229, 1961.

[10] E. J. Woodbury and W. K. Ng. Ruby laser operation in the near IR. *Proceedings of the Institute of Radio Engineers*, 50(11):2367, 1962.

[11] Gisela Eckhardt, R. W. Hellwarth, F. J. McClung, S. E. Schwarz, D. Weiner, and E. J. Woodbury. Stimulated Raman scattering from organic liquids. *Physical Review Letters*, 9(11):455, 1962.

[12] P. D. Maker and R. W. Terhune. Study of optical effects due to an induced polarization third order in the electric field strength. *Physical Review*, 137(3A):A801, 1965.

[13] Nicolaas Bloembergen. Conservation laws in nonlinear optics. *JOSA*, 70(12):1429–1436, 1980.

[14] Ji-Xin Cheng and Xiaoliang Sunney Xie. *Coherent Raman scattering microscopy*. CRC press, 2016.

[15] Robert Boyd. *Nonlinear Optics*, Academic Press, London, 2008.

[16] Francesco S. Pavone and Paul J. Campagnola. *Second harmonic generation imaging*. CRC Press, Boca Raton, 2014.

[17] Charles H. Camp Jr and Marcus T. Cicerone. Chemically sensitive bioimaging with coherent Raman scattering. *Nature photonics*, 9(5):295–305, 2015.

[18] C. Sheppard, J. Gannaway, R. Kompfner, and D. Walsh. The scanning harmonic optical microscope. *IEEE Journal of Quantum Electronics*, 13(9):912–912, 1977.

[19] J. N. Gannaway and C. J. R. Sheppard. Second-harmonic imaging in the scanning optical microscope. *Optical and Quantum Electronics*, 10(5):435–439, 1978.

[20] Winfried Denk, James H. Strickler, and Watt W. Webb. Two-photon laser scanning fluorescence microscopy. *Science*, 248(4951):73–76, 1990.

[21] Andreas Zumbusch, Gary R. Holtom, and X. Sunney Xie. Three-dimensional vibrational imaging by coherent anti-Stokes Raman scattering. *Physical review letters*, 82(20):4142, 1999.

[22] E. Ploetz, S. Laimgruber, S. Berner, W. Zinth, and P. Gilch. Femtosecond stimulated Raman microscopy. *Applied Physics B*, 87(3):389–393, 2007.

[23] Christian W. Freudiger, Wei Min, Brian G. Saar, Sijia Lu, Gary R. Holtom, Chengwei He, Jason C. Tsai, Jing X. Kang, and X. Sunney Xie. Label-free biomedical imaging with high sensitivity by stimulated Raman scattering microscopy. *Science*, 322(5909):1857–1861, 2008.

[24] Warren R. Zipfel, Rebecca M. Williams, and Watt W. Webb. Nonlinear magic: multiphoton microscopy in the biosciences. *Nature Biotechnology*, 21:1369–1377, 2003.

[25] Renan Cunha, Lucas Lafeta, Emerson A. Fonseca, Alexandre Barbosa, Marco A. Romano-Silva, Rafael Vieira, Ado Jorio, and Leandro Malard. Nonlinear and vibrational microscopy for label-free characterization of amyloid-β plaques in Alzheimer's disease model. *Analyst*, 146(9):2945–2954, 2021.

[26] Renan Cunha, Alisson Cadore, Sérgio L. L. M. Ramos, Kenji Watanabe, Takashi Taniguchi, Sejeong Kim, Alexander S. Solntsev, Igor Aharonovich, and Leandro M. Malard. Second harmonic generation in defective hexagonal boron nitride. *Journal of Physics: Condensed Matter*, 32(19):19LT01, 2020.

[27] Ziyi Luo, Hao Xu, Liwei Liu, Tymish Y. Ohulchanskyy, and Junle Qu. Optical imaging of beta-amyloid plaques in Alzheimer's disease. *Biosensors*, 11(8):255, 2021.

[28] Sandeep Chakraborty, Sheng-Tse Chen, Yang-Ting Hsiao, Ming-Jang Chiu, and Chi-Kuang Sun. Additive-color multi-harmonic generation microscopy for simultaneous label-free differentiation of plaques, tangles, and neuronal axons. *Biomedical Optics Express*, 11(2):571–585, 2020.

[29] Alex C. Kwan, Karen Duff, Gunnar K. Gouras, and Watt W. Webb. Optical visualization of Alzheimer's pathology via multiphoton-excited intrinsic fluorescence and second harmonic generation. *Optics Express*, 17(5):3679–3689, 2009.

[30] Shu Wang, Bingbing Lin, Guimin Lin, Caihong Sun, Ruolan Lin, Jia Huang, Jing Tao, Xingfu Wang, Yunkun Wu, Lidian Chen, and Jianxin Chen. Label-free multiphoton imaging of β-amyloid plaques in Alzheimer's disease mouse models. *Neurophotonics*, 6(4):1–11, 2019.

[31] Juris Kiskis, Helen Fink, Lena Nyberg, Jacob Thyr, Jia-Yi Li, and Annika Enejder. Plaque-associated lipids in Alzheimer's diseased brain tissue visualized by nonlinear microscopy. *Scientific Reports*, 5:13489, 2015.

[32] Jang Hyuk Lee, Dae Hwan Kim, Woo Keun Song, Myoung-Kyu Oh, and Do-Kyeong Ko. Label-free imaging and quantitative chemical analysis of Alzheimer's disease brain samples with multimodal multiphoton nonlinear optical microspectroscopy. *Journal of Biomedical Optics*, 20(5):1–7, 2015.

[33] Minbiao Ji, Michal Arbel, Lili Zhang, Christian W. Freudiger, Steven S. Hou, Dongdong Lin, Xinju Yang, Brian J. Bacskai, and X. Sunney Xie. Label-free imaging of amyloid plaques in Alzheimer's disease with stimulated Raman scattering microscopy. *Science Advances*, 4(11):eaat7715, 2018.

[34] T. E. Tsai, M. A. Saifi, E. J. Friebele, D. L. Griscom, and U. Österberg. Correlation of defect centers with second-harmonic generation in Ge-doped and Ge–P-doped silica-core single-mode fibers. *Optics Letters*, 14(18):1023–1025, 1989.

[35] M. A. Saifi and M. J. Andrejco. Second-harmonic generation in single-mode and multimode fibers. *Optics letters*, 13(9):773–775, 1988.

[36] M. S. Yeganeh, J. Qi, A. G. Yodh, and M. C. Tamargo. Influence of heterointerface atomic structure and defects on second-harmonic generation. *Physical review letters*, 69(24):3579, 1992.

[37] Ryohei Tanuma and Hidekazu Tsuchida. Three-dimensional imaging of extended defects in 4H-SiC by optical second-harmonic generation and two-photon-excited photoluminescence. *Applied Physics Express*, 7(2):021304, 2014.

[38] Leandro M. Malard, Thonimar V. Alencar, Ana Paula M. Barboza, Kin Fai Mak, and Ana M. De Paula. Observation of intense second harmonic generation from $MoS_2$ atomic crystals. *Physical Review B*, 87(20):201401, 2013.

[39] Yilei Li, Yi Rao, Kin Fai Mak, Yumeng You, Shuyuan Wang, Cory R. Dean, and Tony F. Heinz. Probing symmetry properties of few-layer $MoS_2$ and h-BN by optical second-harmonic generation. *Nano Letters*, 13(7):3329–3333, 2013.

[40] Hualing Zeng, Gui-Bin Liu, Junfeng Dai, Yajun Yan, Bairen Zhu, Ruicong He, Lu Xie, Shijie Xu, Xianhui Chen, Wang Yao, and Xiaodong Cui. Optical signature of symmetry variations and spin-valley coupling in atomically thin tungsten dichalcogenides. *Scientific reports*, 3(1):1–5, 2013.

[41] Yu Song, Ruijuan Tian, Jiulong Yang, Rui Yin, Jianlin Zhao, and Xuetao Gan. Second harmonic generation in atomically thin $MoTe_2$. *Advanced Optical Materials*, 6(17):1701334, 2018.

[42] Nils Bernhardt, Kirill Koshelev, Simon J. U. White, Kelvin Wong Choon Meng, Johannes E. Froch, Sejeong Kim, Toan Trong Tran, Duk-Yong Choi, Yuri Kivshar, and Alexander S. Solntsev. Quasi-BIC resonant enhancement of second-harmonic generation in $WS_2$ monolayers. *Nano Letters*, 20(7):5309–5314, 2020.

[43] Nils Bernhardt, Sejeong Kim, Johannes E. Fröch, Simon J. U. White, Ngoc My Hanh Duong, Zhe He, Bo Chen, Jin Liu, Igor Aharonovich, and Alexander S. Solntsev. Large few-layer hexagonal boron nitride flakes for nonlinear optics. *Optics Letters*, 46(3):564–567, 2021.

[44] Toan Trong Tran, Kerem Bray, Michael J. Ford, Milos Toth, and Igor Aharonovich. Quantum emission from hexagonal boron nitride monolayers. *Nature Nanotechnology*, 11(1):37–41, 2016.

[45] Nathan Chejanovsky, Mohammad Rezai, Federico Paolucci, Youngwook Kim, Torsten Rendler, Wafa Rouabeh, Felipe Fávaro de Oliveira, Patrick Herlinger, Andrej Denisenko, Sen Yang, Ilja Gerhardt, Amit Finkler, Jurgen H. Smet, and Jörg Wrachtrup. Structural attributes and photodynamics of visible spectrum quantum emitters in hexagonal boron nitride. *Nano Letters*, 16(11):7037–7045, 2016.

[46] Toan Trong Tran, Cameron Zachreson, Amanuel Michael Berhane, Kerem Bray, Russell Guy Sandstrom, Lu Hua Li, Takashi Taniguchi, Kenji Watanabe, Igor Aharonovich, and Milos Toth. Quantum emission from defects in single-crystalline hexagonal boron nitride. *Physical Review Applied*, 5(3):034005, 2016.

[47] Toan Trong Tran, Christopher Elbadawi, Daniel Totonjian, Charlene J. Lobo, Gabriele Grosso, Hyowon Moon, Dirk R. Englund, Michael J. Ford, Igor Aharonovich, and Milos Toth. Robust multicolor single photon emission from point defects in hexagonal boron nitride. *ACS Nano*, 10(8):7331–7338, 2016.

[48] Yuen-Ron Shen. *The Principles of Nonlinear Optics*, Wiley-Interscience, New York, 2003.

[49] C. H. Monken. Aplicação da óptica de Fourier à conversão paramétrica descendente, 1998-2004. Apostila de curso.

[50] Cid B. De Araújo, Anderson S. L. Gomes, and Georges Boudebs. Techniques for nonlinear optical characterization of materials: a review. *Reports on Progress in Physics*, 79(3):036401, 2016.

[51] Hervé Rigneault and Pascal Berto. Tutorial: Coherent Raman light matter interaction processes. *Apl Photonics*, 3(9):091101, 2018.

[52] Dustin W. Shipp, Faris Sinjab, and Ioan Notingher. Raman spectroscopy: techniques and applications in the life sciences. *Advances in Optics and Photonics*, 9(2):315–428, 2017.

[53] Ji-Xin Cheng and X. Sunney Xie. Vibrational spectroscopic imaging of living systems: An emerging platform for biology and medicine. *Science*, 350(6264), 2015.

[54] Leonard Mandel and Emil Wolf. *Optical coherence and quantum optics*. Cambridge university press, 1995.

[55] Robert Splinter. *Handbook of Physics in Medicine and Biology*. 2010.

[56] Joseph R. Lakowicz. *Principles of fluorescence spectroscopy*. Springer science & business media, 2013.

[57] Pablo Artal. *Handbook of Visual Optics, Volume Two: Instrumentation and Vision Correction*. Taylor & Francis, 2017.

[58] Mohammad Adnan, Jeremy J. Baumberg, and G. Vijaya Prakash. Linear and nonlinear optical probing of various excitons in 2D inorganic-organic hybrid structures. *Scientific reports*, 10(1):1–10, 2020.

[59] "Icon Pack - Mice", by BioRender.com (2020). Retrieved from https://app.biorender.com/biorender-templates.

[60] Valentin Besse, Hervé Leblond, and Georges Boudebs. Fifth-order nonlinear susceptibility: Effect of third-order resonances in a classical theory. *Physical Review A*, 92(1):013818, 2015.

[61] Klaus-Dieter Bauer and Kurt Hingerl. Bulk quadrupole contribution to second harmonic generation from classical oscillator model in silicon. *Optics express*, 25(22):26567–26580, 2017.

[62] Klaus-Dieter Bauer, Martin Panholzer, and Kurt Hingerl. Bulk quadrupole contribution to second harmonic generation from a microscopic response function. *Physica status solidi (b)*, 253(2):234–240, 2016.

[63] Klaus-Dieter Bauer. Second harmonic generation in centrosymmetric media, 2019. Ph.D. Thesis.

[64] R. A. Ganeev. Nonlinear refraction and nonlinear absorption of various media. *Journal of Optics A: Pure and Applied Optics*, 7(12):717, 2005.

[65] Daniel S. Corrêa, Leonardo De Boni, Lino Misoguti, Ion Cohanoschi, Florencio E. Hernandez, and Cleber R. Mendonça. Z-scan theoretical analysis for three-, four-and five-photon absorption. *Optics communications*, 277(2):440–445, 2007.

[66] R. Feynman, R. Leighton, and M. Sands. *The Feynman Lectures on Physics, Vol. II, The New Millennium Edition: Mainly Electromagnetism and Matter*. 2015.

[67] Daniel A. Fleisch. *A student's guide to vectors and tensors*. Cambridge University Press, 2012.

[68] Jeffery J. Maki, Michelle S. Malcuit, J. E. Sipe, and Robert W. Boyd. Linear and nonlinear optical measurements of the lorentz local field. *Physical Review Letters*, 67:972–975, 1991.

[69] Hendrik A. Lorentz. *Theory of electrons, 2nd edn.(1915)*. Dover, New York, 1952.

[70] Bobo Gu, Chujun Zhao, Alexander Baev, Ken-Tye Yong, Shuangchun Wen, and Paras N. Prasad. Molecular nonlinear optics: recent advances and applications. *Advances in Optics and Photonics*, 8(2):328–369, 2016.

[71] Matt M. Coles, Mathew D. Williams, and David L. Andrews. Second harmonic generation in isotropic media: six-wave mixing of optical vortices. *Optics express*, 21(10):12783–12789, 2013.

[72] M. Ferray, Anne L'Huillier, X. F. Li, L. A. Lompre, G. Mainfray, and C. Manus. Multiple-harmonic conversion of 1064 nm radiation in rare gases. *Journal of Physics B: Atomic, Molecular and Optical Physics*, 21(3):L31, 1988.

[73] Aleksey Korobenko, Soham Saha, Alan T. K. Godfrey, Marina Gertsvolf, A. Yu Naumov, David M. Villeneuve, Alexandra Boltasseva, Vladimir M. Shalaev, and Paul B. Corkum. High-harmonic generation in metallic titanium nitride. *Nature communications*, 12(1):1–6, 2021.

[74] Zenghu Chang, Andy Rundquist, Haiwen Wang, Margaret M. Murnane, and Henry C. Kapteyn. Generation of coherent soft X rays at 2.7 nm using high harmonics. *Physical Review Letters*, 79(16):2967, 1997.

[75] K. J. Schafer, Baorui Yang, L. F. DiMauro, and K. C. Kulander. Above threshold ionization beyond the high harmonic cutoff. *Physical review letters*, 70(11):1599, 1993.

[76] Chao-Yu John Chung and Eric O. Potma. Biomolecular imaging with coherent nonlinear vibrational microscopy. *Annual review of physical chemistry*, 64:77–99, 2013.

[77] Yongchang Dong, Prakash Parajuli, Apparao M. Rao, Wim Thielemans, Samuel Eyley, Krishna Rani Sahoo, T. N. Narayanan, and Ramakrishna Podila. Intrinsic five-photon non-linear absorption of two-dimensional BN and its conversion to two-photon absorption in the presence of photo-induced defects. *Optical Materials*, 86:414–420, 2018.

[78] Stefan T. Jagsch, Ludwig A. Th. Greif, Stephan Reitzenstein, and Andrei Schliwa. Ground-state resonant two-photon transitions in wurtzite GaN/AlN quantum dots. *Physical Review B*, 99(24):245303, 2019.

[79] Richard C. Prince, Renee R. Frontiera, and Eric O. Potma. Stimulated Raman scattering: from bulk to nano. *Chemical reviews*, 117(7):5070–5094, 2017.

[80] Luigi Sirleto, Alessandro Vergara, and Maria Antonietta Ferrara. Advances in stimulated Raman scattering in nanostructures. *Advances in Optics and photonics*, 9(1):169–217, 2017.

[81] Wei Min, Christian W. Freudiger, Sijia Lu, and X. Sunney Xie. Coherent nonlinear optical imaging: Beyond fluorescence microscopy. *Annual Review of Physical Chemistry*, 62(1):507–530, 2011.

[82] Christophe Humbert and Thomas Noblet. A unified mathematical formalism for first to third order dielectric response of matter: Application to surface-specific two-colour vibrational optical spectroscopy. *Symmetry*, 13(1):153, 2021.

[83] Fei Chen, Lea Gozdzialski, Kuo-Kai Hung, Ulrike Stege, and Dennis K. Hore. Assessing the molecular specificity and orientation sensitivity of infrared, Raman, and vibrational sum-frequency spectra. *Symmetry*, 13(1):42, 2021.

[84] Alba Alfonso-García, Richa Mittal, Eun Seong Lee, and Eric O. Potma. Biological imaging with coherent Raman scattering microscopy: a tutorial. *Journal of biomedical optics*, 19(7):071407, 2014.

[85] Giovanni Guzman-Santiago, Adrian E. Villanueva-Luna, Jacob Licea-Rodriguez, and Israel Rocha-Mendoza. Tutorial for analyzing coherent Raman spectra excited with chirped femtosecond sources. *OSA Continuum*, 4(2):464–476, 2021.

[86] Andreas Otto. Theory of first layer and single molecule surface enhanced Raman scattering (SERS). *physica status solidi (a)*, 188(4):1455–1470, 2001.

[87] Barbara Fazio, Alessia Irrera, Stefano Pirotta, Cristiano D'Andrea, Salvatore Del Sorbo, Maria Josè Lo Faro, Pietro Giuseppe Gucciardi, Maria Antonia Iati, Rosalba Saija, Maddalena Patrini, Paolo Musumeci, Cirino Salvatore Vasi, Diederik S. Wiersma,

Matteo Galli, and Francesco Priolo. Coherent backscattering of Raman light. *Nature Photonics*, 11(3):170–176, 2017.

[88] Paula Machado and Sebastião Pádua. Quantum coherence of spatial photonic qudits: experimental measurement and path-marker analysis. *Journal of Optics*, 22(6):065201, 2020.

[89] Robert W. Hellwarth. Theory of stimulated Raman scattering. *Physical Review*, 130(5):1850, 1963.

[90] G. Batignani, G. Fumero, S. Mukamel, and T. Scopigno. Energy flow between spectral components in 2D broadband stimulated Raman spectroscopy. *Physical Chemistry Chemical Physics*, 17(16):10454–10461, 2015.

[91] G. Batignani, E. Pontecorvo, G. Giovannetti, C. Ferrante, G. Fumero, and T. Scopigno. Electronic resonances in broadband stimulated Raman spectroscopy. *Scientific reports*, 6(1):1–8, 2016.

[92] Upendra Harbola, Siva Umapathy, and Shaul Mukamel. Loss and gain signals in broadband stimulated-Raman spectra: Theoretical analysis. *Physical Review A*, 88(1):011801, 2013.

[93] Chao-Yu Chung, Julie Hsu, Shaul Mukamel, and Eric O. Potma. Controlling stimulated coherent spectroscopy and microscopy by a position-dependent phase. *Physical Review A*, 87(3):033833, 2013.

[94] Pascal Berto, Esben Ravn Andresen, and Hervé Rigneault. Background-free stimulated Raman spectroscopy and microscopy. *Physical review letters*, 112(5):053905, 2014.

[95] Delong Zhang, Mikhail N. Slipchenko, Daniel E. Leaird, Andrew M. Weiner, and Ji-Xin Cheng. Spectrally modulated stimulated Raman scattering imaging with an angle-to-wavelength pulse shaper. *Optics express*, 21(11):13864–13874, 2013.

[96] Delong Zhang, Ping Wang, Mikhail N. Slipchenko, and Ji-Xin Cheng. Fast vibrational imaging of single cells and tissues by stimulated Raman scattering microscopy. *Accounts of chemical research*, 47(8):2282–2290, 2014.

[97] Marco Andreana, Marie-Andrée Houle, Douglas J. Moffatt, Andrew Ridsdale, Edlef Buettner, François Légaré, and Albert Stolow. Amplitude and polarization modulated hyperspectral stimulated Raman scattering microscopy. *Optics express*, 23(22):28119–28131, 2015.

[98] Thomas Würthwein, Niklas M. Lüpken, Niels Irwin, and Carsten Fallnich. Mitigating cross-phase modulation artifacts in femtosecond stimulated Raman scattering. *Journal of Raman Spectroscopy*, 51(11):2265–2271, 2020.

[99] Julian Moger, Natalie L. Garrett, David Begley, Larisa Mihoreanu, Aikaterini Lalatsa, Maria Victoria Lozano, Mariarosa Mazza, Andreas Schatzlein, and Ijeoma Uchegbu. Imaging cortical vasculature with stimulated Raman scattering and two-photon photothermal lensing microscopy. *Journal of Raman Spectroscopy*, 43(5):668–674, 2012.

[100] Cheng Zong, Ranjith Premasiri, Haonan Lin, Yimin Huang, Chi Zhang, Chen Yang, Bin Ren, Lawrence D. Ziegler, and Ji-Xin Cheng. Plasmon-enhanced stimulated Raman scattering microscopy with single-molecule detection sensitivity. *Nature communications*, 10(1):1–11, 2019.

[101] Govind P. Agrawal, P. L. Baldeck, and R. R. Alfano. Temporal and spectral effects of cross-phase modulation on copropagating ultrashort pulses in optical fibers. *Physical Review A*, 40(9):5063, 1989.

[102] Govind P. Agrawal. Induced focusing of optical beams in self-defocusing nonlinear media. *Physical Review Letters*, 64(21):2487, 1990.

[103] J. Miguel Hickmann, A. S. L. Gomes, and Cid B. de Araújo. Observation of spatial cross-phase modulation effects in a self-defocusing nonlinear medium. *Physical review letters*, 68(24):3547, 1992.

[104] Andrea Bertoncini, Sergey P. Laptenok, Luca Genchi, Vijayakumar P. Rajamanickam, and Carlo Liberale. 3D-Printed high-NA catadioptric thin lens for suppression of XPM background in Stimulated Raman Scattering microscopy. *Journal of Biophotonics*, 14(5):e202000219, 2021.

[105] Catxere A. Casacio, Lars S. Madsen, Alex Terrasson, Muhammad Waleed, Kai Barnscheidt, Boris Hage, Michael A. Taylor, and Warwick P. Bowen. Quantum-enhanced nonlinear microscopy. *Nature*, 594(7862):201–206, 2021.

[106] Xavier Audier, Sandro Heuke, Peter Volz, Ingo Rimke, and Hervé Rigneault. Noise in stimulated Raman scattering measurement: From basics to practice. *Apl Photonics*, 5(1):011101, 2020.

[107] Chi Zhang, Delong Zhang, and Ji-Xin Cheng. Coherent Raman scattering microscopy in biology and medicine. *Annual review of biomedical engineering*, 17:415–445, 2015.

[108] Chien-Sheng Liao and Ji-Xin Cheng. In situ and in vivo molecular analysis by coherent Raman scattering microscopy. *Annual Review of Analytical Chemistry*, 9:69–93, 2016.

[109] Erwin Schrödinger. *What Is Life? The Physical Aspect of the Living Cell*. 1944.

[110] Niels Bohr. Light and life. *Nature*, 131:457–459, 1933.

[111] Francis A. Duck. The origins of medical physics. *Physica Medica*, 30(4):397–402, 2014.

[112] Stephen F. Keevil. Physics and medicine: a historical perspective. *The Lancet*, 379(9825):1517–1524, 2012.

[113] Harold Varmus. The impact of physics on biology and medicine. *Physics World*, 1999.

[114] Roberto de Andrade Martins. Robert hooke e a pesquisa microscópica dos seres vivos. *Filosofia e História da Biologia*, 6(1):105–142, 2011.

[115] Robert Hooke. *Micrographia: or, Some physiological descriptions of minute bodies made by magnifying glasses*. 1665. London: J. Martyn and J. Allestry (first edition).

[116] Robert H. Webb. Confocal optical microscopy. *Reports on Progress in Physics*, 59(3):427–471, 1996.

[117] James Pawley. *Handbook of Biological Confocal Microscopy*. 2006.

[118] Gufeng Wang and Ning Fang. Chapter four - Detecting and Tracking Nonfluorescent Nanoparticle Probes in Live Cells. In P. Michael Conn, editor, *Imaging and Spectroscopic Analysis of Living Cells*, volume 504 of *Methods in Enzymology*, pages 83–108. Academic Press, 2012.

[119] Amicia D. Elliott. Confocal microscopy: Principles and modern practices. *Current Protocols in Cytometry*, 92(1):e68, 2020.

[120] James Jonkman, Claire M. Brown, Graham D. Wright, Kurt I. Anderson, and Alison J. North. Tutorial: guidance for quantitative confocal microscopy. *Nature Protocols*, 15:1585–1611, 2020.

[121] "Diabetic Retinopathy Laser Photocoagulation Treatment", by BioRender.com (2020). Retrieved from https://app.biorender.com/biorender-templates.

[122] "Fluorescence Microscopy", by BioRender.com (2020). Retrieved from https://app.biorender.com/biorender-templates.

[123] Karlie A. Neilson, Naveid A. Ali, Sridevi Muralidharan, Mehdi Mirzaei, Michael Mariani, Gariné Assadourian, Albert Lee, Steven C. van Sluyter, and Paul A. Haynes. Less label, more free: Approaches in label-free quantitative mass spectrometry. *Proteomics*, 11(4):535–553, 2011.

[124] Arne D. Hofemeier, Henning Hachmeister, Christian Pilger, Matthias Schürmann, Johannes F. W. Greiner, Lena Nolte, Holger Sudhoff, Christian Kaltschmidt, Thomas Huser, and Barbara Kaltschmidt. Label-free nonlinear optical microscopy detects early markers for osteogenic differentiation of human stem cells. *Scientific Reports*, 6:26716, 2016.

[125] A. D. Cohen, M. D. Ikonomovic, E. E. Abrahamson, W. R. Paljug, S. T. DeKosky, I. M. Lefterov, R. P. Koldamova, L. Shao, M. L. Debnath, C. A. Mason, N. S. Mathis, and W. E. Klunk. Anti-amyloid effects of small molecule Aβ-binding agents in PS1/APP mice. *Letters in Drug Design & Discovery*, 6(6):437–444, 2009.

[126] Sabine Liebscher and Melanie Meyer-Luehmann. A peephole into the brain: Neuropathological features of Alzheimer's disease revealed by in vivo two-photon imaging. *Frontiers in Psychiatry*, 3:26, 2012.

[127] "Tissue-specific Effects of Connective Tissue and Mucosal Mast Cells: Inhalation", by BioRender.com (2020). Retrieved from https://app.biorender.com/biorender-templates.

[128] Samuel R. Pygall, Joanne Whetstone, Peter Timmins, and Colin D. Melia. Pharmaceutical applications of confocal laser scanning microscopy: The physical characterisation of pharmaceutical systems. *Advanced Drug Delivery Reviews*, 59(14):1434–1452, 2007. Intersection of Nanoscience and Modern Surface Analytical Methodology.

[129] Karel Svoboda and Ryohei Yasuda. Principles of two-photon excitation microscopy and its applications to neuroscience. *Neuron*, 50(6):823–839, 2006.

[130] J. G. White, W. B. Amos, and M. Fordham. An evaluation of confocal versus conventional imaging of biological structures by fluorescence light microscopy. *Journal of Cell Biology*, 105(1):41–48, 1987.

[131] Rafael Yuste and Winfried Denk. Dendritic spines as basic functional units of neuronal integration. *Nature*, 375(6533):682–684, 1995.

[132] Karel Svoboda, David W. Tank, and Winfried Denk. Direct measurement of coupling between dendritic spines and shafts. *Science*, 272(5262):716–719, 1996.

[133] Fritjof Helmchen, Karel Svoboda, Winfried Denk, and David W. Tank. In vivo dendritic calcium dynamics in deep-layer cortical pyramidal neurons. *Nature neuroscience*, 2(11):989–996, 1999.

[134] R. H. Christie, B. J. Bacskai, W. R. Zipfel, R. M. Williams, S. T. Kajdasz, W. W. Webb, and B. T. Hyman. Growth arrest of individual senile plaques in a model of Alzheimer's disease observed by in vivo multiphoton microscopy. *Journal of Neuroscience*, 21(3):858–864, 2001.

[135] Fritjof Helmchen and Jack Waters. Ca2+ imaging in the mammalian brain in vivo. *European journal of pharmacology*, 447(2-3):119–129, 2002.

[136] Megan E. McLellan, Stephen T. Kajdasz, Bradley T. Hyman, and Brian J. Bacskai. In vivo imaging of reactive oxygen species specifically associated with Thioflavine S-positive amyloid plaques by multiphoton microscopy. *Journal of Neuroscience*, 23(6):2212–2217, 2003.

[137] Dan Oron, Eirini Papagiakoumou, F. Anselmi, and Valentina Emiliani. Chapter 7 - Two-photon optogenetics. In Thomas Knöpfel and Edward S. Boyden, editors, *Optogenetics: Tools for Controlling and Monitoring Neuronal Activity*, volume 196 of *Progress in Brain Research*, pages 119–143. Elsevier, 2012.

[138] Jayne M. Squirrell, David L. Wokosin, John G. White, and Barry D. Bavister. Long-term two-photon fluorescence imaging of mammalian embryos without compromising viability. *Nature biotechnology*, 17(8):763–767, 1999.

[139] Weigang Wang, Jeffrey B. Wyckoff, Victoria Centonze Frohlich, Yuri Oleynikov, Stefan Hüttelmaier, Jiri Zavadil, Lukas Cermak, Erwin P. Bottinger, Robert H. Singer, John G. White, Jeffrey E. Segall, and John S. Condeelis. Single cell behavior in metastatic primary mammary tumors correlated with gene expression patterns revealed by molecular profiling. *Cancer research*, 62(21):6278–6288, 2002.

[140] Mark J. Miller, Sindy H. Wei, Ian Parker, and Michael D. Cahalan. Two-photon imaging of lymphocyte motility and antigen response in intact lymph node. *Science*, 296(5574):1869–1873, 2002.

[141] Michael D. Cahalan, Ian Parker, Sindy H. Wei, and Mark J. Miller. Two-photon tissue imaging: seeing the immune system in a fresh light. *Nature Reviews Immunology*, 2(11):872–880, 2002.

[142] Donald M. McDonald and Peter L. Choyke. Imaging of angiogenesis: from microscope to clinic. *Nature medicine*, 9(6):713–725, 2003.

[143] R. Mouras, P. Bagnaninchi, A. Downes, and A. Elfick. Multimodal, label-free nonlinear optical imaging for applications in biology and biomedical science. *Journal of Raman Spectroscopy*, 44(10):1373–1378, 2013.

[144] M. Weinigel, H. G. Breunig, M. Kellner-Höfer, R. Bückle, M. E. Darvin, M. Klemp, J. Lademann, and K. König. *In vivo* histology: optical biopsies with chemical contrast using clinical multiphoton/coherent anti-Stokes Raman scattering tomography. *Laser Physics Letters*, 11(5):055601, 2014.

[145] Michael Jermyn, Joannie Desroches, Kelly Aubertin, Karl St-Arnaud, Wendy-Julie Madore, Etienne De Montigny, Marie-Christine Guiot, Dominique Trudel, Brian C. Wilson, Kevin Petrecca, and Frederic Leblond. A review of Raman spectroscopy advances with an emphasis on clinical translation challenges in oncology. *Physics in Medicine & Biology*, 61(23):R370, 2016.

[146] E. B. Hanlon, R. Manoharan, T.-W. Koo, K. E. Shafer, J. T. Motz, M. Fitzmaurice, J. R. Kramer, I. Itzkan, R. R. Dasari, and M. S. Feld. Prospects for in vivo Raman spectroscopy. *Physics in Medicine & Biology*, 45(2):R1, 2000.

[147] Abigail S. Haka, Zoya Volynskaya, Joseph A. Gardecki, Jon Nazemi, Joanne Lyons, David Hicks, Maryann Fitzmaurice, Ramachandra R. Dasari, Joseph P. Crowe, and Michael S. Feld. In vivo margin assessment during partial mastectomy breast surgery using Raman spectroscopy. *Cancer research*, 66(6):3317–3322, 2006.

[148] Todd Hollon, Spencer Lewis, Christian W. Freudiger, X. Sunney Xie, and Daniel A. Orringer. Improving the accuracy of brain tumor surgery via Raman-based technology. *Neurosurgical focus*, 40(3):E9, 2016.

[149] Joannie Desroches, Michael Jermyn, Kelvin Mok, Cédric Lemieux-Leduc, Jeanne Mercier, Karl St-Arnaud, Kirk Urmey, Marie-Christine Guiot, Eric Marple, Kevin Petrecca, and Frédéric Leblond. Characterization of a Raman spectroscopy probe system for intraoperative brain tissue classification. *Biomedical optics express*, 6(7):2380–2397, 2015.

[150] Inês P. Santos, Elisa M. Barroso, Tom C. Bakker Schut, Peter J. Caspers, Cornelia G. F. van Lanschot, Da-Hye Choi, Martine F. Van Der Kamp, Roeland W. H. Smits, Remco Van Doorn, Rob M. Verdijk, Vincent Noordhoek Hegt, Jan H. von der Thüsen, Carolien H. M. van Deurzen, Linetta B. Koppert, Geert J. L. H. van Leenders, Patricia C. Ewing-Graham, Helena C. van Doorn, Clemens M. F. Dirven, Martijn B. Busstra, Jose Hardillo, Aniel Sewnaik, Ivo ten Hove, Hetty Mast, Dominiek A. Monserez, Cees Meeuwis, Tamar Nijsten, Eppo B. Wolvius, Robert J. Baatenburg de Jong, Gerwin J. Puppels, and Senada Koljenović. Raman spectroscopy for cancer detection and cancer surgery guidance: translation to the clinics. *Analyst*, 142(17):3025–3047, 2017.

[151] Andreas Barth and Christian Zscherp. What vibrations tell about proteins. *Quarterly Reviews of Biophysics*, 35(4):369–430, 2002.

[152] Dmitry Kurouski, Richard P. Van Duyne, and Igor K. Lednev. Exploring the structure and formation mechanism of amyloid fibrils by Raman spectroscopy: a review. *Analyst*, 140:4967–4980, 2015.

[153] Sean D. Moran and Martin T. Zanni. How to get insight into amyloid structure and formation from infrared spectroscopy. *The journal of physical chemistry letters*, 5(11):1984–1993, 2014.

[154] Katharina Klein, Alexander M. Gigler, Thomas Aschenbrenner, Roberto Monetti, Wolfram Bunk, Ferdinand Jamitzky, Gregor Morfill, Robert W. Stark, and Jürgen Schlegel. Label-free live-cell imaging with confocal Raman microscopy. *Biophysical journal*, 102(2):360–368, 2012.

[155] Wenlong Yang. *Biomedical Applications of Stimulated Raman Scattering Microscopy*. PhD thesis, Harvard University, Graduate School of Arts & Sciences, 2017.

[156] Inês Raquel Martins Ramos, Alison Malkin, and Fiona Mary Lyng. Current advances in the application of Raman spectroscopy for molecular diagnosis of cervical cancer. *BioMed research international*, 2015, 2015.

[157] Fanghao Hu, Lixue Shi, and Wei Min. Biological imaging of chemical bonds by stimulated Raman scattering microscopy. *Nature methods*, 16(9):830–842, 2019.

[158] Yihui Shen, Fanghao Hu, and Wei Min. Raman imaging of small biomolecules. *Annual review of biophysics*, 48:347–369, 2019.

[159] Lu Wei, Fanghao Hu, Yihui Shen, Zhixing Chen, Yong Yu, Chih-Chun Lin, Meng C. Wang, and Wei Min. Live-cell imaging of alkyne-tagged small biomolecules by stimulated Raman scattering. *Nature methods*, 11(4):410–412, 2014.

[160] Minbiao Ji, Daniel A. Orringer, Christian W. Freudiger, Shakti Ramkissoon, Xiaohui Liu, Darryl Lau, Alexandra J. Golby, Isaiah Norton, Marika Hayashi, Nathalie Y. R. Agar, Geoffrey S. Young, Cathie Spino, Sandro Santagata, Sandra Camelo-Piragua, Keith L. Ligon, Oren Sagher, and X. Sunney Xie. Rapid, label-free detection of brain tumors with stimulated Raman scattering microscopy. *Science translational medicine*, 5(201):201ra119–201ra119, 2013.

[161] Han-Wei Wang, Thuc T. Le, and Ji-Xin Cheng. Label-free imaging of arterial cells and extracellular matrix using a multimodal CARS microscope. *Optics communications*, 281(7):1813–1822, 2008.

[162] Hyeon Jeong Lee and Ji-Xin Cheng. Imaging chemistry inside living cells by stimulated Raman scattering microscopy. *Methods*, 128:119–128, 2017.

[163] Iwan W. Schie, Christoph Krafft, and Jürgen Popp. Applications of coherent Raman scattering microscopies to clinical and biological studies. *Analyst*, 140(12):3897–3909, 2015.

[164] Conor L. Evans, Eric O. Potma, Mehron Puoris' haag, Daniel Côté, Charles P. Lin, and X. Sunney Xie. Chemical imaging of tissue in vivo with video-rate coherent anti-Stokes Raman scattering microscopy. *Proceedings of the National Academy of Sciences*, 102(46):16807–16812, 2005.

[165] Brian G. Saar, Christian W. Freudiger, Jay Reichman, C. Michael Stanley, Gary R. Holtom, and X. Sunney Xie. Video-rate molecular imaging in vivo with stimulated Raman scattering. *science*, 330(6009):1368–1370, 2010.

[166] María Salazar-Roa and Marcos Malumbres. Fueling the cell division cycle. *Trends in cell biology*, 27(1):69–81, 2017.

[167] Fa-Ke Lu, Srinjan Basu, Vivien Igras, Mai P. Hoang, Minbiao Ji, Dan Fu, Gary R. Holtom, Victor A. Neel, Christian W. Freudiger, David E. Fisher, and X. Sunney

Xie. Label-free DNA imaging in vivo with stimulated Raman scattering microscopy. *Proceedings of the National Academy of Sciences*, 112(37):11624–11629, 2015.

[168] Alexandre Guimarães de Almeida Barros, Jessika Cristina Bridi, Bruno Rezende de Souza, Celio de Castro Junior, Karen Cecilia de Lima Torres, Leandro Malard, Ado Jorio, Débora Marques de Miranda, Kaveh Ashrafi, and Marco Aurélio Romano-Silva. Dopamine signaling regulates fat content through $\beta$-oxidation in caenorhabditis elegans. *PLoS One*, 9(1):e85874, 2014.

[169] Yan Fu, Haifeng Wang, Terry B. Huff, Riyi Shi, and Ji-Xin Cheng. Coherent anti-stokes Raman scattering imaging of myelin degradation reveals a calcium-dependent pathway in lyso-PtdCho-induced demyelination. *Journal of neuroscience research*, 85(13):2870–2881, 2007.

[170] Yunzhou Shi, Riyi Shi, Ji-Xin Cheng, Delong Zhang, Terry B. Huff, Xiaofei Wang, and Xiao-Ming Xu. Longitudinal in vivo coherent anti-Stokes Raman scattering imaging of demyelination and remyelination in injured spinal cord. *Journal of biomedical optics*, 16(10):106012, 2011.

[171] Ji-xin Cheng, Andreas Volkmer, Lewis D. Book, and X. Sunney Xie. An epi-detected coherent anti-Stokes Raman scattering (E-CARS) microscope with high spectral resolution and high sensitivity. *The Journal of Physical Chemistry B*, 105(7):1277–1280, 2001.

[172] Jean-Claude Diels and Wolfgang Rudolph. *Ultrashort laser pulse phenomena*. Elsevier, 2006.

[173] Xu Zhang, Maarten B. J. Roeffaers, Srinjan Basu, Joseph R. Daniele, Dan Fu, Christian W. Freudiger, Gary R. Holtom, and X. Sunney Xie. Label-free live cell imaging of nucleic acids using stimulated Raman scattering (SRS) microscopy. *ChemPhysChem*, 13(4):1054–1059, 2012.

[174] Lu Wei, Yong Yu, Yihui Shen, Meng C. Wang, and Wei Min. Vibrational imaging of newly synthesized proteins in live cells by stimulated Raman scattering microscopy. *Proceedings of the National Academy of Sciences*, 110(28):11226–11231, 2013.

[175] Christian W. Freudiger, Rolf Pfannl, Daniel A. Orringer, Brian G. Saar, Minbiao Ji, Qing Zeng, Linda Ottoboni, Wei Ying, Christian Waeber, John R. Sims, Philip L. De Jager, Oren Sagher, Martin A. Philbert, Xiaoyin Xu, Santosh Kesari, X. Sunney Xie, and Geoffrey S. Young. Multicolored stain-free histopathology with coherent Raman imaging. *Laboratory investigation*, 92(10):1492–1502, 2012.

[176] Minbiao Ji, Spencer Lewis, Sandra Camelo-Piragua, Shakti H. Ramkissoon, Matija Snuderl, Sriram Venneti, Amanda Fisher-Hubbard, Mia Garrard, Dan Fu, Anthony C.

Wang, Jason A. Heth, Cormac O. Maher, Nader Sanai, Timothy D. Johnson, Christian W. Freudiger, Oren Sagher, Xiaoliang Sunney Xie, and Daniel A. Orringer. Detection of human brain tumor infiltration with quantitative stimulated Raman scattering microscopy. *Science translational medicine*, 7(309):309ra163–309ra163, 2015.

[177] Fa-Ke Lu, David Calligaris, Olutayo I. Olubiyi, Isaiah Norton, Wenlong Yang, Sandro Santagata, X. Sunney Xie, Alexandra J. Golby, and Nathalie Y. R. Agar. Label-free neurosurgical pathology with stimulated Raman imaging. *Cancer research*, 76(12):3451–3462, 2016.

[178] M. Strassnig and M. Ganguli. About a peculiar disease of the cerebral cortex: Alzheimer's original case revisited. *Psychiatry (Edgmont)*, 2(9):30–33, 2005.

[179] K. A. Jellinger. Alzheimer 100 – highlights in the history of Alzheimer research. *Journal of Neural Transmission*, 113:1603–1623, 2006.

[180] Masashi Kitazawa, Rodrigo Medeiros, and Frank M. LaFerla. Transgenic mouse models of Alzheimer disease: developing a better model as a tool for therapeutic interventions. *Current pharmaceutical design*, 18(8):1131–1147, 2012.

[181] Eleanor Drummond and Thomas Wisniewski. Alzheimer's disease: experimental models and reality. *Acta neuropathologica*, 133(2):155–175, 2017.

[182] Association Alzheimer's. 2018 Alzheimer's disease facts and figures. *Alzheimer's & Dementia*, 14(3):367–429, 2018.

[183] Andre Zeug, Michal Stawarski, Katarzyna Bieganska, Svetlana Korotchenko, Jakub Wlodarczyk, Alexander Dityatev, and Evgeni Ponimaskin. Chapter 13 - Current microscopic methods for the neural ECM analysis. In Alexander Dityatev, Bernhard Wehrle-Haller, and Asla Pitkänen, editors, *Brain Extracellular Matrix in Health and Disease*, volume 214 of *Progress in Brain Research*, pages 287–312. Elsevier, 2014.

[184] M. Citron. Alzheimer's disease: treatments in discovery and development. *Nature Neuroscience*, 5:1055–1057, 2002.

[185] Emerson A. Fonseca, Lucas Lafetá, Renan Cunha, Hudson Miranda, João Campos, Helton G. Medeiros, Marco A. Romano-Silva, Raigna A. Silva, Alexandre S. Barbosa, Rafael P. Vieira, Leandro M. Malard, and Ado Jorio. A fingerprint of amyloid plaques in a bitransgenic animal model of Alzheimer's disease obtained by statistical unmixing analysis of hyperspectral Raman data. *Analyst*, 144:7049–7056, 2019.

[186] John K. J. Archer, Caroline D. Sudworth, Rachel Williams, Thien How, Nicholas Stone, David Mann, and Richard A. Black. Improvements in Alzheimer's disease diagnosis using principle components analysis (PCA) in combination with Raman spectroscopy. *Proceedings of the Society of Photo-Optical Instrumentation Engineers*, 6628:218–227, 2007.

[187] Pu Chen, Aiguo Shen, Wei Zhao, Seong-Joon Baek, Hua Yuan, and Jiming Hu. Raman signature from brain hippocampus could aid Alzheimer's disease diagnosis. *Applied Optics*, 48(24):4743–4748, 2009.

[188] Francesca Palombo, Francesco Tamagnini, J. Charles G. Jeynes, Sara Mattana, Imogen Swift, Jayakrupakar Nallala, Jane Hancock, Jonathan T. Brown, Andrew D. Randall, and Nick Stone. Detection of Aβ plaque-associated astrogliosis in Alzheimer's disease brain by spectroscopic imaging and immunohistochemistry. *Analyst*, 143(4):850–857, 2018.

[189] "Pathology of Alzheimer's Disease 2", by BioRender.com (2020). Retrieved from https://app.biorender.com/biorender-templates.

[190] Frank M. LaFerla and Kim N. Green. Animal models of Alzheimer disease. *Cold Spring Harbor perspectives in medicine*, 2(11):a006320, 2012.

[191] David R. Borchelt, Tamara Ratovitski, Judy van Lare, Michael K. Lee, Vicki Gonzales, Nancy A. Jenkins, Neal G. Copeland, Donald L. Price, and Sangram S. Sisodia. Accelerated amyloid deposition in the brains of transgenic mice coexpressing mutant presenilin 1 and amyloid precursor proteins. *Neuron*, 19(4):939 – 945, 1997.

[192] Joanna L. Jankowsky, Hilda H. Slunt, Tamara Ratovitski, Nancy A. Jenkins, Neal G. Copeland, and David R. Borchelt. Co-expression of multiple transgenes in mouse CNS: a comparison of strategies. *Biomolecular Engineering*, 17(6):157 – 165, 2001.

[193] Monica Garcia-Alloza, Elissa M. Robbins, Sandy X. Zhang-Nunes, Susan M. Purcell, Rebecca A. Betensky, Susan Raju, Claudia Prada, Steven M. Greenberg, Brian J. Bacskai, and Matthew P. Frosch. Characterization of amyloid deposition in the APPswe/PS1dE9 mouse model of Alzheimer disease. *Neurobiology of Disease*, 24(3):516 – 524, 2006.

[194] Howard Eichenbaum, Tim Otto, and Neal J. Cohen. The hippocampus—what does it do? *Behavioral and neural biology*, 57(1):2–36, 1992.

[195] William E. Klunk, Brian J. Bacskai, Chester A. Mathis, Stephen T. Kajdasz, Megan E. McLellan, Matthew P. Frosch, Manik L. Debnath, Daniel P. Holt, Yanming Wang, and Bradley T. Hyman. Imaging Aβ plaques in living transgenic mice with multiphoton microscopy and Methoxy-X04, a systemically administered Congo Red derivative. *Journal of Neuropathology & Experimental Neurology*, 61(9):797–805, 2002.

[196] C. Condello, P. Yuan, A. Schain, and J. Grutzendler. Microglia constitute a barrier that prevents neurotoxic protofibrillar $A\beta_{42}$ hotspots around plaques. *Nature Communication*, 6:6176, 2015.

[197] P. Yuan, C. Condello, C. D. Keene, Y. Wang, T. D. Bird, S. M. Paul, W. Luo, M. Colonna, D. Baddeley, and J. Grutzendler. TREM2 haplodeficiency in mice and humans impairs

the microglia barrier function leading to decreased amyloid compaction and severe axonal dystrophy. *Neuron*, 90(4):724 – 739, 2016.

[198] C. Condello, A. Schain, and J. Grutzendler. Multicolor time-stamp reveals the dynamics and toxicity of amyloid deposition. *Scientific Reports*, 1:19, 2011.

[199] Luciano Bachmann, Denise Maria Zezell, Adriana da Costa Ribeiro, Laércio Gomes, and Amando Siuiti Ito. Fluorescence spectroscopy of biological tissues—a review. *Applied Spectroscopy Reviews*, 41(6):575–590, 2006.

[200] Monica Monici. Cell and tissue autofluorescence research and diagnostic applications. *Biotechnology Annual Review*, 11:227 – 256, 2005.

[201] Rebecca Richards-Kortum and Eva Sevick-Muraca. Quantitative optical spectroscopy for tissue diagnosis. *Annual Review of Physical Chemistry*, 47(1):555–606, 1996.

[202] Alexandra Moreno-García, Alejandra Kun, Olga Calero, Miguel Medina, and Miguel Calero. An overview of the role of lipofuscin in age-related neurodegeneration. *Frontiers in Neuroscience*, 12:464, 2018.

[203] P. J. Campagnola, A. C. Millard, M. Terasaki, P. E. Hoppe, C. J. Malone, and W. A. Mohler. Three-dimensional high-resolution second-harmonic generation imaging of endogenous structural proteins in biological tissues [published correction appears in Biophys. J. 2012 aug 8;103(3):627]. *Biophysical Journal*, 82((1 Pt 1)):493–508, 2002.

[204] Warren R. Zipfel, Rebecca M. Williams, Richard Christie, Alexander Yu Nikitin, Bradley T. Hyman, and Watt W. Webb. Live tissue intrinsic emission microscopy using multiphoton-excited native fluorescence and second harmonic generation. *Proceedings of the National Academy of Sciences*, 100(12):7075–7080, 2003.

[205] N. H. Green, R. M. Delaine-Smith, H. J. Askew, R. Byers, G. C. Reilly, and S. J. Matcher. A new mode of contrast in biological second harmonic generation microscopy. *Scientific Reports*, 7:13331, 2017.

[206] M. Rivard, M. Laliberté, A. Bertrand-Grenier, C. Harnagea, C. P. Pfeffer, M. Vallières, Y. St-Pierre, A. Pignolet, M. Khakani, and F. Légaré. The structural origin of second harmonic generation in fascia. *Biomedical Optics Express*, 2(1):26–36, 2011.

[207] P. Hanczyc, M. Samoc, and B. Norden. Multiphoton absorption in amyloid protein fibres. *Nature Photonics*, 7:969–972, 2013.

[208] J. Tsai, J. Grutzendler, K. J. Duff, and W-B. Gan. Fibrillar amyloid deposition leads to local synaptic abnormalities and breakage of neuronal branches. *Nature Neuronscience*, 7:1181–1183, 2004.

[209] H. B. Rajamohamedsait and E. M. Sigurdsson. *Histological Staining of Amyloid and Pre-amyloid Peptides and Proteins in Mouse Tissue. In: Sigurdsson E., Calero M., Gasset M. (eds) Amyloid Proteins*, volume 849. Humana Press, 2012.

[210] Li Fu, Zhuguang Wang, Brian T. Psciuk, Dequan Xiao, Victor S. Batista, and Elsa C. Y. Yan. Characterization of parallel β-sheets at interfaces by chiral sum frequency generation spectroscopy. *The Journal of Physical Chemistry Letters*, 6(8):1310–1315, 2015.

[211] S. J. Roeters, C. N. van Dijk, A. Torres-Knoop, E. H. G. Backus, R. K. Campen, M. Bonn, and S. Woutersen. Determining in situ protein conformation and orientation from the amide-I sum-frequency generation spectrum: Theory and experiment. *The Journal of Physical Chemistry A*, 117(29):6311–6322, 2013.

[212] Junjun Tan, Jiahui Zhang, Yi Luo, and Shuji Ye. Misfolding of a human islet amyloid polypeptide at the lipid membrane populates through β-sheet conformers without involving α-helical intermediates. *Journal of the American Chemical Society*, 141(5):1941–1948, 2019.

[213] Emerson Fonseca, Lucas Lafetá, João Campos, Renan Cunha, Alexandre Barbosa, Marco A. Romano-Silva, Rafael Vieira, Leandro Malard, and Ado Jorio. Micro-Raman spectroscopy of lipid halo and dense-core amyloid plaques: aging process characterization in the Alzheimer's disease APPswePS1ΔE9 mouse model. *Analyst*, 146(19):6014–6025, 2021.

[214] Jefferson W. Kinney, Shane M. Bemiller, Andrew S. Murtishaw, Amanda M. Leisgang, Arnold M. Salazar, and Bruce T. Lamb. Inflammation as a central mechanism in Alzheimer's disease. *Alzheimer's & Dementia: Translational Research & Clinical Interventions*, 4:575 – 590, 2018.

[215] M.T. Heneka, M.K. O'Banion, D. Terwel, and M. P. Kummer. Neuroinflammatory processes in Alzheimer's disease. *Journal of Neural Transmission*, 177:919 – 947, 2010.

[216] Elodie Martin, Céline Boucher, Bertrand Fontaine, and Cécile Delarasse. Distinct inflammatory phenotypes of microglia and monocyte-derived macrophages in Alzheimer's disease models: effects of aging and amyloid pathology. *Aging Cell*, 16(1):27–38, 2017.

[217] Robert G. Nagele, Jerzy Wegiel, Venkat Venkataraman, Humi Imaki, Kuo-Chiang Wang, and Jarek Wegiel. Contribution of glial cells to the development of amyloid plaques in Alzheimer's disease. *Neurobiology of aging*, 25(5):663–674, 2004.

[218] M. Ahmed, J. Davis, D. Aucoin, T. Sato, S. Ahuja, S. Aimoto, J. I. Elliott, W. E. Van Nostrand, and S. O. Smith. Structural conversion of neurotoxic amyloid-$\beta_{1\text{-}42}$ oligomers to fibrils. *Nature Structural & Molecular Biology*, 17:561–567, 2010.

[219] Risto Cukalevski, Barry Boland, Birgitta Frohm, Eva Thulin, Dominic Walsh, and Sara Linse. Role of aromatic side chains in amyloid β-protein aggregation. *ACS Chemical Neuroscience*, 3(12):1008–1016, 2012.

[220] Andreas Barth. Infrared spectroscopy of proteins. *Biochimica et Biophysica Acta (BBA) - Bioenergetics*, 1767(9):1073 – 1101, 2007.

[221] Keith A. Oberg, Jean-Marie Ruysschaert, and Erik Goormaghtigh. The optimization of protein secondary structure determination with infrared and circular dichroism spectra. *European Journal of Biochemistry*, 271(14):2937–2948, 2004.

[222] Christoph Heinrich, Alexander Hofer, Andreas Ritsch, Christian Ciardi, Stefan Bernet, and Monika Ritsch-Marte. Selective imaging of saturated and unsaturated lipids by wide-field CARS-microscopy. *Optics Express*, 16(4):2699–2708, 2008.

[223] Luyuan Zhang, Longwei Yin, Chengxiang Wang, Ning Lun, Yongxin Qi, and Dong Xiang. Origin of visible photoluminescence of ZnO quantum dots: defect-dependent and size-dependent. *The Journal of Physical Chemistry C*, 114(21):9651–9658, 2010.

[224] Andrea C. Ferrari, Jannik C. Meyer, Vittorio Scardaci, Cinzia Casiraghi, Michele Lazzeri, Francesco Mauri, Stefano Piscanec, Dingde Jiang, Konstantin Sergeevich Novoselov, Siegmar Roth, and Andre K. Geim. Raman spectrum of graphene and graphene layers. *Physical review letters*, 97(18):187401, 2006.

[225] Ruben Mas-Balleste, Cristina Gomez-Navarro, Julio Gomez-Herrero, and Felix Zamora. 2D materials: to graphene and beyond. *Nanoscale*, 3(1):20–30, 2011.

[226] Fengnian Xia, Han Wang, Di Xiao, Madan Dubey, and Ashwin Ramasubramaniam. Two-dimensional material nanophotonics. *Nature Photonics*, 8(12):899–907, 2014.

[227] Ganesh R. Bhimanapati, Zhong Lin, Vincent Meunier, Yeonwoong Jung, Judy Cha, Saptarshi Das, Di Xiao, Youngwoo Son, Michael S. Strano, Valentino R. Cooper, Liangbo Liang, Steven G. Louie, Emilie Ringe, Wu Zhou, Steve S. Kim, Rajesh R. Naik, Bobby G. Sumpter, Humberto Terrones, Fengnian Xia, Yeliang Wang, Jun Zhu, Deji Akinwande, Nasim Alem, Jon A. Schuller, Raymond E. Schaak, Mauricio Terrones, and Joshua A. Robinson. Recent advances in two-dimensional materials beyond graphene. *ACS nano*, 9(12):11509–11539, 2015.

[228] Debasis Bera, Lei Qian, Teng-Kuan Tseng, and Paul H. Holloway. Quantum dots and their multimodal applications: a review. *Materials*, 3(4):2260–2345, 2010.

[229] Andres Galdámez-Martinez, Guillermo Santana, Frank Güell, Paulina R. Martínez-Alanis, and Ateet Dutt. Photoluminescence of ZnO nanowires: a review. *Nanomaterials*, 10(5):857, 2020.

[230] K. S. Novoselov, A. K. Geim, S. V. Morozov, D. Jiang, Y. Zhang, S. V. Dubonos, I. V. Grigorieva, and A. A. Firsov. Electric field effect in atomically thin carbon films. *Science*, 306:666–669, 2004.

[231] Zhong Lin, Bruno R. Carvalho, Ethan Kahn, Ruitao Lv, Rahul Rao, Humberto Terrones, Marcos A. Pimenta, and Mauricio Terrones. Defect engineering of two-dimensional transition metal dichalcogenides. *2D Materials*, 3(2):022002, 2016.

[232] Valeria Nicolosi, Manish Chhowalla, Mercouri G. Kanatzidis, Michael S. Strano, and Jonathan N. Coleman. Liquid exfoliation of layered materials. *Science*, 340(6139):1226419, 2013.

[233] Anton Autere, Henri Jussila, Yunyun Dai, Yadong Wang, Harri Lipsanen, and Zhipei Sun. Nonlinear optics with 2D layered materials. *Advanced Materials*, 30(24):1705963, 2018.

[234] J. W. You, S. R. Bongu, Q. Bao, and N. C. Panoiu. Nonlinear optical properties and applications of 2D materials: theoretical and experimental aspects. *Nanophotonics*, 8(1):63–97, 2019.

[235] Nardeep Kumar, Sina Najmaei, Qiannan Cui, Frank Ceballos, Pulickel M. Ajayan, Jun Lou, and Hui Zhao. Second harmonic microscopy of monolayer $MoS_2$. *Physical Review B*, 87(16):161403, 2013.

[236] Alexander A. Puretzky, Liangbo Liang, Xufan Li, Kai Xiao, Kai Wang, Masoud Mahjouri-Samani, Leonardo Basile, Juan Carlos Idrobo, Bobby G. Sumpter, Vincent Meunier, and David B. Geohegan. Low-frequency Raman fingerprints of two-dimensional metal dichalcogenide layer stacking configurations. *ACS nano*, 9(6):6333–6342, 2015.

[237] Guillaume Cassabois, Pierre Valvin, and Bernard Gil. Hexagonal boron nitride is an indirect bandgap semiconductor. *Nature Photonics*, 10(4):262, 2016.

[238] Yong-Nian Xu and W. Y. Ching. Calculation of ground-state and optical properties of boron nitrides in the hexagonal, cubic, and wurtzite structures. *Physical Review B*, 44:7787, 1991.

[239] W. J. Yu, W. M. Lau, S. P. Chan, Z. F. Liu, and Q. Q. Zheng. Ab initio study of phase transformations in boron nitride. *Physical Review B*, 67(1):014108, 2003.

[240] S. Reich, A. C. Ferrari, R. Arenal, A. Loiseau, I. Bello, and J. Robertson. Resonant Raman scattering in cubic and hexagonal boron nitride. *Physical Review B*, 71(20):205201, 2005.

[241] Jiwei Ling, Xianchong Miao, Yangye Sun, Yiqing Feng, Liwu Zhang, Zhengzong Sun, and Minbiao Ji. Vibrational imaging and quantification of two-dimensional hexagonal boron nitride with stimulated Raman scattering. *ACS nano*, 13(12):14033–14040, 2019.

[242] Leandro M. Malard, Lucas Lafeta, Renan S. Cunha, Rafael Nadas, Andreij Gadelha, Luiz Gustavo Cançado, and Ado Jorio. Studying 2D materials with advanced Raman spectroscopy: CARS, SRS and TERS. *Physical Chemistry Chemical Physics*, 23(41):23428–23444, 2021.

[243] Representation of single layer of h-BN from Graphene Supermarket.

[244] Darshana Wickramaratne, Leigh Weston, and Chris G. Van de Walle. Monolayer to bulk properties of hexagonal boron nitride. *The Journal of Physical Chemistry C*, 122(44):25524–25529, 2018.

[245] Kenji Watanabe, Takashi Taniguchi, and Hisao Kanda. Direct-bandgap properties and evidence for ultraviolet lasing of hexagonal boron nitride single crystal. *Nature Materials*, 3(6):404, 2004.

[246] Cory R. Dean, Andrea F. Young, Inanc Meric, Chris Lee, Lei Wang, Sebastian Sorgenfrei, Kenji Watanabe, Takashi Taniguchi, Phillip Kim, Kenneth L. Shepard, and J. Hone. Boron nitride substrates for high-quality graphene electronics. *Nature Nanotechnology*, 5(10):722, 2010.

[247] Lu Hua Li, Elton J. G. Santos, Tan Xing, Emmanuele Cappelluti, Rafael Roldán, Ying Chen, Kenji Watanabe, and Takashi Taniguchi. Dielectric screening in atomically thin boron nitride nanosheets. *Nano Letters*, 15(1):218–223, 2015.

[248] James H. Edgar, Timothy B. Hoffman, B. Clubine, M. Currie, X. Z. Du, J. Y. Lin, and H. X. Jiang. Characterization of bulk hexagonal boron nitride single crystals grown by the metal flux technique. *Journal of Crystal Growth*, 403:110–113, 2014.

[249] Qunhong Weng, Dmitry G. Kvashnin, Xi Wang, Ovidiu Cretu, Yijun Yang, Min Zhou, Chao Zhang, Dai-Ming Tang, Pavel B. Sorokin, Yoshio Bando, and Dmitri Golberg. Tuning of the optical, electronic, and magnetic properties of boron nitride nanosheets with oxygen doping and functionalization. *Advanced Materials*, 29(28):1700695, 2017.

[250] K. H. Michel and B. Verberck. Theory of elastic and piezoelectric effects in two-dimensional hexagonal boron nitride. *Physical Review B*, 80(22):224301, 2009.

[251] Sejeong Kim, Johannes E. Fröch, Augustine Gardner, Chi Li, Igor Aharonovich, and Alexander S. Solntsev. Second-harmonic generation in multilayer hexagonal boron nitride flakes. *Optics letters*, 44(23):5792–5795, 2019.

[252] Bruno R. Carvalho, Yuanxi Wang, Kazunori Fujisawa, Tianyi Zhang, Ethan Kahn, Ismail Bilgin, Pulickel M. Ajayan, Ana M. De Paula, Marcos A. Pimenta, Swastik Kar, Vincent H. Crespi, Mauricio Terrones, and Leandro M. Malard. Nonlinear dark-field imaging of one-dimensional defects in monolayer dichalcogenides. *Nano letters*, 20(1):284–291, 2019.

[253] Qijie Liang, Qian Zhang, Xiaoxu Zhao, Meizhuang Liu, and Andrew T. S. Wee. Defect engineering of two-dimensional transition-metal dichalcogenides: applications, challenges, and opportunities. *ACS nano*, 15(2):2165–2181, 2021.

[254] A. Katzir, J. T. Suss, A. Zunger, and A. Halperin. Point defects in hexagonal boron nitride. I. EPR, thermoluminescence, and thermally-stimulated-current measurements. *Physical Review B*, 11(6):2370, 1975.

[255] A. Zunger and A. Katzir. Point defects in hexagonal boron nitride. II. Theoretical studies. *Physical review B*, 11(6):2378, 1975.

[256] E. Y. Andrei, A. Katzir, and J. T. Suss. Point defects in hexagonal boron nitride. III. EPR in electron-irradiated BN. *Physical Review B*, 13(7):2831, 1976.

[257] Romain Bourrellier, Sophie Meuret, Anna Tararan, Odile Stéphan, Mathieu Kociak, Luiz H. G. Tizei, and Alberto Zobelli. Bright UV single photon emission at point defects in h-BN. *Nano letters*, 16(7):4317–4321, 2016.

[258] Yu-Ming He, Genevieve Clark, John R. Schaibley, Yu He, Ming-Cheng Chen, Yu-Jia Wei, Xing Ding, Qiang Zhang, Wang Yao, Xiaodong Xu, Chao-Yang Lu, and Jian-Wei Pan. Single quantum emitters in monolayer semiconductors. *Nature Nanotechnology*, 10(6):497, 2015.

[259] M. Koperski, K. Nogajewski, A. Arora, V. Cherkez, P. Mallet, J-Y. Veuillen, J. Marcus, P. Kossacki, and M. Potemski. Single photon emitters in exfoliated $WSe_2$ structures. *Nature Nanotechnology*, 10(6):503, 2015.

[260] Marcus W. Doherty, Neil B. Manson, Paul Delaney, Fedor Jelezko, Jörg Wrachtrup, and Lloyd C. L. Hollenberg. The nitrogen-vacancy colour centre in diamond. *Physics Reports*, 528(1):1–45, 2013.

[261] S. Castelletto, B. C. Johnson, Viktor Ivády, N. Stavrias, T. Umeda, A. Gali, and T. Ohshima. A silicon carbide room-temperature single-photon source. *Nature Materials*, 13(2):151, 2014.

[262] Joshua D. Caldwell, Igor Aharonovich, Guillaume Cassabois, James H. Edgar, Bernard Gil, and D. N. Basov. Photonics with hexagonal boron nitride. *Nature Reviews Materials*, 4(8):552–567, 2019.

[263] Gabriel Constantinescu, Agnieszka Kuc, and Thomas Heine. Stacking in bulk and bilayer hexagonal boron nitride. *Physical review letters*, 111(3):036104, 2013.

[264] Jonathan N. Coleman, Mustafa Lotya, Arlene O'Neill, Shane D. Bergin, Paul J. King, Umar Khan, Karen Young, Alexandre Gaucher, Sukanta De, Ronan J. Smith, Igor V. Shvets, Sunil K. Arora, George Stanton, Hye-Young Kim, Kangho Lee, Gyu Tae Kim, Georg S. Duesberg, Toby Hallam, John J. Boland, Jing Jing Wang, John F.

Donegan, Jaime C. Grunlan, Gregory Moriarty, Aleksey Shmeliov, Rebecca J. Nicholls, James M. Perkins, Eleanor M. Grieveson, Koenraad Theuwissen, David W. McComb, Peter D. Nellist, and Valeria Nicolosi. Two-dimensional nanosheets produced by liquid exfoliation of layered materials. *Science*, 331(6017):568–571, 2011.

[265] Luc Museur, Eduard Feldbach, and Andrei Kanaev. Defect-related photoluminescence of hexagonal boron nitride. *Physical review B*, 78(15):155204, 2008.

[266] Nasim Alem, Rolf Erni, Christian Kisielowski, Marta D. Rossell, Will Gannett, and A. Zettl. Atomically thin hexagonal boron nitride probed by ultrahigh-resolution transmission electron microscopy. *Physical Review B*, 80(15):155425, 2009.

[267] Stephen J. Pennycook and Christian Colliex. Spectroscopic imaging in electron microscopy. *MRS Bulletin*, 37(1):13–18, 2012.

[268] L. Weston, D. Wickramaratne, M. Mackoit, A. Alkauskas, and C. G. Van de Walle. Native point defects and impurities in hexagonal boron nitride. *Physical Review B*, 97(21):214104, 2018.

[269] J. R. Toledo, D. B. de Jesus, M. Kianinia, A. S. Leal, C. Fantini, L. A. Cury, G. A. M. Sáfar, I. Aharonovich, and K. Krambrock. Electron paramagnetic resonance signature of point defects in neutron-irradiated hexagonal boron nitride. *Physical Review B*, 98:155203, 2018.

[270] Sherif Abdulkader Tawfik, Sajid Ali, Marco Fronzi, Mehran Kianinia, Toan Trong Tran, Catherine Stampfl, Igor Aharonovich, Milos Toth, and Michael J. Ford. First-principles investigation of quantum emission from hBN defects. *Nanoscale*, 9(36):13575–13582, 2017.

[271] A. Sajid, Jeffrey R. Reimers, and Michael J. Ford. Defect states in hexagonal boron nitride: Assignments of observed properties and prediction of properties relevant to quantum computation. *Physical Review B*, 97(6):064101, 2018.

[272] Mehdi Abdi, Jyh-Pin Chou, Adam Gali, and Martin B. Plenio. Color centers in hexagonal boron nitride monolayers: a group theory and ab initio analysis. *ACS Photonics*, 5(5):1967–1976, 2018.

[273] Maciej Koperski, Karol Nogajewski, and Marek Potemski. Single photon emitters in boron nitride: More than a supplementary material. *Optics Communications*, 411:158–165, 2018.

[274] Thonimar Vieira de Alencar Souza. *Espectroscopia de femtossegundos e propriedades ópticas não lineares em nanomateriais bidimensionais*. PhD thesis, Universidade Federal de Minas Gerais, Programa de Pós-graduação em Física, 2014.

# Appendix A - Additional defects 1PL spectra

Figure A.1 show 1PL spectra associated with defect states in the sample discussed in subsection 4.7.2. These spectra have been previously reported in literature [44, 47] and recent *ab initio* calculations proposed the association of some of these spectra[1] with certain types of point defects. Spectra A.1A, A.1B, and A.1C were associated with neutral and charged vacancy-

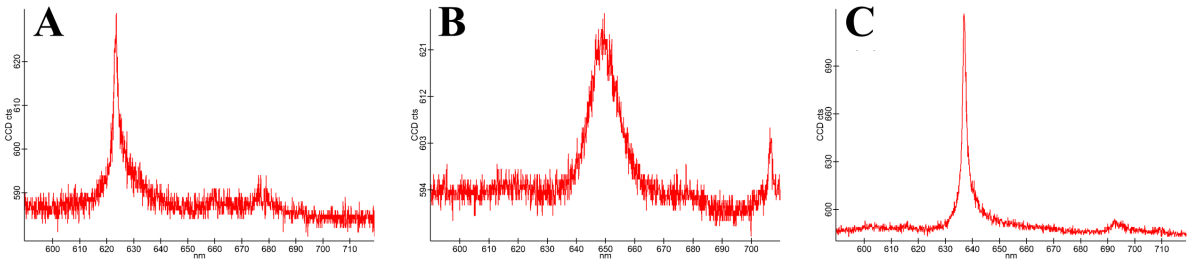


Figure A.1: 1PL spectra (A-C) associated with defect states in the sample used in chapter 4. The different spectra were taken at different spots of the sample.

related defects [44, 271, 272]. A recent analysis based on group theory has shown that these defects (present in h-BN samples) belong to symmetry groups that lack inversion symmetry [272].

[1] Additional spectra can be found in the supplementary material for reference [26].

# Appendix B - Four-fold rotational symmetry of SHG in h-BN

From expression (2.34), the second-order polarization, responsible for SHG in h-BN, can be written as [15]

$$P_i^{(2)} = \epsilon_0 \sum_{j,k} \chi_{ijk}^{(2)} E_j E_k. \tag{B.1}$$

The evaluation of expression (B.1) for SHG is usually facilitated by a contracted notation in which we express the susceptibility as the two-indices tensor $d_{is}$. In such a case, $d_{is}$ satisfies the expression $2d_{is} \equiv \chi_{ijk}^{(2)}$ [15], where $i$ represents the components $x$, $y$ and $z$ (expressed as 1, 2, and 3, respectively), while $s$ varies from 1 to 6 following the relation [15, 48, 274]:

| $s$ | 1 | 2 | 3 | 4 | 5 | 6 |
|---|---|---|---|---|---|---|
| $ij$ | xx | yy | zz | yz | zx | xy |

.

Therefore, for SHG, expression (B.1) can take the form [15]:

$$\begin{bmatrix} P_x^{(2)}(2\omega) \\ P_y^{(2)}(2\omega) \\ P_z^{(2)}(2\omega) \end{bmatrix} = 2\epsilon_0 \begin{bmatrix} d_{11} & d_{12} & d_{13} & d_{14} & d_{15} & d_{16} \\ d_{21} & d_{22} & d_{23} & d_{24} & d_{25} & d_{26} \\ d_{31} & d_{32} & d_{33} & d_{34} & d_{35} & d_{36} \end{bmatrix} \begin{bmatrix} E_x^2(\omega) \\ E_y^2(\omega) \\ E_z^2(\omega) \\ 2E_y(\omega)E_z(\omega) \\ 2E_x(\omega)E_z(\omega) \\ 2E_x(\omega)E_y(\omega) \end{bmatrix}. \tag{B.2}$$

As is the case of the second-order susceptibility tensor $\chi_{ijk}^{(2)}$, the contracted tensor $d_{is}$ also depends on the symmetry properties of the material. Since the h-BN monolayer belongs to the group $D_{3h}$, $d_{is}$ is reduced to [15, 48]:

$$d_{is}^{D_{3h}} = \begin{bmatrix} 0 & 0 & 0 & 0 & 0 & d_{16} \\ d_{21} & d_{22} & 0 & 0 & 0 & 0 \\ 0 & 0 & 0 & 0 & 0 & 0 \end{bmatrix}, \tag{B.3}$$

where symmetry conditions[1] lead to $d_{22} = -d_{21} = -d_{16} \propto \chi_{xxy}^{(2)}$ [15, 48, 274]. Hence,

[1] The explicit form of the second-order susceptibility tensor for each of the 32 crystal classes can be found in Table 1.5.2 of reference [15].

expression (B.2) further reduces to

$$\begin{bmatrix} P_x^{(2)}(2\omega) \\ P_y^{(2)}(2\omega) \\ P_z^{(2)}(2\omega) \end{bmatrix} = \epsilon_0 \chi_{xxy}^{(2)} \begin{bmatrix} 2E_x(\omega)E_y(\omega) \\ E_x^2(\omega) - E_y^2(\omega) \\ 0 \end{bmatrix}. \tag{B.4}$$

Thus, if a sufficiently intense field of the form $\vec{E} = E_0 sen(\phi)\hat{x} + E_0 cos(\phi)\hat{y}$ interacts with the h-BN monolayer, according to (B.4), the angular dependence of SHG polarization in the material can be expressed as

$$\begin{bmatrix} P_x^{(2)}(2\omega) \\ P_y^{(2)}(2\omega) \\ P_z^{(2)}(2\omega) \end{bmatrix} = \epsilon_0 \chi_{xxy}^{(2)} \begin{bmatrix} sin(2\phi) \\ -cos(2\phi) \\ 0 \end{bmatrix}, \tag{B.5}$$

where $\phi$ is the polarization angle of the incident light.

Second harmonic generation intensity $I(2\omega)$ is given by the square modulus of the SHG field $\vec{E}(2\omega)$. This field is proportional to $\vec{P}^{(2)}(2\omega)$, for which we have the components in equation (B.5). Therefore, we can write the SHG field $\vec{E}(2\omega)$ as

$$\vec{E}^{(2)}(2\omega) \propto sen(2\phi)\hat{x} + cos(2\phi)\hat{y}. \tag{B.6}$$

In our experiment presented in section 4.7.4, we used a fixed polarizer in front of the detector,

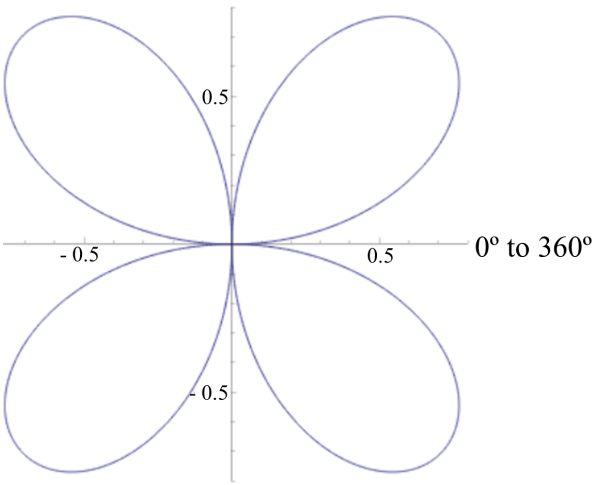


Figure B.1: Polar plot of expression (B.7). Adapted from Wolfram Alpha online software.

so that the measured intensity $I_m(2\omega)$, associated with the field $\vec{E}_m(2\omega)$, only concerns the $x$ component of the field B.6:

$$I_m(2\omega) \propto \left|\vec{E}_m(2\omega)\right| \equiv \left|\vec{E}(2\omega) \cdot \hat{x}\right| \propto sin\,(2\phi)\,, \tag{B.7}$$

which yields the four-fold rotational symmetry in figure B.1.

# Appendix C - Third-order nonlinearities in 2D materials

One of the perspectives of studying nonlinear optics for imaging 2D materials is the investigation of materials with different bandgap energies and different resonance mechanisms within the bandgap. As discussed in section 4.7, resonance mechanisms, such as defects, can modulate the efficiency of nonlinear effects. Furthermore, since many 2D materials, such as TMDs, exhibit strong optical nonlinearities, the study can also involve competing effects. This is expected to occur more frequently for third-order nonlinearities since second-order nonlinear effects can only occur in the absence of inversion symmetry. Figure C.1 shows SRS

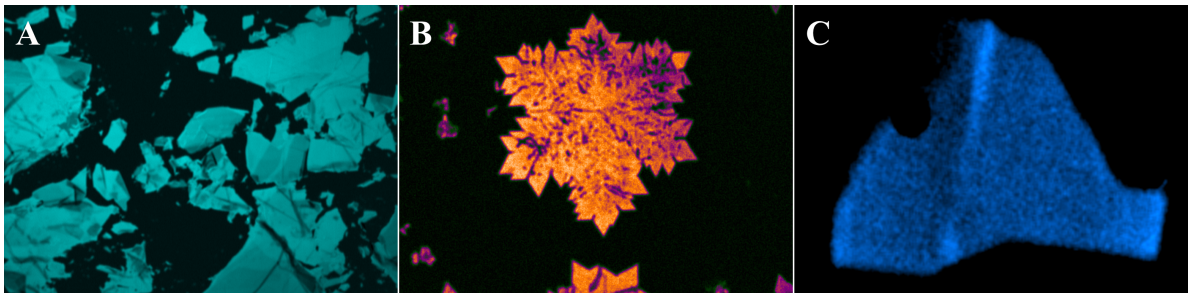


Figure C.1: Third-order nonlinearities in 2D materials. SRS images of (A) graphene, (B) $MoS_2$, and (C) h-BN (adapted from reference [242]).

images of three materials with increasing gap energy: graphene (zero bandgap semiconductor, figure C.1A), $MoS_2$ (semiconductor, figure C.1B), and h-BN (insulator, figure C.1C). This study seeks to investigate the origin of different third-order effects on 2D materials, different mechanisms of signal enhancement, and applications.